LHCb 上底介子含粲衰变过程中强子谱学的实验研究

Experimental study of hadron spectroscopy in beauty meson to open charm decays at LHCb

(申请清华大学理学博士学位论文)

培养单位：工程物理系
学　　科：物理学
研 究 生：陈　晨
指导教师：张黎明　副教授

二〇二二年三月

Experimental study of hadron spectroscopy in beauty meson to open charm decays at LHCb

Dissertation Submitted to
Tsinghua University
in partial fulfillment of the requirement
for the degree of
Doctor of Philosophy
in
Physics

by

Chen Chen

Dissertation Supervisor: Professor Liming Zhang

March, 2022

摘 要

描述强相互作用的量子色动力学（QCD）具有渐近自由的特性，在高能标下适用于微扰展开, 而在低能标下由非微扰效应主导。通过强子谱学研究深入理解 QCD 的低能非微扰性质是当前粒子物理学的重要前沿，其中重味强子尤其是重味奇特强子态的研究具有独特的优势。本论文基于欧洲核子研究中心大型强子对撞机上的底夸克实验（LHCb), 首次研究了底介子的两个含粲衰变过程, $B^0 \to D^+D^-K^+\pi^-$ 和 $B^+ \to D_s^+D_s^-K^+$，发现了一个新的粲介子激发态 $D_{s0}(2590)^+$ 和一个四夸克态候选者 $X(3960)$，并用振幅分析方法测量了它们的性质。

论文工作利用 LHCb 实验于 2016–2018 年采集的质子-质子对撞数据重建了 $B^0 \to D^+D^-K^+\pi^-$ 衰变过程，并在 $D^+K^+\pi^-$ 质量谱中发现了多个全新的峰结构。由于 B^0 四体衰变过程的成分很复杂，论文仅研究了 $D^+K^+\pi^-$ 质量阈值附近的新结构，其几乎所有信息都包含在低 $K^+\pi^-$ 质量区间 ($m(K^+\pi^-) < 0.75\,\mathrm{GeV}$) 的数据中。通过对这部分数据的振幅分析，论文以超过 10 倍标准差的统计显著性发现了新激发态 $D_{s0}(2590)^+$，并测量其质量、宽度和自旋宇称为 $m = 2591 \pm 6 \pm 7\,\mathrm{MeV}$, $\Gamma = 89 \pm 16 \pm 12\,\mathrm{MeV}$ 和 $J^P = 0^-$。$D_{s0}(2590)^+$ 是基态 D_s^+ 介子径向激发态 $D_s(2^1S_0)^+$ 的候选者。实验测量的 $D_{s0}(2590)^+$ 质量和势模型预言的 $D_s(2^1S_0)^+$ 质量有较大差异，引起了理论家对 $D_{s0}(2590)^+$ 内部结构的兴趣。

利用 LHCb 实验 2011–2018 年采集的所有质子-质子对撞数据，论文工作还发现了新的衰变道 $B^+ \to D_s^+D_s^-K^+$，并测量了它与 $B^+ \to D^+D^-K^+$ 过程的相对分支比，结果为 $\mathcal{B}(B^+ \to D_s^+D_s^-K^+)/\mathcal{B}(B^+ \to D^+D^-K^+) = 0.525 \pm 0.033 \pm 0.027 \pm 0.034$。同时，在 $D_s^+D_s^-$ 系统中还发现了一个新的阈值结构 $X(3960)$，统计显著性超过 10 倍标准差。通过振幅分析测量了它的质量、宽度和自旋宇称，结果为$m = 3955 \pm 6 \pm 11\,\mathrm{MeV}$, $\Gamma = 48 \pm 17 \pm 10\,\mathrm{MeV}$和$J^{PC} = 0^{++}$。$X(3960)$ 与之前在 D^+D^- 末态发现的 $\chi_{c0}(3930)$ 具有相同的自旋宇称，且质量宽度一致，暗示二者可能是同一个粒子，记为 X。在此假设下，论文计算得到分宽度之比为$\Gamma(X \to D^+D^-)/\Gamma(X \to D_s^+D_s^-) = 0.29 \pm 0.09 \pm 0.10 \pm 0.08$。$X \to D^+D^-$ 分宽度小于 $X \to D_s^+D_s^-$ 分宽度，这预示 $X(3960)/\chi_{c0}(3930)$ 可能是奇特粲偶素。

以上所有结果中，第一项不确定度为统计不确定度，第二项为系统不确定度，第三项来自于 D^+ 和 D_s^+ 衰变分支比等输入参数的不确定度。

关键词：量子色动力学；粲介子；奇特粲偶素；振幅分析；LHCb 实验

ABSTRACT

Quantum chromodynamics (QCD) is the fundamental theory describing the strong interaction in the Standard Model (SM) of particle physics. It has an important feature called the asymptotic freedom. The QCD coupling asymptotically goes to zero at high energy scale and thus the perturbative method is applicable, while the strong coupling in low energy region results in a failure of the perturbative method and makes the QCD calculation extremely difficult. Studies of hadron spectroscopy are at the frontier of modern particle physics to promote the understanding of the nonperturbative property of the low energy QCD. Heavy-flavor hadrons, especially the exotic states containing heavy-flavor quark(s), provide a unique platform for the studies of the nonperturbative QCD. This thesis presents the first analyses of two B-meson decays to open-charm final state, $B^0 \to D^+D^-K^+\pi^-$ and $B^+ \to D_s^+D_s^-K^+$, using the proton–proton collision data collected by the Large Hadron Collider beauty (LHCb) experiment at CERN. Two new mesons, a charm-strange meson $D_{s0}(2590)^+$ and a tetraquark candidate $X(3960)$, are observed in the $D^+K^+\pi^-$ and $D_s^+D_s^-$ systems, respectively. Amplitude analyses are performed to measure the properties of the two states.

The $B^0 \to D^+D^-K^+\pi^-$ decay is studied with the pp collision data collected at a center-of-mass energy of 13 TeV during the 2016–2018 period, corresponding an integrated luminosity $5.4\,\text{fb}^{-1}$. Two new peaking structures in the $D^+K^+\pi^-$ mass spectrum are observed, corresponding to undiscovered excited D_s^+ mesons. Due to the complexity of the four-body B-meson decay, this thesis only focuses on the study of the state near the $D^+K^+\pi^-$ mass threshold. This state can be isolated from the messy structures at higher mass by requiring the $K^+\pi^-$ system in the low mass region, $m(K^+\pi^-) < 0.75\,\text{GeV}$. An amplitude analysis is performed on the $B^0 \to D^+D^-K^+\pi^-$ data in the low $K^+\pi^-$ mass region to measure the properties of the new D_s^+ state, whose mass and width, and spin-parity are $m = 2591 \pm 6 \pm 7\,\text{MeV}$, $\Gamma = 89 \pm 16 \pm 12\,\text{MeV}$ and $J^P = 0^-$. The statistical significance of the new D_s^+ state is found over 10 standard deviations (σ). The new resonance, denoted as $D_{s0}(2590)^+$, is a strong candidate to be the $D_s(2^1S_0)^+$ state, the radial excitation of the pseudoscalar ground-state D_s^+ meson. A large discrepancy is found between the measured mass of the $D_{s0}(2590)^+$ resonance and theoretical mass of the $D_s(2^1S_0)^+$ state, arousing the interest of theorists to study the inner structure of the $D_{s0}(2590)^+$ meson.

The $B^+ \to D_s^+ D_s^- K^+$ decay is observed for the first time using the full LHCb dataset collected in 2011, 2012 and 2015–2018 at center-of-mass energies of 7, 8 and 13 TeV, respectively. The corresponding integrated luminosity is roughly $9\,\mathrm{fb}^{-1}$. The branching fraction of the $B^+ \to D_s^+ D_s^- K^+$ decay is measured relative to that of the $B^+ \to D^+ D^- K^+$ process as $\mathcal{B}(B^+ \to D_s^+ D_s^- K^+)/\mathcal{B}(B^+ \to D^+ D^- K^+) = 0.525 \pm 0.033 \pm 0.027 \pm 0.034$. A near-threshold $X(3960)$ is observed in the $D_s^+ D_s^-$ mass spectrum with statistical significance over 10σ. The mass, width and spin-parity of the $X(3960)$ state are measured with an amplitude analysis to be $m = 3955 \pm 6 \pm 11\,\mathrm{MeV}$, $\Gamma = 48 \pm 17 \pm 10\,\mathrm{MeV}$ and $J^{PC} = 0^{++}$. The mass and width of the $X(3960)$ state are comparable to those of $\chi_{c0}(3930)$ meson previously observed in the D^+D^- final state, and they both have spin-parity $J^{PC} = 0^{++}$, indicating that they could be an identical state, denoted as X. Under this assumption, the partial width ratio of the two decay modes is obtained, $\Gamma(X \to D^+D^-)/\Gamma(X \to D_s^+ D_s^-) = 0.29 \pm 0.09 \pm 0.10 \pm 0.08$. The fact that $\Gamma(X \to D_s^+ D_s^-) > \Gamma(X \to D^+ D^-)$ indicates the exotic nature of the $X(3960)/\chi_{c0}(3930)$ state. This is understood as that the $X \to D_s^+ D_s^-$ decay is suppressed compared with the $X \to D^+ D^-$ process if the X state is a conventional charmonium meson, because it is harder to excite an $s\bar{s}$ pair than a $d\bar{d}$ pair from vacuum and the former decay also has a much smaller phase space volume than that of the latter process.

In all the numerical results presented above, the first uncertainty is statistical, the second systematic, and the third (optional) is due to the uncertainties on the input parameters, *e.g.* branching fractions of the D^+ and D_s^+ decays.

Keywords: QCD; Charm meson; Exotic charmonium; Amplitude analysis; LHCb

TABLE OF CONTENTS

LIST OF FIGURES AND TABLES

LIST OF SYMBOLS AND ACRONYMS

SM	Standard Model
QCD	Quantum chromodynamics
QED	Quantum electrodynamics
EW	Electroweak theory
GIM	Glashow–Iliopoulos–Maiani mechanism
CKM	Cabibbo–Kobayashi–Maskawa matrix
OZI	Okubo–Zweig–Iizuka rule
GI	Godfrey–Isgur model
GI-S	Godfrey–Isgur model with the screen effect
LHC	Large Hadron Collider
LHCb	Large Hadron Collider beauty experiment
CERN	European Organization for Nuclear Research
LINAC	Linear Particle Accelerator
PSB	Proton Synchrotron Booster
SPS	Super Proton Synchrotron
Run *n*	The *n*-th run period of the LHC
PID	Particle identification
VELO	Vertex Locator
TT	Tracker Turicensis
OT	Outer Tracker
IT	Inner Tracker
IP	Impact parameter
PV	Primary vertex
nTracks	Number of tracks
MagUp	Magnetic field pointing upwards
MagDown	Magnetic field pointing downwards
RICH	Ring Imaging Cherenkov detector
SPD	Scintillator Pad Detector
PS	Preshower
ECAL	Electromagnetic Calorimeter
HCAL	Hadron Calorimeter
MWPC	Multi-Wire Proportional Chambers

GEM	Gas Electron Multiplier
L0	Level-0 hardware trigger
HLT	High level software trigger
TOS	Trigger on signal
TIS	Trigger independent of signal
TOB	Trigger on between
MC	Monte Carlo simulation
DTF	Decay Tree Fitter
NDC	Non-double-charm background
CB	Crystal Ball function
PDF	Probability density function
NR	Non-resonant component
FWHM	Full width at half maximum
BW	Breit-Wigner function
MVA	Multivariate analysis
BDTG	Gradient-boosting decision tree
KDE	kernel density estimation

CHAPTER 1 INTRODUCTION

Particle physics attempts to answer the most fundamental questions about the basic building blocks of matter and the interactions in the Universe. To date, the best knowledge of particle physics is embodied in a unified theory, the Standard Model (SM), which classifies all known elementary particles and describes three of the four known fundamental interactions: the electromagnetic, weak and strong forces (gravity excepted). In the SM, the strong interaction is described by quantum chromodynamics (QCD), which has an interesting feature of the so-called asymptotic freedom[1]. The strength of the interaction decreases at high energy, allowing perturbative calculations; while at low energy, the strength increases, resulting in a failure of perturbative methods and thus making precise calculations extremely difficult. The strong interaction at low energy region has not been fully understood yet. A synergy of theoretical and experimental exploration is underway to promote the understanding of the low-energy QCD. One of the important aspects is the study of hadron spectroscopy.

Hadrons are composite particles formed by the elementary particles called quarks via the strong interaction. They generally have masses and binding energies in the non-perturbative region of QCD. Studies of hadron spectroscopy are at the frontier to promote the understanding of the strong interaction at low energy scale. Among all hadrons, mesons with the quark content $q\overline{q}$ have the simplest structure and thus provide essential tests on theoretical calculations. There are also mesons containing more than two quarks, referred to as being exotic, which have more complex inner structure than that of conventional $q\overline{q}$ mesons and thus arouse great interest of physicists to study the dynamics of their formation. One of the important physical topics is the investigation of mesons containing the charm quark, *e.g.* the charm-strange ($c\bar{s}$) and charmonium ($c\bar{c}$) mesons, as well as the exotic states containing additional quarks. The charm-strange and charmonium meson spectra have drawn particular attention since the discoveries of the $\chi_{c1}(3872)$[2], $D_{s0}^*(2317)^+$[3] and $D_{s1}(2460)^+$[4] states in 2003. The three mesons are inferred to be exotic because their properties are inconsistent with theoretical predictions for conventional states[5-8]. However, there are no conclusive interpretations of these states, and their inner structures remain as mysteries today. Since 2003, many new mesons containing $c\bar{s}$ or $c\bar{c}$ quarks are observed in experiment. Some are found well fitted into the conventional spectrum, while others are exotic with their nature remaining to be understood. More experimental results are essential to reveal the inner structure of these mesons.

Studies of $B \to D^{(*)}\overline{D}^{(*)}K^{(*)}$ decays ① have shown great potential to discover new charm-strange and charmonium mesons, as well as to measure their properties[9-14]. In 2008, the Belle collaboration observed the $D_{s1}^{*}(2700)^{+}$ state in the $B^{+} \to D^{0}\overline{D}^{0}K^{+}$ decay[9]. More recently in 2021, the LHCb collaboration reported two $X(2900)$ states decaying into $D^{-}K^{+}$ in the $B^{+} \to D^{+}D^{-}K^{+}$ decay[13-14], establishing the first observation of open-charm tetraquark candidates composed of $cs\bar{u}\bar{d}$. The analysis also observed a new state in the $D^{+}D^{-}$ system, $\chi_{c0}(3930)$, whose mass is close to the $D_{s}^{+}D_{s}^{-}$ mass threshold. Besides the conventional $c\bar{c}$ interpretation, the $\chi_{c0}(3930)$ state could also be regarded as a $c\bar{c}s\bar{s}$ tetraquark[15] or a $D_{s}^{+}D_{s}^{-}$ molecular[16] due to its near-threshold feature, and thus it can decay into $D_{s}^{+}D_{s}^{-}$. The $B^{+} \to D_{s}^{+}D_{s}^{-}K^{+}$ decay provides a unique opportunity to search for the $\chi_{c0}(3930) \to D_{s}^{+}D_{s}^{-}$ process, as well as other resonances decaying into $D_{s}^{+}D_{s}^{-}$. The study of the $B^{0} \to D^{+}D^{-}K^{+}\pi^{-}$ decay is a natural extension of that of the $B^{+} \to D^{+}D^{-}K^{+}$ process. Besides the possibility to investigate the states in the $B^{+} \to D^{+}D^{-}K^{+}$ decay, this channel also provides a particular opportunity to search for charm-strange mesons in the $D^{+}K^{+}\pi^{-}$ system. This thesis aims at searching for new mesons containing charm quark(s) in the $B^{0} \to D^{+}D^{-}K^{+}\pi^{-}$ and $B^{+} \to D_{s}^{+}D_{s}^{-}K^{+}$ decays and measuring their properties, to provide experimental tests and inputs to theoretical studies of the hadron spectrum and to further promote the understanding of the strong interaction in low energy region.

In the following sections of this chapter, a brief introduction to the theoretical background is presented, including the SM (QCD included) and the quark model. Then, overviews on the experimental and theoretical progresses are given on the charm-strange and charmonium mesons that are studied in the $B^{0} \to D^{+}D^{-}K^{+}\pi^{-}$ and $B^{+} \to D_{s}^{+}D_{s}^{-}K^{+}$ decays in this thesis.

---

① The inclusion of charge-conjugate processes is always implied, and natural units with $\hbar = c = 1$ are taken throughout this thesis.

1.1 Standard Model of particle physics

1.1.1 Rise of the SM

By the early 1960s, physicists already had quantum electrodynamics (QED) to handle the electromagnetism. QED can make extremely precise calculations for the magnetic moment of the electron[17] and the Lamb shift[18]. However, the success of QED was not repeated in the quantum-field descriptions of the strong and weak interactions[19].

The solution to the theory of the strong interaction started from the classification of hadrons. In 1961, Gell-Mann and Ne'eman generalized the SU(2) isospin symmetry [20-22] and the strangeness conservation [23-24] to an SU(3) symmetry, and the "Eightfold Way" they invented made great success classifying observed hadrons [25-26]. Subsequently in 1964, the quark model proposed by Gell–Mann and Zweig[27-28] explained that hadrons are composed of three type of quarks: up (u), down (d) and strange (s), and the SU(3) symmetry of hadrons are in fact the consequence of the symmetry of quarks. Later, a new degree of freedom with an SU(3) symmetry, color, was found necessary to govern the Fermi statistics of the Ω^- particle[29-31]. Though the concept of quarks made a great success classifying hadrons, it remained as a mystery whether quarks are real particles or not. There was positive evidence that the point-like structures discovered in nucleons could correspond to real quarks[32-33], but there was also negative evidence that no free quark was observed in experiment. The puzzle was finally solved by an SU(3) gauge theory of the strong interaction with the color degree as the field source, the so-called QCD[34], which treats quarks as elementary particles and explains that the non-observation of free quarks is due to the color confinement resulting from the stronger coupling strength at the larger distance.

The path to the theory of the weak interaction started from the improvement of the Fermi four-fermion theory[35] in 1950s. The $V-A$ structure of the weak interaction was proposed to account for the parity violation[36-39]. Meanwhile, it was realized that the weak interaction should be mediated by massive vector bosons[40-41], and there were attempts to build a gauge theory for the weak interaction[42-47]. However, the masses of the bosons in these theories had to be inserted by hand, which violates the gauge invariance, resulting in the non-renormalizability of the theories. The problem was finally solved by Weinberg and Salam in 1967[48-49], who applied the brilliant ideas of the spontaneous symmetry breaking[50-55] to the SU(2)×U(1) gauge theory[46-47], and derived a model describing the electromagnetic and weak interactions simultaneously, the so-called eletroweak (EW) theory. This theory was proved renormalizable[56]. The EW theory predicts three massive gauge bosons $W^{\pm}$ and Z^0 as force carriers of the weak interaction and the Higgs boson responsible for the masses of particles. Investigation of the weak interaction in the quark sector made further progress. Following the quark mixing picture proposed by Cabibbo[57], a fourth quark was realized necessary to account for the abnormally small $K_{\mathrm{L}}^0 \to \mu^+\mu^-$ branching fraction via the GIM mechanism in 1970[58], establishing the second generation of quarks, and the third generation came soon in 1973 to explain the *CP* violation in K^0 decays[59].

In 1974, the SM was finally developed into the formation it is today. The particles it predicts were observed one after another. With the last missing piece, the Higgs boson, observed in 2012[60-61], the SM finally met its accomplishment in experiment. However, there are still clouds in the sky of particle physics. The SM does not allow the neutrino mass, explain the size of matter-antimatter asymmetry in the Universe, describe dark matter and dark energy, *etc.* These unsolved mysteries remain to be answered with ongoing studies.

1.1.2 Elementary particles

Elementary particles in the SM are classified in Fig. 1.1, including twelve spin-half fermions and their antiparticles, four spin-one gauge bosons and the spin-zero Higgs boson. The fermions fall into two categories, quarks and leptons, which are basic building blocks of matter. Different species of the fermions are referred to as different flavors. All quarks and leptons participate in the weak interaction, while only quarks and three of the leptons (e, μ and τ) are electrically charged and interact electromagnetically. In addition, Quarks have a unique property called color charge, with which they involve in the strong interaction, and are bound to form composite particles called hadrons. The gauge bosons are force carriers of the three interactions, where the photon is responsible for electromagnetic interaction, the $W^{\pm}$ and Z^0 bosons mediate the weak interaction, and the gluon carries the strong force. The Higgs boson serves as the origin of masses of particles, and interacts with all massive particles. Neutrinos remain massless in the SM, but are found massive in experiment to account for the neutrino oscillation. This is the only confirmed phenomenon beyond the SM[62].

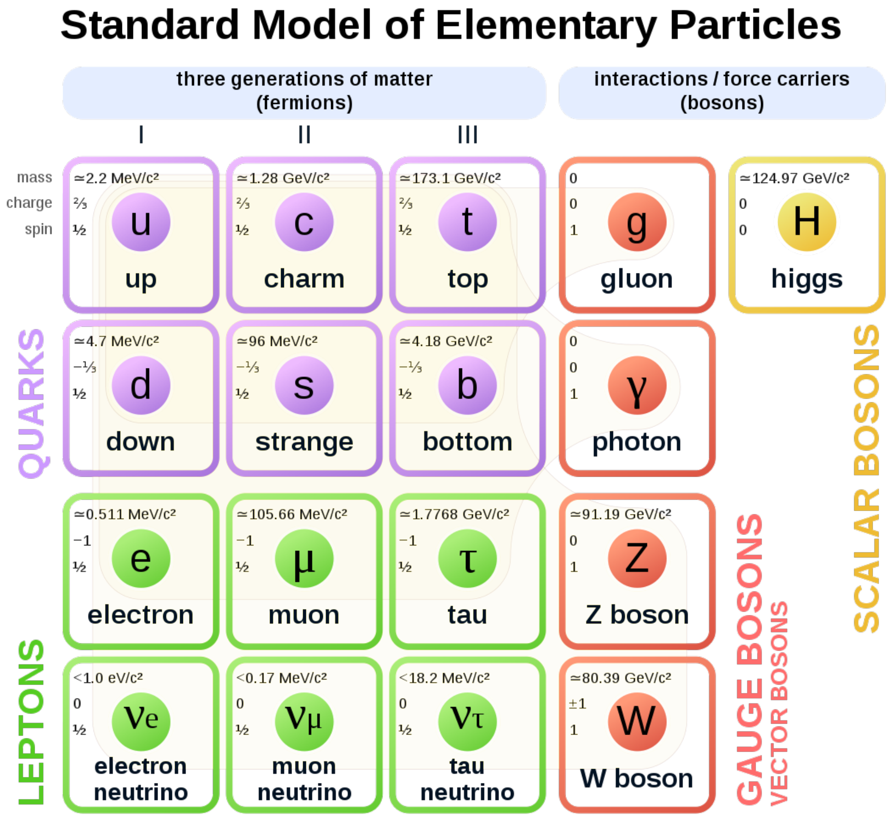

Figure 1.1 Elementary particles in the SM. The plot is taken from Ref.[63]。

1.1.3 Electroweak theory

The electromagnetic and weak interactions are unified in the EW theory represented by three SU(2) weak isospin fields $W^{(1,2,3)}$ and the U(1) weak hypercharge field B. The $W^{(1,2,3)}$ fields couple to left-handed chiral fermions and right-handed chiral anti-fermions in the weak isospin doublets, as classified in the three generations shown in Fig. 1.1. The B field couples equally to left- and right-handed chiral fermions. Besides, there are interactions between the $W^{(1,2,3)}$ bosons. The SU(2)×U(1) gauge invariance conserves the weak isospin and hypercharge, and requires all interacting particles being massless. The masses of particles are originated by the Higgs field with a nonzero vacuum expectation, which results in the spontaneous breaking of the SU(2)×U(1) invariance. The physical gauge bosons come after the symmetry breaking. The $W^{\pm}$ boson is the superposition of the W^1 and W^2 fields, while the Z^0 boson and the photon are combinations of the W^3 and B fields. As the $W^{\pm}$ and Z^0 bosons are massive and only the photon is massless, the SU(2)×U(1) symmetry is broken into the U(1) symmetry in QED, corresponding to the conservation of the electric charge. The eletroweak theory also includes a spin-zero

Higgs boson, which interacts with all massive particles.

The eletroweak sector is at the frontier to challenge the SM. For example, New Physics beyond the SM could have detectable contributions to the *CP* violation in weak decays of hadrons and the properties of rare decays like Flavor-Changing-Neutral-Current processes[64]. Investigations of the potential non-SM effects require both precision experimental measurements and accurate SM predictions. The calculations generally require a good knowledge of the effect of the strong interaction and the properties of hadrons, and thus are closely related to QCD and the quark model.

1.1.4 Quantum chromodynamics

QCD is an SU(3) gauge field theory describing the strong interaction. Its dynamics is governed by the Lagrangian,

$$\mathcal{L} = \bar{\psi}_{f,i}(i\delta_{ij}\gamma^{\mu}\partial_{\mu} - g\gamma^{\mu}A^{c}_{\mu}T^{c}_{ij} - m_f\delta_{ij})\psi_{f,j} - \frac{1}{4}F^{a\mu\nu}F^{a}_{\mu\nu}\,, \tag{1.1}$$

where the repeated indices are summed over. The symbols $\psi_{f,i}$ are quark fields with f and i being the flavor and color, respectively. The γ^{μ} are the Dirac γ-matrices. The gluon fields are denoted as A^{c}_{μ} with the index c running from 1 to 8. The T^{c} are the eight generators of the SU(3) group, represented as 3×3 matrices. The symbol g is the coupling constant of QCD and m_f the quark mass. These two quantities are the only two fundamental parameters of QCD. The $F^{a}_{\mu\nu}$ stands for the gluon field strength tensor, which is

$$F^{a}_{\mu\nu} = \partial_{\mu}A^{a}_{\nu} - \partial_{\nu}A^{a}_{\mu} + gf^{abc}A^{b}_{\mu}A^{c}_{\nu}\,, \tag{1.2}$$

where f^{abc} are the structure constants of the SU(3) group that define the communication relation of the generators: $\left[T^{a}, T^{b}\right] = if^{abc}T^{c}$. The QCD Lagrangian in Eq. 1.1 is invariant under the SU(3) gauge transformation, corresponding to the conservation of the color charge in the strong interaction ①.

In the perturbation theory, the effective coupling of QCD varies at different energy scale of the concerned process. The coupling evolution is characterized by the so-called renormalization group equation[65]

$$\mu\frac{d\alpha_s}{d\mu} \equiv \beta(\alpha_s) = -\frac{\alpha_s^2}{2\pi}\sum_{i=0}\beta_i\left(\frac{\alpha_s}{4\pi}\right)^{i}, \tag{1.3}$$

where $\alpha_s = \frac{g^2}{4\pi}$ and μ is the renormalization scale. The $\beta(\alpha_s)$ is the so-called β-function

---

① A mass term of gluons will violate the gauge invariance, so gluons must be massless.

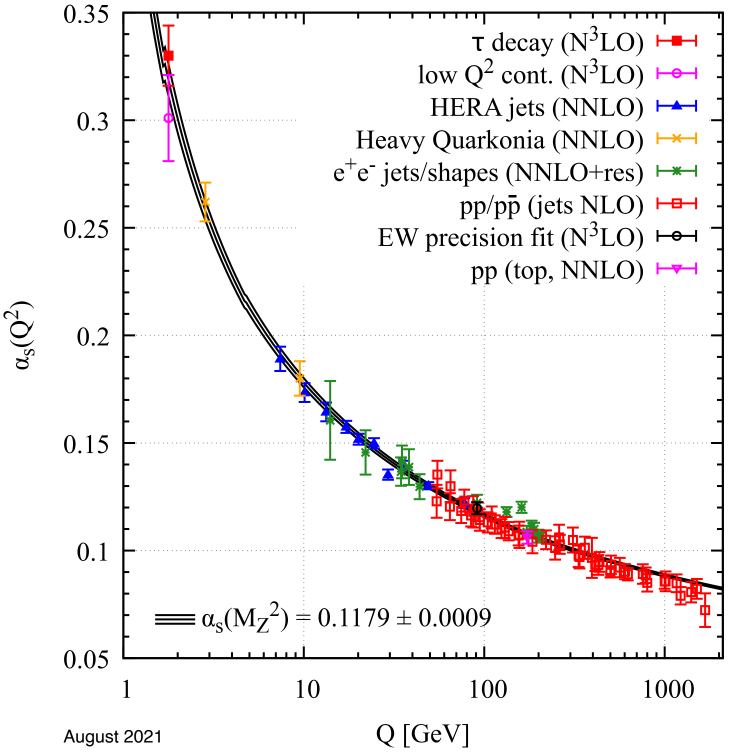

Figure 1.2 Variation of α_s with the energy scale Q[1].

that can be perturbatively expanded as the series of α_s with β_i denoting the coefficients. Taking only the lowest order, also referred to as the one-loop renormalization, $\beta_0 = 11 - 2n_f/3$ with n_f to be the number of the contributing quark flavors. In this case, $\alpha_s(\mu)$ is solved as

$$\alpha_s(\mu) = \frac{2\pi}{\beta_0} \frac{1}{\ln \frac{\mu}{\Lambda_{\text{QCD}}}}. \tag{1.4}$$

The Λ_{QCD} is the Landau pole of QCD where α_s diverges, representing the boundary that divides the perturbative and non-perturbative energy regions. The value of Λ_{QCD} ranges from 0.34 to 1.10 GeV depending on the renormalization schemes[66]. In the SM, β_0 is definitely positive at any energy scale because $n_f \leq 6$, resulting in the decrease (increase) of α_s with the increase (decrease) of the energy scale, as shown in Fig. 1.2. This feature is called the asymptotic freedom.

In the high energy scattering process where the momentum transfer $Q \gg \Lambda_{\text{QCD}}$, α_s tends to zero, so quarks and gluons can be regarded as quasi-free particles as suggested in the parton model[67-68]. The small α_s at high energy scale enables the perturbative calculations and thus establishes the most precision tests of QCD to date. One of the successful examples is the α_s evolution, where a good agreement is found between calculations and measurements, as shown in Fig. 1.2.

At low energy scale where $Q \leq \Lambda_{\text{QCD}}$, α_s becomes so large that no free quark or gluon can be isolated, resulting in the color confinement. If someone attempts to separate two colored objects in space, the energy stored in the color field will increase linearly with the separation distance and new quark-antiquark pairs are continuously excited from the vacuum. This process will not stop until all quarks and gluons form colorless objects, *i.e.* hadrons. The large α_s at low energy scale disables the perturbative theory and thus makes calculations extremely difficult. One of the unsolved puzzles is the determination of hadron properties from the QCD Lagrangian. Though the non-perturbative method called Lattice QCD[1] has made a success predicting the properties of some hadrons, providing the tests of QCD in low energy region, its precision is quite limited and there are still a large number of hadrons that are hard to be quantified, especially the excited states, due to the extremely high consumption of computing resources. Due to the difficulty of the first-principle calculations, phenomenological models have been developed to understand the features of the numerous hadrons, providing effective descriptions of the strong interaction in the low energy region. Most of them are closely related to the well-known quark model.

1.2 Quark model

As introduced in Sec. 1.1.1, the quark model proposed by Gell-Mann and Zweig in 1964[27-28] made a great success classifying the observed hadrons at that time and played an utmost role in the establishment of the SM, and is still at the heart of hadron spectroscopy studies today to give phenomenological descriptions of hadrons and to connect QCD to experimental observations.

In the quark model, quarks are the elementary building blocks of hadrons, whose quantum numbers are listed in Table 1.1. The charge Q is related to the flavor quantum numbers via the Gell-Mann–Nishijima formula

$$Q = I_z + \frac{\mathcal{B} + S + C + B + T}{2}, \tag{1.5}$$

where $\mathcal{B}$ is the baryon number, and other symbols denote quark flavors. Hadrons are composite particles formed by quarks. They are generally classified into two categories: mesons and baryons. Mesons are composed of a quark and an antiquark ($q\bar{q}$), and baryons are made up of three quarks (qqq) ①.

---

① In this section, mesons and baryons only refer to the conventional hadrons without explicitly mentioned, the exotic mesons and baryons containing more quarks will be discussed later.

Table 1.1 Quantum numbers of quarks (the weak hypercharge and the color charge excluded). Antiquarks have opposite quantum numbers except the isospin. The table is taken from Ref.[1].

	d	u	s	c	b	t
Isospin (I)	$\frac{1}{2}$	$\frac{1}{2}$	0	0	0	0
Isospin third component (I_3)	$-\frac{1}{2}$	$+\frac{1}{2}$	0	0	0	0
Strangeness (S)	0	0	-1	0	0	0
Charm (C)	0	0	0	$+1$	0	0
Bottomness (B)	0	0	0	0	-1	0
Topness (T)	0	0	0	0	0	$+1$
Baryon number ($\mathcal{B}$)	$+\frac{1}{3}$	$+\frac{1}{3}$	$+\frac{1}{3}$	$+\frac{1}{3}$	$+\frac{1}{3}$	$+\frac{1}{3}$
Electric charge (Q)	$-\frac{1}{3}$	$+\frac{2}{3}$	$-\frac{1}{3}$	$+\frac{2}{3}$	$-\frac{1}{3}$	$+\frac{2}{3}$

The wave function of a hadron is composed of several parts:

$$\psi = \xi_{\text{color}}\, \eta_{\text{space}}\, \chi_{\text{spin}}\, \phi_{\text{flavor}}\,, \tag{1.6}$$

corresponding to the flavor-, spin-, color-space and spatial wave functions, respectively. The ξ_{color} is always in the color singlet, respecting the color confinement, while others are related to the combination schemes and interactions of the quarks. The exact formula of the total wave function depends on the dedicated characterization of the dynamics, and thus is generally extremely complicated, but there are still some direct results without referring to the exact formula of the description. For example, the angular part of the spatial wave function of a hadron can be usually solved in analogous to that of the hydrogen system, where the spin and parity of the hadron can be derived from the spin and orbital angular momenta of the contained quarks. Conventional mesons are usually denoted by the symbol $n^{2S+1}L_J$, where $n = 1, 2, 3, \cdots$ is the principal quantum number representing the radial excitation, $S = 0, 1$ the spin sum of $q_1\bar{q}_2$ and $L = S, P, D, F, \cdots$, corresponding to $L = 0, 1, 2, 3, \cdots$, is the orbital angular momentum between the two quarks. The spin of the hadron J is the magnitude of the total angular momentum $\vec{J} = \vec{S} + \vec{L}$. Then space-inversion parity is $P = (-1)^{L+1}$ and the charge conjugation is $C = (-1)^{L+S}$, where the latter is defined only for mesons composed of a quark-antiquark pair of the same flavor. Baryons can be classified in a similar way[69].

The spin-space wave function of a hadron is constructed as the direct product of the SU(2) group describing the quark spins, which is $\mathbf{2} \otimes \mathbf{2} = \mathbf{3}_{\text{S}} \oplus \mathbf{1}_{\text{A}}$ for mesons, and $\mathbf{2} \otimes \mathbf{2} \otimes \mathbf{2} = \mathbf{4}_{\text{S}} \oplus \mathbf{2}_{\text{MS}} \oplus \mathbf{2}_{\text{MA}}$ for baryons. The symbol S (A) indicates the spin-space

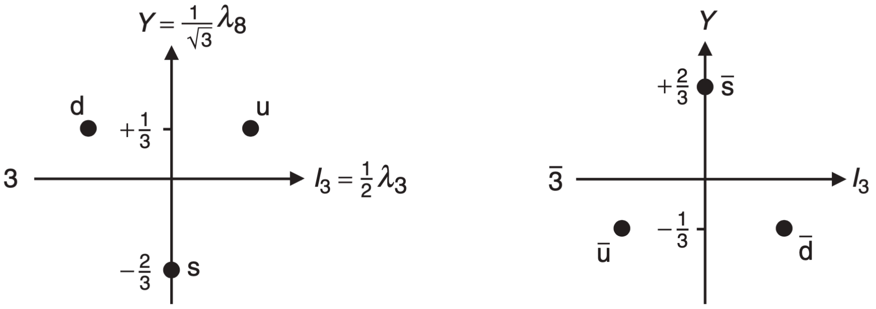

Figure 1.3 Weight diagrams for quarks (left) and antiquarks (right). The plot is taken from Ref.[70].

wave function is symmetric (antisymmetric) under the exchange of any two quarks, and MS (MA) indicates the spin-space wave function is asymmetric (antisymmetric) under the exchange of the first two quarks in qqq.

The construction of the flavor-space wave function is the core concept of the quark model. The idea is analogous to the SU(2) representation of the spin-space wave function. Different flavors of quarks are regarded as the eigenstates of the representations of the flavor group SU(N), with N denoting the number of quark flavors involved. The flavor-space wave functions of hadrons can be constructed as the direct products of the representations of quarks. Let's start from the SU(3) flavor group of the light quarks (u, d and s).

1.2.1 SU(3) flavor group of the light-flavor quarks

The (u, d, s) quarks lie in a **3** dimensional representation of the SU(3) group, and their antiquarks lie in its complex conjugation $\bar{\mathbf{3}}$. The transformations between the light-flavor quarks can be expressed in terms of the eight generators of the SU(3) group, which are represented as the λ-matrices[1]. Among all the matrices, λ_3 and λ_8 commute with each other and thus they can be used to define compatible quantities for the u, d and s quarks: the third component of the isospin $I_3 \equiv \frac{1}{2}\lambda_3$ and the hypercharge $Y \equiv \frac{1}{\sqrt{3}}\lambda_8 = \mathcal{B} + S$ ①, as shown in the weight diagrams in Fig. 1.3.

Light mesons containing only the u, d and s quarks with the same spin and parity lie in the same irreducible representations of the direct product of the **3** and $\bar{\mathbf{3}}$: $\mathbf{3} \otimes \bar{\mathbf{3}} = \mathbf{8} \oplus \mathbf{1}$. For example, the ground-state mesons with $L = 0$ and $S = 0, 1$ are well classified into two families with $J^P = 0^-$ and 1^-, each in an $\mathbf{8} \oplus \mathbf{1}$ representation, as shown in Fig. 1.4. Excited mesons with $L \neq 0$ can also be classified in the similar way.

---

① $Y = \mathcal{B} + S - \frac{C - B + T}{3}$ if taking all quark flavors into account.

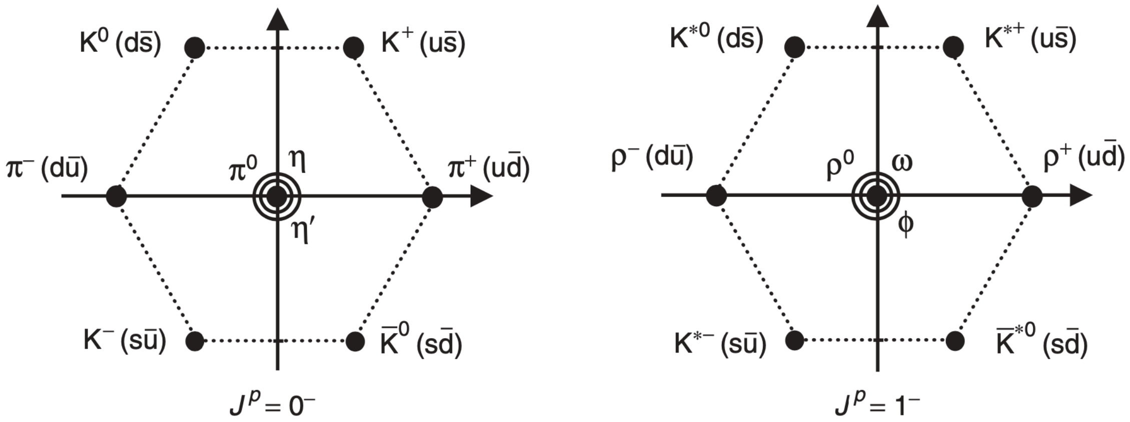

Figure 1.4 Weight diagrams for ground-state light mesons. For the mesons in the centers of the diagrams, the π^0 and ρ^0 mesons are in isospin triplet, represented as $\frac{1}{\sqrt{2}}(u\bar{u} - d\bar{d})$, and others are mixture of the isospin singlet $\frac{1}{\sqrt{6}}(u\bar{u} + d\bar{d} - 2s\bar{s})$ and flavor singlet $\frac{1}{\sqrt{3}}(u\bar{u} + d\bar{d} + s\bar{s})$. The axis labels are the same as Fig. 1.3. The plot is taken from Ref.[70].

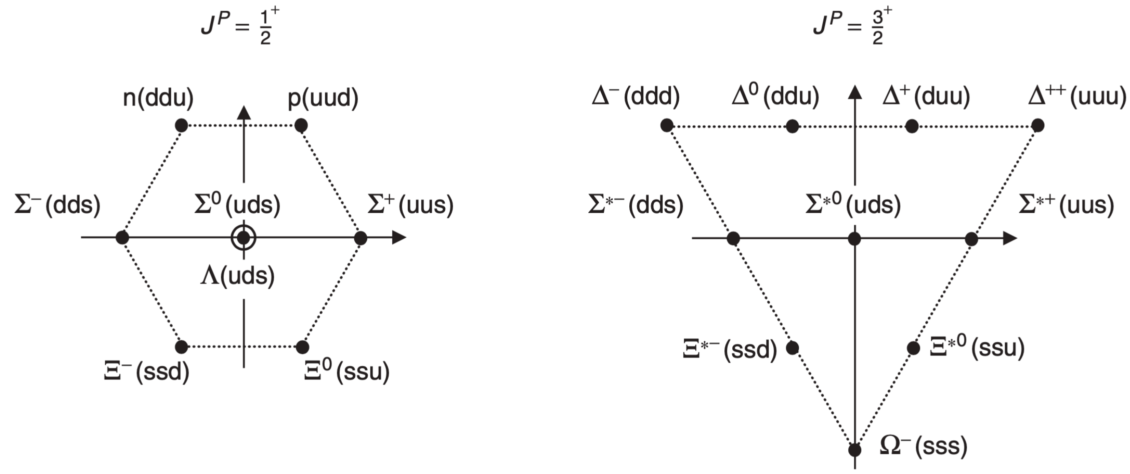

Figure 1.5 Weight diagrams for ground-state light baryons. The Λ baryon is the isospin singlet. The octet is the mixture of $\mathbf{8}_{\mathrm{MS}}$ and $\mathbf{8}_{\mathrm{MA}}$. The axis labels are the same as Fig. 1.3. The plot is taken from Ref.[70].

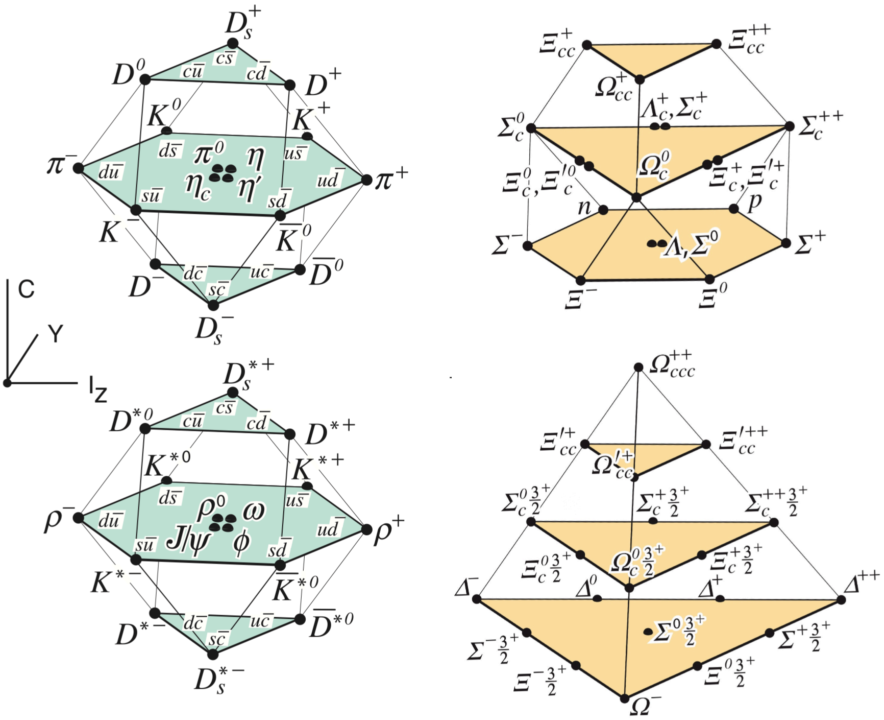

Figure 1.6 Weight diagrams for ground-state mesons (left) and baryons (right) of the SU(4) flavor group with the charm quark included. The plot is taken from Ref.[1].

Analogously, light baryons with the same spin and parity lie in the same irreducible representations of the direct product of three **3**: $\mathbf{3}\otimes\mathbf{3}\otimes\mathbf{3} = \mathbf{10}_{\rm S}\oplus\mathbf{8}_{\rm MS}\oplus\mathbf{8}_{\rm MA}\oplus\mathbf{1}_{\rm A}$. For the simplest case of ground-state baryons with no orbital excitation ($L = 0$), the spatial wave function $\eta_{\rm space}$ is symmetric and the color wave function is always antisymmetric, so the remaining part ($\phi_{\rm flavor}$, $\chi_{\rm spin}$) is required to be symmetric, which can be constructed either as ($\mathbf{10}_{\rm S}, \mathbf{4}_{\rm S}$) or the combination of ($\mathbf{8}_{\rm MS}, \mathbf{4}_{\rm MS}$)+($\mathbf{8}_{\rm MA}, \mathbf{4}_{\rm MA}$). The former corresponds to the $J^P = \frac{3}{2}^+$ baryons and the latter the $J^P = \frac{1}{2}^+$ baryons, as shown in Fig. 1.5. The antisymmetric-flavor baryon does not exist in the ground-state families as its total wave function cannot be antisymmetric, but can be possible when the orbital freedom is excited, where the lightest one is expected to have $J^P = 1/2^-$[71].

1.2.2 Heavy-flavor hadrons

The charm (c), bottom (b) and top (t) quarks are called heavy-flavor quarks as they have masses much larger than those of the light-flavor quarks. The charm and bottom quarks can make up heavy hadrons, but the top quark is extremely short-lived and decays before forming hadrons.

Heavy hadrons can be classified by extending the SU(3) light-flavor group to an SU(4) group including only one type of the heavy-flavor quark, or even an SU(5) group including both the charm and bottom quarks. For example, the ground-state hadrons containing charm quarks are classified together with the light ones in the weight diagrams of the SU(4) group, shown in Fig. 1.6. The extended groups predict the existence of many heavy hadrons. Up to now, all the ground-state heavy mesons and singly heavy baryons are observed in experiment[1]. However, among the baryons containing at least two heavy quarks, only the Ξ_{cc}^{++} baryon is discovered[72]. Efforts to search for the missing particles are underway[73-77]. There are also many excited heavy hadrons observed in experiment[1]. Most of them well fit into the quark model, but there are exceptions. For example, the masses of the $D_{s0}^{*}(2317)^{+}$ and $D_{s1}(2460)^{+}$ states are far below the quark-model predictions, and there are also some states with $c\bar{c}$ as part of the quark content cannot fit into the conventional charmonium spectrum[1]. The charm-strange and charmonium states can be accessed in the $B^{0} \rightarrow D^{+}D^{-}K^{+}\pi^{-}$ and $B^{+} \rightarrow D_{s}^{+}D_{s}^{-}K^{+}$ decays, so the studies in this thesis can provide more experimental inputs to solve the existing puzzles.

1.2.3 Exotic hadrons

Besides the hadrons with quark contents $q\bar{q}$ and qqq, there is no restriction that forbids the existence of hadrons containing more quarks, *e.g.* the tetraquark ($q\bar{q}q\bar{q}$) and pentaquark ($qqqq\bar{q}$) states[78-79]. These hadrons are called multiquark states. QCD also suggests a kind of hadrons containing gluons as the constituents, *e.g.* glueballs (gg) and hybrid states ($q\bar{q}g$), which stand outside the quark model and are referred to, together with the multiquark states, as exotic hadrons. Thus those with the $q\bar{q}$ and qqq quark contents are referred to as being conventional.

Study of exotic hadrons has always been a hot area since the birth of the quark model. Many observed hadrons are inferred to be exotic candidates. Some of them are certainly confirmed to be exotic because they must contain at least four or five quarks, *e.g.* $Z_{c}(3900)^{+}$ $[c\bar{c}u\bar{d}]$, $X(2900)$ $[c\bar{d}s\bar{u}]$, $P_{c}(4312)^{+}$ $[c\bar{c}uud]$[1], *etc.*, but others remain controversial. There are attempts to interpret some hadrons unexpected by the quark model as exotic states, *e.g.* $\Lambda(1405)$[80], $\chi_{c1}(3872)$[81], $D_{s0}^{*}(2317)^{+}$ and $D_{s1}(2460)^{+}$[82-85], and they are inferred to contain a $q\bar{q}$ pair of the same light flavor. However, the light $q\bar{q}$ pair in these states could annihilate and thus the conventional interpretations for them cannot be excluded. Investigations of these states in different decays and precision measurements on the properties are expected to help reveal their nature. In the $B^{0} \rightarrow D^{+}D^{-}K^{+}\pi^{-}$ and $B^{+} \rightarrow D_{s}^{+}D_{s}^{-}K^{+}$ decay studied in this thesis, exotic mesons containing $c\bar{c}$ and cs quarks could be accessed in the $D^+_{(s)}D^-_{(s)}$ and $D^-K^+(\pi^+)$ systems, respectively.

1.2.4 Connection between QCD and the quark model

In the modern perspective, QCD is at the most fundamental level to provide universal and accurate descriptions of hadrons. The quark model is phenomenological and is somewhat an approximation that is expected being in principle derivable from QCD. However, the solution is still missing due to the non-perturbative property of QCD in the low energy region.

There are simple relations between the quark-model conclusions and QCD, *e.g.* the SU(3) light-flavor symmetry introduced in Sec. 1.2.1, which is expected in QCD if neglecting the mass differences of the light quarks. The QCD Lagrangian in Eq. 1.1 is invariant under the SU(3) transformations between the light-flavor quarks if they have equal masses, and thus the physical observables remain the same. It is known that the SU(3) light-flavor symmetry is just approximate, which is violated by the different masses of the light quarks and results in the mass splittings of hadrons in the same representations. The approximate isospin invariance is usually regarded as an effective symmetry, thanks to the small mass splittings of the u and d quarks.

Phenomenological descriptions of dynamics can be embedded in the quark model to derive the properties of hadrons, *e.g.* mass and decay width (lifetime equivalently). These descriptions are usually motivated by QCD to some extent. For example, the potential models describing conventional hadrons generally include a Coulomb-type potential and a linear potential[1], where the former describes the short-distance interaction of one-gluon-exchange and arises from the three-point interaction of quarks and gluons in the QCD Lagrangian (Eq. 1.1), and the latter reflects the color confinement at the long distance and is inferred from the Lattice-QCD calculations[86]. The ones do not fit into the conventional potential models are usually inferred to be exotic, and there are also QCD-motivated models to interpret their natures[81].

Lattice QCD is the first-principle approach to calculate hadron properties by computing the Feynman path integral numerically in a lattice of discrete space-time points. It in general requires extreme computation resources to handle the huge amount of lattices that are necessary to achieve an acceptable precision of hadron properties. With the development of computing technology, Lattice QCD has made steady progresses in recent years. For example, the masses of the low-lying hadrons solved by the Lattice-QCD

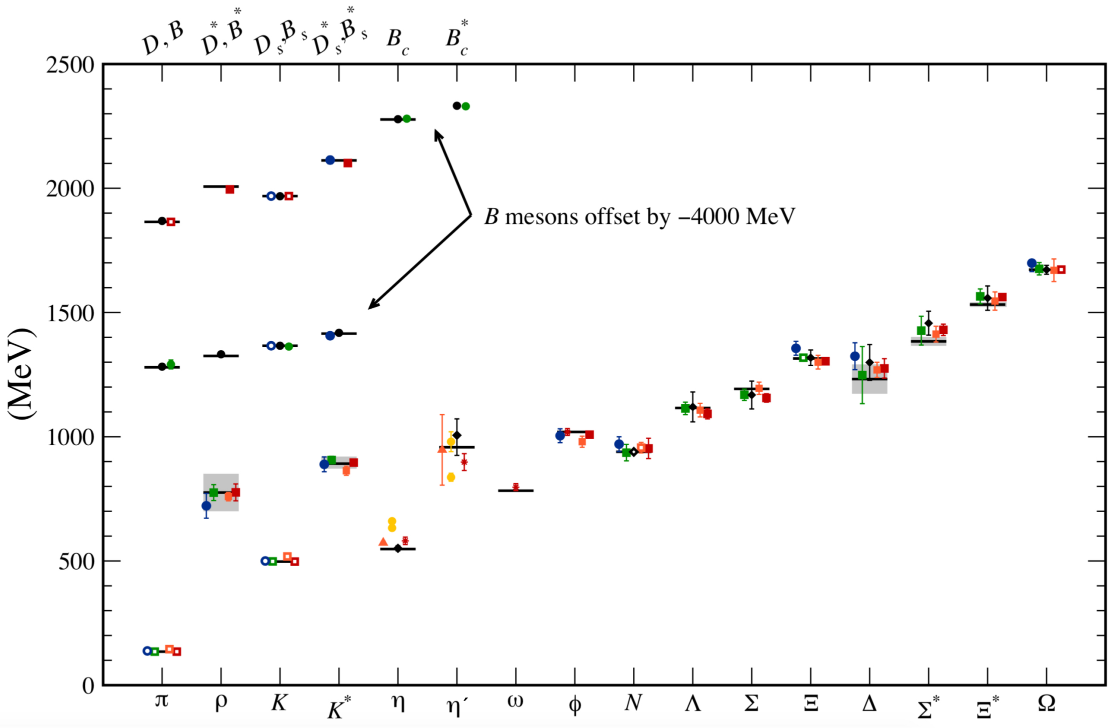

Figure 1.7 Comparisons of the hadron masses from the Lattice-QCD calculations (colored lines) and the measurements (black lines). The plot is taken from Ref.[1].

calculations show good agreements with the measurements, seen in Fig. 1.7. However, it is still hard to perform calculations for highly excited hadrons due to the presence of the strong decay modes, and it is even harder to calculate the properties of exotic states because they have more number of degrees of the combinations of the contained quarks compared with that of the conventional hadrons. Regardless of the limited precision, Lattice QCD in principle can directly connect to the experimental observables without referring to the quark model. Even so, the quark model still plays a key role as the benchmark to build the fields in Lattice QCD and provides phenomenological understandings of the Lattice-QCD results.

1.3 Charm-strange meson spectrum

In almost all contexts, charm-strange mesons refer to the conventional D_s^+ mesons composed of the $c\bar{s}$ quarks, the spectrum of which has been studied for a long time since the observation of the ground-state D_s^+ meson in 1977[87]. Recently in 2020, the LHCb collaboration reported two exotic-meson candidates of minimum quark content $cs\bar{u}\bar{d}$ in the D^-K^+ system, $X_{(0,1)}(2900)$[13-14], which are also classified in the category of charm-strange mesons[1]. The D_s^+ states, as well as the $cs\bar{q}\bar{q}$ states with $q \in \{u, d\}$, can

Table 1.2 Measured properties and observed decay modes of the discovered D_s^+ states. The values are taken from Ref.[1].

State	J^P	Mass (MeV)	Width (MeV)	Observed decay modes
D_s^+	0^-	1968.35 ± 0.07	$\frac{1}{(5.04\pm0.04)\times10^{-13}\ \mathrm{s}}$	$\eta\pi^+$, $K^+K^-\pi^+$, *etc.*
$D_{s1}^*(2112)^+$	1^-	2112.2 ± 0.4	< 1.9	$D_s^+\gamma$, $D_s^+e^+e^-$, $D_s^+\pi^0$
$D_{s0}^*(2317)^+$	0^+	2317.8 ± 0.5	< 3.8	$D_s^+\pi^0$
$D_{s1}(2460)^+$	1^+	2459.5 ± 0.6	< 3.5	$D_s^+\gamma$, $D_s^{*+}\pi^0$, $D_s^+\pi^+\pi^-$
$D_{s1}(2536)^+$	1^+	2535.11 ± 0.06	0.92 ± 0.05	$D_s^+\pi^+\pi^-$, D^*K, $DK\pi$
$D_{s2}^*(2573)^+$	2^+	2569.1 ± 0.8	16.9 ± 0.7	DK, D^*K
$D_{s1}^*(2700)^+$	1^-	2714 ± 5	122 ± 10	DK, D^*K
$D_{s1}^*(2860)^+$	1^-	2859 ± 27	159 ± 80	DK
$D_{s3}^*(2860)^+$	3^-	2860 ± 7	53 ± 10	DK, D^*K
$D_{sJ}(3040)^+$	$?^?$	3044^{+31}_{-9}	239 ± 60	D^*K

be accessed in the $D^+K^+\pi^-$ and D^-K^+ (π^-) systems of the $B^0 \to D^+D^-K^+\pi^-$ process, respectively, and the search for them is one of the goals of this thesis. This section gives a brief overview on the charm-strange meson spectrum.

1.3.1 Experimental progress in the D_s^+ spectrum

In collider experiments, the D_s^+ states can be produced promptly in the collision process (*e.g.* e^+e^- and pp) or as the secondary particles in the weak decay of b-hadrons. In the prompt production, the D_s^+ states can be studied in the combinations of their expected decay products. In the b-hadron decays, the full decay chain can be reconstructed and the spin-parity analyses of the D_s^+ states are possible. The discovered D_s^+ states are listed in Table 1.2. Almost all of them were first observed in the inclusive productions[3-4,87-91], except the $D_{s1}^*(2860)^+$ state that was instead observed in the exclusive $B_s^0 \to \overline{D}^0K^-\pi^+$ decay[92-93]. The D_s^+ states are denoted as either D_s or D_s^* regarding to their spin-parity assignments. States with $P = (-1)^J$ $(J^P = 0^+, 1^-, 2^+, ...)$ are referred to having natural parity and are denoted as D_s^*, which can strongly decay into two pseudoscalar mesons with $J^P = 0^-$ if the process is kinematically allowed. Other states with $P = (-1)^{J+1}$ $(J^P = 0^-, 1^+, 2^-, ...)$ have unnatural parity and are denoted as D_s, which cannot decay into two pseudoscalar mesons via the strong interaction due to the restriction of the parity and angular momentum conservations.

Presented decay channels of the D_s^+ states are closely related to their properties.

The ground-state D_s^+ meson decays weakly and has over 100 decay modes[1], providing numerous opportunities to study the light-hadron spectrum. All other D_s^+ states decay through the electromagnetic or strong interactions. The states lying below the $D^{(*)}K$ mass threshold decay into the $D_s^{(*)+}$ meson plus either pions or γ/e^+e^-. The former is the OZI-suppressed strong decay[94-96] with the emission of hard gluons and the latter the electromagnetic process with the radiation of a photon. Such decays are much weaker than the OZI-allowed strong decays, so the low-lying states usually have much smaller widths compared with those lying above the $D^{(*)}K$ mass threshold and strongly decaying into $D^{(*)}K(\pi)$. The $D_{s1}(2536)^+$ state is an exception. It has a narrow width, and both the OZI-suppressed and OZI-allowed decay modes. This is understood as the partial widths of its OZI-allowed decays being strongly suppressed by the small phase-space due to its near-threshold mass. Even though, the partial widths of the OZI-allowed decays of the $D_{s1}(2536)^+$ state are much larger than that of the decay to the $D_s^+\pi^+\pi^-$ final state. The $D_{s1}^*(2860)^+$ state is expected also decaying into D^*K, which can be searched for in the ongoing studies. Moreover, for the states above the $DK\pi$ mass threshold, their decays into $DK\pi$ are possible. These states can be investigated in the $B^0 \to D^+D^-K^+\pi^-$ decay analyzed in this thesis.

Masses and widths of the D_s^+ states are usually determined by the investigations of the peaking structures in the mass spectrum of their decay products. An example of the $D^{*+}K_{\mathrm{S}}^0$ system is shown as Fig. 1.8, where the masses and widths of the presented D_s^+ states are extracted from the overlaid fit. The width of the ground-state D_s^+ meson is extremely narrow due to the weak-decay nature and thus it cannot be measured in the mass spectrum, and instead its lifetime (the inverse of the width) is determined by measuring its flying distance and momentum[97]. The three states, $D_{s1}^*(2112)^+$, $D_{s0}^*(2317)^+$ and $D_{s1}(2460)^+$, have undetermined widths with only the upper limits set. These are understood as due to their narrow nature resulting from the only electromagnetic and OZI-suppressed decays, as well as the limited mass resolution of the detectors. However, these values have not been updated over 15 years, and are expected to be measured with more advanced experiments sensitive to photons and neutral pions. The $D_{s1}(2860)^0$ width is measured with an extremely large uncertainty, indicating that this state is not be well established[98]. The measured masses and widths of the $D_{s1}^*(2700)^+$, $D_{s3}(2860)^+$ and $D_{sJ}(3040)^+$ states also have relatively large uncertainties, which are expected to be reduced in future measurements.

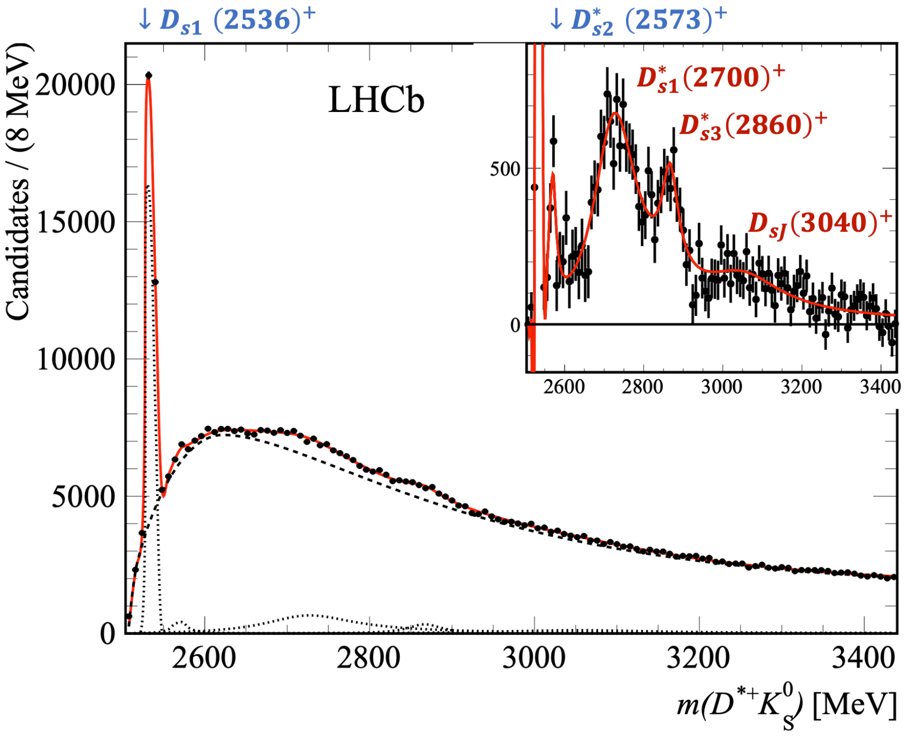

Figure 1.8 $D^{*+}K^0_S$ mass spectrum in the inclusive $pp \to D^*KX$ process from the LHCb experiment[99]. Data is shown as black points, while the fit to extract the properties of the presented D_s^+ states is shown as the red curve. The zoomed-in plot shows the mass spectrum with the background subtracted.

Table 1.2 also lists the spin-parity of the observed D_s^+ states. Some of them are directly determined in the studies of exclusive b-hadron decays, while others are assigned by considering both experimental results and the quark-model predictions. The spin-zero nature of the ground-state D_s^+ meson is strongly supported by the angular distributions of the $\phi \to K^+K^-$ and $\bar{K}^*(892)^0 \to K^-\pi^+$ decays in the $D_s^+ \to \phi\pi^+$ and $D_s^+ \to K^+\bar{K}^*(892)^0$ modes[100-102], and its parity is assigned to be negative due to its ground-state classification in the quark model. The $D^*_{s1}(2112)^+$ and $D^*_{s0}(2317)^+$ states are observed decaying into two pseudoscalar mesons and thus have natural parity, while the $D_{s1}(2460)^+$ and $D_{s1}(2536)^+$ states are unnatural-parity states because they do not decay into two pseudoscalar mesons. Spins of the above four states are assigned by comparing their masses, widths and decays with the quark-model expectations. The spin-parity of the other four states, $D^*_{s2}(2573)^+$, $D^*_{s1}(2700)^+$, $D_{s1}(2860)^+$ and $D_{s3}(2860)^+$, are determined by the angular or amplitude analyses to the B-meson decays[9,12,92-93], where the contributions of the D_s^+ states decays are shown in Fig. 1.9. The spin-parity of the $D_{sJ}(3040)^+$ state is not determined yet. As only observed in the D^*K system, it is possibly an unnatural-parity state. If the $D_{sJ}(3040)^+$ state appears in the $D^+K^+\pi^-$ system in the

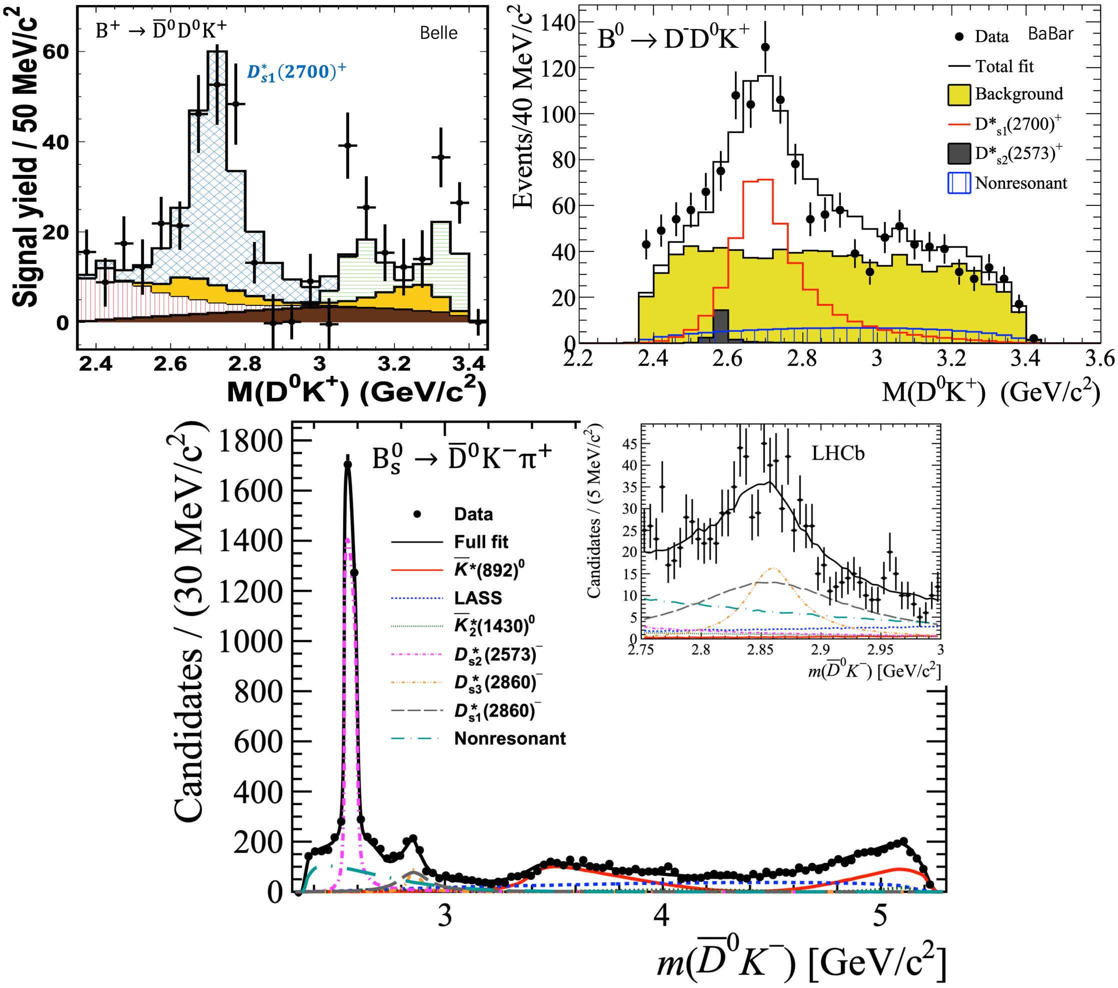

Figure 1.9 D_s^+ states studied in the angular or amplitude analyses to the B-meson decays. The plots are taken from Refs.[9,12,92], respectively.

$B^0 \to D^+ D^- K^+ \pi^-$ decay studied in this thesis, an amplitude analysis could be possible to determine its spin parity.

1.3.2 Theoretical overview on the D_s^+ spectrum

There are theoretical calculations on the properties of the D_s^+ states. The results can be compared with the experimental measurements and can be used to provide interpretations of the observed states. Theoretical studies also make predictions to new excited D_s^+ mesons and thus guide the experimental searches for them. This subsection gives a brief introduction to the theoretical calculations on the D_s^+ masses and widths, followed by the classification of the observed states and the prospect of the searches for new ones.

1.3.2.1 Solving the D_s^+ masses

The first-principle approach to solve the D_s^+ mass spectrum is Lattice QCD, where steady progresses have been made[103-105]. However, the Lattice-QCD calculations are quite complicated and the precision is generally limited, so the potential model is still the most common method to utilize.

The most successful potential model is the Godfrey-Isgur (GI) relativized quark model[106-107], which determines the D_s^+ mass spectrum in analogous to the hydrogen system by solving the Schrödinger-type equation for the $c\bar{s}$ two-body system. The Hamiltonian is composed of a relativistic kinematic term and a momentum-dependent potential that includes a Coulomb-type term to describe the short-ranged one-gluon-exchanged force, a linear term to account for the long-ranged color confinement, and several terms to manifest the spin-spin and spin-orbital interactions. The solved wave functions are the eigenstates of the Hamiltonian (mass), represented as $|n^{2S+1}L_J\rangle$. The spin-orbital interaction also causes the mixing of $|n^3L_L\rangle$ and $|n^1L_L\rangle$, and the mass eigenstates are the superpositions of them,

$$\begin{pmatrix} |nL_L\rangle \\ |nL'_L\rangle \end{pmatrix} = \begin{pmatrix} \cos\theta_{13} & \sin\theta_{13} \\ -\sin\theta_{13} & \cos\theta_{13} \end{pmatrix} \begin{pmatrix} |n^1L_L\rangle \\ |n^3L_L\rangle \end{pmatrix},$$

where θ_{13} is related to the interacting strength. The solved D_s^+ mass spectrum is shown in Fig. 1.10, and the masses are listed in Table 1.3. The observed states are matched to the most promising states expected in theory. The measured masses are consistent with the predictions for most of the states except for the $D_{s0}^*(2317)^+$ and $D_{s1}(2460)^+$ mesons. Their masses are significantly smaller compared with the theoretical values.

Modifications of the GI model are introduced sometimes. Two popular ideas are the coupled-channel effect[85,108-109] and the screen effect[6]. The former arises from the couple between a D_s^+ state and a scattering channel of two mesons. Its effect is significant when a D_s^+ state locates near the two-meson mass threshold. For example, the unexpected masses of the $D_{s0}^*(2317)^+$ and $D_{s1}(2460)^+$ states in the GI model could be explained as partially caused by the coupled-channel effect[85,108-109]. The screen effect comes from the $q\bar{q}$ productions from the vacuum at the long distance that soften (screens) the linear potential, and is expected to significant for the states with higher masses. The D_s^+ masses solved using the GI model with the screen effect considered also shown in Table 1.3. The predicted masses are slightly lower than the values from the original GI model and show better agreements with the measured masses.

Table 1.3 Masses and widths of the D_s^+ states from the experimental measurements (Exp.) and theoretical calculations. The GI and GI-Screen models are used to solve masses, and then the corresponding wave functions are used as inputs to obtain widths for electromagnetic (E1 and M1) and OZI-allowed ($^3P_0$) decays. The observed states are assigned to the most promising $n^{2S+1}L_J$. The values for “-” are absent.

State	$n^{2S+1}L_J$	Mass (MeV)			Width (MeV)		
		Exp.[1]	GI[5]	GI-S[6]	Exp.[1]	GI[5]	GI-S[6]
D_s^+	1^1S_0	1968.35 ± 0.07	1979	1967	$\frac{1}{(5.04\pm0.04)\times10^{-13}\ \mathrm{s}}$	-	-
$D_{s1}^*(2112)^+$	1^3S_1	2112.2 ± 0.4	2129	2115	< 1.9	1.03×10^{-3}	-
$D_{s0}^*(2317)^+$	1^3P_0	2317.8 ± 0.5	2484	2463	< 3.8	221	-
$D_{s1}(2460)^+$	$1P_1$	2459.5 ± 0.6	2549	2529	< 3.5	0.135	-
$D_{s1}(2536)^+$	$1P_1'$	2535.11 ± 0.06	2556	2534	0.92 ± 0.05	140	-
$D_{s2}^*(2573)^+$	1^3P_2	2569.1 ± 0.8	2592	2571	16.9 ± 0.7	10.07	-
$D_{s1}^*(2860)^+$	1^3D_1	2859 ± 27	2899	2865	159 ± 80	197.2	-
-	$1D_2$	-	2900	-	-	115.1	-
-	$1D_2'$	-	2926	-	-	195	-
$D_{s3}^*(2860)^+$	1^3D_3	2860 ± 7	2917	2883	53 ± 10	46	14
-	1^3F_2	-	3208	3159	-	292.5	416
-	$1F_3$	-	3186	-	-	182.6	372
-	$1F_3'$	-	3218	-	-	323	193
-	1^3F_4	-	3190	3143	-	182	151
-	2^1S_0	-	2673	2646	-	73.6	76.6
$D_{s1}^*(2700)^+$	2^3S_1	2714 ± 5	2732	2704	122 ± 10	123.4	-
-	2^3P_0	-	3005	2960	-	145.6	166.6
$D_{sJ}(3040)^+$	$2P_1$	3044^{+31}_{-9}	3018	-	239 ± 60	143	286
	$2P_1'$		3038	2992		147.6	131.3
-	2^3P_2	-	3048	3004	-	131.5	86.3

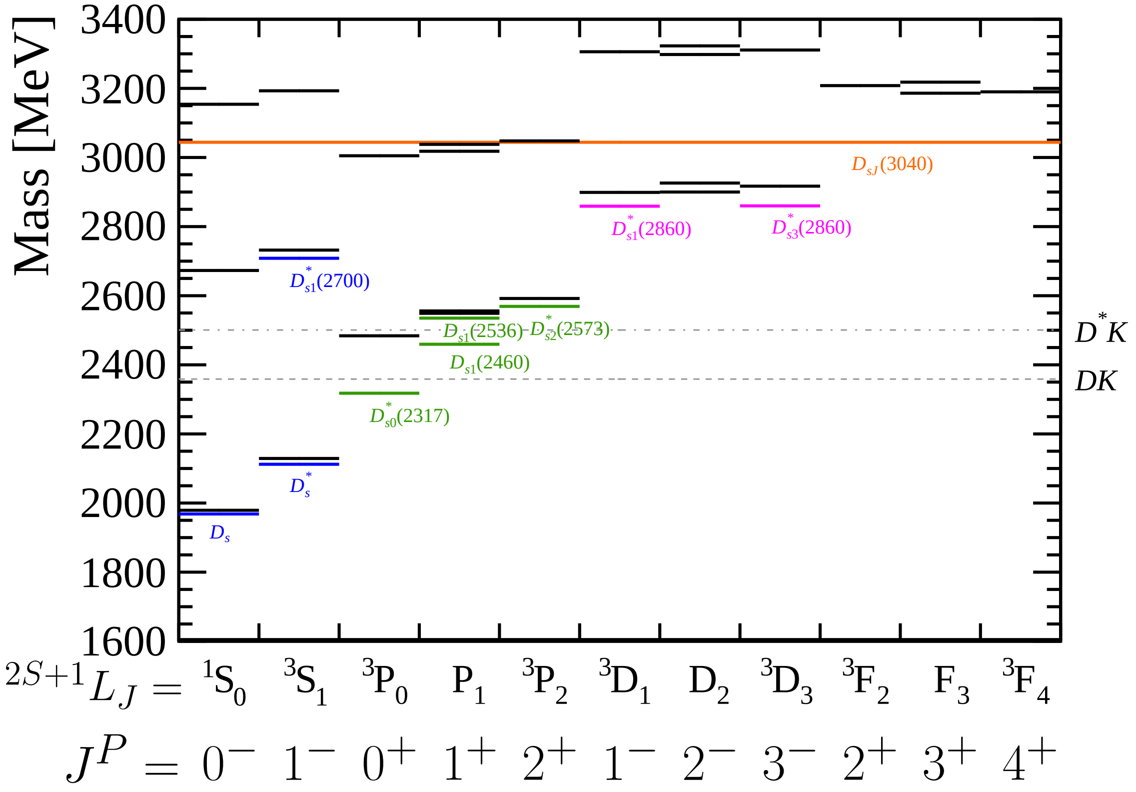

Figure 1.10 D_s^+ mass spectrum. The black lines are the predicted states of the GI model[5]. The colored lines denote the observed states with masses taken from Ref.[1], placed in the column with the most promising ${}^{2S+1}L_J$ assignments, except the $D_{sJ}(3040)$ state, whose J^P is not determined. The symbol L_L (P_1, D_2, F_3, $\cdots$) denotes the two states L_L and L'_L, superpositions of ${}^1L_L$ and ${}^3L_L$. The long dashed lines denote the thresholds of the DK and D^*K system.

1.3.2.2 Solving the D_s^+ widths

The D_s^+ states decay via the electromagnetic or strong interactions except the $D_s(1^1S_0)^+$ meson ①. The description of the electromagnetic decay is similar to that of the hydrogen system, basically including the electric- and magnetic-dipole transitions that account for the changes of $L \to L \pm 1$ and $S \to S \pm 1$, respectively. The solved wave functions discussed in Sec. 1.3.2.1 are used as the inputs to derive the widths. The detailed width formulas for the electric- and magnetic-dipole transitions can be found in Ref.[5]. The strong decay is usually described by some quark pair creation models, and the most famous one is the ${}^3P_0$ model[110], which are utilized to determine the OZI-allowed two-body decay widths. In the ${}^3P_0$ model, the $q\bar{q}$ pair is produced with the vacuum quantum numbers ($J^{PC} = 0^{++}$), and is then combined with the initial $c\bar{s}$ quarks to form the two final-state mesons. The width formula of the ${}^3P_0$ model is detailed in Ref.[111].

---

① The ground state $D_s(1^1S_0)^+$ decays weakly, whose decay property is not related to this thesis and thus is not discussed.

The partial widths of all decay channels are summed over to obtain the total widths, which are shown in Table 1.3. The $D_{s1}^*(2112)^+$ state is expected decaying electromagnetically and the predicted width of it is consistent with the measured upper limit. All other excited D_s^+ states are expected lying above the D^*K mass threshold as shown in Table 1.3 and thus decaying into the OZI-allowed final state $D^{(*)}K$, Their widths are derivable using the ${}^3P_0$ model. The theoretical values are in good agreements with the measured widths for the states far above the D^*K mass threshold, but large discrepancies are seen for the $D_{s0}^*(2317)^+$, $D_{s1}(2460)^+$ and $D_{s1}(2536)^+$ states. This is indirectly caused by the overestimate of their masses in the theoretical calculation as shown in Table 1.3. The $D_{s0}^*(2317)^+$ and $D_{s1}(2460)^+$ are observed lying below the DK and D^*K mass thresholds, respectively, so they only decay into the OZI-suppressed final states and their decay properties do not fit to the ${}^3P_0$ model. The $D_{s1}(2536)^+$ mass is observed just slightly above the D^*K mass threshold, resulting in the strong suppress of its OZI-allowed decay and thus the small decay width.

1.3.2.3 Classifying the observed D_s^+ states

From the discussions in Secs. 1.3.1, 1.3.2.1 and 1.3.2.2, as well as the detailed review on the decay properties in Ref.[112], the classifications of the observed D_s^+ states are concluded as follows:

- The D_s^+ and $D_{s1}^*(2112)^+$, $D_{s1}(2536)^+$ and $D_{s2}^*(2573)^+$ states are believed falling into the $1S$ and $1P$ families, respectively.
- The $D_{s1}^*(2700)^+$, $D_{s1}^*(2860)^+$ and $D_{s3}^*(2860)^+$ states are good candidates for 2^3S_1, 1^3D_1 and 1^3D_3, respectively. With their properties measured more precisely, their nature will be clearer. There is also a possible interpretation that the $D_{s1}^*(2700)^+$ and $D_{s1}^*(2860)^+$ mesons are mixtures of the 2^3S_1 and 1^3D_1 states[112],

$$\begin{pmatrix} \left|D_{s1}^*(2700)\right\rangle \\ \left|D_{s1}^*(2860)\right\rangle \end{pmatrix} = \begin{pmatrix} \cos\theta_{SD} & \sin\theta_{SD} \\ -\sin\theta_{SD} & \cos\theta_{SD} \end{pmatrix} \begin{pmatrix} \left|2^3S_1\right\rangle \\ \left|1^3D_1\right\rangle \end{pmatrix}.$$

  The mixing angle $\theta_{SD} \in (6.8^\circ, 11.2^\circ)$ can reproduce the measured $D_{s1}^*(2700)^+$ width ratio $\Gamma\left(D^*K\right)/\Gamma(DK)$[1]. The mixture interpretation predicts partial width ratio of the $D_{s1}^*(2860)^+$ state to be $\Gamma\left(D^*K\right)/\Gamma(DK) = 0.6 \sim 0.8$, which can be tested in future measurements.
- The $D_{sJ}(3040)^+$ meson could be identified as a candidate for the $2P_1$ or $2P_1'$ state because its measured mass is close to the corresponding predictions, but the $1D_2^{(\prime)}$

interpretation cannot be excluded[113].

- The $D_{s0}^*(2317)^+$ and $D_{s1}(2460)^+$ states do not simply fit to the D_s^+ spectrum as their masses are significantly lower than the predictions. They could be instead interpreted as the compact tetraquarks, the DK and D^*K molecules or the conventional D_s^+ mesons with the coupled-channel effect[112]. The former two explanations raise new puzzles. If the two states are exotic, where are the conventional 1^3P_0 and $1P_1$ states? The compact-tetraquark interpretation also predicts the light-flavor partners of the two states, but they have not been discovered yet. The partners are also possible in the molecule scheme, *e.g.* the ones composed of $\overline{D}K$ and $\overline{D}^*K$. The observation of the $X_{(0,1)}(2900)$ states with the minimum quark content $cs\bar{u}\bar{d}$ quarks[13-14] sheds light on the searches of the partners of the $D_{s0}^*(2317)^+$ and $D_{s1}(2460)^+$ states under the exotic assumption.

1.3.2.4 Searching for the missing D_s^+ states

There are many predicted states that are not observed in experiment yet as shown in Fig. 1.10 and Table 1.3. The searches for them generally start from the ones with relatively low masses. Below 3.1 GeV, there are six states undiscovered: the 2^1S_0 (0^-) state around 2.6 GeV, two $1D_2$ (2^-) states around 2.86 GeV, and three P-wave states (2^3P_0 (0^+), $2P_1^{(\prime)}$ (1^+), 2^3P_2 (2^+)) around 3 GeV. In addition to the expected $D^{(*)}K$ mode, these states are also possible decaying into the $D^+K^+\pi^-$ final state. For example, if restricting $K^+\pi^-$ to be from the $K^*(892)^0$ state with $J^P = 1^-$, both natural- and unnatural-parity D_s^+ states (0^+ excepted) with masses above the D^+K^{*0} mass threshold (~ 2.79 GeV)can decay into D^+K^{*0}, *e.g.* the unobserved $1D_2$ and $2P$ states. If restricting the $K^+\pi^-$ mass lower than that of the $K^*(892)^0$ state, the $K^+\pi^-$ system is expected to be in S-wave and thus has $J^P = 0^+$. In this case the unnatural-parity D_s^+ states are accessible in the $D^+K^+\pi^-$ system, *e.g.* the missing 2^1S_0 state. The $B^0 \to D^+D^-K^+\pi^-$ decay studied in this thesis provides an excellent opportunity to search for these states.

1.3.3 $cs\overline{u}\overline{d}$ tetraquark candidates

In 2020, the LHCb collaboration analyzed the $B^+ \to D^+D^-K^+$ decay and observed a peaking structure at about 2.9 GeV in the D^-K^+ mass spectrum[13-14] as shown in Fig. 1.11. The structure appears as a band in the Dalitz plot of $m^2(D^+D^-)$ *vs.* $m^2(D^-K^+)$ and thus could correspond to some new state(s) decaying to D^-K^+. A model–independent study showed that the peaking structure in the D^-K^+ mass spectrum cannot result from

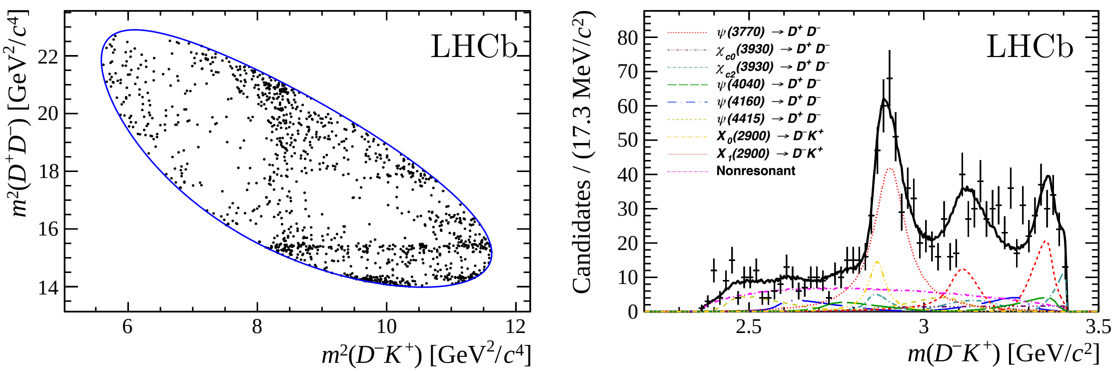

Figure 1.11 Dalitz plot of $m^2(D^+D^-)$ and $m^2(D^-K^+)$ (left) and the $m(D^-K^+)$ mass spectrum with the fit result overlaid for the $B^+ \to D^+D^-K^+$ decay. The plots are taken from Refs.[13-14].

the reflections of the $c\bar{c}$ resonances decaying into D^+D^-[13], and thus the existence of the D^-K^+ resonance(s) is strongly indicated. Later, an amplitude analysis was performed to the $B^+ \to D^+D^-K^+$ decay[1], and shows that it is necessary to include two D^-K^+ states with spin-0 and spin-1, $X_{0,1}(2900)$, to obtain a good description of the data. Masses, widths, and J^P of the two states are measured to be

$$X_0(2900): \quad M = 2.866 \pm 0.007 \pm 0.002\,\text{GeV}, \quad \Gamma = 57 \pm 12 \pm 4\,\text{MeV}, \quad J^P = 1^-,$$
$$X_1(2900): \quad M = 2.904 \pm 0.005 \pm 0.001\,\text{GeV}, \quad \Gamma = 110 \pm 11 \pm 4\,\text{MeV}, \quad J^P = 0^+,$$

where the uncertainties are statistical and systematic, respectively. The $X_{0,1}(2900)$ states are exotic candidates because they must have a minimum quark content of $cs\bar{u}\bar{d}$. This is the first time that the exotic open-charm mesons are discovered in experiment.

The $X_{0,1}(2900)$ states have raised great interest of theorists to interpret their nature. They could be either the compact tetraquarks[114], the $D^*\bar{K}^*$ and $D_1\bar{K}$ molecules[115-122], or due to the kinematic effects[123-124]. Similar to the $D^*_{s0}(2317)^+$ and $D_{s1}(4160)^+$ cases, the light-flavor partners of the $X_{0,1}(2900)$ states are predicted, and the searches for them will help identify the nature of the two states. The $B^0 \to D^+D^-K^+\pi^-$ decay analyzed in this thesis has a great potential to study the open-charm exotic mesons. Besides the $X_{0,1}(2900)$ states that are expected to be re-observed in the D^-K^+ system, it is also possible to have charged X states in the $D^-K^+\pi^-$ system, and exotic candidates containing $c\bar{s}$ in the $D^+K^+\pi^-$ system if they are unexpected in the predicted D_s^+ spectrum.

1.4 Charmonium spectrum

The charmonium spectrum includes the conventional mesons composed of the $c\bar{c}$ pair and the exotic states containing additional light quarks. A brief introduction to such mesons is given in this section, with a particular focus on those possibly accessible in the $D^+D^-(\pi^+)$ and $D_s^+D_s^-$ systems of the $B^0 \to D^+D^-K^+\pi^-$ and $B^+ \to D_s^+D_s^-K^+$ decays studied in this thesis.

1.4.1 Conventional $c\bar{c}$ states

The conventional charmonium states are categorized according to the assignments of the PC quantum numbers: $\{\chi_c(++),\ \psi(--)\}$ with $S = 1$, and $\{\eta_c(-+),\ h_c(+-)\}$ with $S = 0$. The experimentally established $c\bar{c}$ mesons are shown in Fig. 1.12 with the measured masses and widths listed in Table 1.4. In analogous to the D_s^+ spectrum, the observed states are classified by comparing their measured properties and the theoretical calculations. As usual, the masses of the $c\bar{c}$ states are calculated using some potential models, *e.g.* the GI model or the nonrelativistic model[7], and the open-charm decay widths are solved using the ${}^3P_0$ model introduced in Sec. 1.3.2.2. The theoretical results are listed in Table 1.4, which for most of the states show good agreements with the measured values.

The $c\bar{c}$ states lying below the $D^{(*)}\overline{D}^{(*)}$ mass threshold have electromagnetic and OZI-suppressed decay processes. Besides the decays into the lower-mass $c\bar{c}$ states, they also have the $c\bar{c}$ annihilating decays where intermediate gluons or photons are produced from the $c\bar{c}$ pair and then generate light hadrons or leptons (with associated photons sometimes) in the final state. The $c\bar{c}$ states lying above the $D^{(*)}\overline{D}^{(*)}$ mass threshold primarily decay into the $D^{(*)}\overline{D}^{(*)}$ final state. This is an important feature to identify whether a state is conventional or not.

In the D^+D^- final state investigated in this thesis, the natural-parity $c\bar{c}$ states above the D^+D^- mass threshold are expected. These states have already been studied in the $B^+ \to D^+D^-K^+$ analysis[13-14], and their contributions are shown in Figs. 1.11 and 1.13. Besides the well established mesons, the $B^+ \to D^+D^-K^+$ analysis also observed a new $J^{PC} = 0^{++}$ state, $\chi_{c0}(3930)$, whose mass and width are measured to be $M = 3923.8 \pm 1.5 \pm 0.4\,\text{MeV}, \Gamma = 17.4 \pm 5.1 \pm 0.8\,\text{MeV}$, where the uncertainties are statistical and systematic, respectively. The $\chi_{c0}(3930)$ meson could be a candidate for the $\chi_c(2^3P_0)$ state because its measured mass is consistent with the GI-model prediction shown in Table 1.4. However, this classification is controversial because its mass is not consistent with the predictions of another two models. There is another candidate for the $\chi_c(2^3P_0)$ state, the $\chi_{c0}(3860)$ meson, whose measured mass, $M = 3862^{+50}_{-35}\,\text{MeV}$, is close to the $\chi_c(2^3P_0)$ mass prediction in the non-relativistic quark model (3852 MeV) and is only observed

Table 1.4 Masses and widths of the conventional $c\bar{c}$ mesons. The experimental values (Exp.) are taken from Ref.[1], while the theoretical results are taken from Refs.[7-8]. GI denotes the GI model, NR represents the non-relativistic quark model and GI-S is the GI model with the screen potential. The widths are solved for the OZI-allowed decays using the $^3P_0$ model with the NR wave functions as inputs. The classifications for the states in the braces are controversial and need more experimental inputs.

State	$n^{2S+1}L_J$	Mass (MeV)				Width (MeV)	
		Exp.	NR	GI	GI-S	Exp.	NR
$\eta_c(1S)$	$\eta_c(1^1S_0)$	2983.9 ± 0.4	2982	2975	2979	32.0 ± 0.7	-
J/ψ	$\psi(1^3S_1)$	3096.900 ± 0.006	3090	3098	3097	0.0926 ± 0.0017	-
$\eta_c(2S)$	$\psi(2^1S_0)$	3637.5 ± 1.1	3630	3623	3623	$11.3^{+3.2}_{-2.9}$	-
$\psi(2S)$	$\psi(2^3S_1)$	3686.10 ± 0.06	3672	3676	3673	0.294 ± 0.008	-
-	$\eta_c\left(3^1S_0\right)$	-	4043	4064	3991	-	80
$\psi(4040)$	$\psi(3^3S_1)$	4039 ± 1	4072	4100	4022	80 ± 10	74
-	$\eta_c\left(4^1S_0\right)$	-	4384	4425	4250	-	61
$\psi(4415)$	$\psi\left(4^3S_1\right)$	4421 ± 4	4406	4450	4463	62 ± 20	78
$\chi_{c0}(1P)$	$\chi_c\left(1^3P_0\right)$	3414.71 ± 0.30	3424	3445	3433	10.8 ± 0.6	-
$\chi_{c1}(1P)$	$\chi_c\left(1^3P_1\right)$	3510.67 ± 0.05	3505	3510	3510	0.84 ± 0.04	-
$\chi_{c2}(1P)$	$\chi_c\left(1^3P_2\right)$	3556.17 ± 0.07	3556	3550	3554	1.97 ± 0.09	-
$h_c(1P)$	$h_c\left(1^1P_1\right)$	3525.38 ± 0.11	3516	3517	3519	0.7 ± 0.4	-
$\{\chi_{c0}(3860)\}$ $\{\chi_{c0}(3930)\}$	$\chi_c\left(2^3P_0\right)$	3862^{+50}_{-35} 3923.8 ± 1.6	3852	3916	3842	201^{+180}_{-110} 17.4 ± 5.1	30
$\{X(3940)\}$	$\chi_c\left(2^3P_1\right)$	3942 ± 9	3925	3953	3901	37^{+27}_{-17}	165
$\chi_{c2}(3930)$	$\chi_c\left(2^3P_2\right)$	3922.5 ± 1.0	3972	3979	3937	35.2 ± 2.2	80
-	$h_c\left(2^1P_1\right)$	-	3934	3956	3908	-	87
$\psi(3770)$	$\psi\left(1^3D_1\right)$	3773.7 ± 0.4	3785	3819	3787	27.2 ± 1.0	43
$\psi(3823)$	$\psi\left(1^3D_2\right)$	3823.7 ± 0.5	3800	3838	3798	< 5.2	-
$\psi(3842)$	$\psi\left(1^3D_3\right)$	3842.71 ± 0.20	3806	3849	3799	2.8 ± 0.6	0.5
-	$\eta_c\left(1^1D_2\right)$	-	3799	3837	3796	-	-
$\psi(4160)$	$\psi\left(2^3D_1\right)$	4191 ± 5	4142	4194	4089	70 ± 10	74
-	$\psi\left(2^3D_2\right)$	-	4158	4208	4100	-	92
-	$\psi\left(2^3D_3\right)$	-	4167	4217	4103	-	148
-	$\eta_c\left(2^1D_2\right)$	-	4158	4208	4099	-	111

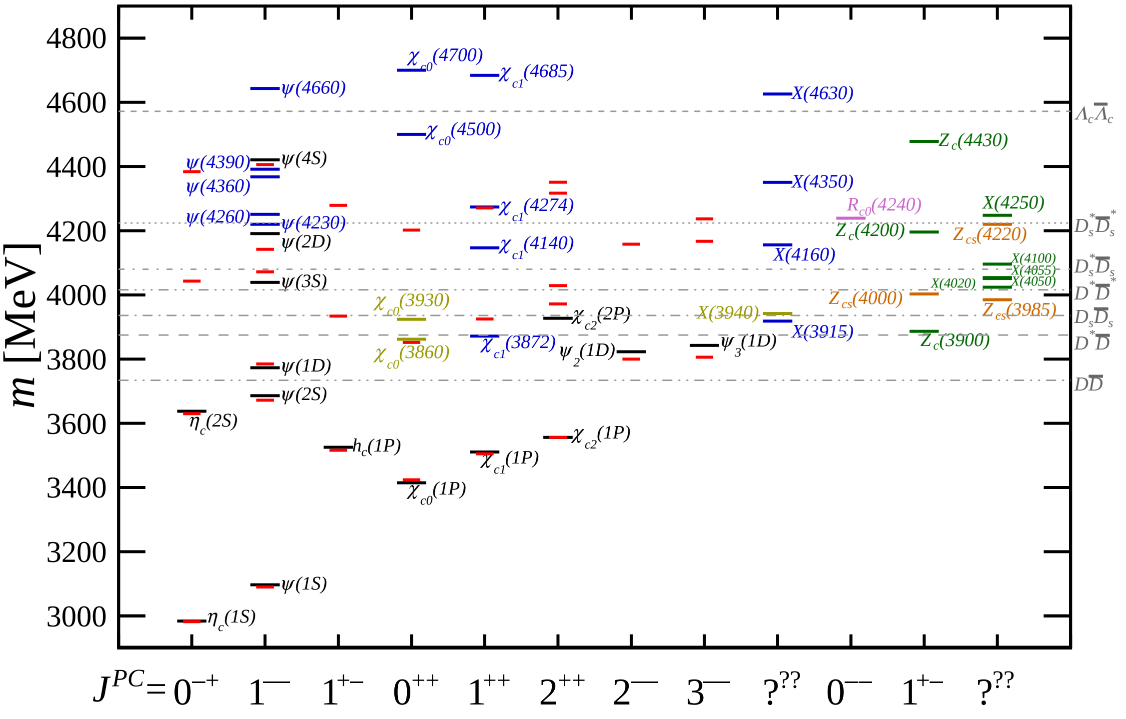

Figure 1.12 Charmonium spectrum. The observed conventional $c\bar{c}$ states are denoted as black lines, with the predictions of the non-relativistic quark model shown in the red lines. The possible conventional candidates are represented by the yellow lines. The discovered exotic candidates are shown in blue, green, purple and orange lines, where the latter three kinds are isospin multiplets and the C-parity is only defined for the neutral ones. The gray dashed lines indicate the mass thresholds of the open-flavor hadrons shown near the right Y-axis. The experimental masses are taken from Refs.[1,14,125-126], while the theoretical values are taken from Ref.[7].

decaying into the $D\bar{D}$ final state. However, uncertainties on the $\chi_{c0}(3860)$ measured properties are quite large[1], indicating this state is not well experimentally established. Future measurements will help interpret the $\chi_{c0}(3930)$ and $\chi_{c0}(3860)$ nature. Anyway, all of the states shown in Fig. 1.13 could be tested in the $B^0 \to D^+D^-K^+\pi^-$ analysis presented in this thesis. New $c\bar{c}$ states are in principle possible, but are not expected because the $B^0 \to D^+D^-K^+\pi^-$ decay does not have higher sensitivity to the $c\bar{c}$ states than that of the $B^+ \to D^+D^-K^+$ process due to the presence of more decay chains resulting from more particles final-state particles.

Similar to D^+D^-, the $D_s^+D_s^-$ system can also be used to study the natural-parity $c\bar{c}$ states above its mass threshold. As these states are expected to primarily decay into $D^{(*)}\overline{D}^{(*)}$, only the observed ones need to be investigated in the $D_s^+D_s^-$ system, including $\chi_{c0,2}(3930)$ ①, $\psi(4040)$, $\psi(4160)$ and $\psi(4415)$. All of them are presented in the D^+D^-

---

① The $\chi_{c0,2}(3930)$ states lie slightly below the $D_s^+D_s^-$ mass threshold but could also have contributions from their tails.

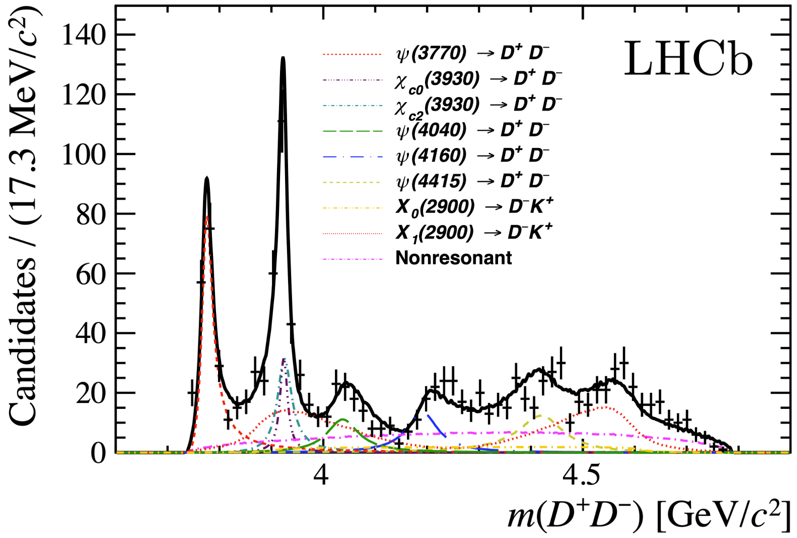

Figure 1.13 Mass spectrum of the D^+D^- system with the fit result overlaid for the $B^+ \to D^+D^-K^+$ decay. The plot is taken from Ref.[14].

mass spectrum as shown in Fig. 1.13. To date, only the $\psi(4040) \to D_s^+D_s^-$ process is observed[127-129] with its partial width remaining undetermined. The $B^+ \to D_s^+D_s^-K^+$ decay studied in this thesis provides an opportunity to search for the $c\bar{c} \to D_s^+D_s^-$ decay of these $c\bar{c}$ states, as well as to measure the width fraction of them decaying into D^+D^- and $D_s^+D_s^-$ if the latter is observed,

$$\frac{\Gamma\left(c\bar{c} \to D^+D^-\right)}{\Gamma\left(c\bar{c} \to D_s^+D_s^-\right)} = \frac{\mathcal{B}\left(B^+ \to D^+D^-K^+\right)\mathcal{FF}^{c\bar{c}}_{B^+\to D^+D^-K^+}}{\mathcal{B}\left(B^+ \to D_s^+D_s^-K^+\right)\mathcal{FF}^{c\bar{c}}_{B^+\to D_s^+D_s^-K^+}}, \tag{1.7}$$

where $\mathcal{B}(X)$ is the branching fraction of the decay X and $\mathcal{FF}^{c\bar{c}}_X$ is the contributing fraction of the $c\bar{c}$ state in the decay. The width fraction will be an important test of the theoretical calculations. To determine it, a branching fraction measurement and an amplitude analysis to the $B^+ \to D_s^+D_s^-K^+$ decay are essential, which are presented in this thesis.

1.4.2 Exotic $c\bar{c}$ candidates

The discovered exotic $c\bar{c}$ candidates are shown simultaneously with the conventional ones in Fig. 1.12. The mesons in the last three columns are confirmed to be in the isospin multiplets due to the observations of the charged states. All others are neutral states and correspond to isospin singlets. They are inferred to be exotic because they show properties different from the conventional $c\bar{c}$ mesons. There is usually no position in the predicted $c\bar{c}$ mass spectrum for these states, and more importantly, as shown in Table 1.5, almost all of them lie above the $D^{(*)}\overline{D}^{(*)}$ mass threshold but are found dominantly decaying into the $c\bar{c}$ states associated with one or several light hadrons. Such processes are

Table 1.5 The exotic $c\bar{c}$ candidates observed in experiment[1,14,125-126].

State	J^{PC}	Decay(s)	State	J^{PC}	Decay(s)
$\chi_{c1}(3872)$	1^{++}	$D^0\bar{D}^0\pi^0, \bar{D}^{*0}D^0,$	$X(4630)$	$?^{?+}$	$J/\psi\phi$
		$J/\psi\pi\pi, J/\psi\omega, J/\psi\rho,$	$\psi(4660)$	1^{--}	$\psi(2S)\pi\pi, \Lambda_c^+\Lambda_c^-,$
		$J/\psi\gamma, \chi_{c1}\pi^0$			$D_s^+D_{s1}(2536)^-$
$X(3915)$	$(0,2)^{++}$	$J/\psi\omega, \gamma\gamma$	$\chi_{c1}(4685)$	1^{++}	$J/\psi\phi$
$\chi_{c1}(4140)$	1^{++}	$J/\psi\phi$	$\chi_{c0}(4700)$	0^{++}	$J/\psi\phi$
$\psi(4230)$	1^{--}	$\chi_{c0}\omega, h_c\pi\pi,$	$Z_c(3900)$	1^{+-}	$J/\psi\phi, D\bar{D}^*$
		$\eta_c 3\pi, J/\psi\eta,$	$X(4020)^{\pm}$	$?^{?-}$	$h_c\pi, D^*\bar{D}^*$
		$J/\psi\pi\pi, \psi(2S)\pi\pi,$	$X(4050)^{\pm}$	$?^{?+}$	$\chi_{c1}\pi$
		$\gamma\chi_{c1}(3872),$	$X(4055)^{\pm}$	$?^{?-}$	$\psi(2S)\pi$
		$D_s^+D_{s1}(2536)^-, l\bar{l}$	$X(4100)^{\pm}$	$?^{??}$	$\eta_c\pi$
$\psi(4260)$	1^{--}	$e^+e^-, J/\psi\pi\pi,$	$Z_c(4200)^{\pm}$	1^{+-}	$J/\psi\pi, \psi(2S)\pi$
		$J/\psi KK$	$R_{c0}(4240)^{\pm}$	0^{--}	$\psi(2S)\pi$
$\chi_{c1}(4274)$	1^{++}	$J/\psi\phi$	$X(4250)^{\pm}$	$?^{?+}$	$\chi_{c1}\pi$
$X(4350)$	$?^{?+}$	$J/\psi\phi, \gamma\gamma$	$Z_c(4430)$	1^{+-}	$J/\psi\pi, \psi(2S)\pi$
$\psi(4360)$	1^{--}	$e^+e^-, J/\psi\pi\pi, \psi(2S)\pi\pi$	$Z_{cs}(3985)^{\pm}$	1^{+}	$D^{*0}D_s^-, D^0D_s^{*-}$
$\psi(4390)$	1^{--}	$h_c\pi\pi, J/\psi\eta$	$Z_{cs}(4000)^{\pm}$	1^{+}	$J/\psi K^{\pm}$
$\chi_{c0}(4500)$	0^{++}	$J/\psi\phi$	$Z_{cs}(4220)^{\pm}$	1^{+}	$J/\psi K^{\pm}$

OZI-suppressed for conventional $c\bar{c}$ mesons. Some of the exotic $c\bar{c}$ candidates even have a non-negligible width decaying into photons or leptons governed by the electromagnetic interaction that is much weaker than the strong force. There are many theoretical works discussing the inner structures of the exotic $c\bar{c}$ states, which as usual include the compact tetraquarks, molecules and the near-threshold kinematic effects. A detailed review is available in Ref.[1]. Besides descriptions of existing experimental results, these models also make some predictions that can be further tested in experiment. For example, the compact-tetraquark interpretation of the $\chi_{c1}(3872)$ state predicts its charged partners[82] and the molecule picture predicts the width fractions of the $\chi_{c1}(3872)$ decays[130-133]. The theoretical predictions can be justified in future experimental studies.

It is noticed that there are charged exotic $c\bar{c}$ mesons decaying into $D\overline{D}^*$ and $c\bar{c}+\pi/K$ final states, as shown in the Table 1.5. Such decay patterns are available in the $D^+D^-\pi^+$ system of the $B^0 \to D^+D^-K^+\pi^-$ decay studied in this thesis. The D^+D^- or $D^+\pi^-$ pair could be from some intermediate $c\bar{c}$ or D^{*0} resonances, and it can be further combined with the π^+ or D^- meson to form charged exotic $c\bar{c}$ states. The $c\bar{c}$ pair could also be combined with the K^+ meson to access the Z_{cs} states, *e.g.* $Z_{cs}(4000)$[125].

The $B^+ \to D_s^+ D_s^- K^+$ decay studied in this thesis provides an opportunity to search for exotic $c\bar{c}$ mesons in the $D_s^+ D_s^-$ system. The states decaying into open-charm final states, *e.g.* $\psi(4230)$ and $\psi(4460)$ shown in Table 1.5, could possibly decay into $D_s^+ D_s^-$. Some mesons observed in the $J/\psi\phi$ final state has the possible interpretation of $c\bar{c}s\bar{s}$ tetraquarks and thus are also possible to decay into $D_s^+ D_s^-$, *e.g.* $\chi_{c0}(4500)$ and $\chi_{c0}(4700)$[134]. Moreover, there are two $J^{PC} = 0^{++}$ candidates lying near the $D_s^+ D_s^-$ mass threshold, $\chi_{c0}(3930)$ and $X(3915)$, which could also be searched for in the $D_s^+ D_s^-$ system. The $\chi_{c0}(3930)$ meson is inferred not fitting into the conventional $c\bar{c}$ spectrum as discussed in Sec. 1.4.1, while the $X(3915)$ state is regarded to be exotic because it was only found decaying into $J/\psi\omega$ and $\gamma\gamma$ though it is above the $D\overline{D}$ threshold. As the two candidates have comparable masses and widths, it is natural to suppose them to be the same state, and due to the near-threshold feature, it could be interpreted as either the $D_s^+ D_s^-$ molecular[16] or the $c\bar{c}s\bar{s}$ tetraquark[15]. If it is really observed in the $D_s^+ D_s^-$ final state, the width fraction of the $D_s^+ D_s^-$ and $D^+ D^+$ decay modes as defined in Eq. 1.7 will provide additional information to interpret the $\chi_{c0}(3930)$ and $X(3915)$ nature.

1.5 Structure of this thesis

This chapter demonstrates the great potential of two undiscovered decays, $B^0 \to D^+ D^- K^+ \pi^-$ and $B^+ \to D_s^+ D_s^- K^+$, to search for charm-strange mesons and charmonium states and measure their properties, thus providing important tests on the theoretical calculations and inputs to theories for further predictions, which further contributes to the efforts to promote the understanding of the strong interaction in the low energy region. The studies presented in this thesis based on the proton-proton collision data collected by the LHCb detector, which is specially designed to efficiently and precisely reconstruct b- and c-hadron decays. Introductions to the LHC and the LHCb experiment are given in Chapter. 2. The $B^0 \to D^+ D^- K^+ \pi^-$ decay can be used to re-observe the resonances previously discovered in the $B^+ \to D^+ D^- K^+$ decay[13-14], and especially, it provides a unique opportunity to search for excited D_s^+ mesons in the $D^+ K^+ \pi^-$ system, which is rarely touched before. The study of the $B^0 \to D^+ D^- K^+ \pi^-$ decay is presented in Chapter 3. Two new excited D_s^+ candidates are observed with masses around 2.6 GeV and 2.93 GeV, and an amplitude analysis is performed to measure the properties of the new state with a lower mass. The $B^+ \to D_s^+ D_s^- K^+$ process offers a particular chance to search for both conventional and exotic charmonium states in the $D_s^+ D_s^-$ system, including the ones observed in the $D^+ D^-$ final state of the $B^+ \to D^+ D^- K^+$ decay[13-14]. The study of the $B^+ \to D_s^+ D_s^- K^+$ decay is presented in Chapter 4. The branching fraction of the $B^+ \to D_s^+ D_s^- K^+$ decay is at first measured, providing the essential input to help interpret the natures of the states expected in the $D_s^+ D_s^-$ system. A near-threshold peaking structure is observed in the $D_s^+ D_s^-$, and an amplitude analysis is employed to measure its properties. Finally, a summary of the analyses in this thesis and the future prospects are discussed in Chapter 5.

CHAPTER 2 LHCB EXPERIMENT

The studies in this thesis use the data collected by the Large Hadron Collider beauty (LHCb) detector[135] at the Large Hadron Collider (LHC)[136]. In this chapter, a brief description of the LHC is firstly given in Sec.2.1, followed by the introduction to the design and performance of the LHCb experiment in Sec. 2.2.

2.1 Large Hadron Collider

The LHC is a high-energy particle accelerator located at the European Organization for Nuclear Research (CERN), which is the largest and the most powerful human-built machine in the world. It lies in a circular underground tunnel with a length of 26.7 km and a typical depth of 100 m straddling the France-Switzerland border near Geneva. The LHC ring contains two parallel beamlines, each holding a particle beam maintained by superconducting magnets and accelerated by radio-frequency cavities. The two beams circulate in the opposite directions and finally collide at an energy of TeV level. The colliding particles are usually protons, offering opportunities to make precise tests of the SM and search for the phenomena beyond it. Heavy–ion collisions are also available at the LHC, opening a window for quark-gluon plasma studies that aim at the exploration of the evolution of the early universe.

To reach the energy of TeV scale, particles are speeded up by a series of accelerators, as shown in Fig. 2.1. Protons are at first generated by stripping the electrons from the hydrogen atoms and are injected into the Linear particle accelerator (LINAC2), where they are initially accelerated to an energy of 50 MeV. Protons are then sent to the Proton Synchrotron Booster (PSB) and are further boosted to 1.4 GeV, followed by the Proton Synchrotron (PS) where the beam energy is increased to 25 GeV. Afterwards, the Super Proton Synchrotron (SPS) further push the protons to 450 GeV and transfer them to the LHC, where they finally reaches the maximum energy of 7 to 13 TeV. Ions are initially injected into the LINAC3 and Lower Energy Ion Ring (LEIR). They are then transferred to the PS and then follow the accelerating route of protons. The fully accelerated particles finally collide inside the four main detectors at the LHC, and they are designed for different physics purpose. The ALICE experiment[137] is specialized for heavy-ion physics. The ATLAS[138] and CMS experiments[139] are designed for general physical purposes, *e.g.*

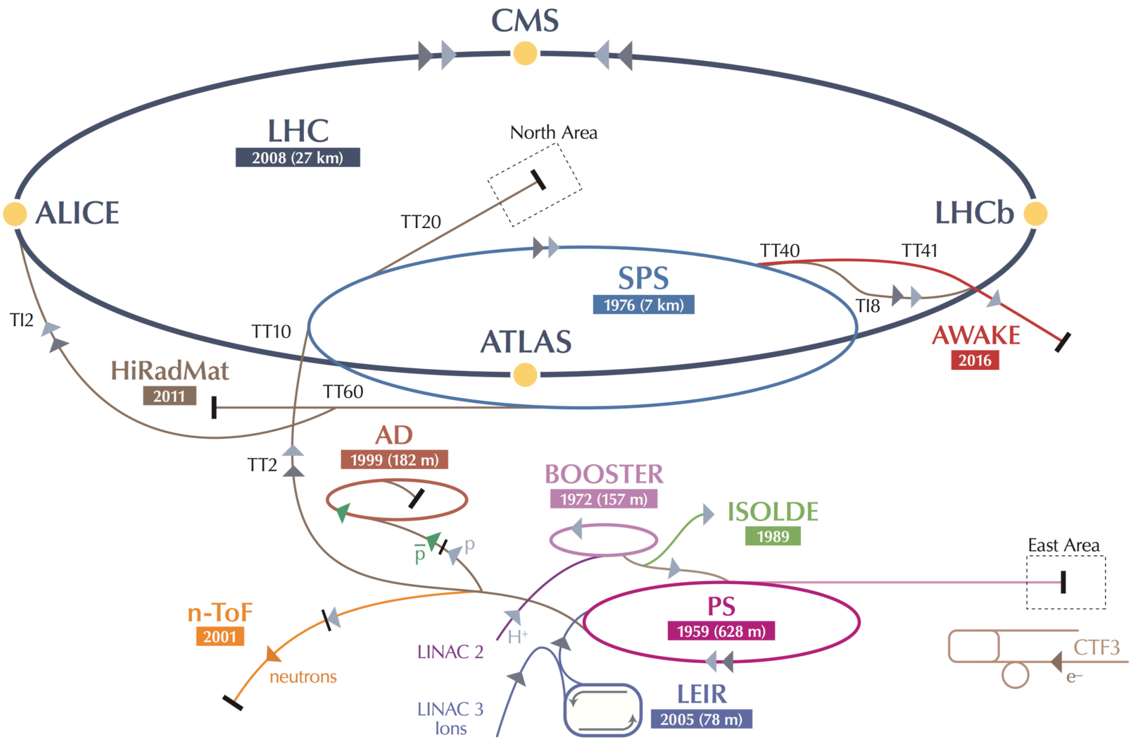

Figure 2.1 CERN accelerator complex [140].

researches about the Higgs boson and the top quark. The LHCb experiment focuses on studies of heavy-flavor hadrons. Locations of the four experiments at the LHC are shown in Fig. 2.1.

The analyses in this thesis use the proton-proton (*pp*) collision data produced by the LHC in different periods and under different conditions. The Run 1 operation mainly proceeded in 2011 and 2012, when the center-of-mass energies of *pp* collisions are 7 TeV and 8 TeV, respectively, and the peaking instantaneous luminosity of the LHC is around $8\times10^{33}\text{cm}^{-2}\text{s}^{-1}$. In the next two years, the LHC was shut down (Long Shutdown 1, LS1) for the upgrades to reach a higher collision energy. The Run 2 operation started from 2015 with a center-of-mass energy of 13 TeV, and the peaking instantaneous luminosity is increased to around $2\times10^{34}\text{cm}^{-2}\text{s}^{-1}$. The Run 2 operation ended in 2018. The typical instantaneous luminosity of the LHC is designed for the ATLAS and CMS detectors, but is too high for the LHCb experiment to efficiently collect and process data of heavy-hadron decays. Therefore, the beam focus at the collision point in the LHCb detector is tuned to achieve a lower luminosity in the range of $2\sim4\times10^{32}\text{cm}^{-2}\text{s}^{-1}$. The lower luminosity can also reduce the radiation damage of the detector. The luminosity accumulation of the LHCb detector in shown in Fig. 2.2. During the Run 1 and Run 2 operating periods, the LHCb experiment collected *pp* collision data of a total integrated luminosity of around

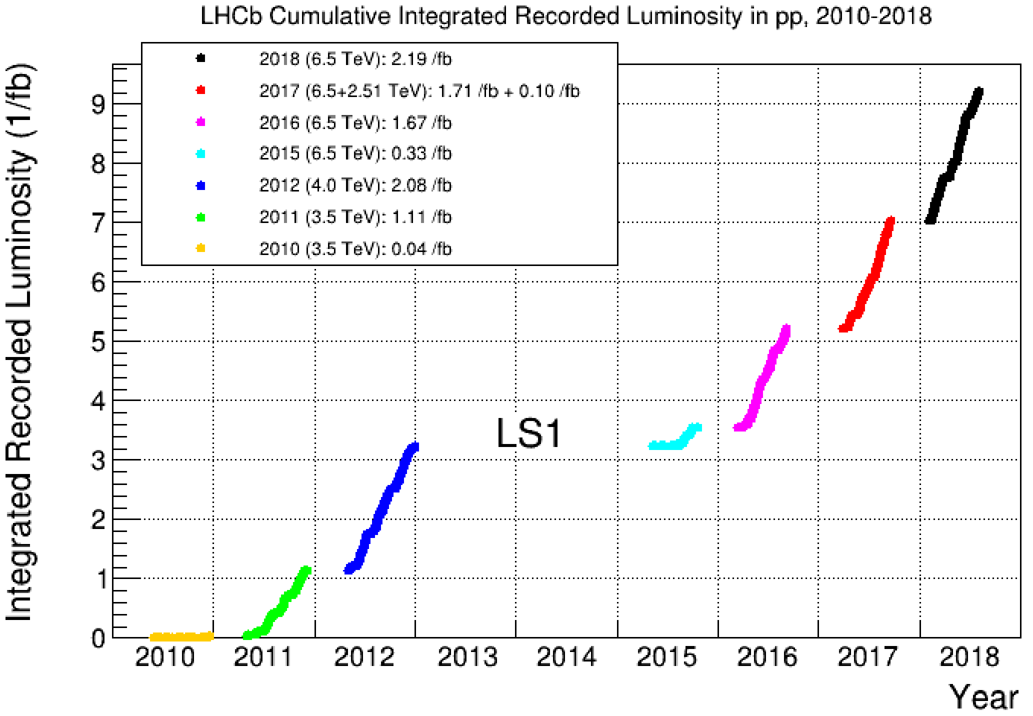

Figure 2.2 Cumulative integrated luminosity recorded by the LHCb experiment[141].

$9\,\mathrm{fb}^{-1}$. Such a large sample makes it practicable to perform the studies presented in this thesis.

2.2 LHCb experiment

The primary goal of the LHCb experiment is the precision studies on the *CP* violation and rare decays of the charm and beauty hadrons, to indirectly search for the evidence of New Physics beyond the SM. In addition, it also covers a wide range of other physics subjects, *e.g.* heavy-ion physics, electroweak physics, hadron spectroscopy, *etc.* To achieve these goals, the LHCb geometry and sub-detectors are designed to have an excellent ability for efficient collection and high-precision measurement of the heavy-hadron decays. The layout of the LHCb experiment is shown in Fig. 2.4, placed in a coordinate system with the pp collision point as the origin, the beam line as the z-axis, and the horizontal and vertical directions as the x- and y- axes, respectively. The commonly-used cylindrical (r, ϕ, z) or spherical (r, θ, ϕ) coordinates are also taken sometimes.

The LHCb geometric acceptance covers the forward angular region of approximately $10\,\mathrm{mrad} < \theta < 300\ (250)\,\mathrm{mrad}$ in the horizontal (vertical) plane, roughly corresponding to a pseudorapidity range $2 < \eta < 5$, where $\eta \equiv -\ln[\tan(\theta/2)]$. This configuration is chosen based on the production feature of heavy hadrons at the LHC. In pp collisions at

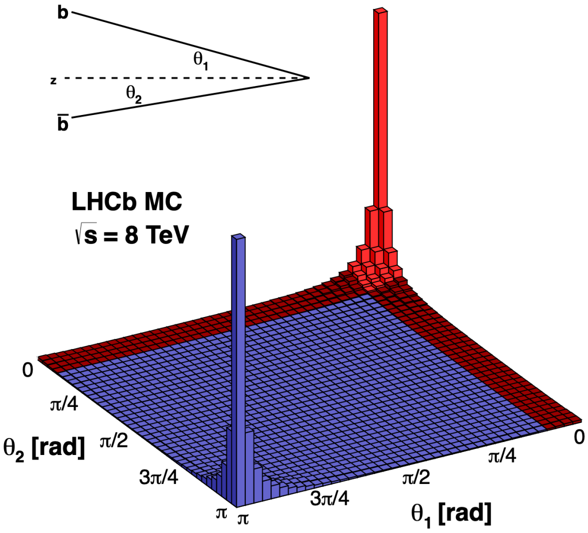

Figure 2.3 Polar angle distributions of the $b\bar{b}$ pairs produced in the pp collisions at the center-of-mass energy $\sqrt{s} = 8\,\mathrm{TeV}$[142]. The red regions are covered by the LHCb acceptance.

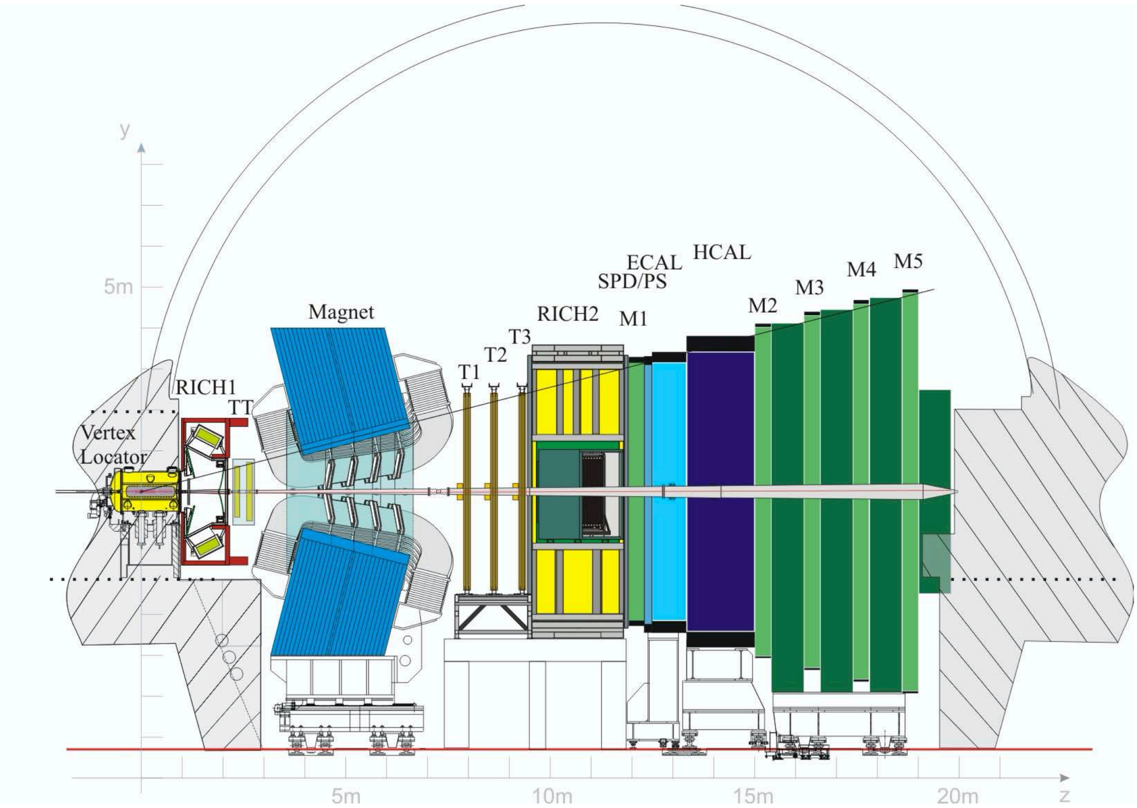

Figure 2.4 View of the LHCb detector[135].

the TeV energy scale, the $b\bar{b}$ pairs are predominantly produced in the narrow cones close to the beam axis, as shown in Fig. 2.3. With the forward construction, the LHCb detector can access around 25% of the $b\bar{b}$ pairs with just about a 2.4% coverage of the full solid angle.

The sub-detectors of the LHCb detector, shown in Fig. 2.4, are specially designed for the precise reconstruction of beauty- and charm-hadron decays, and they are categorized into two systems according to different purposes: tracking and particle identification (PID). The tracking system is responsible for the high-precision trajectory reconstructions of charged final-state particles, as well as vertices of pp collisions and heavy-hadron decays, and the PID system can provide efficient discrimination on the species of final-state particles. Detailed descriptions of the tracking and PID systems are presented below, followed by brief introductions to the LHCb trigger system and simulation.

2.2.1 Tracking system

The tracking system consists of the Vertex Locator (VELO), the Tracker Turicensis (TT), the magnet and three Tracking stations (T1-T3). Their locations are illustrated in Fig. 2.4.

2.2.1.1 Vertex Locator

The VELO is positioned around the pp collision region. Its primary goal is to perform high-precision reconstruction of the pp interaction point, *i.e.* primary vertex (PV) and decay vertices of the weakly decaying beauty- and charm-hadrons. A significant isolation of the decay vertices from the PV is essential for precision measurements on lifetimes of weakly decaying heavy hadrons. In addition, for the studies of the exclusive decays such as those presented in this thesis, the requirement on the impact parameter (IP) of tracks, defined as the closest approach between a track and the PV, can sufficiently suppress the large amount of background from pp collisions.

The VELO is composed of silicon microstrip sensors that are arranged to a series of stations placed along the beam axis, as shown in Fig. 2.5. Except for the pileup system, Each station contains two silicon sensors of two types, the R- and ϕ-sensors, to record hit coordinates in the radial and azimuthal angle directions, respectively. The z-coordinate is given as the location of the station along the beam axis. The cylindrical design is chosen for fast track and vertex reconstructions. The pileup system contains two R-sensors, to

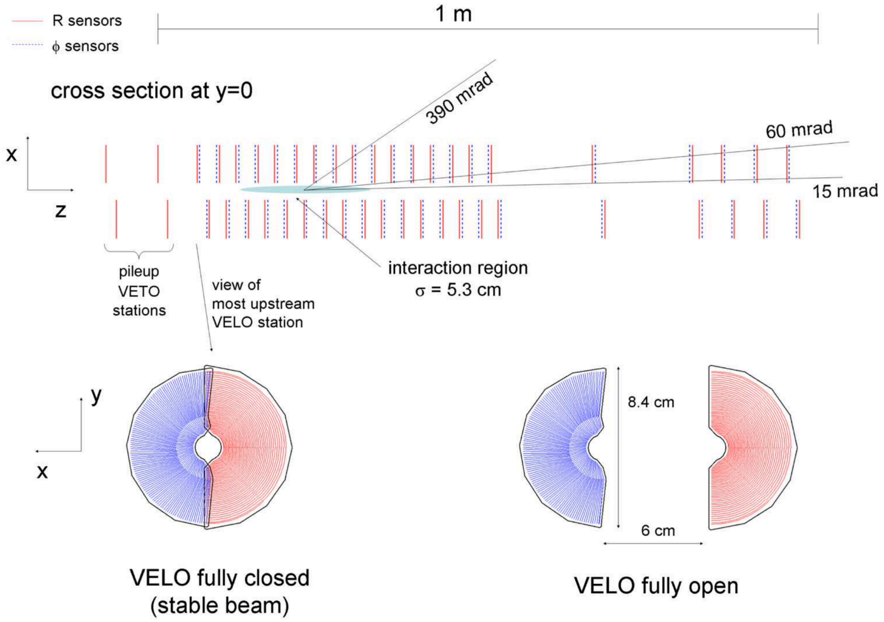

Figure 2.5 A side view of the VELO modules at $y = 0$ is shown on the top and the illustration of the status of the sensors on the bottom [135].

provide additional information to help improve the PV reconstruction. The sensors are designed as two retractable sectors. During the beam injection and acceleration of the LHC, the two sectors are separated 3 cm away from the beam axis for safety consideration, and when the beams get stable, they are pulled back to a distance of just 8 mm, to achieve a high-resolution reconstruction of the PV and IP. The geometry of the VELO is chosen to cover the LHCb acceptance. Especially, at the maximum polar angle of 390 mrad, a trajectory is required to pass through three stations.

The VELO shows an excellent performance on trajectory and vertex reconstructions[143]. Firstly, a very high tracking efficiency is achieved, which is generally at the level of 98%. Secondly, the PV and IP are reconstructed with high resolutions, as shown in Fig. 2.6. The PV resolution depends on the number of tracks (nTracks) that are used to make the PV, as shown in Fig. 2.6. For the typical nTracks of 25, the resolution is about 13 µm in the x and y directions, and 71 µm in the z direction. The IP resolution is momentum dependent, and is asymptotically about 25 µm for tracks with high momentum and 12 µm for tracks with high transverse momentum.

2.2.1.2 Tracker Turicensis

The TT is a silicon detector composed of microstrip sensors, positioned before the the dipole magnet. The size of the TT is designed to cover the LHCb acceptance. There are four rectangular detection layers of the TT, arranged in an $x-u-v-x$ geometry with

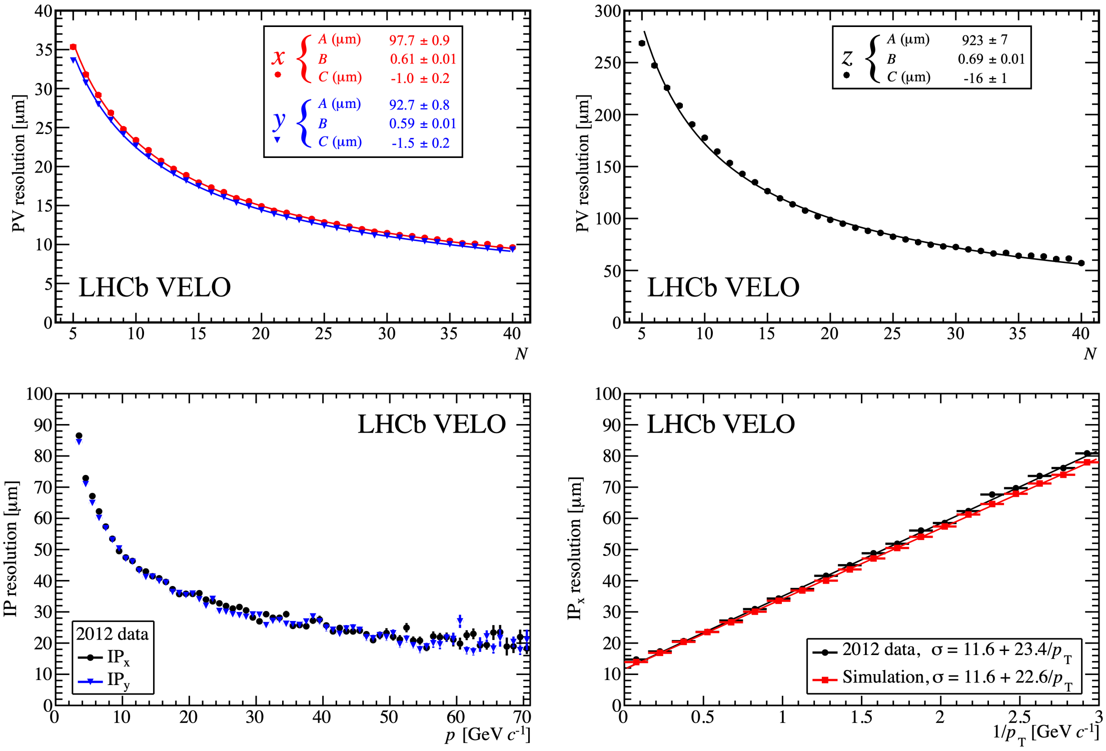

Figure 2.6 PV resolutions (top) as a function of the number of tracks used to obtain the PV, and the IP resolutions (bottom) as a function of track momentum p and transverse momentum p_{T}.[143].

the x-layer set to be vertical, and the u- and v-layers rotated around the z axis by $\pm 5^{\circ}$. The layout of the v-layer is shown Fig. 2.7. To benefit track reconstructions, the four layers are grouped into two sets of (x, u) and (v, x), and the two sets are placed 27 cm away from each other in the z-direction. Track segments are reconstructed by connecting the two hit positions on the two sets. The hit efficiency of the TT is found to be greater than 99.7% and the spatial resolution is typically 50 μm[144].

2.2.1.3 Magnet

A dipole magnet with saddle-shaped coils is employed to bend trajectories of the charged final-state particles, to provide information for the momentum measurement. The magnetic field is mainly in the y-direction and so charged particles are deflected in the horizontal plane. The magnetic field strength along the z-axis is shown in Fig. 2.8. The integrated field is 4 Tm. The direction of the magnetic field is reversed periodically. Roughly the same amount of the pp collision data is collected under the magnet polarity down (MagDown) and up (MagUp) conditions, so the detection asymmetry is expected to be largely canceled in the full LHCb dataset.

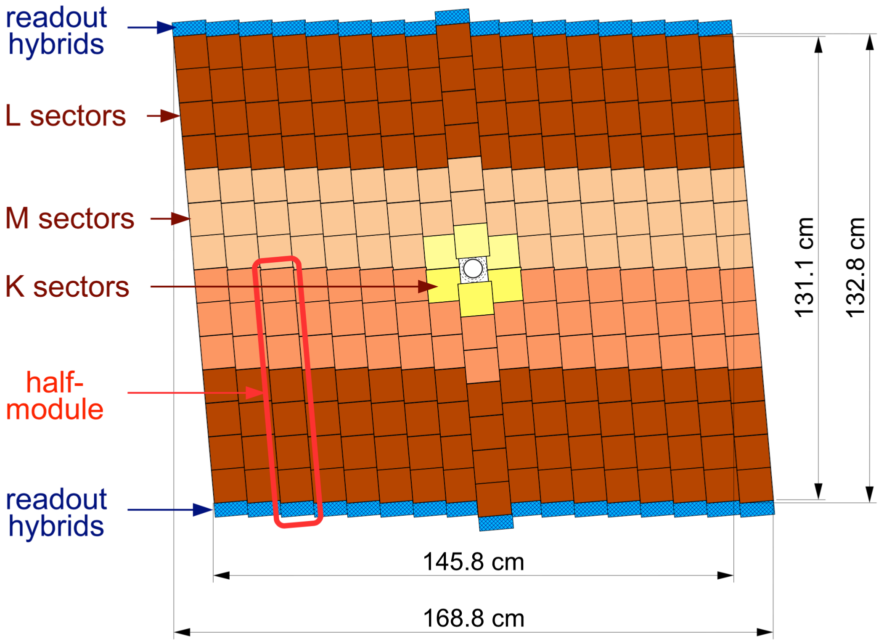

Figure 2.7 Layout of the v-layer of the TT[145].

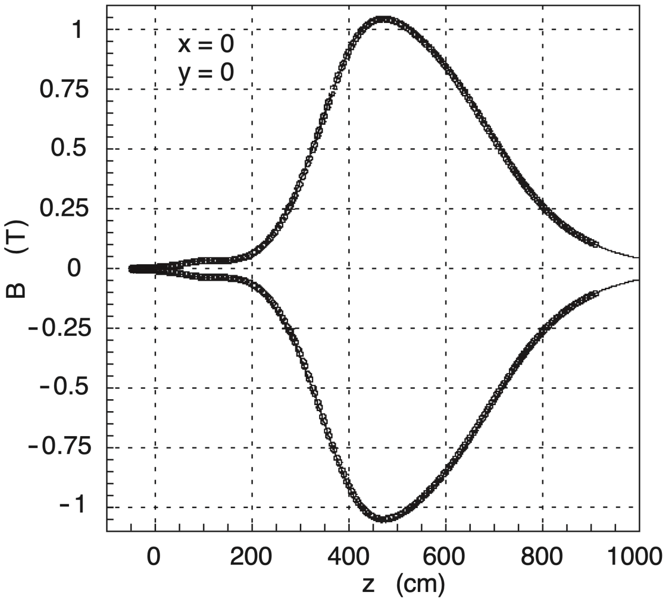

Figure 2.8 Variation of the magnetic field strength along the z-direction[145].

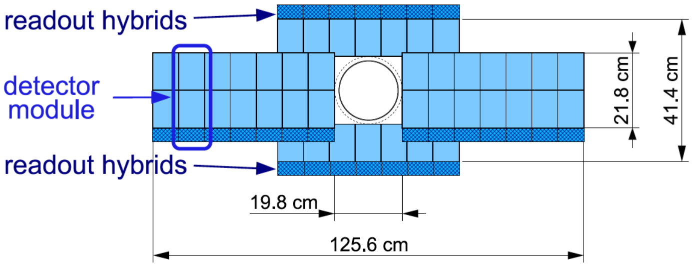

Figure 2.9 Layout of the first layer of the IT in the T2 station[145].

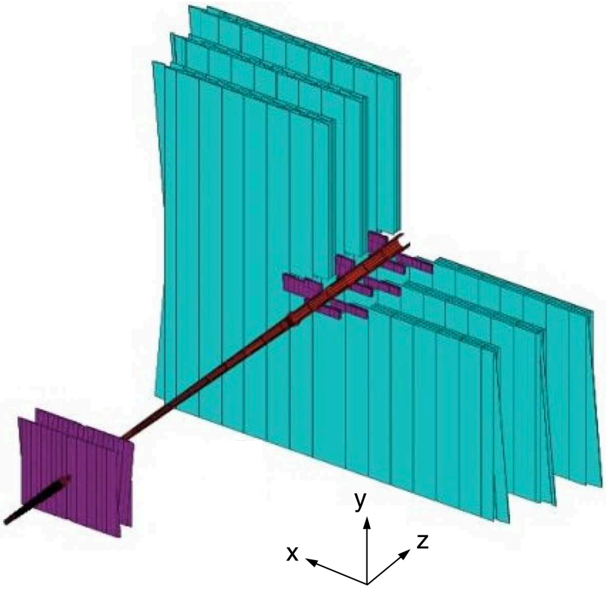

Figure 2.10 Arrangement of the OT straw-tube modules (cyan) in the $x - u - v - x$ structure. The silicon trackers TT and IT are also shown (purple)[145].

2.2.1.4 T–stations

The T–stations are composed of three modules, Ti with $i \in 1, 2, 3$, located downstream of the magnet. each T–station consists of four layers in the same $x-u-v-x$ structure as that for the TT. In the region close to the beam axis, silicon microstrip sensors are used to achieve a high spatial resolution of hits. The sensors compose the Inner Tracker (IT), whose layout is shown in Fig. 2.9. The performance of the IT is similar to that of the TT. The other region of a T-station is covered by a drift-time detector called the Outer Tracker (OT), shown in Fig. 2.10. The counting gas is chosen as a mixture of 70% Argan, 28.5% Carbon Dioxide and 1.5% Oxygen to achieve a drift time below 50 ns and a spatial resolution of 200 μm. The hit efficiency in the OT is also as high as 99%.

2.2.1.5 Track reconstruction

The hits recorded in the tracking system are combined to reconstruct trajectories of charged particles. The LHCb trajectories are categorized into different types according to

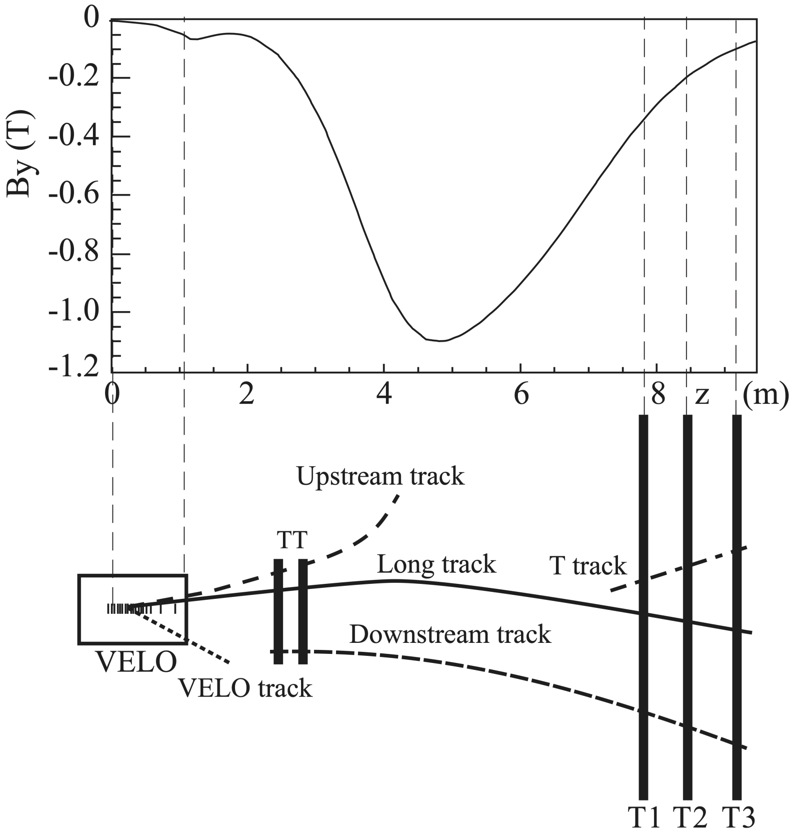

Figure 2.11 Graphical explanation of LHCb track types[144]. The variation of the magnetic field strength along the z-direction is shown as the reference.

the positions of hits that are used. The track types are illustrated in Fig. 2.11, including:

- **Long tracks** traverse the full tracking system. They usually leaves hits in all the tracking detectors and thus have the highest resolutions of IP and momentum. Long tracks mainly serve for the physics studies.
- **Downstream tracks** only have hits recorded by the TT and T-stations. They usually correspond to the long-lived particles that do not decay inside the VELO, *e.g.* K_S^0 and Λ.
- **Upstream tracks** pass only the VELO and the TT. They have relatively low momentum and thus are severely deflected by the magnet. They generally cannot arrive the T-stations. Such tracks are useful to understand the PID performance of the Cherenkov detector before the TT.
- **T tracks** do not leave hits in the sub-detectors except the T-stations. They generally result from the secondary interactions, and can be used to validate the Cherenkov detector downstream of the T-stations.
- **VELO tracks** only have hits in the VELO. They generally result from the charged particles flying backward or having a large polar angle. VELO tracks play an

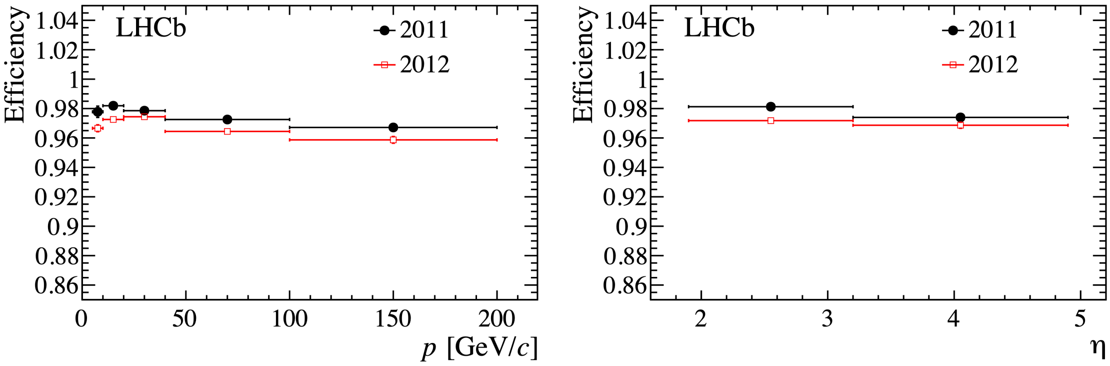

Figure 2.12 Tracking finding efficiency as a function of track momentum p (left) and pseudorapidity η (right)[144].

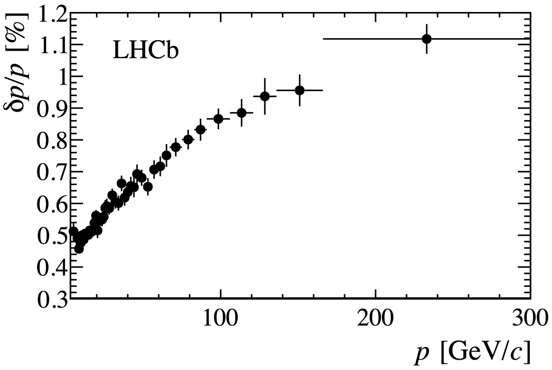

Figure 2.13 Relative resolution of track momentum[144].

important role in the PV reconstruction.

The track reconstruction starts from the hits in the VELO and T-stations, where charged particles are expected to fly straightforward due to the weak magnetic field in the two regions. When the VELO and T tracks are reconstructed, they can be extrapolated to look for the corresponding hits in the TT and combine them to form upstream and downstream tracks, respectively. The long track reconstruction uses the hits in the VELO and T-stations, and is performed using two complementary strategies. The primary one is the forward tracking, where the VELO tracks are extrapolated to the T-stations to search for the expected hits. The second strategy is to match the VELO and T tracks. The TT hits compatible with the long tracks are further added to improve the momentum resolution. At the final stage, a Kalman-filter fit is performed to extract the quantities of the tracks, *e.g.* momentum. In the fit, the multiple scattering effect and the correction of energy loss are considered.

The long tracks are the most widely used type in the LHCb analyses, including the studies in this thesis. The performance of the tracking system is detailed in Ref.[144]. The long track finding efficiency is measured as a function of kinematic variables of tracks, as shown in Fig. 2.12. The efficiency is found typically above 96% for those with momentum $5\,\text{GeV} < p < 200\,\text{GeV}$ and pseudorapidity $2 < \eta < 5$. The relative resolution of the track momentum as a function of p is shown in Fig. 2.13, which varies in the range $0.5\% - 1.0\%$ for $20\,\text{GeV} < p < 150\,\text{GeV}$. The IP resolution is dominated by the VELO performance as discussed in the Sec. 2.2.1.1, where the values for tracks with high p or p_{T} are roughly 25 μm or 12 μm, respectively.

2.2.2 Particle identification system

The particle identification system consists of two Ring Imaging Cherenkov detectors (RICHI1/2), the Muon stations (M1-M5), and the calorimeter system that includes the Scintillator Pad Detector (SPD), the Preshower (PS), the Electromagnetic Calorimeter (ECAL) and the Hadron Calorimeter (HCAL). Their positions are illustrated in Fig. 2.4.

2.2.2.1 Ring Imaging Cherenkov detectors

The RICH1 and RICH2 provide the primary information for particle identification of charged final-state hadrons, *i.e.*, π^+, K^+ and p. The detecting principle is the Cherenkov effect. When a charged particle traverses a medium with a speed v larger than that of the light, it emits Cherenkov photons in the direction with a angle of $\theta_c = \cos^{-1}(\frac{c}{nv})$ with respect to its flying direction, where c is the speed of light in the vacuum and n the refractive index of the medium. In principle, the velocity of a particle can be determined by measuring the Cherenkov angle θ_c, and can be combined with the momentum provided by the tracking system to determine the species of particles.

To provide particle identification for almost all kinds of tracks, the positions and the mediums of the two RICH detectors are specially selected. The RICH1 is placed between the VELO and the TT and thus it can identify the upstream tracks with relatively low momentum. To achieve this, the medium of the RICH1 is chosen to be a mixture of aerogel and C_4F_{10} with a relatively large refractive index, which enables the particle identification in the momentum range of $1\,\text{GeV} < p < 60\,\text{GeV}$, as shown in Fig. 2.14. The RICH2 is placed downstream of the tracking system, covering the tracks traversing the T-stations, especially the long tracks with relatively high momentum ($15\,\text{GeV} < p < 100\,\text{GeV}$). The medium of the RICH2 is chosen to be CF_4. The layouts of the two RICH detectors are shown in Fig. 2.15, where the mirrors are used to guide the Cherenkov lights to the photon detectors that are placed in the low-radiation regions outside the LHCb acceptance.

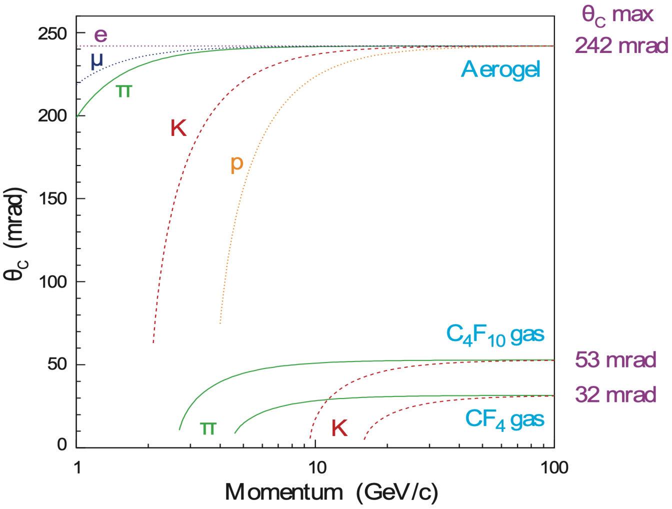

Figure 2.14 Cherenkov angle verses particle momentum for the RICH mediums[135].

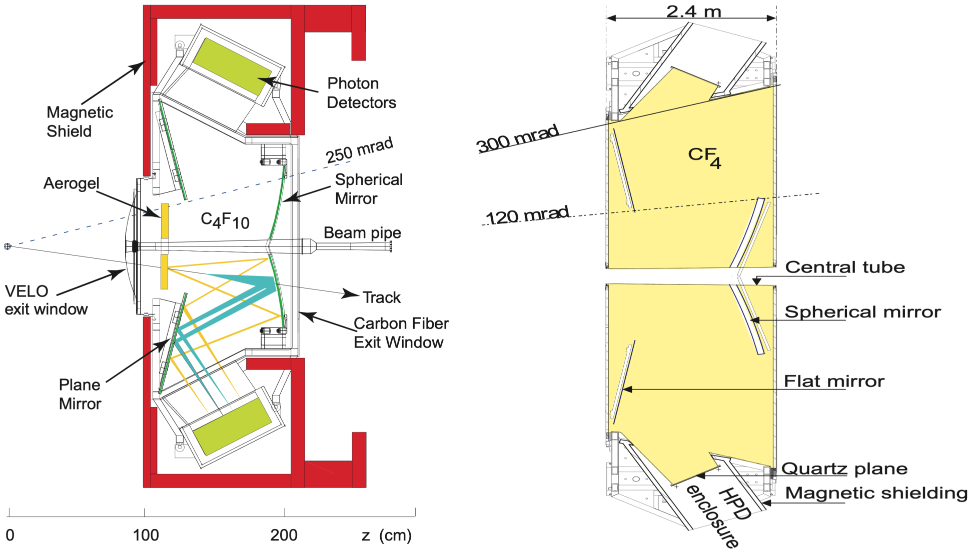

Figure 2.15 Layouts of the RICH1 (left) and RICH2 (right)[135].

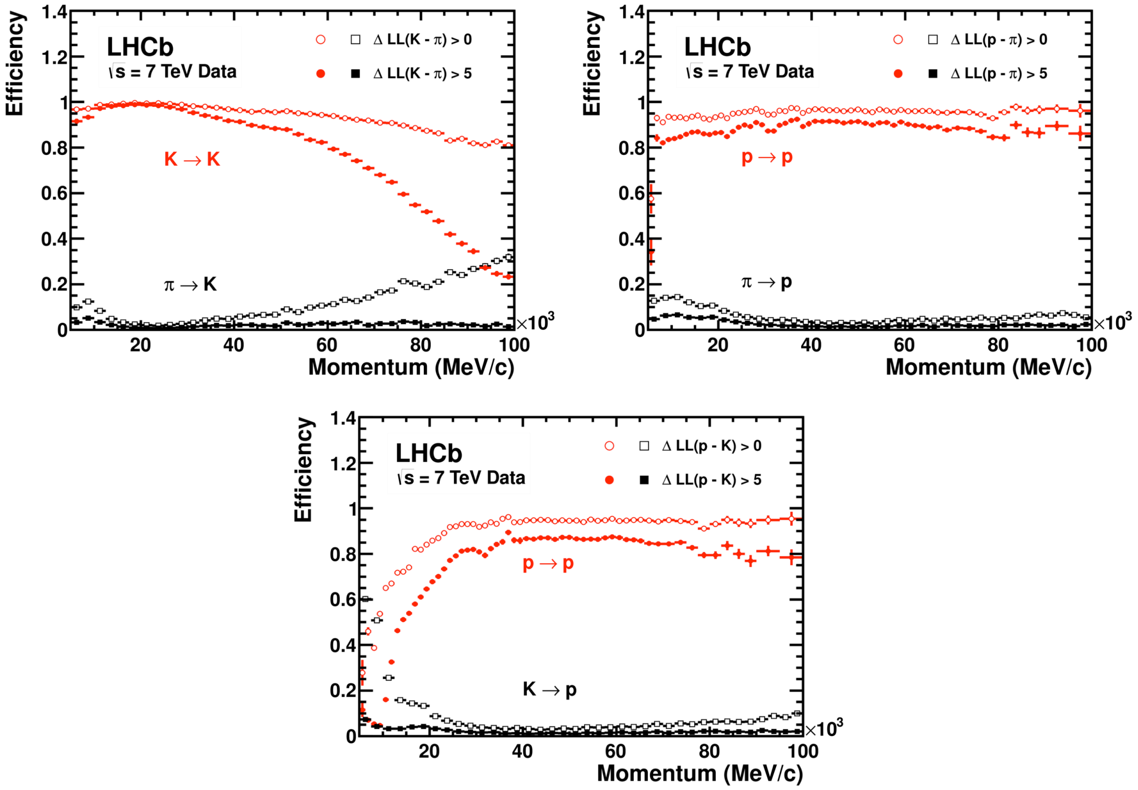

Figure 2.16 Efficiency and misidentification rate as a function of the track momentum under different $\Delta \log \mathcal{L}$ requirements[146].

The discrimination of different particle hypotheses for a track, h_1 and h_2, is quantified as the PID variable $\Delta \log \mathcal{L}(h_1 - h_2) \equiv \log \mathcal{L}_{h_1} - \log \mathcal{L}_{h_2}$[146], where $\log \mathcal{L}_h$ can be qualitatively understood as the probability for the track being resulted from the particle of type h. A larger value of $\Delta \log \mathcal{L}(h_1 - h_2)$ indicates the preference of h_1 over h_2. The requirement on the PID variables can efficiently reduce the background from the wrong combinations of tracks when reconstructing the heavy-hadron decays. The efficiencies and misidentification rates as functions of the track momentum under several PID requirements are shown in Fig. 2.16. Good performance is found in a large momentum range for the discrimination of charged kaons, pions and protons.

2.2.2.2 Calorimeters

The task of the calorimeter system is to reconstruct neutral particles (γ, π^0) and measure their energies, as well as to provide the discrimination of electrons, photons and hadrons. The information from the calorimeters are also essential inputs for the fast trigger at the hardware level.

As shown in Fig. 2.4, the SPD is the most upstream detector in the calorimeter system, followed by the PS, the ECAL and the HCAL. They are all designed to have a higher

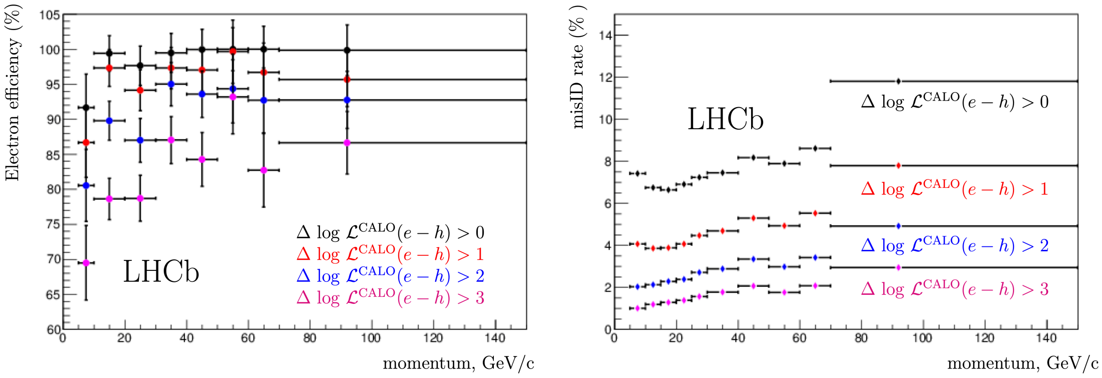

Figure 2.17 Efficiency and misidentification rate as a function of the track momentum under different $\Delta \log \mathcal{L}^{\mathrm{CALO}}(e-h)$ requirements[144].

granularity of detecting modules in the inner region than that of the outer region because the hits are more intensive close to the beam. The SPD and the PS are designed to be two scintillator pads. The SPD records the hits of traversing charged particles and thus has the ability to separate charged and neutral particles, *e.g.* electrons and π^0/γ. The number of recorded hits in it represents the detector occupancy and is a prompt decision to remove the busy events in the hardware trigger. The PS distinguishes electrons and charged pions by detecting the electromagnetic shower initiated by the lead layer before it. The ECAL is designed to have a shashlik structure of scintillator/lead and a thickness of 25 radiation length, to fully absorb the energy of electrons and photons. Its main task is to provide the energy and position measurements of electrons and photons, thus enabling the reconstruction and identification of photons and neutral pions ($\pi^0 \to \gamma\gamma$). The energy information from the ECAL is also a part of the hardware trigger. The HCAL has a similar shashlik structure to that of the ECAL, with iron as the absorber instead of lead. Its thickness is 5.6 interaction lengths due to the space limitation. The HCAL provides the energy information of hadrons required by the hardware trigger.

The electron identification takes the responses of the PS, the ECAL and the HCAL simultaneously, where the PID variable $\Delta \log \mathcal{L}^{\mathrm{CALO}}(e-h)$ is calculated to quantify the discrimination power between the electron and the hadron h[144]. The performance of the electron PID is illustrated in Fig. 2.17.

2.2.2.3 Muon stations

The Muon stations, M1-M5, are employed to identify muons and provide the information for the hardware trigger. The layout of the Muon stations is shown in Fig. 2.18.

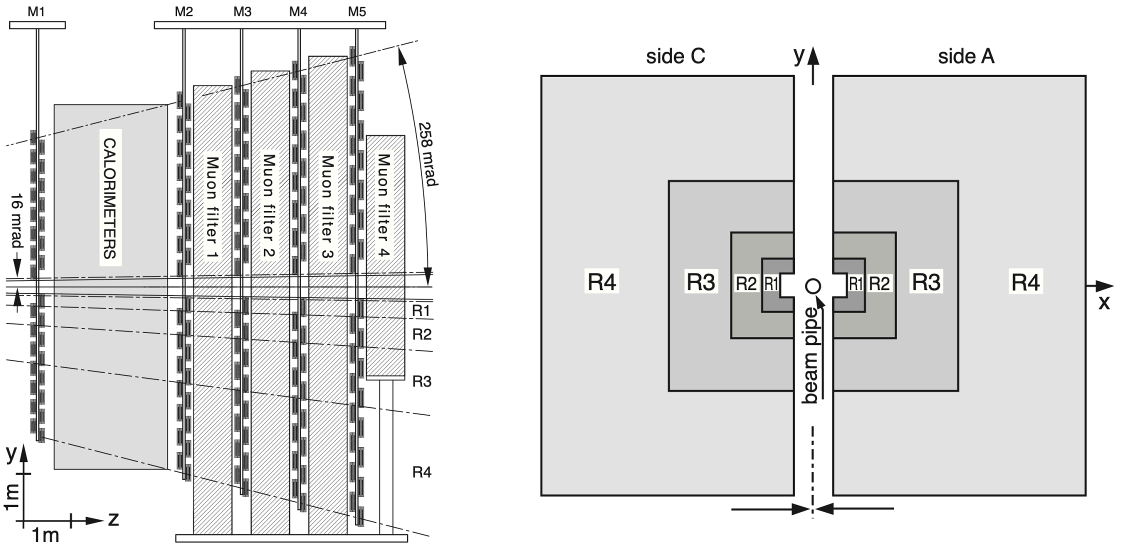

Figure 2.18 Layout of the Muon stations. Left: side view; Right: right view[147].

The M1 station is located upstream of the calorimeter system, while the remaining four stations placed downstream of the calorimeters. Three iron pads with the thickness of 80 cm are installed between the M2-M5 stations as the absorber to select muons with high momentum. To adapt to the hit intensity variation in the $x - y$ plane, all M1-M5 are divided into four regions R1-R4 with the side length ratio of $1 : 2 : 4 : 8$. With this design, the four region have comparable occupancies. All of the M1-M5 stations are Multi Wire Proportional Chambers (MWPC), except for the R1 region of the M1 station that is instead composed of Gas Electron Multiplier (GEM) due to the radiation resistance requirement.

The M1 station primarily provides additional information to improve the p_{T} measurement in the trigger, The M4-M5 stations contribute to the muon identification, and the M2-M3 stations, which have better spatial resolution than the others, can also participate in the fast reconstructions of the muon tracks in the trigger. The identification of muons starts from the extrapolation of trajectories reconstructed by the tracking system to the Muon stations. A track is identified as a muon according to the number of hits in the M1-M5 stations that can be associated to it (IsMuon). An alternative method is comparing the responses of the Muon stations under the muon and non-muon hypotheses for a track, with which the discriminating variable, muDLL, is calculated to represent the identification power. The muon identification efficiency and misidentification rates as functions of the track momentum are shown in Fig. 2.19. The performance of the two identification method are asymptotically the same in the high momentum region.

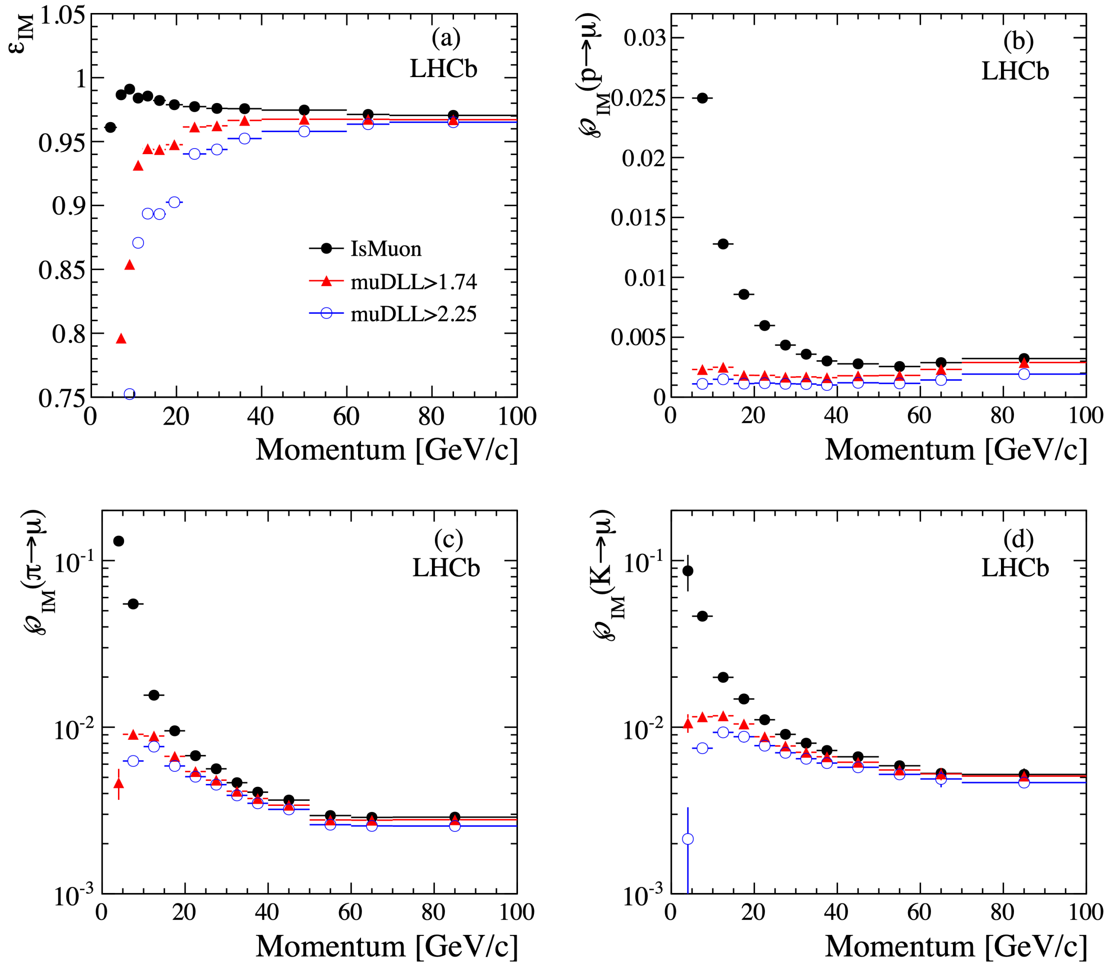

Figure 2.19 Muon identification efficiency (a) and misidentification rates for protons (b), pions (c) and kaons (d) as a function of the track momentum [148].

For the tracks with low momentum, IsMuon tends to have high efficiency but also high misidentification rates, while muDLL is just the reverse.

2.2.2.4 Combined particle identification

The PID information from the RICH detectors, the calorimeter system and the Muon stations can be combined to obtain new PID variables, which are generally the ones used in physics analyses. As more information is utilized, the combined variables have better performance than the original ones. There are two sets of the combined PID variables. The first set is derived by directly summing over the log likelihoods from all sub-detectors, denoted as $\Delta \log \mathcal{L}_{\text{comb}}(X_1 - X_2)$, where X_i with $i \in \{1, 2\}$ is either the kaon, pion, proton, electron or muon. The second set is derived using the multivariate technique, and takes into account the correlations of the sub-detectors and some other additional information. This kind of PID variables is denoted as ProbNNX. Fig. 2.20 shows the comparisons of

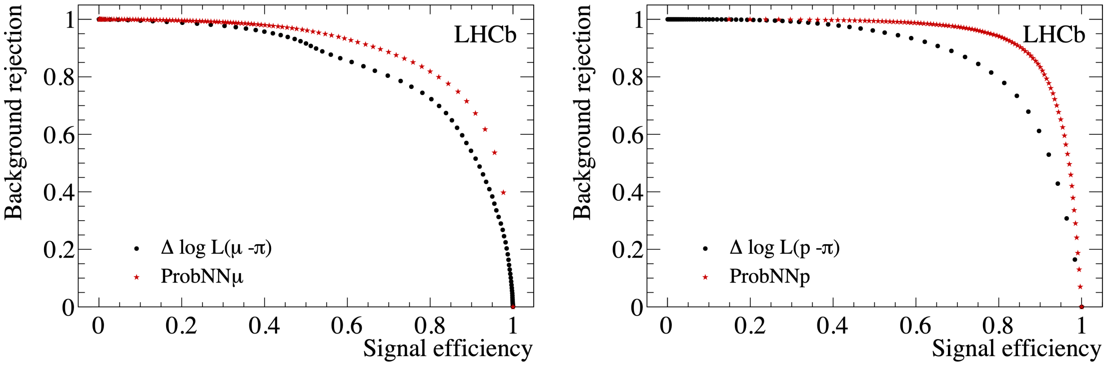

Figure 2.20 Misidentification rates *vs.* muon (left) and proton (right) identification efficiencies for the $\Delta \log \mathcal{L}_{\mathrm{comb}}$-type (black) and ProbNN-type (red) PID variables[148].

the two kinds of PID variables for the muon and the proton, where the ProbNN-type has better performance.

The $B^0 \to D^+D^-K^+\pi^-$ and $B^+ \to D_s^+D_s^-K^+$ decays studied in this thesis have charged kaons and pions in the final states. The requirements on the ProbNN-type variables sufficiently significantly reduce the background levels with high efficiencies, thus enabling the detailed investigations of the two decays.

2.2.3 Trigger system

In the Run 1 and Run 2 periods, the LHCb experiment was operating at a bunch crossing rate of 40 MHz and an instantaneous luminosity of $2 \sim 4{\times}10^{32}\,\mathrm{cm}^{-2}\,\mathrm{s}^{-1}$. Among all the pp collision events, only a tiny fraction of them involve the physical processes of interest. A fast and efficient trigger system is essential to catch up the interesting events containing heavy-hadron processes. The LHCb trigger system consists of two levels, the hardware level-0 (L0) trigger that reduces the event rate to 1 MHz, and the software high-level trigger (HLT) that reads the L0 outputs and further filters the events to a rate of the 10 kHz level. The data selected by the HLT trigger is finally written to the storage. The layout of the trigger system is shown in Fig. 2.21. For flexible selections, all stages of the trigger system are composed of a series of decisions (lines), which are designed to be sensitive to different physical processes.

2.2.3.1 Level-0 trigger

The L0 trigger uses the information provided by the calorimeter system and Muon stations to make decisions, which are based on the presence of high-p_{T} or high-E_{T} (transverse energy) final-state particles of heavy-hadron decays. The calorimeter

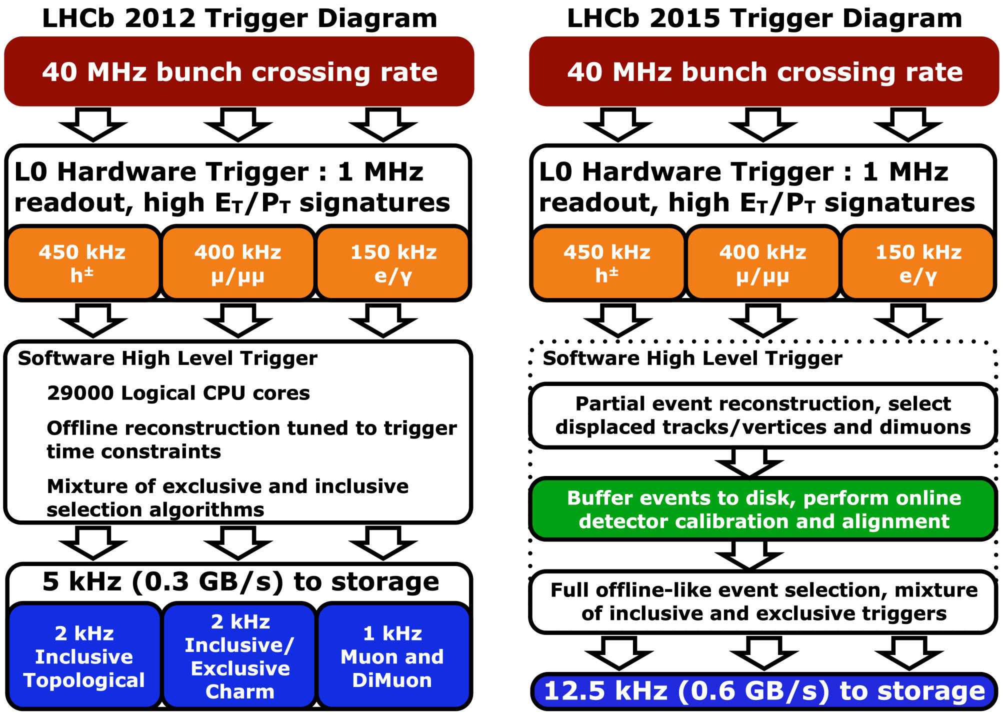

Figure 2.21 Layout of the trigger system in Run 1 (left) and Run 2 (right) operating periods[149].

system is responsible for the decisions involving high-E_{T} electrons, photons and hadrons, where the E_{T} information is provided by the ECAL and HCAL. The cells in the two detectors are grouped into clusters of the 2×2 shape, and the E_{T} in each cluster is determined as $\sum_{i=1}^{4} E_i \cdot \sin\theta_i$ with E_i being the deposited energy in the cell i of the cluster and θ_i being the polar angle of the cell position in the detector coordinate system defined in Fig. 2.4. Among all the clusters in the ECAL or HCAL, the one having the largest E_{T} is associated to a high-E_{T} particle candidate, whose species is then determined using the additional information provided by the SPD and PS. Finally, the E_{T} of the candidate is compared with the fixed threshold for the corresponding particle species to make the trigger decision. The Muon stations account for the rough measurements on the p_{T} of muons according to the x–y quadrants and the $R1$–$R4$ regions to which they belong. The muon trigger decision is then determined by requiring the largest or the two largest p_{T} above the single- or di-muon threshold, respectively. The L0 trigger lines usually have an additional requirement on the maximum number of hits in the SPD detector, to remove the events that are hard to be well reconstructed due to presence of too many final-state particles. Events passing at least one of the L0 trigger lines are transferred to the HLT for further reconstructions.

2.2.3.2 High-level trigger

The HLT is composed of two sequential stages, the HLT1 and HLT2. The HLT1 performs partial event reconstructions mainly using the hits recorded in the tracking system. Long tracks of charged particles are reconstructed using the forward tracking strategy introduced in Sec. 2.2.1.5. A Kalman-filter fit is then performed to measure the track momentum. PVs are reconstructed using the VELO tracks. With the PV information available, IP calculations of the long tracks are enabled. The HLT1 decisions are made by comparing the track-fit quality, IP and p_{T} of the reconstructed tracks with the set thresholds. For muon candidates, the particle identification information provided by the Muon stations is used, and the di-muon decision also set a mass threshold on the combination. The HLT1 reduces the event rate from 1 MHz to about 100 kHz[150-151], thus allowing the full event reconstruction at the HLT2 stage, where heavy-hadron candidates are formed and events are classified according to the kinds of physics processes. There are several kinds of HLT2 lines, as shown in Fig. 2.21. Especially, the studies presented in this thesis use the data filtered by the inclusive topological lines that are dedicated for b-hadron decay reconstructions. At the HLT stage, events passing at least one HLT1 line and one HLT2 line are saved into the storage for offline processing.

During the Run 1 period, due to the limitation of computing resources, a simplified but fast reconstruction without the detector alignment and calibration was performed at the HLT2 stage. The reconstructed strategy was improved in the Run 2 period thanks to the increase in computing power[152-154]. As illustrated in Fig. 2.21, at first the HLT1-stage events are buffered to the disk storage such that the data can be processed in the beam inter-fill periods of the LHC, and the real-time alignment and calibration for the sub-detectors can be carried out. Then, an offline-quality reconstruction is performed at the HLT2 stage, enabling the real-time analysis directly using the reconstructed objects of HLT2. These events enter the Turbo stream in the storage with only the information associated to the candidates retained. There is also the full stream that contains the raw data with the trigger reconstruction discarded due to the storage constraint. The raw data in the full stream is further reconstructed offline, and is filtered into a variety of Stripping lines that are dedicated for relatively specific physical purposes. The studies presented in this thesis use the data read from several Stripping lines.

2.2.3.3 Offline trigger decisions

In the online trigger system, events are recorded as long as they trigger at least one L0, one HLT1 and one HLT2 decisions. In a specific physical analysis, one just needs to care about only a few signal-related trigger lines, and for a better understanding of the data, it is usually necessary to know which parts of the events fire the trigger. So the trigger decisions are categorized to:

- Trigger on signal (TOS), which is fired by the components of the signal candidates;
- Trigger independent of signal (TIS), which is due to the components of the events irrelevant to the signal candidates.
- Trigger on between (TOB), which is decided by the objects from both the signal candidates and the irrelevant part in the event.

Such classification enables the determination of the trigger efficiency using the data that has already be filtered by the online trigger system. The TIS and TOS triggers in general can be regarded to be independent because they are decided by different parts in the event. Thus the TOS efficiency can be evaluated as

$$\varepsilon^{\mathrm{TOS}} = \frac{N_{\mathrm{TIS\&\&TOS}}}{N_{\mathrm{TIS}}}, \tag{2.1}$$

where N_{TIS} and $N_{\mathrm{TIS\&\&TOS}}$ are the number of the signal candidates after the TIS and TIS&&TOS requirements, respectively.

2.2.4 LHCb simulation

Monte Carlo (MC) simulation is usually employed to understand the detector responses. For example, it is essential to determine the detector resolution and efficiency of selections in the analyses presented in this thesis. The LHCb MC simulation is produced by a series of applications with the specific LHCb configuration. The *pp* collisions are simulated using Pythia 8[155-156]. Decays of unstable particles are modeled using EvtGen[157], in which photons radiated by the final-state particles are described by Photos[158]. Interactions between the generated particles and the detector are simulated by the Geant4 toolkit[159-161]. In the analyses studied in thesis, the `ReDecay` method[162] is used to accelerate the MC production by reusing the Geant4-simulated interactions of underlying *pp* collisions multiple times for different independently generated signal decays. The detector responses are digitized as the inputs for the L0 trigger, and then the remaining processes of MC simulation is the same as that of the real data.

CHAPTER 3 AMPLITUDE ANALYSIS OF THE $B^0 \to D^+D^-K^+\pi^-$ DECAY

The $B^0 \to D^+D^-K^+\pi^-$ decay proceeds via the $\bar{b} \to c\bar{c}\bar{s}$ transition at the quark level, governed by the W-boson exchange. The tree-level Feynman diagrams are shown in Fig. 3.1, including the external and internal W emissions. The four mesons in the final state have flexible combinations and thus provide an ideal platform to search for the intermediate resonances, as discussed in Secs. 1.3 and 1.4. The excited D_s^+ mesons decaying into $D^+K^+\pi^-$ can be produced in the external W-emission process, while the conventional and exotic $c\bar{c}$ states can be accessed in the internal W-emission process. Especially for the $D^+K^+\pi^-$ three-body system, both natural and unnatural parity D_s^+ states are accessible depending on the presence of the intermediate K^{*0} or D^{*0} resonances. If restricting the final-state particles $K^+\pi^-$ or $D^+\pi^-$ to be from the $K^*(892)^0$ or $D_2^*(2460)^0$ states, excited D_s^+ states with all spin-parity numbers except for the $J^P = 0^+$ one are accessible. If the $K^+\pi^-$ and $D^+\pi^-$ masses are restricted to be lower than the production thresholds for any K^{*0} and D^{*0} states with $J \geq 1$, the $K^+\pi^-$ or $D^+\pi^-$ system can be assumed to be in S-wave, and thus has $J^P = 0^+$. The further combination with the $J^P = 0^-$ D^+ or K^+ meson results in the unnatural parity ($J^P = 0^-, 1^+, 2^-, \cdots$) of the $D^+K^+\pi^-$ system, and thus enables the search for the $D_s(2^1S_0)$ state that has the lowest mass among the missing resonances in the D_s^+ spectrum[5].

This chapter presents the search for the intermediate resonances in the $B^0 \to D^+D^-K^+\pi^-$ decay at the LHCb experiment. Two new excited D_s^+ candidates are

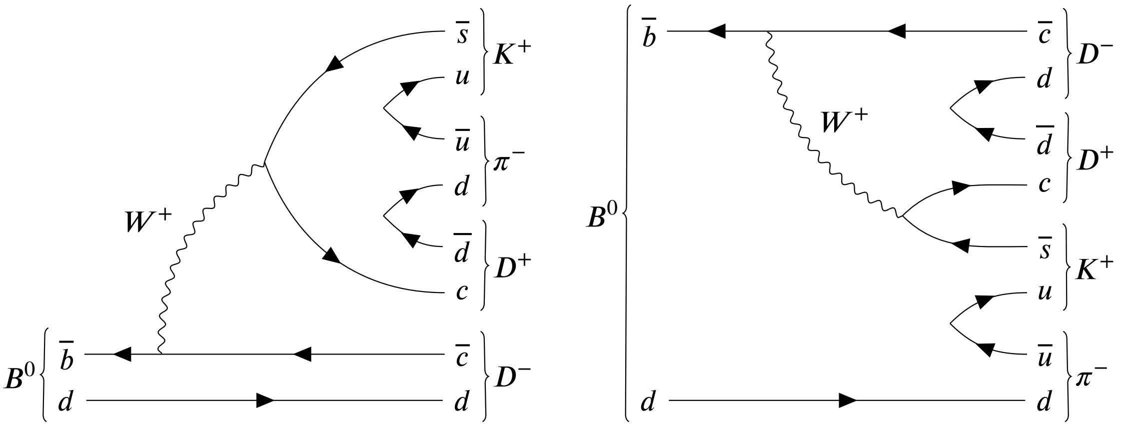

Figure 3.1 Feynman diagrams of the external (left) and internal (right) W-emission contributing to the $B^0 \to D^+D^-K^+\pi^-$ decay.

observed in the $D^+K^+\pi^-$ mass spectrum, and an amplitude analysis is employed to measure the properties of the new state near the $D^+K^+\pi^-$ mass threshold.

3.1 Dataset

This analysis uses the data collected by the LHCb experiment at a center-of-mass energy of $\sqrt{s} = 13\,\text{TeV}$ during the 2016-2018 period. The corresponding integrated luminosity is $5.4\,\text{fb}^{-1}$. Data samples of two decays, $B^0 \to D^+D^-K^+\pi^-$ and $B^0 \to D_s^+D^-$, are reconstructed and selected. MC samples for the two decays are also produced to study the effects of detector responses and the imposed selections. The $B^0 \to D^+D^-K^+\pi^-$ process is the concerned decay in this analysis for the search of possible intermediate resonances, and is referred to as the signal channel. Since the B^0 kinematics and some detector responses, *e.g.* multiplicity and L0 trigger, are generally not well described in the simulation, the $B^0 \to D_s^+D^-$ data and MC samples are utilized to introduce corrections on the $B^0 \to D^+D^-K^+\pi^-$ MC samples to improve the data/MC agreement. The $B^0 \to D_s^+D^-$ decay is referred to as the control channel. This section describes the data and MC samples used in this analysis.

3.1.1 Data samples

Available data samples of the $B^0 \to D^+D^-K^+\pi^-$ and $B^0 \to D_s^+D^-$ candidates are read from the Stripping lines `B02DDKstBeauty2CharmLine` and `B02DDBeauty2CharmLine`, respectively, where the *pp* collision data recorded by the trigger system is reconstructed offline with a preliminary selection imposed. The D^+ and D_s^+ mesons are reconstructed in the $K^-\pi^+\pi^+$ and $K^-K^+\pi^+$ final states, respectively. In both of the two Stripping lines, a pre-filter composed of a specific set of HLT2 topological trigger decisions are required, which are dedicated to select partially reconstructed *b*-hadron decays involving two- and multi-body decay products. Events passing the pre-filter enter the full reconstruction and the preliminary selection stage. The latter is mainly based on the requirements on the topological and kinematic information associated to the candidates. The topology-based requirements include those on the final-state tracks and vertices of the composite particles. All final-state particles should have a good track-fit quality and a small fake-track probability, and are inconsistent with originating from all PVs. The vertices they formed should have good vertex-fit qualities and the corresponding intermediate decaying particles are required to have detectable flight distances in the

VELO. In addition, the B^0 candidates should be consistent with originating from the originating PV, also referred to as the associated PV. The kinematic-based selection requires the p and p_T of the final-state and intermediate decaying particles to be generally larger than those of the typical soft QCD processes in the pp collision, and requires the reconstructed mass of the D^+, D_s^+ and B^0 candidates in adequate mass windows around the known masses[163]. The detailed criteria of `B02DDKstBeauty2CharmLine` and `B02DDBeauty2CharmLine` are listed in Table 3.1, where the variables are explained below:

- HLT2: "`Hlt2Topo.*Decision || Hlt2.*IncPhi.*Decision`" selects two-, three- and four-body b-hadron decay candidates involving hadron and muon final states.
- χ^2_trk/ndof: track-fit χ^2 per degree of freedom.
- P(ghost): probability for a track to be fake.
- χ^2_IP: difference of the PV-fit χ^2 with and without the candidate track included in the PV reconstruction. Larger value of χ^2_IP indicates smaller possibility of the track originating from the PV.
- M/MM: invariant mass with/without the vertex fit.
- SUM p_T: scalar sum of the p_T of all decay products.
- χ^2_vtx/ndof: χ^2 per degree of freedom for decay-vertex fit.
- DOCA: closest approach of two tracks.
- χ^2_FD: χ^2-distance from the associated PV, defined as $(\vec{V}_\mathrm{vtx} - \vec{V}_\mathrm{PV})^\mathrm{T}(\mathrm{COV}_\mathrm{vtx} + \mathrm{COV}_\mathrm{PV})^{-1}(\vec{V}_\mathrm{vtx} - \vec{V}_\mathrm{PV})$, where $\vec{V}$ is the position of the decay vertex or PV, and COV is the covariance matrix in the vertex fit.
- BPV $\cos\theta_p$: cosine of the angle between the $D^\pm_{(s)}$ momentum and $\vec{V}_\mathrm{vtx} - \vec{V}_\mathrm{PV}$.
- $\Delta\log\mathcal{L}_\mathrm{comb}(K-\pi)$: the combined PID variable to discriminate $K^\pm$ and $\pi^\pm$, introduced in Sec. 2.2.2.4.
- τ: mean lifetime.
- χ^2_minIP/minIP: minimum χ^2-distance/distance of a trajectory with respect to all PVs.
- B2CBBDT: a parameterized boosted decision three (BDT) dedicated to select candidates for b-hadron decaying into c-hadron(s)[164].

In the reconstruction, the momentum scale calibration is performed on the data to correct biases due to the non-perfect alignment of the tracking system, imprecise description of the material effect, and the uncertainty on magnetic field. The calibration

Table 3.1 Stripping requirements to select $B^0 \to D^+D^-K^+\pi^-$ and $B^0 \to D_s^+D^-$ candidates.

Particle	Variable	Criterion	
		$B^0 \to D^+D^-K^+\pi^-$	$B^0 \to D_s^+D^-$
	HLT2	Hlt2Topo.*Decision || Hlt2.*IncPhi.*Decision	
All $K^\pm$ and $\pi^\pm$	χ^2_{trk}/ndof	< 4	
	P(ghost)	< 0.4	
	p_{T}	$> 100\,\text{MeV}$	
	p	$> 1000\,\text{MeV}$	
	χ^2_{IP}	> 4	
$D^\pm_{(s)}$	MM	$> 1769.62\,\text{MeV}$ & $< 2068.49\,\text{MeV}$	
	SUM p_{T}	$> 1800\,\text{MeV}$	
	χ^2_{vtx}/ndof	< 10	
	DOCA (any 2 tracks)	$< 0.5\,\text{mm}$	
	χ^2_{FD}	> 36	
	BPV $\cos(\theta_p)$	> 0	
	At least one track with	$p_{\text{T}} > 500\,\text{MeV}$, $p > 5000\,\text{MeV}$	
	$\Delta\log\mathcal{L}_{\text{comb}}(K-\pi)$ for $K^\pm$	> -10	
	$\Delta\log\mathcal{L}_{\text{comb}}(K-\pi)$ for $\pi^\pm$	< 20	
Bachelor K^- and π^+ from B^0	$p(K), p(\pi)$	$> 2000\,\text{MeV}$	-
	$p_{\text{T}}(K) + p_{\text{T}}(\pi)$	$> 1000\,\text{MeV}$	-
	$\text{M}(K\pi)$	$< 5.2\,\text{GeV}$	-
	DOCA (K, π)	$< 0.5\,\text{mm}$	-
	$\chi^2_{\text{vtx}}/\text{ndof}(K\pi)$	< 10	-
	$\chi^2_{\text{FD}}(K\pi)$	> 16	-
	BPV $\cos(\theta_p)(K\pi)$	> 0	-
	K or π with	$p_{\text{T}} > 500\,\text{MeV}$, $p > 5000\,\text{MeV}$	-
B^0	χ^2_{vtx}/ndof	< 10	
	τ	> 0.2 ps	
	χ^2_{IP}	< 25	
	BPV $\cos(\theta_p)$	> 0.999	
	At least one track with	$p_{\text{T}} > 1.7\,\text{GeV}$, $p > 10\,\text{GeV}$, $\chi^2_{\text{minIP}} > 16$, minIP > 0.1 mm	
	At least two tracks with	$p_{\text{T}} > 500\,\text{MeV}$, $p > 5000\,\text{MeV}$	
	SUM p_{T}	$> 5\,\text{GeV}$	
	MM	$> 4.75\,\text{GeV}$ & $< 6\,\text{GeV}$	
	$V_z\left(D^\pm_{(s)}\right) - V_z\left(B^0\right)$	-	-1.5 mm
	B2CBBDT response	>0.5	

information is obtained from the large data samples of the detached J/ψ candidates in $B^0 \to J/\psi\mu^+\mu^-$ and $B^0 \to J/\psi K^+$ decays[165]. Decay Tree Fitter (DTF)[166] is employed to improve the mass resolution of the composite particles. For the purpose of investigating the B^0 mass distribution, the mass of each charm meson ($D^\pm$ or $D_s^\pm$) is constrained to its known value[163] and the B^0 momentum is forced to point to the associated PV. For the study of the intermediate resonant structures, besides the above constraints, the mass of B^0 candidates is also fixed to the known value[163], and the resulting four momenta of the final-state tracks are used to calculate the masses and decay angles of the intermediate resonances in the $B^0 \to D^+D^-K^+\pi^-$ decay.

3.1.2 MC samples

MC samples for the years of 2016 to 2018 are produced using the software packages described in Sec. 2.2.4. Two kinds of simulated samples relevant to the signal channel are produced, *i.e.* $B^0 \to D^+D^-K^+\pi^-$ and $B^0 \to D_{s1}(2536)^+D^-$. The two decays both have $D^+D^-K^+\pi^-$ in the final state. The former is used to model the detector effect in the full phase region of the $B^0 \to D^+D^-K^+\pi^-$ four-body decay, and the latter is utilized to give a more precise description of the detector effect in the phase space region of the near-threshold $D_{s1}(2536)^+$ state that was observed decaying into the $D^+K^+\pi^-$ final state[163] and thus is expected in the $B^0 \to D^+D^-K^+\pi^-$ decay. In the productions of both processes, B^0 decays are generated uniformly in the phase space using the `PHSP` generator[167], the $D^+ \to K^-\pi^+\pi^+$ decay is modeled by the `D_DALITZ` generator[167] with the intermediate resonant contributions extracted from the data collected by the CLEO experiment[168], and the $D_{s1}(2536)^+$ resonance is modeled by the relativistic Breit-Wigner (RBW) function[167]. As the uniformly distributed MC events in the phase space are demanded in the amplitude analysis, the $B^0 \to D_{s1}(2536)^+D^-$ MC sample is further weighted by the inverse of the modulus square of the RBW function. The weight sum is scaled to match the expected number of events in the $B^0 \to D^+D^-K^+\pi^-$ MC sample in the $D_{s1}(2536)^+$ mass region, *i.e.* $(2535 \pm 2)\,\text{MeV}$. The numbers of the generated MC events of the $B^0 \to D^+D^-K^+\pi^-$ and $B^0 \to D_{s1}(2536)^+D^-$ decays for the years of 2016–2018 are listed in Table 3.2. The MC events are filtered by `B02DDKstBeauty2CharmLine`.

The $B^0 \to D_s^+D^-$ MC sample is used to extract the corrections to improve the data/MC agreement in the signal channel by comparing the relevant responses in data and MC simulation. The details are described in Sec. 3.5. Similar to that for the

Table 3.2 MC events information. “Filtered” indicates that the available MC events are already filtered by the Stripping line described in the text. The $B^0 \to D^+D^-K^+\pi^-$ MC events are generated with $m(K^+\pi^-) <$ 0.85 GeV.

Decay	Events (16/17/18)	Filtered
$B^0 \to D^+D^-K^+\pi^-$	66K/66K/88K	Yes
$B^0 \to D_{s1}(2536)^+D^-$	6.6K/6.6K/8.8K	Yes
$B^0 \to D_s^+D^-$	4M/4M/4M	No

$B^0 \to D^+D^-K^+\pi^-$ MC sample, the $B^0 \to D_s^+D^-$ MC events are produced with the B^0 decay described by the `PHSP` generator and the D_s^+ (D^+) decay by `D_DALITZ`, where the intermediate resonant contributions in the $D_s^+ \to K^-K^+\pi^+$ process are extracted from the data collected by the BaBar collaboration[102]. The number of the $B^0 \to D_s^+D^-$ MC events for different years are listed in Table 3.2.

MC samples used in this analysis are read from the two Stripping lines, and in the reconstruction, the same DTFs as those used in data are applied. To select candidates corresponding to true B^0 signals, 70% of the hits in the tracks are required to result from the final-state particles in the demanded B^0 decays. This procedure is the so-called truth matching.

The PID responses are generally not well described in MC simulation, and thus the raw PID variables are rarely used in selections ①. Before the further offline selection, corrected PID variables of final-state kaons and pions are sampled according to the distributions of the PID variables in the calibration data with high statistics and high purity. The procedure is accomplished using the `PIDGen` tool provided by the `PIDCalib` package[169]. To check if the sampled PID variables in MC simulation well model those for the real processes in data, their distributions are compared between MC simulation and data, shown in Figs. 3.2 and 3.3 for the $B^0 \to D^+D^-K^+\pi^-$ and $B^0 \to D_s^+D^-$ channels, respectively. Good agreements are seen in MC simulation and data for both channels.

3.2 Offline selection

As there are still large amount of background in the data samples after the preliminary selection in the Stripping line, some offline requirements are imposed, including a simple

---

① The imposed requirements on the raw PID variables in the Stripping lines shown in Table 3.1 are extremely loose and thus are expected to cause little bias in the efficiency modeling.

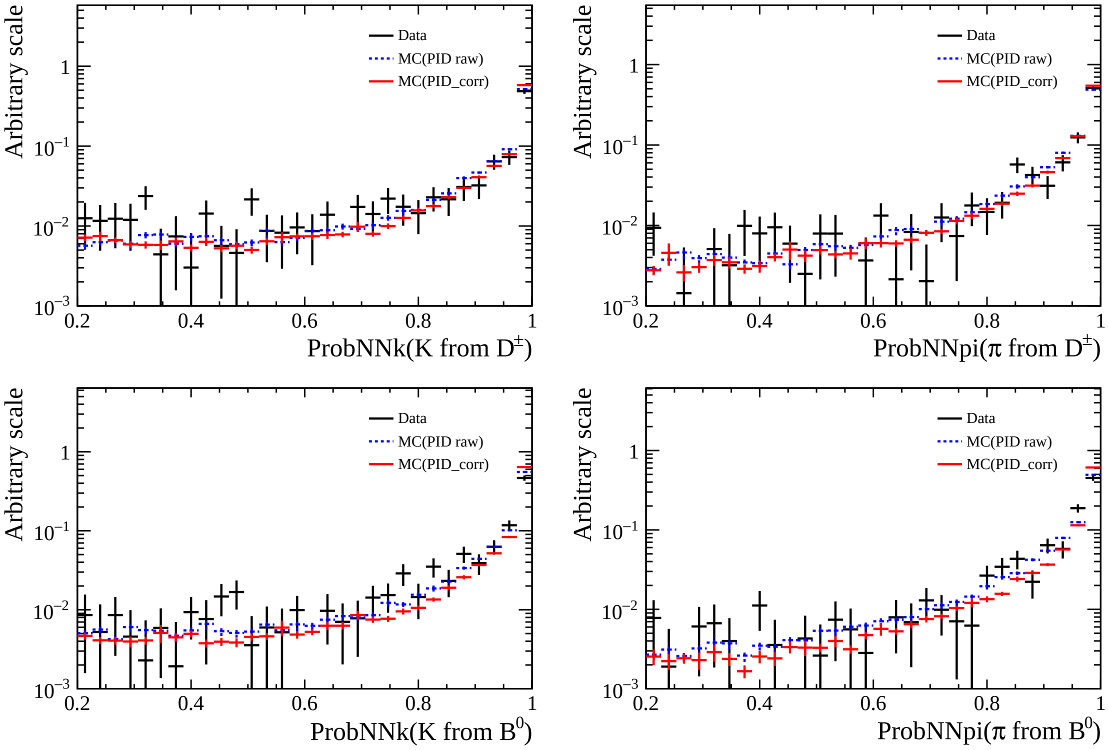

Figure 3.2 Comparisons of the PID variables between MC simulation and data for the $B^0 \to D^+D^-K^+\pi^-$ decay. Background in data is subtracted using the *sPlot* method as discussed in Sec. 3.4.3.1.

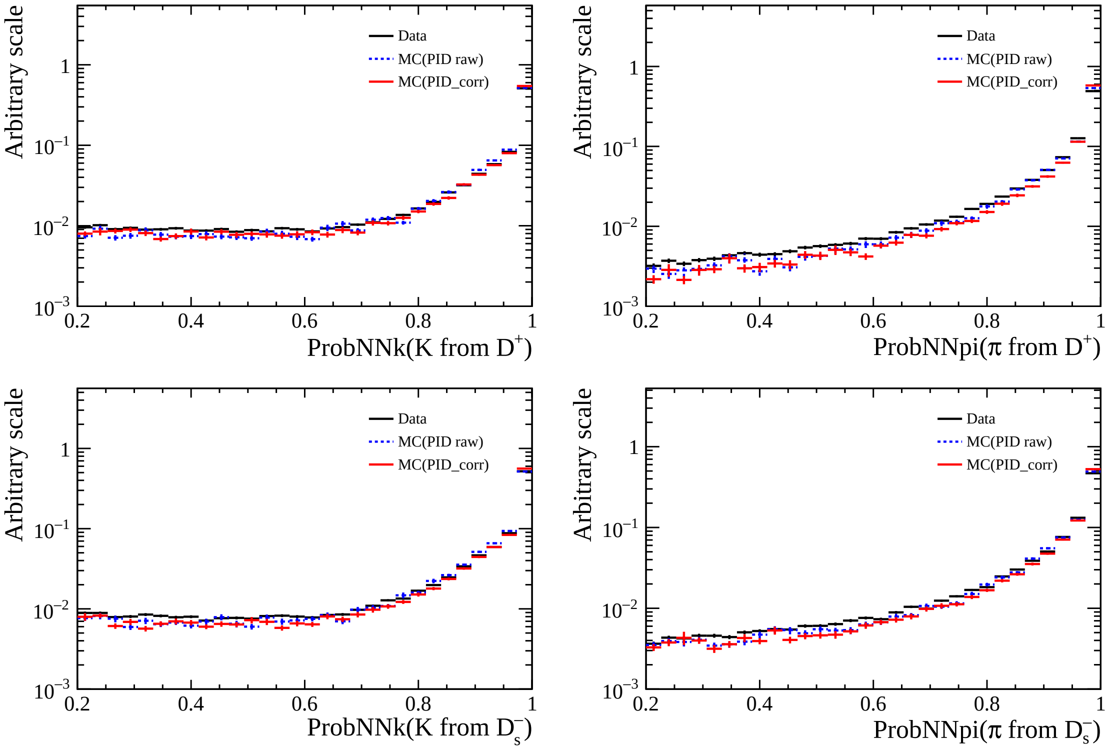

Figure 3.3 Comparisons of the PID variables between MC simulation and data for the $B^0 \to D_s^+D^-$ decay. Background in data is subtracted using the *sPlot* method as discussed in Sec. 3.4.4.

Table 3.3 Cut-based offline selection criteria for the $B^0 \to D^+D^-K^+\pi^-$ and $B^0 \to D_s^+D^-$ decays.

$B^0 \to D^+D^-K^+\pi^-$	$B^0 \to D_s^+D^-$
ProbNNpi > 0.2 for all pions	
ProbNNk > 0.2 for all kaons	
$\chi^2_{\text{vtx}}(D^\pm_{(s)}) < 15$	
$\chi^2_{\text{vtx}}(B^0) < 25$	
$D^\pm_{(s)}$ MM window: ±25 MeV	
B^0 mass window: ±100 MeV	B^0 mass window: ±60 MeV
Open angle > 5 mrad for any two tracks	
DTF_status==0	
$V_z(D^\pm) - V_z(B^0) > 0.5\,\text{mm}$	$V_z(D_s^+) - V_z(B^0) > 1.0\,\text{mm}$

cut-based selection, the offline trigger decisions, and the removal of multiple candidates.

3.2.1 Cut-based selection

The cut-based selection criteria are listed in Table 3.3. The requirements on the ProbNN-type variables of the final-state particles are used to reduce the background due to random combinations of the final-state tracks and their mis-identifications. Better vertex-fit qualities of the D^+, D_s^+, and B^0 candidates and a tighter mass window for the $D^\pm_{(s)}$ candidates than those in the Stripping lines are imposed. The B^0 mass window is chosen to keep the partially reconstructed background with a missing soft particle from $D^*_{(s)} \to D_{(s)}$ decay out of the B^0 fit range, as discussed in Sec. 3.3. To reject the background from the repeated use of the track segments in the event, the opening angle between any two final-state tracks should be $> 0.5\,\text{mrad}$. The two DTFs employed to improve detector resolution described in Sec. 3.1.1 are required to be successfully converged.

To reject the non-double-charm (NDC) background from real B^0 decays but fake $D^\pm_{(s)}$ mesons, *e.g.* $B^0 \to D^+[K^+\pi^-\pi^-]K^+\pi^-$ and $B^0 \to [K^-\pi^+\pi^+][K^-K^+\pi^+]$, an adequate displacement of the $D^\pm_{(s)}$ and B^0 vertices is required. The criterion should sufficiently suppress the NDC background candidates while keeping as high efficiency for real $B^0 \to D^+D^-K^+\pi^-$ ($B^0 \to D_s^+D^-$) decays as possible. The thresholds for the $B^0 \to D^+D^-K^+\pi^-$ and $B^0 \to D_s^+D^-$ data are determined by investigating the B^0 MM distributions of the candidates from the $D^\pm_{(s)}$ mass sidebands, as illustrated in

Fig. 3.4 and 3.5 ①. It is seen that the requirements $V_z(D^\pm) - V_z(B^0) > 0.5$ mm for the $B^0 \to D^+D^-K^+\pi^-$ channel and $V_z(D_s^+) - V_z(B^0) > 1.0$ mm for the $B^0 \to D_s^+D^-$ channel can suppress the B^0 MM peaks in the $D_{(s)}^\pm$ mass sidebands and thus they are taken in the selection.

3.2.2 Multiple candidate removal

There are multiple candidates reconstructed in some pp collision events in data, and almost all of them result from the repeated use of tracks. Most of the multiple candidates share the same $D_{(s)}^+$ or D^-, or have tracks exchanged between the final-state particles of the $D_{(s)}^+$ and D^- decays. The fraction of multiple candidates after the offline selection is found to be 9.3% and 1.1% for the $B^0 \to D^+D^-K^+\pi^-$ and $B^0 \to D_s^+D^-$ data, respectively. The smaller multiple candidate fraction in the $B^0 \to D_s^+D^-$ data is understood as the absence of the bachelor kaon and pion. As the candidate corresponding to a real decay tends to have a good reconstruction quality, the candidate with the minimum DTF-fit χ^2 in the same event is retained. Here, the DTF indicates the one without the B^+ mass constraint. As only one true B^0 decay is generated in a single MC event and the truth matching is required, there are no multiple candidates in the MC samples.

3.2.3 Offline trigger requirements

The offline trigger selection is applied after the removal of multiple candidates. The online trigger is composed of a variety of decisions covering a wide range of physics processes of interests. In this analysis, only several specific trigger decisions relevant to the concerned B^0 hadronic decays are required offline for a better control and understanding of the imposed selections in the trigger. The detailed decisions are listed in Table 3.4. The L0 trigger includes the `L0Hadron_TOS` decision made by the high-E_T HCAL clusters resulting from the final-state tracks of the B^0 decay, and the `L0Global_TIS` decision triggered by the rest part of the events that is generally due to the high-p_T or high-E_T signature of other hadrons, electrons, muons or dimuons. The HLT1 trigger is based on the signature of tracks of the B^0 decay candidates. The `Hlt1TrackMVA_TOS` decision requires at least one final-state track to have high p, high p_T and a good track-fit quality, and is significantly displaced from all PVs. The `Hlt1TwoTrackMVA_TOS` decision not only has constraints on single tracks, but also requires a good-quality vertex formed by

---

① the DTF_status==0 requirement is removed because the constraint in the two DTFs can distort the MM shape of the background candidates.

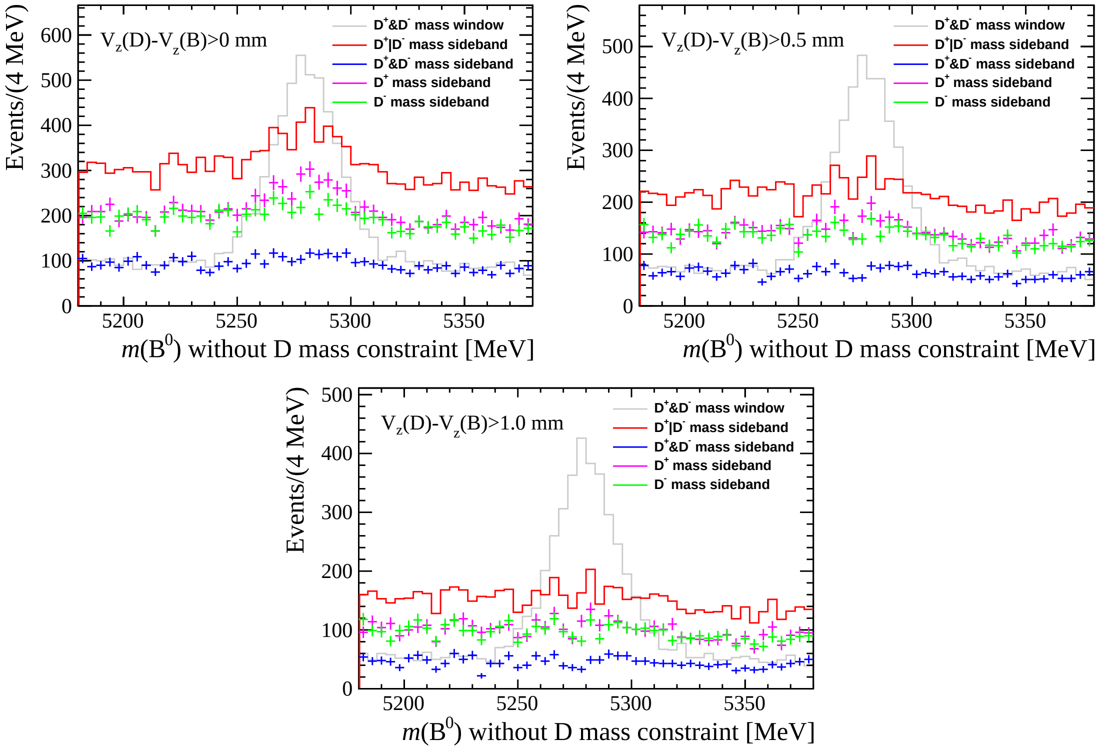

Figure 3.4 B^0 MM distribution under different $V_z(D^{\pm}) - V_z(B^0)$ requirements. The $D^{\pm}$ mass window is ± 25 MeV around the $D^{\pm}$ known mass[163], while the sideband is $(30 - 75)$ MeV away .

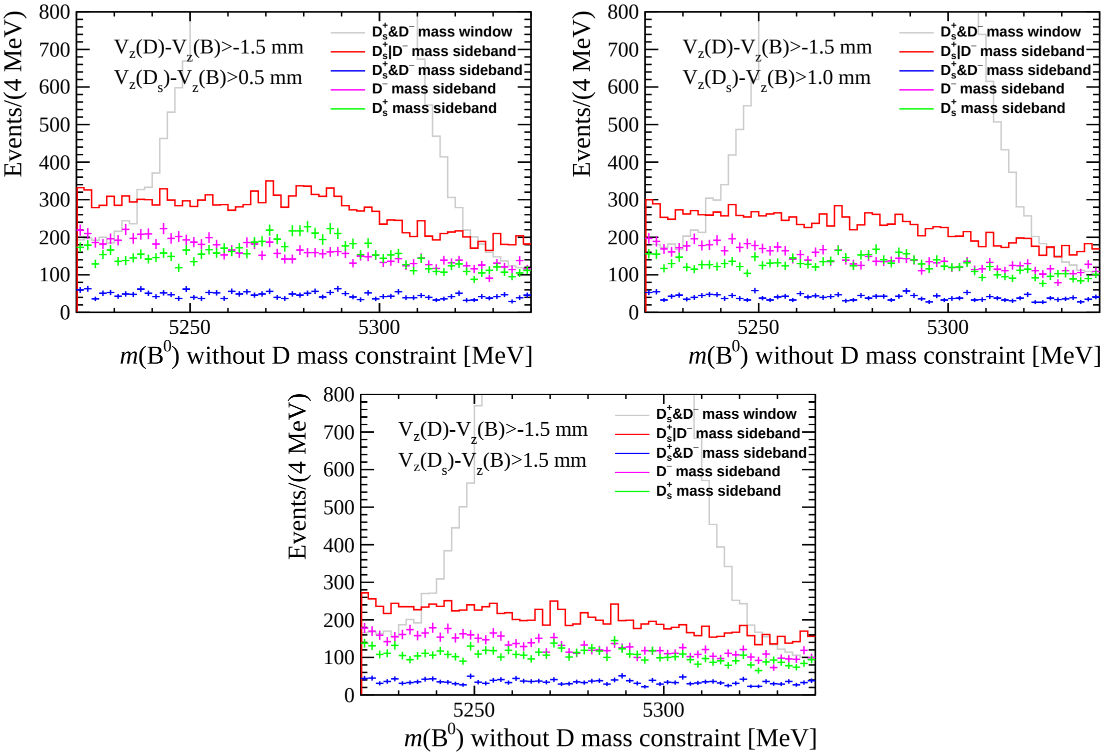

Figure 3.5 B^0 MM distribution under different $V_z(D_{(s)}^{\pm}) - V_z(B^0)$ requirements. The $D_{(s)}^{\pm}$ mass window is ± 25 MeV around the $D_{(s)}^{\pm}$ known mass[163], while the sideband is $(30 - 75)$ MeV away.

Table 3.4 Offline trigger requirements.

L0	Bd_L0HadronDecision_TOS || Bd_L0Global_TIS
HLT1	Bd_Hlt1TrackMVADecision_TOS || Bd_Hlt1TwoTrackMVADecision_TOS
HLT2	Bd_Hlt2Topo2BodyDecision_TOS || Bd_Hlt2Topo3BodyDecision_TOS || Bd_Hlt2Topo4BodyDecision_TOS

two tracks, and the imposed selection is based on a Multivariate classifier[170] with the input variables to be vertex-fit χ^2, the vertex displacement, the SUM p_{T} of the two tracks, and the IPs of the two tracks[153]. The HLT2 trigger includes the topological decisions triggered by the components of the full B^0 decay chain. The decisions generally search for a high-p_{T} vertex formed by two-, three, or four good-quality tracks that is displaced from the PV, and are also implemented in Multivariate classifiers.

3.2.4 Efficiency check on the $B^0 \to D^+D^-K^+\pi^-$ MC sample

The efficiency modeling of the $B^0 \to D^+D^-K^+\pi^-$ decay is an essential input in the amplitude analysis as described in Sec. 3.8, so it is necessary to have a check on the efficiency variation across the phase space. The total efficiency as a function of $m^2(D^+K^+\pi^-)$ and $m^2(D^+D^-)$ is shown in Fig. 3.6. The numerator is obtained from the fully reconstructed MC sample after all the selections and with the correction weights described in Sec. 3.5 applied. In principle, the denominator should be obtained using the generator-level information associated with the fully reconstructed MC sample. Unfortunately, the generator-level MC sample is unavailable because the $B^0 \to D^+D^-K^+\pi^-$ MC events are filtered. The denominator is instead obtained from 100k new generator-level events produced using Gauss without the detector acceptance imposed, and the number of the generated events is scaled to equal to that expected for the fully reconstructed MC sample. In Fig. 3.6, it is seen that the efficiency is roughly flat across the Dalitz plot just as expected. To check for the potential efficiency variation in different years, the efficiency ratios for 17/16 and 18/16 are shown in Fig 3.7. All ratios at different bins of the Dalitz plot are consistent with unity within the statistical uncertainty, indicating that no evident variation is found across the three years.

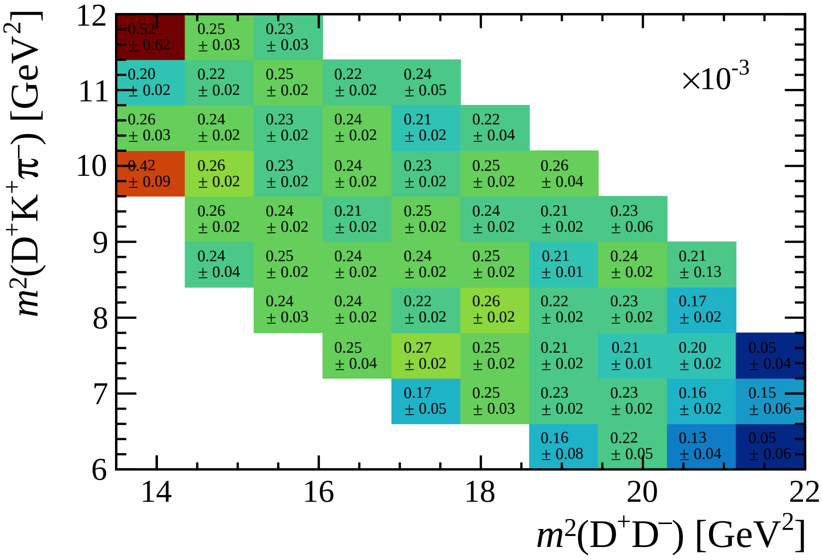

Figure 3.6 Efficiency as a function of $m^2(D^+K^+\pi^-)$ and $m^2(D^+D^-)$ obtained from the $B^0 \to D^+D^-K^+\pi^-$ MC sample.

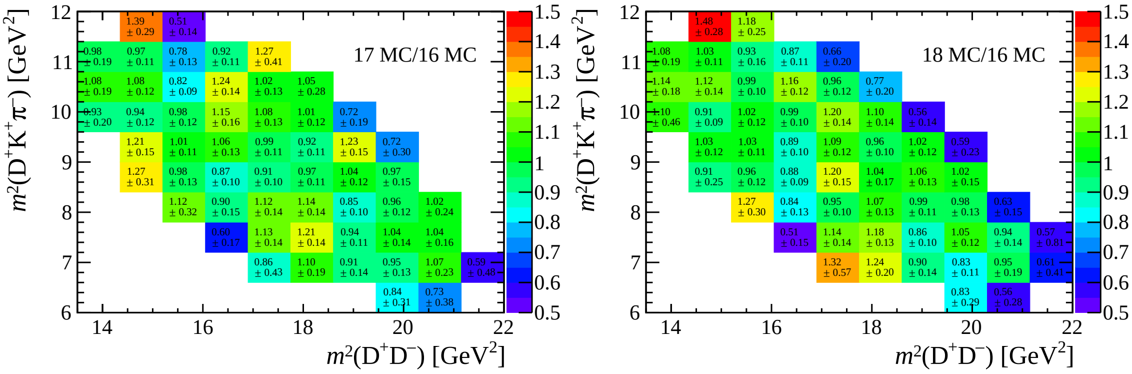

Figure 3.7 Efficiency ratios for 17/16 (left) and 18/16 (right) for the $B^0 \to D^+D^-K^+\pi^-$ MC sample.

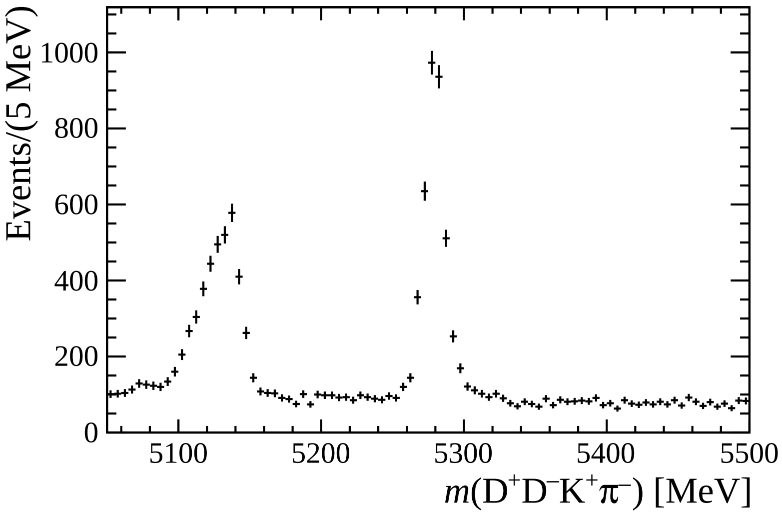

Figure 3.8 B^0 mass distribution of the $B^0 \to D^+D^-K^+\pi^-$ data after the offline selection. The peak at ~ 5100 MeV is from the $B^0 \to D^{*+}D^-K^+\pi^-$ and $B^0 \to D^+D^{*-}K^+\pi^-$ decays with a missing π^0.

3.3 Backgrounds

3.3.1 Possible backgrounds in the signal channel

Potential backgrounds from the misidentification of the final-state $K^\pm$ or $\pi^\pm$ in a real B-meson decay, or the proton in $\Lambda_b^0 \to D^+D^-p\pi^-$ decay are Cabibbo-suppressed, with the exception of $B_s^0 \to D^+D^-K^+K^-$ that is instead suppressed by the ratio of fragmentation fractions f_s/f_d[171-172]. Therefore, such backgrounds are negligible.

Partially reconstructed backgrounds with a missing soft particle from the $D^* \to DX$ decay are also possible. The reconstructed B^0 mass of these backgrounds is shifted away from the true B^0 mass[163], and the shift distance can be approximated by the energy of the missing particle in the B^0 rest frame. So for the $D^* \to D\pi$ decay the shift is at least the pion mass, as shown in Fig. 3.8, and the background due to the missing π is rejected by requiring a ± 100 MeV mass window around the known B^0 mass[163], as listed in Table 3.3. The background from the $B^0 \to D^{*+}D^-K^+\pi^-$ or $D^+D^{*-}K^+\pi^-$ decay with a missing photon could have a tail that enters the mass window but is suppressed by $\mathcal{B}\left(D^{*+} \to D^+\gamma\right) = (1.6 \pm 0.4)\%$[163] and therefore expected to be negligible.

Following the above discussion, the only background that has a non-negligible contribution is due to the random combinations of the final-state tracks, referred to as the combinatorial background. In the amplitude analysis, the combinatorial background is statistically subtracted using the *sPlot* method as discussed in Sec. 3.4.

3.3.2 Possible backgrounds in the control channel

Similar to the $B^0 \to D^+D^-K^+\pi^-$ channel, possible backgrounds from the misidentification of the final-state $K^\pm$ or $\pi^\pm$ are Cabibbo-suppressed. The exception $B_s^0 \to D_s^+D_s^-$ is suppressed by the ratio of fragmentation fractions f_s/f_d[171-172].

Partially reconstructed backgrounds with a missing soft particle from the $D^* \to DX$ and $D_s^{*+} \to D_s^+X$ decays are also possible. The background from the $D^* \to D\gamma$ partial reconstruction is negligible for the same as that for the $B^0 \to D^+D^-K^+\pi^-$ channel. The background from the $D_s^{*+} \to D_s^+\gamma$ decay is not suppressed due to the large branching fraction $B\left(D_s^{*+} \to D_s^+\gamma\right) = (93.5 \pm 0.7)\%$[163], and it contributes as a long descending tail in the $D_s^+D^-$ mass spectrum with the increase of the reconstructed B^0 mass. However, this background is expected to be negligible in the ± 60 MeV window around the known B^0 mass[163]. The mass window is also sufficient to exclude the $B_s^0 \to D_s^+D^-$ decay candidates that peak at ~ 5367 MeV and the background candidates from the $D^* \to D\pi$ partial reconstruction. The choice of the B^0 mass window is supported by a previous analysis[173], where the backgrounds in the $B^0 \to D_s^+D^-$ data are thoroughly investigated.

Therefore, only the combinatorial background needs to be considered in the ± 60 MeV mass window around the known B^0 mass[163]. When extracting the true B^0 kinematic and nTracks distributions in data, as well as the L0 trigger efficiency in Sec. 3.5, the combinatorial background is statistically subtracted using the *sPlot* method as discussed in Sec. 3.4.

3.4 Signal extraction

The B^0 mass fits are performed on the $B^0 \to D^+D^-K^+\pi^-$ and $B^0 \to D_s^+D^-$ data to determine the signal yields of the real B^0 decays and to serve as the basis of the background subtraction using the *sPlot* method[174]. The latter is essential in the amplitude analysis and the MC correction procedure.

3.4.1 Fit strategy

For both the $B^0 \to D^+D^-K^+\pi^-$ and $B^0 \to D_s^+D^-$ data, there are two components in the reconstructed B^0 mass distributions, the signal and the combinatorial background. The probability density function (PDF) for the signal component is chosen as a sum of two Crystal-Ball (CB) functions[175] with tails on opposite sides and each fraction set to

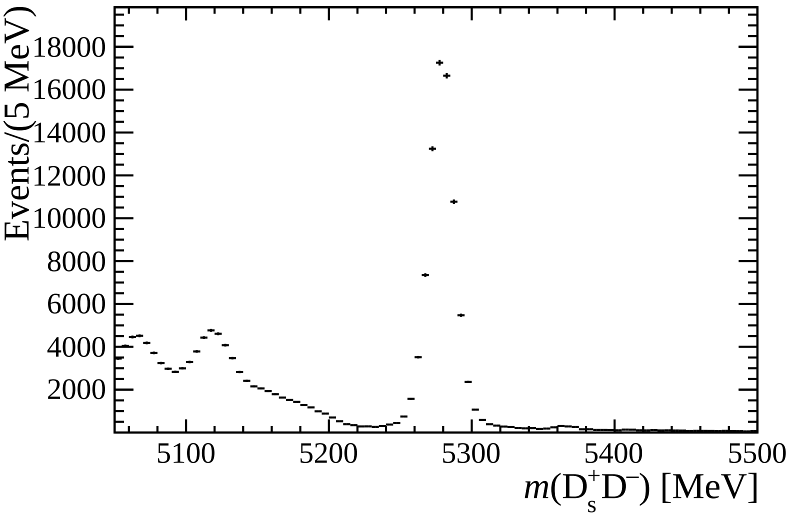

Figure 3.9 B^0 mass distribution of the $B^0 \to D_s^+D^-$ data after the offline selection. The two peak structures at about 5100 MeV are from the $B^0 \to D_s^+D^{*-}$ decay with a missing π^0. The long descending tail with the increase of the reconstructed B^+ mass in the range of 5140 ~ 5220 MeV is mainly from the $B^0 \to D_s^{*+}D^-$ with a missing γ. A small peak at 5367 MeV is from the $B_s^0 \to D_s^+D^-$ decay.

$a = 50\%$,

$$f_{\mathrm{sig}}(m) = a\, f_{\mathrm{CB}}(m;\alpha_1,n,m_0,\sigma_1) + (1-a)\, f_{\mathrm{CB}}(m;\alpha_2,n,m_0,\sigma_2)\,, \tag{3.1}$$

where m is the reconstructed B^0 mass, and $f_{\mathrm{CB}}(m;\alpha_i,n,m_0,\sigma_i)$ is the CB function, defined as

$$\begin{aligned}
f_{\mathrm{CB}}(m;\alpha_i,n,m_0,\sigma_i) &= \frac{1}{\sigma_i}\begin{cases} f(\frac{m-m_0}{\sigma_i},|\alpha_i|,n,), & \text{if } \alpha_i > 0,\\ f(-\frac{m-m_0}{\sigma_i},|\alpha_i|,n), & \text{if } \alpha_i < 0,\end{cases}\\
f(t,\alpha,n) &= \frac{1}{N}\cdot\begin{cases}\exp\left(\frac{-t^2}{2}\right), & \text{for } t > -\alpha,\\ A\cdot(B-t)^{-n}, & \text{for } t \le -\alpha,\end{cases}\\
A &= \left(\frac{n}{|\alpha|}\right)^n \exp\left(-\frac{|\alpha|^2}{2}\right), \quad B = \frac{n}{|\alpha|} - |\alpha|,\\
N &= \frac{n}{|\alpha|}\frac{1}{n-1}\exp\left(-\frac{|\alpha|^2}{2}\right) + \sqrt{\frac{\pi}{2}}\left[1 + \mathrm{erf}\left(\frac{|\alpha|}{\sqrt{2}}\right)\right].
\end{aligned} \tag{3.2}$$

Among the parameters, m_0 corresponds to the mass peak position, σ_i with $i \in \{1,2\}$ are mass resolutions of the two CB functions and (α_1,α_2,n) are tail parameters. The tail is on the left side if $\alpha_i > 0$, otherwise the tail is on the right side. In this analysis, The configuration of $\{\alpha_1 > 0, \alpha_2 < 0\}$ is taken.

The PDF for the combinatorial background component is chosen as an exponential function,

$$f_{\text{com}}(m) = \frac{1}{N_{\text{exp}}} \exp(\lambda\, m)\ . \tag{3.3}$$

Here λ is the parameter reflecting the variation of the shape with the mass, and $N_{\text{exp}} = \frac{1}{\lambda}\left(e^{\lambda m_{\text{max}}} - e^{\lambda m_{\text{min}}}\right)$ is the normalization factor depending on the fit range $(m_{\text{min}}, m_{\text{max}})$.

The total PDF is the sum of for the signal and combinatorial PDFs

$$f_{\text{tot}}(m) = N_{\text{sig}}\, f_{\text{sig}}(m) + N_{\text{bkg}}\, f_{\text{com}}(m), \tag{3.4}$$

where $N_{\text{sig}}(N_{\text{bkg}})$ is the signal (background) yield. Both the signal and background PDFs are implemented in the fitting package RooFit[176].

The unbinned extended maximum likelihood method is employed for the fit. At first, the fit is performed on the MC sample, where the tail parameters (α_1, α_2, n) are determined. Then these parameters are fixed in the fit to data. For both the $B^0 \to D^+D^-K^+\pi^-$ and $B^0 \to D_s^+D^-$ channels, the data in the 2016-2018 period is combined as single inputs to the B^0 mass fits.

3.4.2 *sPlot* method

There are multiple observables in the LHCb dataset and the candidates are generally from several sources. The *sPlot* is a statistical method to extract the distribution of a set of observables called the control variables for each source, using the known distributions of a set of other observables, called the discriminating variables for all the sources. The *sPlot* method was at first derived in 2004[174]. From then on it has been widely used in a large variety of physical analyses. Recently, a novel derivation of it was raised[177], providing a new perspective to understand this method. This subsection gives a brief introduction to the principle of the *sPlot* method and its application on the dataset to extract the signal distributions of the concerned variables in this analysis.

A dataset composed of only two components: signal (s) and background (b), is taken as an example to illustrate the principle of the *sPlot* method for the sake of simplicity. It is not hard to generalize the derivation for the case with more sources. The discriminating and control variables of the dataset are denoted as x and y, respectively. The signal and background PDFs, $g_s(x)$ and $g_b(x)$, of the discriminating variables are known, and they are usually determined from a fit. The total PDF $g(x)$ of x is expressed as

$$N_t g(x) = N_s g_s(x) + N_b g_b(x), \tag{3.5}$$

where N_t, N_s and N_b are the total, signal and background yields, respectively. There is usually no prior knowledge on the PDFs of the control variables, $h_s(y)$ and $h_b(y)$, and the *sPlot* method aims at estimating these PDFs making use of the known information of the discriminating variables under the condition that the discriminating and control variables are independent of each other for both the signal and background components. The extraction is realized by introducing a weight function $w_{s,b}(x)$ to project out the signal or background distribution of the control variables, and the principle is described below.

At first, the total multi-dimensional PDF of the discriminating and control variables is generally constructed following the independence requirement of x and y,

$$N_t f_t(x, y) = N_s g_s(x) h_s(y) + N_b g_b(x) h_b(y). \tag{3.6}$$

Taking the signal component as an example, one expects that $w_s(x)$ can project out the signal PDF of y, $h_s(y)$, that is,

$$\begin{aligned} N_s h_s(y) &= \int w_s(x) N_t f_t(x, y) dx \\ &= N_s h_s(y) \int w_s(x) g_s(x) dx + N_b h_b(y) \int w_s(x) g_b(x) dx, \end{aligned} \tag{3.7}$$

and so

$$\int w_s(x) g_x(x) dx = 1 \text{ and } \int w_s(x) g_b(x) dx = 0. \tag{3.8}$$

The expectation and variance of $w_s(x)$ are

$$E(w_s) = \int w_s(x) N_t g(x) dx = N_s, \tag{3.9}$$

$$\mathrm{Var}(w_s) = \int w_s^2(x) N_t g(x) dx - N_s^2. \tag{3.10}$$

One would expect $w_s(x)$ to minimize $\mathrm{Var}(w_s)$ so that $\sum_i^{N_t} w_s(x_i)$ gives the minimum-variance estimation of N_s, and thus the corresponding formula of $w_s(x)$ is solved by finding the extremum of the functional $\mathrm{Var}(w_s)$ using variational calculus, which is

$$w_s(x) = \frac{V_{ss} g_s(x) + V_{sb} g_b(x)}{N g(x)}, \tag{3.11}$$

where

$$V_{ij}^{-1} = \int \frac{g_i(x) g_j(x)}{N g(x)} dx \approx \frac{1}{N_t} \sum_a^{N_t} \frac{g_i(x_a) g_j(x_a)}{g^2(x_a)}, \quad i, j \in s, b. \tag{3.12}$$

The last term indicates that the integration can be carried out using the MC integration by summing over all candidates in the dataset (a denotes the index of each candidate). The $w_b(x)$ can be easily obtained by just swapping s and b in Eq. 3.11, and it is also not hard

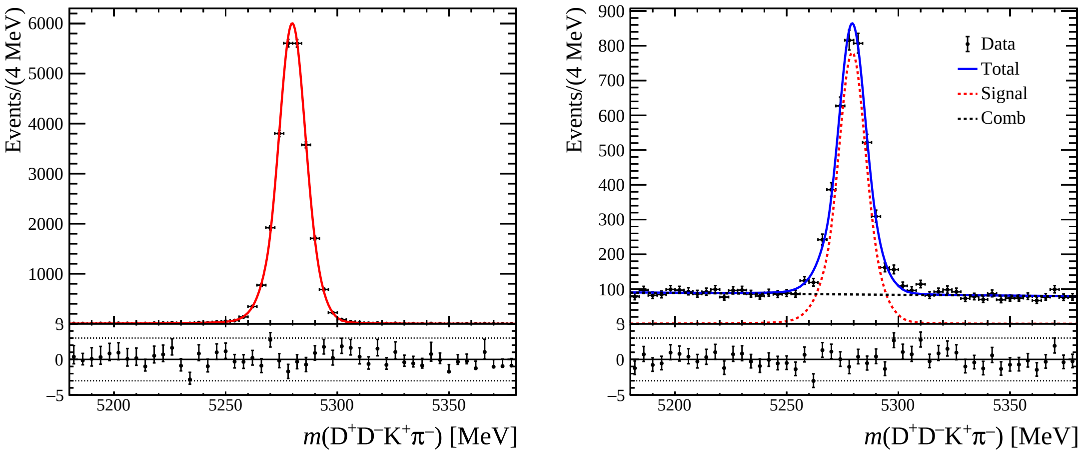

Figure 3.10 B^0 mass distributions in $B^0 \to D^+D^-K^+\pi^-$ MC (left) and data (right) samples. The fit results are overlaid.

to generalize the above derivation to the case of more than two components.

In this analysis, the *sPlot* method is employed to extract the signal distributions of some variables in data. The B^0 mass is chosen as the discriminating variable, for which the signal and background distributions are at first determined by the fit. Then all candidates are assigned a signal weight given by Eq. 3.11. The weighted data gives an estimation to the signal distributions of the concerned variables.

3.4.3 Signal extraction of the signal channel

In the B^0 mass fit for the $B^0 \to D^+D^-K^+\pi^-$ decay, the fit range is chosen to be ±100 MeV around the known B^0 mass[163], as discussed in Sec. 3.3.1. The fit results for the $B^0 \to D^+D^-K^+\pi^-$ MC sample ① and data are shown in Fig. 3.10 and Table 3.5, where all the selection criteria are imposed. It is seen that the fit model can well describe the data. About 3420 ± 72 B^0 signal decays are obtained, and the purity in the ±20 MeV window around the mass peak is found to be 79.6%.

To investigate the intermediate resonant contributions in the $B^0 \to D^+D^-K^+\pi^-$ decay, the combinatorial background is at first subtracted using the *sPlot* method. One- and two-dimensional mass distributions of the combinations of several final-state particles are shown in Figs. 3.11 and 3.12. No peaking structure is seen in the D^-K^+ mass spectrum, indicating no evidence of the $X_{0,1}(2900)$ states that were observed in the $B^+ \to D^+D^-K^+$ decay[13-14] ②. There is no peak in the $D^+D^-\pi^+$ mass spectrum either.

---

① As only $B^0 \to D^+D^-K^+\pi^-$ MC events in the low $K^+\pi^-$ mass region are available when doing the analysis, the MC sample here is the same as that in the fit in the $K^+\pi^-$ mass region.

② The non-presence of the $X_{0,1}(2900)$ states in the $B^0 \to D^+D^-K^+\pi^-$ decay could be understood as due to the larger background from the D_s^+ resonant contributions in this decay than that from the $c\bar{c}$ contributions in the

Table 3.5 Determined parameters in the B^0 mass fits to the $B^0 \to D^+D^-K^+\pi^-$ data and MC samples.

Parameter	MC simulation	Data
a	0.5 (fixed)	0.5 (fixed)
N_{sig}	24879.10 ± 157.73	3419.82 ± 72.28
N_{bkg}	-	4224.18 ± 77.64
m_0(MeV)	5279.83 ± 0.05	5279.36 ± 0.16
σ_1(MeV)	5.25 ± 0.08	5.32 ± 0.25
σ_2(MeV)	8.25 ± 0.11	9.34 ± 0.45
α_1	1.92 ± 0.09	1.92 (fixed)
α_2	-2.57 ± 0.08	-2.57 (fixed)
n	1.62 ± 0.16	1.62 (fixed)
λ(MeV^{-1})	-	$(-6.07 \pm 2.69) \times 10^{-4}$

However, there are several peaking structures presented in other mass distributions. Two significant peaks are seen in the $K^+\pi^-$ and $D^+\pi^-$ mass spectra, corresponding to the known $K^*(892)^0$ and $D_2^*(2460)^0$ resonances, respectively. The peak near the threshold in the D^+D^- mass distribution is the $\psi(3770)$ meson, and the plausible peak at about 3.93 GeV could be the $\chi_{0,2}(3930)$ states.

It is fascinating to observe two significant peaking structures in the $D^+K^+\pi^-$ mass spectrum, whose positions are $\sim$ 2.6 GeV and $\sim$ 2.9 GeV, respectively. These structures do not correspond to any known D_s^+ states introduced in Sec. 1.3.1, and thus are candidates for new D_s^+ resonances. From the two-dimensional distribution of $m(K^+\pi^-)$ and $m(D^+K^+\pi^-)$, the $D^+K^+\pi^-$ peak at $\sim$ 2.9 GeV is in the band around the $K^*(892)^0$ mass, indicating that this new D_s^+ candidate decays into $D^+K^*(892)^0$. The $D^+K^+\pi^-$ peak at $\sim$ 2.6 GeV is far below the $D^+K^*(892)^0$ production threshold, and it exhibits a cluster at the left bottom corner in the two-dimensional distribution of $m(K^+\pi^-)$ and $m(D^+K^+\pi^-)$. There could also be a wide peak at $\sim$ 3.2 GeV, but it is less evident. From the two-dimensional distribution of $m(D^+D^-)$ and $m(D^+K^+\pi^-)$, it is seen that the $D^+K^+\pi^-$ structure at $\sim$ 3.2 GeV could be due to the reflections of the low-lying resonances in the D^+D^- system.

To validate that the peaking structures in the $D^+K^+\pi^-$ and D^+D^- mass spectra are not from the combinatorial background, the Dalitz-plot distribution of $m^2(D^+D^-)$ and

---

$B^+ \to D^+D^-K^+$ decay, because the $X_{0,1}(2900)$ and D_s^+-resonance production are color-favored in the $b \to c\bar{c}s$ transition, while the $c\bar{c}$ production is color-suppressed.

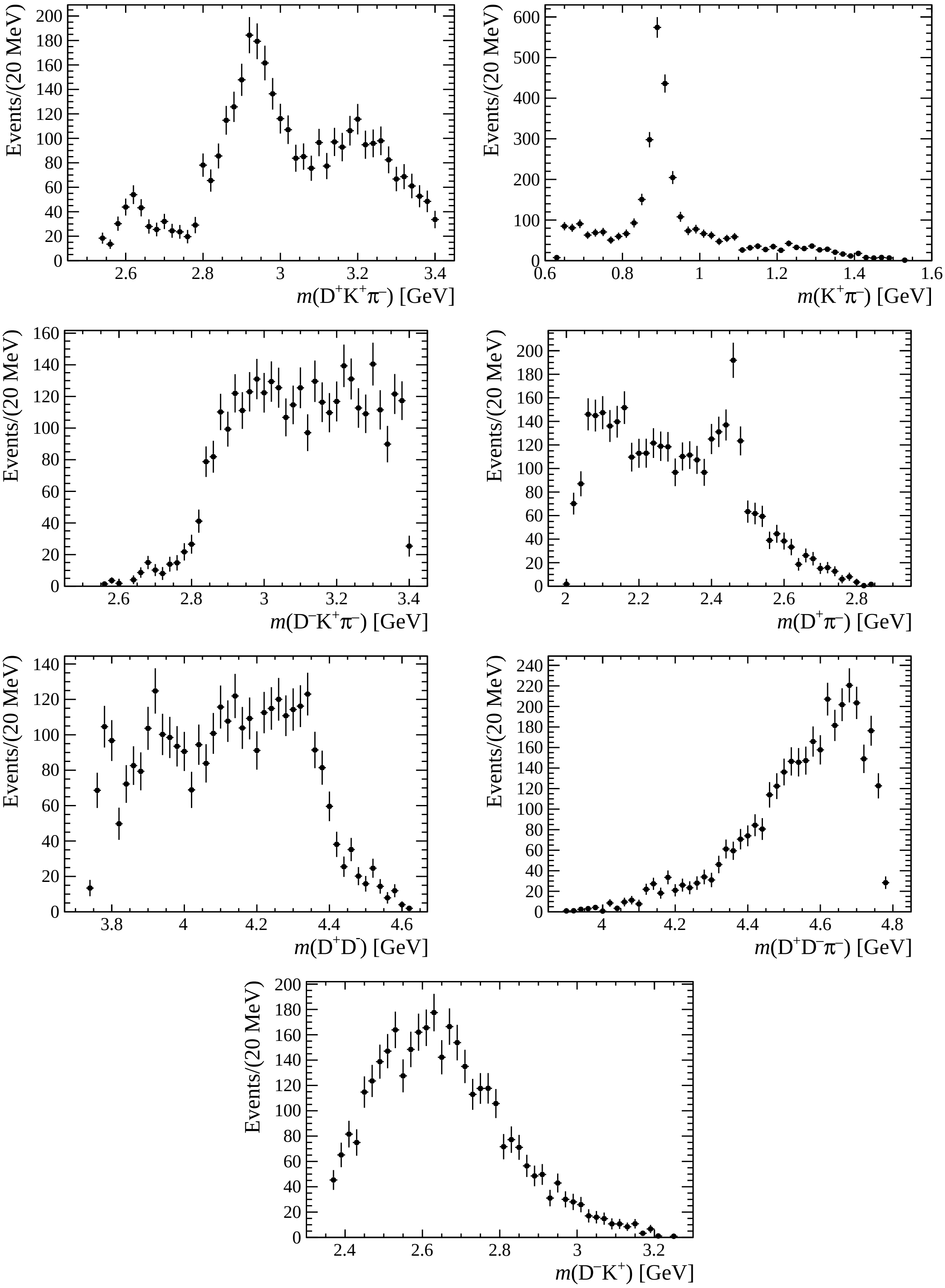

Figure 3.11 Mass projections of the final-state combinations in the $B^0 \to D^+D^-K^+\pi^-$ data. The background is subtracted using the *sPlot* method[174].

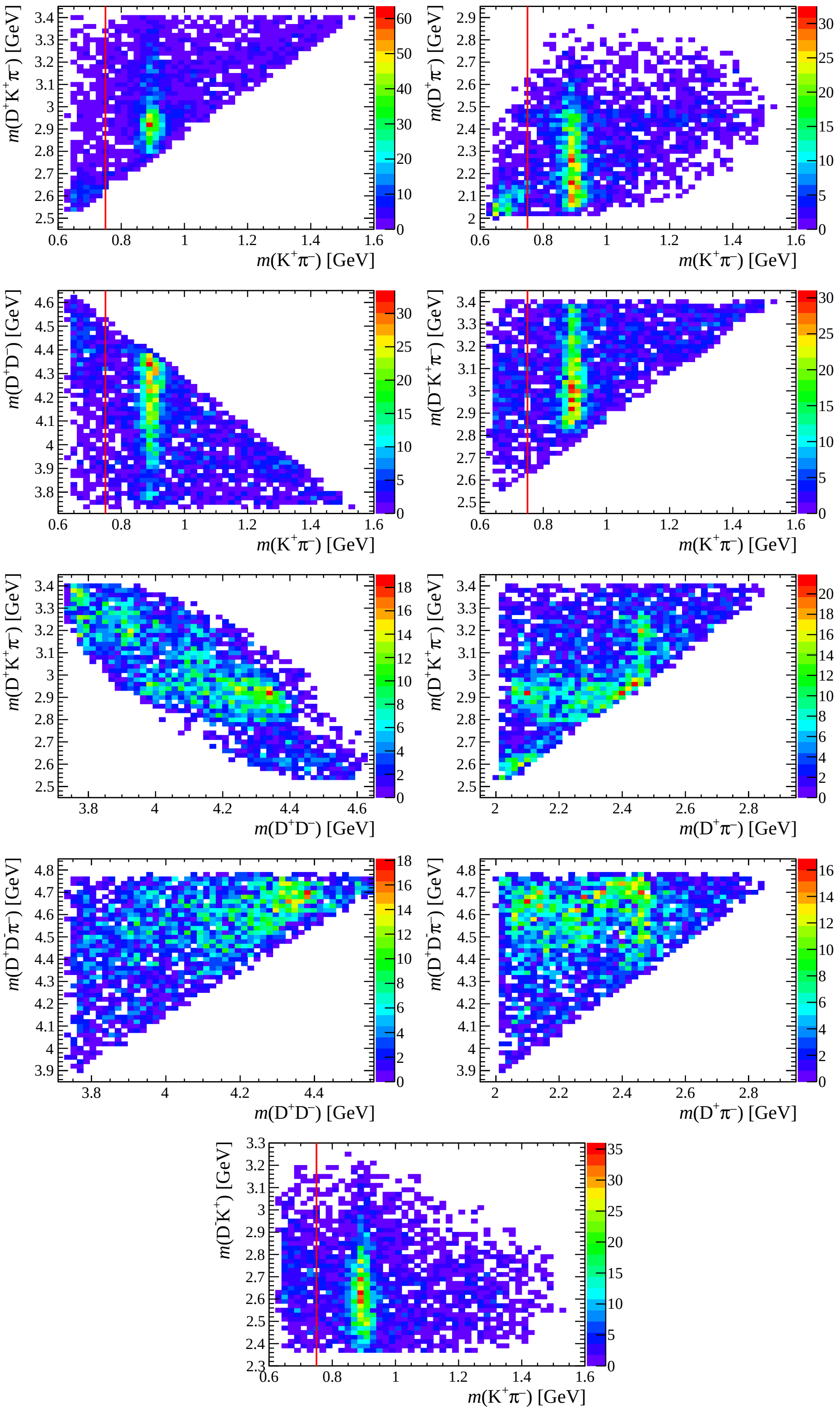

Figure 3.12 Two-dimensional mass distributions of the final-state combinations in the $B^0 \to D^+D^-K^+\pi^-$ data. The red vertical lines is at $m(K^+\pi^-) = 0.75$ GeV. The background is subtracted using the *sPlot* method[174].

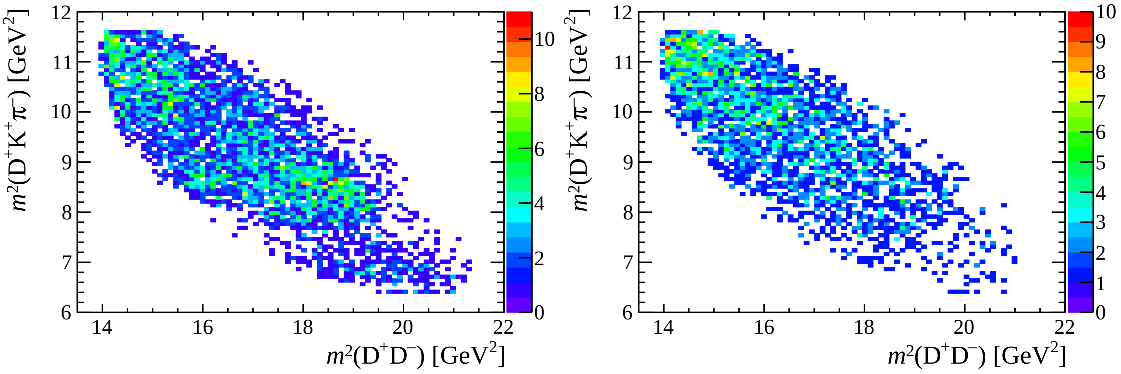

Figure 3.13 Dalitz-plot distributions of $m^2(D^+K^+\pi^-)$ and $m^2(D^+D^-)$ in the $B^0 \to D^+D^-K^+\pi^-$ data within ±20 MeV around the B^0 mass peak (left), and at the sideband ±30 MeV away (right). The combinatorial background is not subtracted.

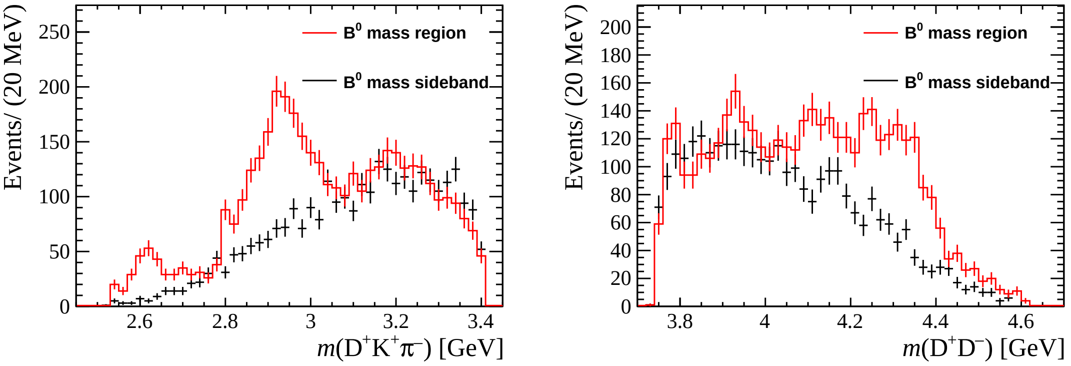

Figure 3.14 Comparisons of the $m(D^+K^+\pi^-)$ (left) and $m(D^+D^-)$ (right) distributions in the $B^0 \to D^+D^-K^+\pi^-$ data. The B^0 mass region is chosen as ±20 MeV around the B^0 mass peak, while the sideband is chosen to be ±30 MeV away. The combinatorial background is not subtracted.

$m^2(D^+K^+\pi^-)$ in the B^0 signal region (±20 MeV around the B^0 mass peak) is compared with that at the B^0 mass sideband (30 MeV away from the B^0 mass peak), as shown in Fig. 3.13, and the corresponding one-dimensional mass projections are shown in Fig. 3.14. It is seen that the $D^+K^+\pi^-$ peaks at $\sim$ 2.6 GeV and $\sim$ 2.9 GeV in the B^0 signal region cannot result from the combinatorial background, but the $\psi(3770)$ and $\chi_{c0,2}(3930)$ peaks are less evident than the two excited D_s^+ candidates.

Due to the presence of resonances in different combinations of final-state particles, the analysis to the full $B^0 \to D^+D^-K^+\pi^-$ data is quite complicated. Fortunately, it is noticed that the peak of the low-lying excited D_s^+ candidate in the $D^+K^+\pi^-$ mass spectrum is far away from the messy structures at the higher mass and can be isolated by requiring $m(K^+\pi^-) < 0.75$ GeV (referred to hereafter as the low $K^+\pi^-$ mass region). This analysis focuses on the study of the low-lying D_s^+ state, whose properties are measured using an amplitude analysis to the $B^0 \to D^+D^-K^+\pi^-$ decay in the low $K^+\pi^-$ mass region in

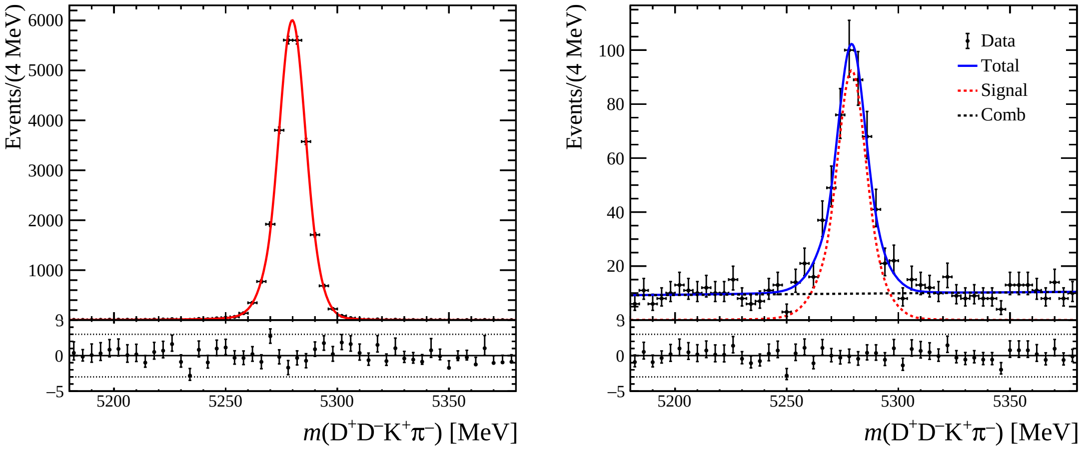

Figure 3.15 B^0 mass distributions in the $B^0 \to D^+D^-K^+\pi^-$ MC (left) and data (right) samples in the low $K^+\pi^-$ mass region. The fit results are overlaid.

Table 3.6 Determined parameters in the B^0 mass fits to $B^0 \to D^+D^-K^+\pi^-$ MC and data samples in the low $K^+\pi^-$ mass region.

Parameter	MC simulation	Data
a	0.5 (fixed)	0.5 (fixed)
N_{sig}	24879.10 ± 157.73	444.07 ± 26.70
N_{bkg}	-	489.95 ± 27.54
m_0(MeV)	5279.83 ± 0.05	5279.09 ± 0.49
σ_1(MeV)	5.25 ± 0.08	5.65 ± 0.74
σ_2(MeV)	8.25 ± 0.11	10.83 ± 1.53
α_1	1.92 ± 0.09	1.92 (fixed)
α_2	-2.57 ± 0.08	-2.57 (fixed)
n	1.62 ± 0.16	1.62 (fixed)
λ(MeV^{-1})	-	$(6.55 \pm 7.93) \times 10^{-4}$

Sec. 3.9.

3.4.3.1 Signal extraction in the low $K^+\pi^-$ mass region

To extract the signal distributions of the amplitude variables in the $B^0 \to D^+D^-K^+\pi^-$ data in the low $K^+\pi^-$ mass region, an additional B^0 mass fit is performed only on the candidates with the $m(K^+\pi^-) < 0.75$ GeV restriction. The fit results are shown in Fig. 3.15, and the determined parameters are listed in Table 3.6. Around 444 ± 27 signal decays are obtained, and the purity in the ± 20 MeV window around the B^0 mass peak is about 81%.

One- and two-dimensional mass distributions of several final-state particle combinations are shown in Figs. 3.16 and 3.17, with the background subtracted using the *sPlot* method[174]. A significant peak at about 2.6 GeV is seen in the $D^+K^+\pi^-$ mass distribution, and it accumulates as a band along the $m(D^+K^+\pi^-)$ axis in the two-dimensional $m(D^+K^+\pi^-)$ *vs.* $m(K^+\pi^-)$ distribution, indicating its resonant nature. This structure probably corresponds to the undiscovered $D_s(2^1S_0)^+$ state as discussed in Sec. 1.3.2. The single-bin peak at the $D^+K^+\pi^-$ mass threshold could result from the $D_{s1}(2536)^+$ state, which was previously observed decaying to $D^+K^+\pi^-$ by the Belle collaboration[178]. There is a small peak at the higher border of the $m(D^+\pi^-)$ distribution, and is suspected to the contribution of the $D_2^*(2460)^0$ state. No other evident peaking structure is seen.

To validate that the peaking structure at $\sim$ 2.6 GeV in the $D^+K^+\pi^-$ mass spectrum is not from the combinatorial background, the Dalitz-plot distribution of $m^2(D^+D^-)$ and $m^2(D^+K^+\pi^-)$ in the B^0 signal region ($\pm$20 MeV around the B^+ mass peak) is compared with that at the B^0 mass sideband (30 MeV away from the B^+ mass peak), as shown in Fig. 3.18, and the corresponding one-dimensional mass projections are shown in Fig. 3.19. It is seen that the $D^+K^+\pi^-$ peak at $\sim$ 2.6 GeV in the B^0 signal region cannot be due to the combinatorial background.

The background-subtracted data is the input to the amplitude analysis in Sec. 3.9. To validate the subtraction does not introduce bias to the signal distributions of the amplitude variables, the independence requirements of the *sPlot* method on the discriminating variable (B^0 mass) and the control variables (amplitude variables) for both the signal and combinatorial background components need to be checked. There are in total five independent variables to describe the four-body $B^0 \to D^+D^-K^+\pi^-$ decay, and those defined in the $B^0 \to D^-D_{sj}^+, D_{sj}^+ \to D^+K_n^{*0}, K_n^{*0} \to K^+\pi^-$ chain are used in the check. The variables are

- Masses: $m_{K^+\pi^-}$ and $m_{D^+K^+\pi^-}$.
- Helicity angles: $\theta_{D_s^+}$ and $\theta_{K^{*0}}$, defined as the polar angles of K^{*0} and K^+ in the $D^+K^+\pi^-$ and $K^+\pi^-$ rest frames, respectively.
- Azimuthal angle: ϕ_π, defined as the angle between the D_s^+ and K^{*0} decay planes).

To check the independence in the signal component, the distributions of the five amplitude variables in the $B^0 \to D^+D^-K^+\pi^-$ MC sample are compared in two B^0 mass regions: a). $\pm$10 MeV around the B^+ mass peak; b).10–30 MeV away from the B^+ mass peak.

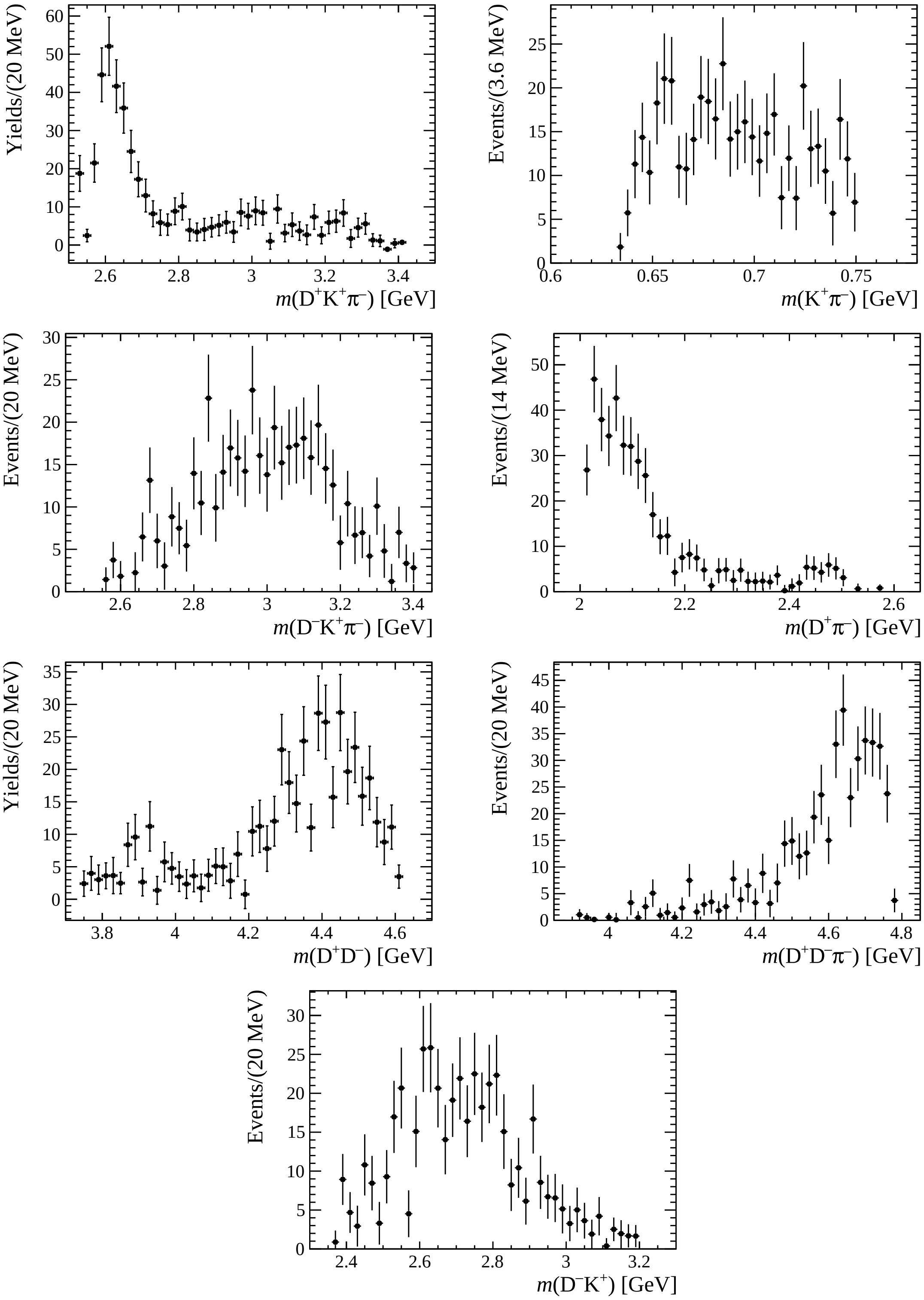

Figure 3.16 Mass projections of the final-state combinations of the $B^0 \to D^+D^-K^+\pi^-$ data in the low $K^+\pi^-$ mass region. The background is subtracted using the *sPlot* method.

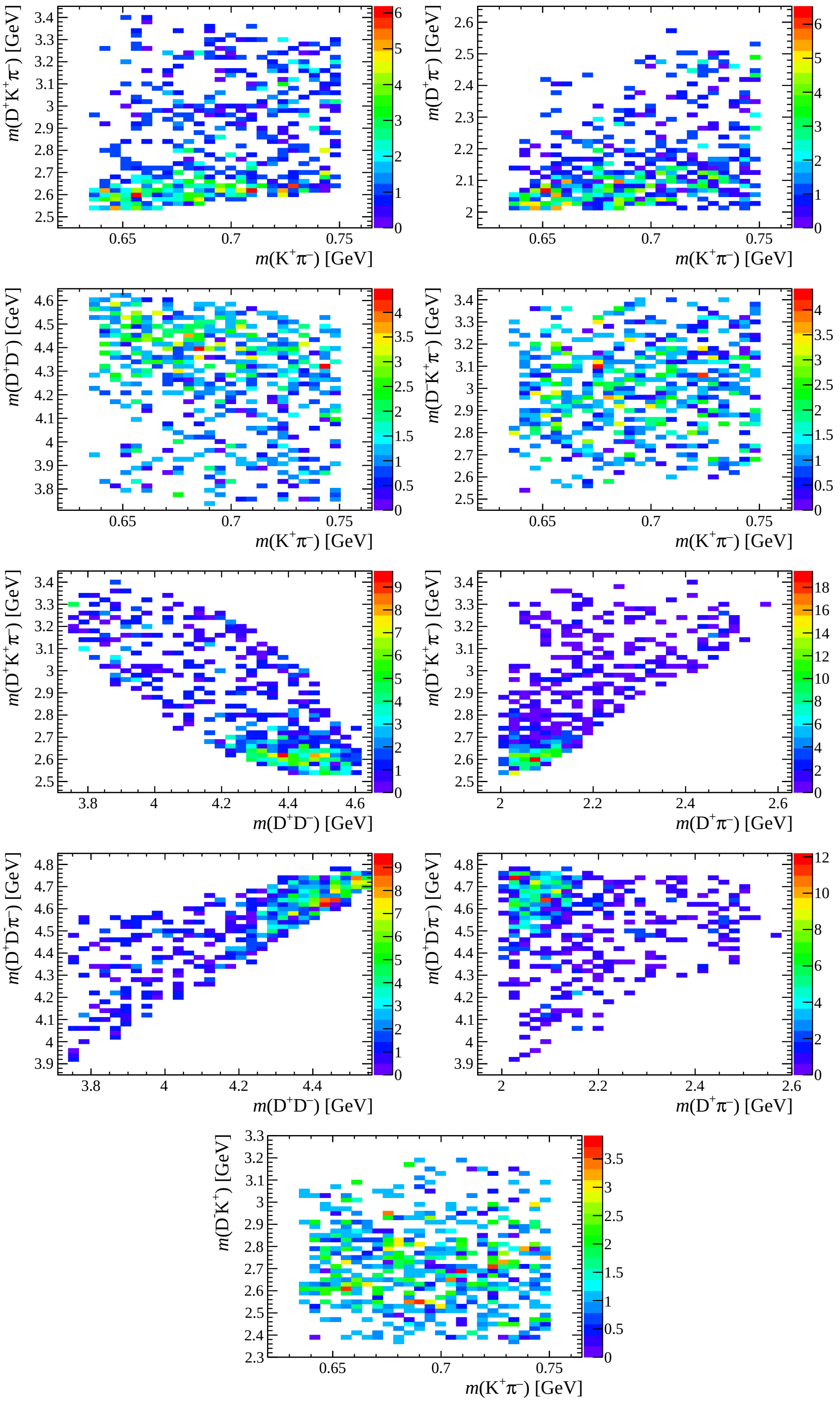

Figure 3.17 Two-dimensional mass distributions of the final-state combinations of the $B^0 \to D^+D^-K^+\pi^-$ data in the low $K^+\pi^-$ mass region. The background is subtracted using the *sPlot* method.

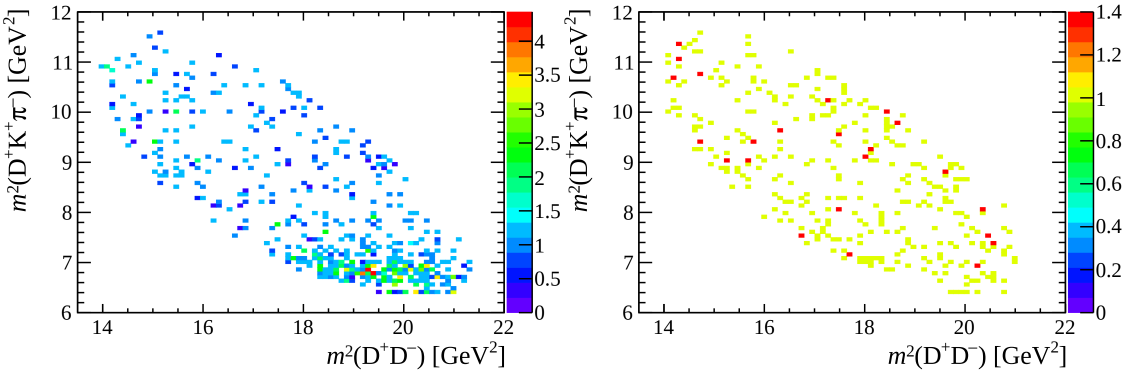

Figure 3.18 Dalitz-plot distributions of $m^2(D^+K^+\pi^-)$ and $m^2(D^+D^-)$ for the $B^0 \to D^+D^-K^+\pi^-$ data candidates within ±20 MeV of the B^0 mass peak (left), and in the sideband ±30 MeV away from the B^0 mass peak (right). Only the candidates in the low $K^+\pi^-$ mass region is shown. The combinatorial background is not subtracted.

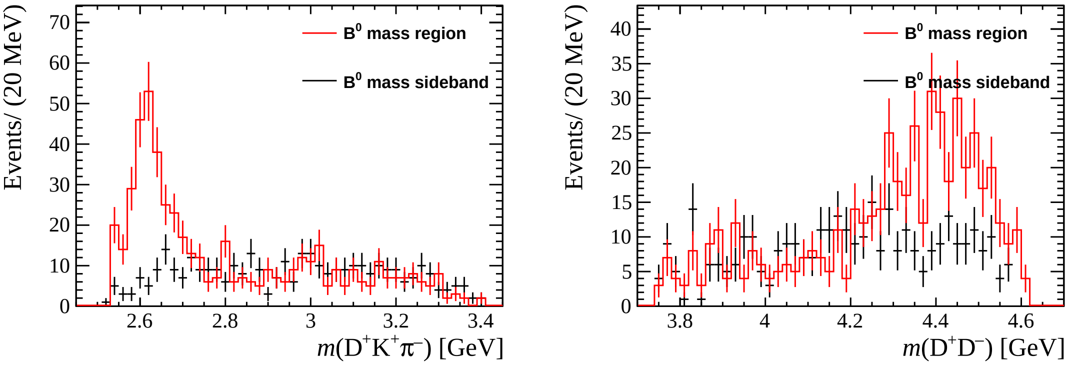

Figure 3.19 Comparisons of the $m(D^+K^+\pi^-)$ (left) and $m(D^+D^-)$ (right) of the $B^0 \to D^+D^-K^+\pi^-$ data candidates in the low $K^+\pi^-$ mass region. The B^0 mass region is chosen as ±20 MeV around the B^0 mass peak, while the sideband is chosen to be ±30 MeV away. The combinatorial background is not subtracted.

No significant discrepancy is seen, as shown in Fig. 3.20, supporting the independence assumption between the B^0 mass and the amplitude variables. The check on the combinatorial background component is carried out in the similar way, using the $B^0 \to D^+D^-K^+\pi^-$ sideband data candidates instead of MC events, as shown in Fig. 3.21. No evident discrepancy is seen for the distributions of the amplitude variables in the lower and higher sidebands of the B^0 mass, suggesting no strong dependence on the discriminating and control variables. A supplemental check is the correlation coefficients between the B^0 mass and the amplitude variables, shown in Fig. 3.22. The small correlation coefficients also support the independence of the discriminating variable and the amplitude variables.

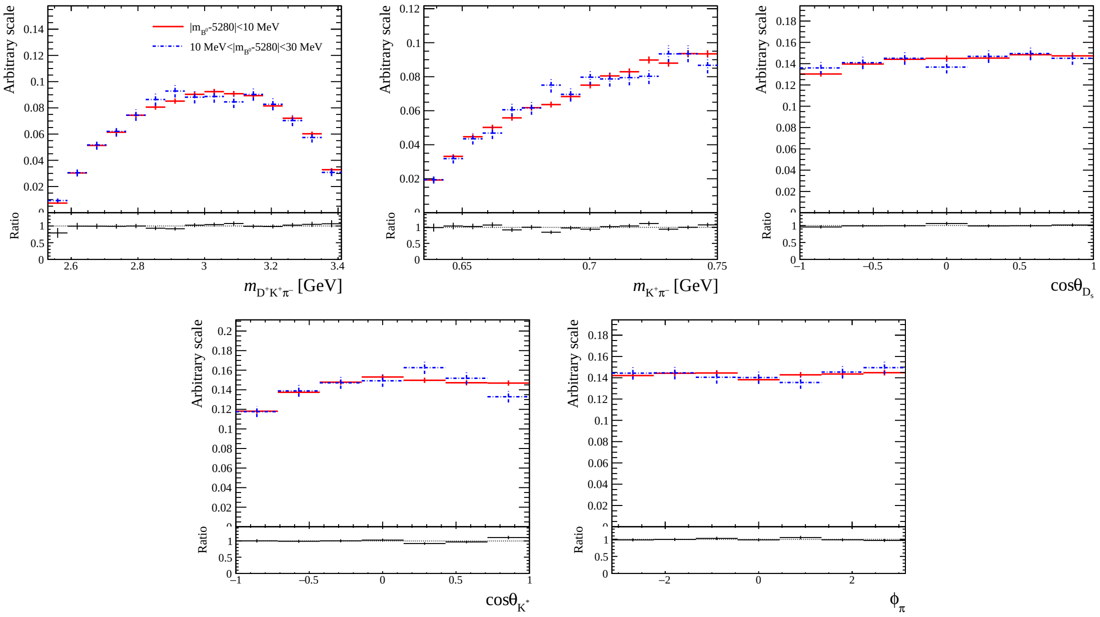

Figure 3.20 Distribution comparisons of the amplitude variables in two B^0 mass regions of the $B^0 \to D^+D^-K^+\pi^-$ MC sample.

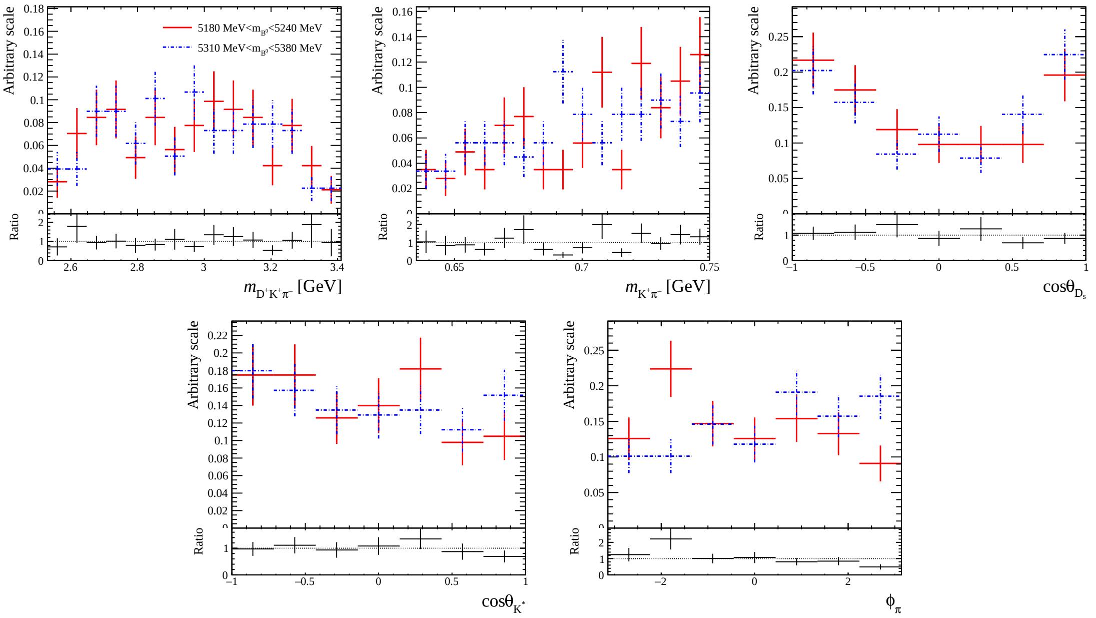

Figure 3.21 Distribution comparisons of the amplitude variables in two B^0 mass sideband regions for the $B^0 \to D^+D^-K^+\pi^-$ data.

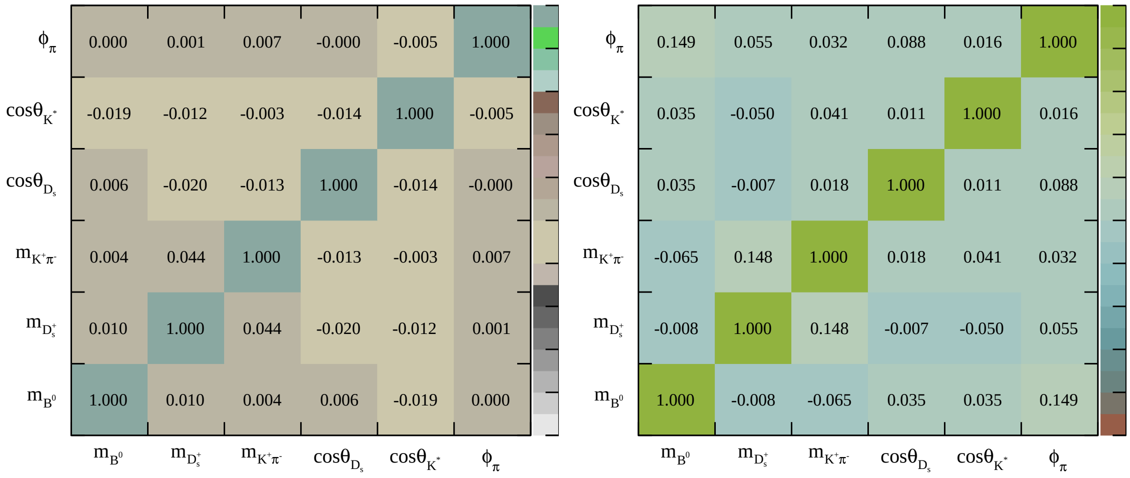

	m_{B^0}	$m_{D_s^+}$	$m_{K^+\pi^-}$	$\cos\theta_{D_s}$	$\cos\theta_{K^*}$	ϕ_π
ϕ_π	0.000	0.001	0.007	-0.000	-0.005	1.000
$\cos\theta_{K^*}$	-0.019	-0.012	-0.003	-0.014	1.000	-0.005
$\cos\theta_{D_s}$	0.006	-0.020	-0.013	1.000	-0.014	-0.000
$m_{K^+\pi^-}$	0.004	0.044	1.000	-0.013	-0.003	0.007
$m_{D_s^+}$	0.010	1.000	0.044	-0.020	-0.012	0.001
m_{B^0}	1.000	0.010	0.004	0.006	-0.019	0.000

	m_{B^0}	$m_{D_s^+}$	$m_{K^+\pi^-}$	$\cos\theta_{D_s}$	$\cos\theta_{K^*}$	ϕ_π
ϕ_π	0.149	0.055	0.032	0.088	0.016	1.000
$\cos\theta_{K^*}$	0.035	-0.050	0.041	0.011	1.000	0.016
$\cos\theta_{D_s}$	0.035	-0.007	0.018	1.000	0.011	0.088
$m_{K^+\pi^-}$	-0.065	0.148	1.000	0.018	0.041	0.032
$m_{D_s^+}$	-0.008	1.000	0.148	-0.007	-0.050	0.055
m_{B^0}	1.000	-0.008	-0.065	0.035	0.035	0.149

Figure 3.22 Correlation coefficients of B^0 mass and the five observables in amplitude analysis in the $B^0 \to D^+ D^- K^+ \pi^-$ MC sample (left) and data sideband (right).

3.4.4 Signal extraction of the control channel

The B^0 mass fit to the $B^0 \to D_s^+ D^-$ data is the first stage for the utilization of the *sPlot* method[174] to extract the signal distributions of the variables to determine MC correction weights to improve the $B^0 \to D^+ D^- K^+ \pi^-$ data/MC agreement in Sec. 3.5. The fit range is chosen to be ±60 MeV around the known B^0 mass[163] to exclude the partially reconstructed background and the peak of the $B_s^0 \to D_s^+ D^-$ signal candidates, as discussed in Sec. 3.3.2. The B^0 mass distributions in the $B^0 \to D_s^+ D^-$ MC and data samples are shown in Fig. 3.23, with the fit results overlaid, where it is seen that the fit can well describe the data. The determined parameters are listed in Table 3.7. The B^0 signal yield in $B^0 \to D_s^+ D^-$ data is 80665 ± 304, and the purity is 97.3% in the ±20 MeV window around the B^0 mass peak.

3.5 MC correction

The LHCb simulation does not well describe the B^0 kinematics, the track multiplicity and the L0 trigger, so corrections regarding to these aspects are introduced to the $B^0 \to D^+ D^- K^+ \pi^-$ MC samples to improve the data/MC agreement. The corrections are performed by applying the event-by-event correction weights obtained from the comparisons of data and MC simulation for the $B^0 \to D_s^+ D^-$ decay.

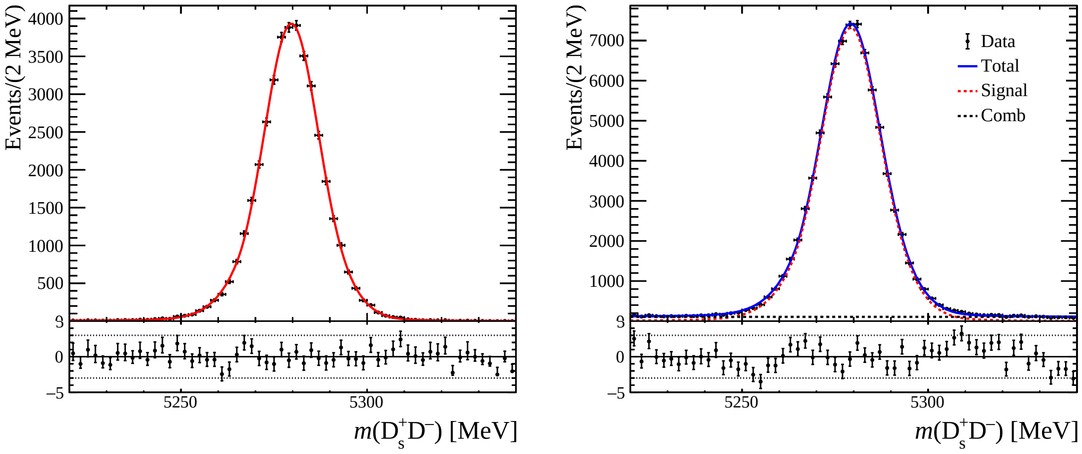

Figure 3.23 B^0 mass distributions in the $B^0 \to D_s^+D^-$ MC (left) and MC (right) samples. The fit results are overlaid.

Table 3.7 Determined parameters in the B^0 mass fits to the $B^0 \to D_s^+D^-$ MC and data samples.

Parameter	MC simulation	Data
a	0.5 (fixed)	0.5 (fixed)
N_{sig}	38942.13 ± 197.34	80664.81 ± 303.58
N_{bkg}	-	6377.53 ± 133.71
m_0(MeV)	5279.78 ± 0.06	5279.21 ± 0.03
σ_1(MeV)	6.64 ± 0.09	7.13 ± 0.07
σ_2(MeV)	10.22 ± 0.17	10.88 ± 0.08
α_1	1.86 ± 0.15	1.86 (fixed)
α_2	-2.48 ± 0.13	-2.48 (fixed)
n	2.15 ± 0.44	2.15 (fixed)
λ(MeV^{-1})	-	$(0.31 \pm 4.20) \times 10^{-4}$

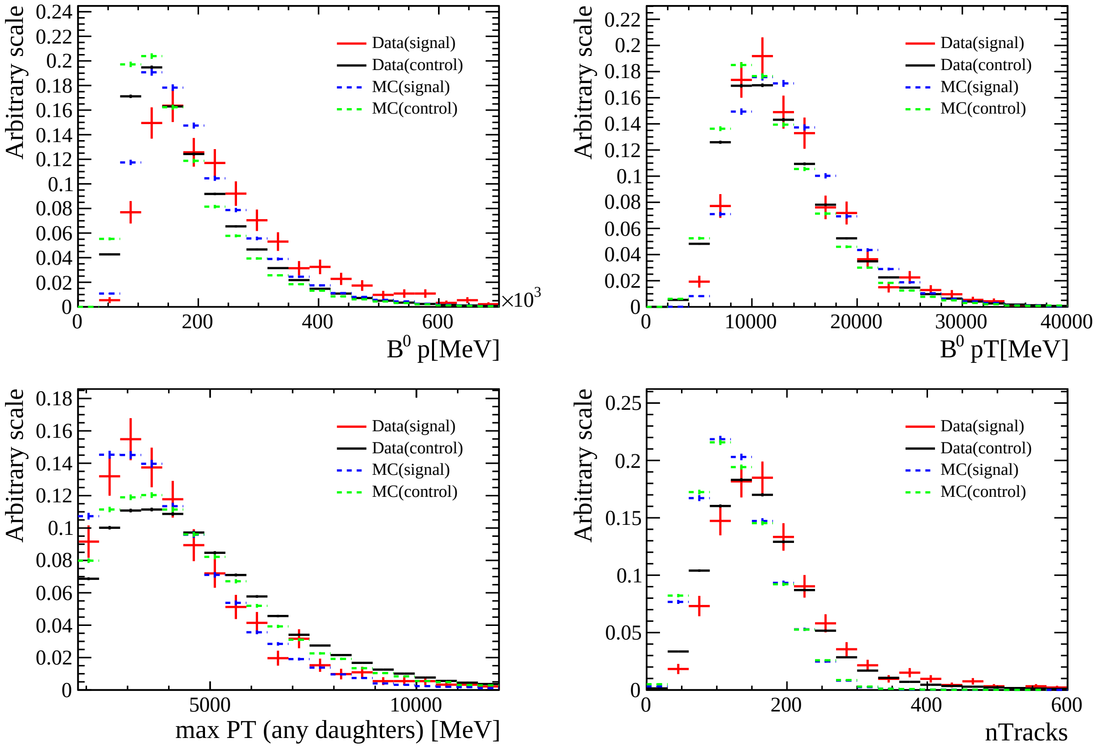

Figure 3.24 Normalized distributions of the variables used in the weights calculation for the signal and control channels.

3.5.1 Check on the range coverage of the input variables for weighting

Before extracting and applying the weights, there is a basic requirement that the range of the variables used to obtain the weights in the $B^0 \to D_s^+D^-$ data and MC samples can cover those for the $B^0 \to D^+D^-K^+\pi^-$ decay. Fig. 3.24 shows the normalized distributions of these variables in data and MC samples for both the $B^0 \to D^+D^-K^+\pi^-$ and $B^0 \to D_s^+D^-$ channels. It is seen that the requirement is satisfied.

3.5.2 L0Hadron_TOS efficiency weight extraction

As the L0Hadron_TOS decision is triggered by the final-state particle with the maximum p_{T} (max_PT), the correction weight is parameterized as a function of max_PT. Before performing the weight extraction, the $B^0 \to D_s^+D^-$ data and MC candidates are required to pass all the selections mentioned in Sec. 3.2 except for the offline trigger requirement. As the trigger requirement is removed, the B^0 mass fit shown in Sec. 3.4.4 can not be utilized as the basis of the *sPlot* method[174] to subtract the background anymore. The signal extraction is instead repeated by an additional fit to the data without the offline trigger requirement. Then, the L0Hadron_TOS efficiency weight is obtained

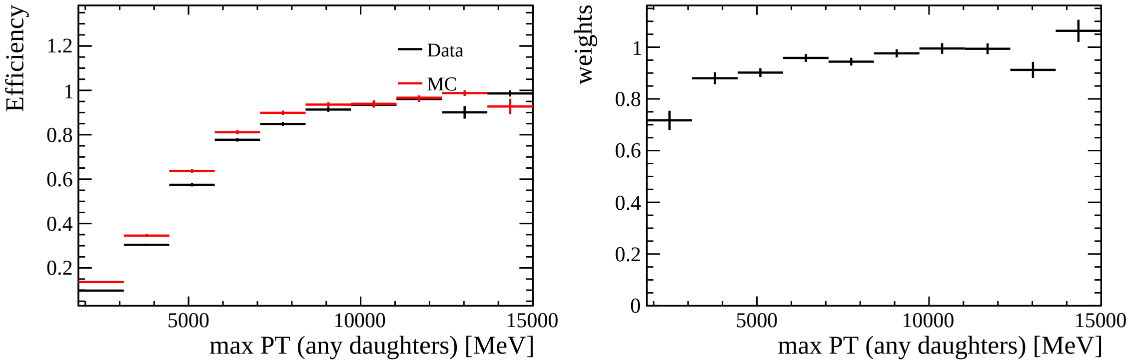

Figure 3.25 L0Hadron_TOS efficiency comparison (left) and the weight (right) for $B^0 \to D_s^+D^-$.

as the ratio of the efficiency obtained from the MC and data samples in different regions of max_PT, as shown in Fig. 3.25, where the efficiency is calculated using the TISTOS method, *i.e.*

$$\varepsilon_{\text{L0Hadron\_TOS}} = \frac{N_{\text{L0Hadron\_TOS\&\&L0Hadron\_TIS}}}{N_{\text{L0Hadron\_TIS}}}. \tag{3.13}$$

where N_{X} is the number of the events under the trigger requirement X. The binning scheme of Fig. 3.25 is detailed in Appendix A.4.

3.5.3 B^0 kinematic weight extraction

The B^0 kinematic weight is determined in different regions of the B^0 p and p_{T}. Before obtaining the weight, the $B^0 \to D_s^+D^-$ data and MC candidates are required to pass all the selections including the offline trigger. The L0Hadron_TOS efficiency weight is also applied to the $B^0 \to D_s^+D^-$ MC sample. The combinatorial background in data is subtracted by the *sPlot* method[174] in Sec. 3.4.4. The B^0 kinematic weight is taken as the ratio of the normalized two-dimensional distributions of B^0 (p, p_{T}) in the MC and data samples, shown in Fig. 3.26. The binning scheme is detailed in Appendix A.4.

3.5.4 nTracks weight extraction

The nTracks weight is obtained as a function of the nTracks variable. Before calculating the weight, the $B^0 \to D_s^+D^-$ data and MC candidates are required to pass all the selections including the offline trigger requirement. The L0Hadron_TOS efficiency weight and B^0 kinematic weight are applied to the $B^0 \to D_s^+D^-$ MC sample. Background in data is subtracted by the *sPlot* method[174], as described in Sec. 3.4.4. The weight is taken as the ratio of normalized nTracks distributions in the data and MC samples, as shown in Fig. 3.27. The binning scheme is detailed in Appendix A.4.

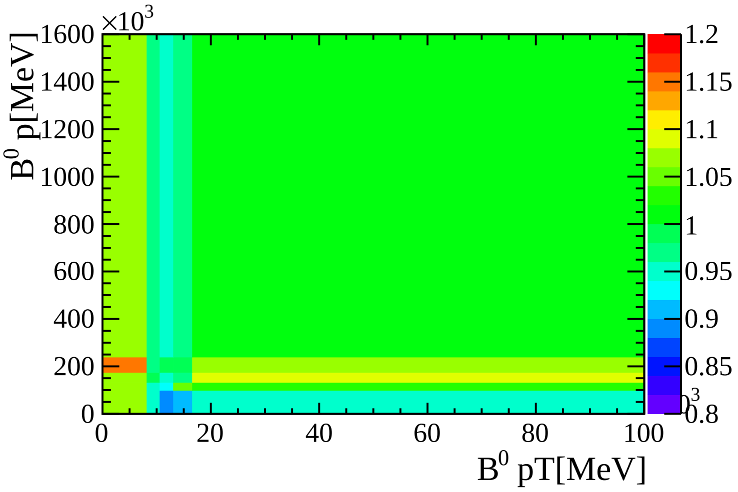

Figure 3.26 2D kinematic weight map obtained from the comparison between the p *vs.* p_{T} distributions in the $B^0 \to D_s^+D^-$ MC and data samples.

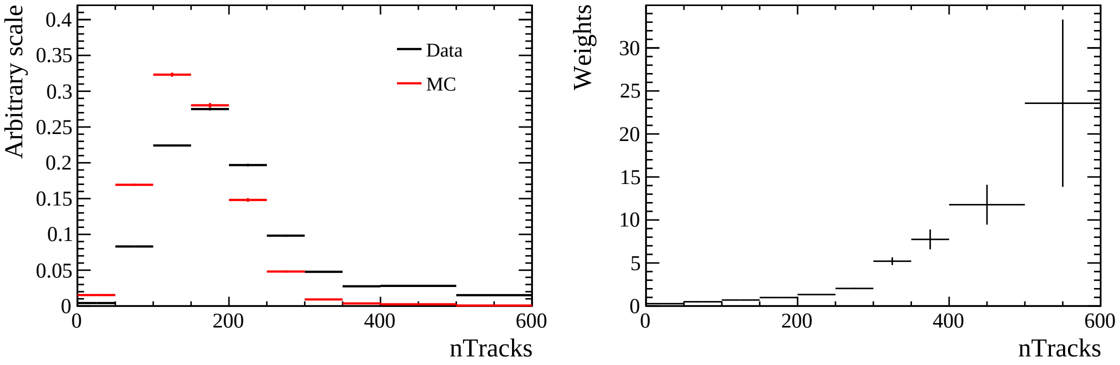

Figure 3.27 nTracks data/MC comparison (left) and the obtained weight (right) for the $B^0 \to D_s^+D^-$ channel.

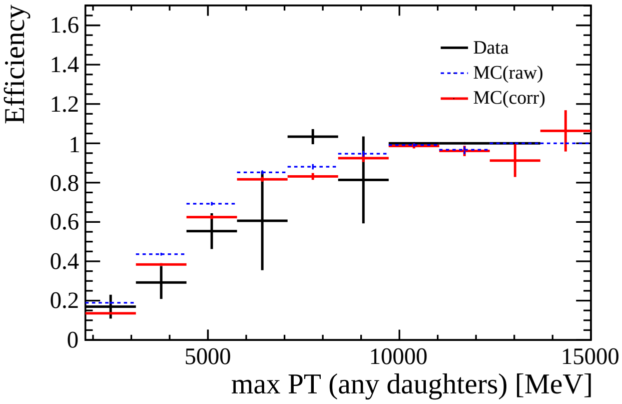

Figure 3.28 L0Hadron_TOS efficiency in different max_PT regions of the $B^0 \to D^+D^-K^+\pi^-$ MC and data samples in the low $K^+\pi^-$ mass region. The red (blue) line denotes the efficiency in the MC sample with (without) the L0Hadron_TOS efficiency weight applied, and the black line denotes the efficiency in data.

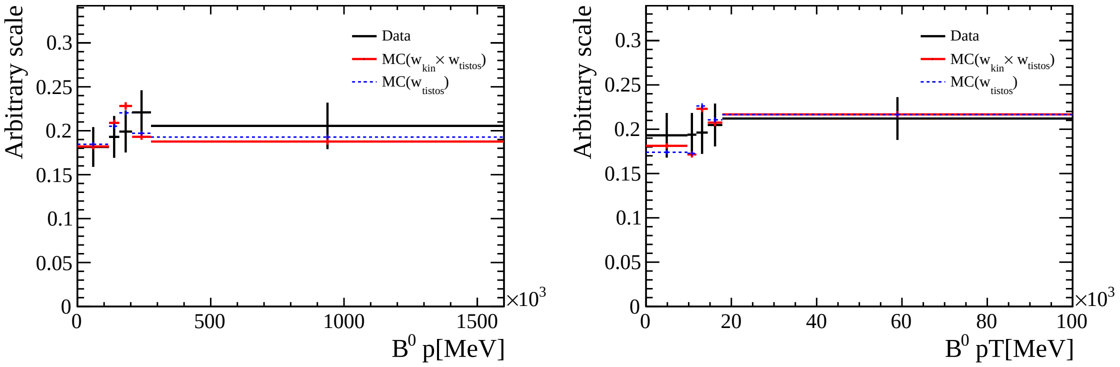

Figure 3.29 B^0 p (left) and $p_{\rm T}$ (right) distributions for the $B^0 \to D^+D^-K^+\pi^-$ channel in the low $K^+\pi^-$ mass region. Black line: data; Blue line: MC simulation with only the L0Hadron_TOS efficiency weight applied; Red line: MC simulation with both the B^0 kinematic and L0Hadron_TOS efficiency weights applied.

3.5.5 MC weights application

The correction weights obtained from the three above subsections are applied to the $B^0 \to D^+D^-K^+\pi^-$ MC sample to improve the its agreement with data. Each candidate in the $B^0 \to D^+D^-K^+\pi^-$ MC sample is assigned a L0Hadron_TOS efficiency weight, a B^0 kinematic weight, and a nTracks weight, according to the values of max_PT, B^0 p and $p_{\rm T}$, and nTracks, respectively. The total correction weight is the product of those from the three sources.

To demonstrate the performance of the correction, the related distributions are compared between the $B^0 \to D^+D^-K^+\pi^-$ data and MC samples with/without the concerned weights applied, as shown in Figs. 3.28, 3.29 and 3.30. Good data/MC agreements are seen for the distributions after the corresponding weights applied.

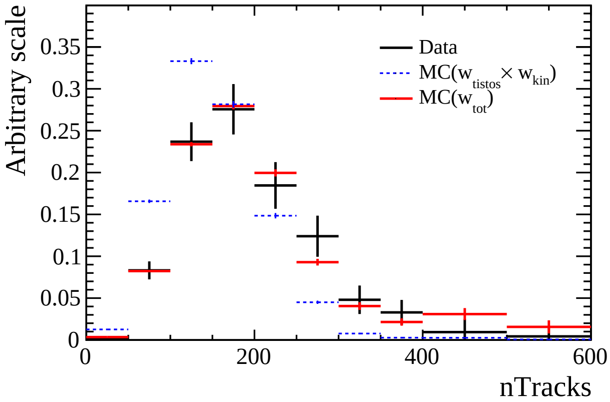

Figure 3.30 nTracks distribution for the $B^0 \to D^+D^-K^+\pi^-$ channel in the low $K^+\pi^-$ mass region. Black line: data; Blue line: MC simulation with the L0Hadron_TOS efficiency and B^0 kinematic weights applied; Red line: MC simulation with all the three weights applied.

3.6 General construction of the amplitude fit model

The amplitude analysis is employed to measure the properties of the new D_s^+ state at 2.6 GeV in the $D^+K^+\pi^-$ mass spectrum. There are just a few resonances expected in the $B^0 \to D^+D^-K^+\pi^-$ data in the low $K^+\pi^-$ mass region, as discussed in Sec. 3.4.3.1, including a new D_s^+ state near 2.6 GeV and the $D_{s1}(2536)^+$ resonance. A non-resonant (NR) component is also needed to model the underlying continuum mass distribution in the $D^+K^+\pi^-$ system. The overall B^0 decay amplitude in the low $K^+\pi^-$ mass region is not expected to be too complicated. So basically, a specific decay amplitude construction focusing on the modeling of the expected states is enough for the amplitude analysis in the low $K^+\pi^-$ mass region. Nevertheless, the description of a general amplitude construction for all possible intermediate processes of the four-body $B^0 \to D^+D^-K^+\pi^-$ decay is still given in this section, not only providing the fit model in the low $K^+\pi^-$ mass region to study the new D_s^+ state in this analysis, but also serving as the basis for the future amplitude analysis in the full phase space.

The B^0 decay amplitude, also referred to as the matrix element, is defined as $\mathcal{M} = \langle f|S|i\rangle$, where the symbol S denotes the S-matrix characterizing the transition from the initial state i to the final state f. In the $B^0 \to D^+D^-K^+\pi^-$ decay, the initial state is the B^0 meson, and the final state is $|D^+D^-K^+\pi^-\rangle$. The construction of the decay amplitude is based on the helicity formalism[179], where the $B^0 \to D^+D^-K^+\pi^-$ decay is regarded as a cascade of two-body decays. There are many possible decay chains, which can be generally classified into two types:

$$B^0 \to R_{1j}R_{2n}, R_{1j} \to P_1P_2, R_{2n} \to P_3P_4. \tag{3.14}$$

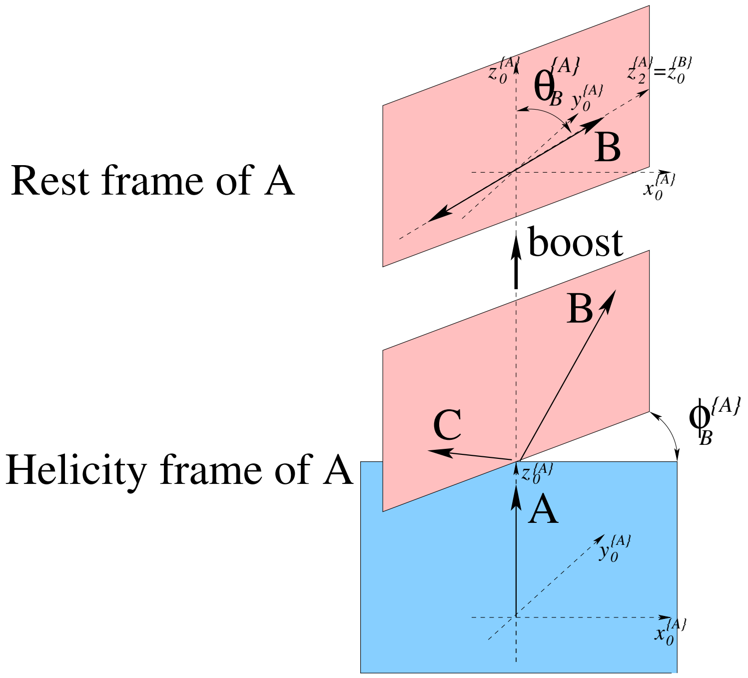

Figure 3.31 The helicity and the rest frame of particle A. Definitions of the angular variables in the $A \to BC$ decay are also shown.

$$B^0 \to P_1 D_{1j}, D_{1j} \to P_2 R_{2n}, R_{2n} \to P_3 P_4. \tag{3.15}$$

Here (P_1, P_2, P_3, P_4) can be any possible permutation of the four final-state particles with intermediate resonant contributions $((D_{1j}, R_{1j}, R_{2n}))$ in the corresponding chain, where the indices j and n are taken to distinguish different resonances. The matrix element for each two-body decay is at first constructed, and the amplitude for each chain is then given as the product of those for the involved cascade two-body processes. Finally, the total decay amplitude is constructed as the sum of the amplitudes of all possible decay chains containing resonant contributions. This section describes how the decay amplitude for the two general chains in Eq. 3.15 are built from the bottom up. For a specific case, one just needs to match the final-state particles to (P_1, P_2, P_3, P_4). Thanks to the spinless initial- and final-state particles, the amplitude formula is greatly simplified.

3.6.1 Matrix element for the two-body process $A \to BC$

The basic ingredient of the total decay amplitude is the matrix element of the two-body decay $A \to BC$. To describe this process, a coordinate system $(x_0^{\{A\}}, y_0^{\{A\}}, z_0^{\{A\}})$ is set up in the rest frame of A, as shown in Fig. 3.31. The $z_0^{\{A\}}$ axis is defined as the momentum direction of A in the lab frame if it is from the pp collision, otherwise in the rest frame of its originating particle. Directions of another two axes depend on the convention to define the spin eigenstate. The helicity formalism describes the matrix element in terms of a series of partial amplitude defined for the spin/helicity eigenstates. The initial state is $|J_A, m_A\rangle$, where J_A is the spin of A and m_A the spin component in the $z_0^{\{A\}}$ direction. The final state is defined as $|J_B, \lambda_B; J_C, \lambda_C\rangle$, where J_B (J_C) is the spin of B (C), and λ_B (λ_C) is the helicity defined as the spin projection along the B (C) momentum direction in the A rest frame.

$$\mathcal{M}_{A\to BC} = \mathcal{H}^{A\to BC}_{\lambda_B,\lambda_C} D^{J_A}_{m_A,\lambda_B-\lambda_C}\left(\phi_B, \theta_B, 0\right)^* (-1)^{I_C}, \tag{3.16}$$

where $\mathcal{H}^{A\to BC}_{\lambda_B,\lambda_C}$ is the complex-valued helicity coupling that characterizes the strength of the amplitude, and $D^{J_A}_{m_A,\lambda_B-\lambda_C}\left(\phi_B, \theta_B, 0\right)$ is the Wigner-D function to describe the angular distribution. The particle-two factor $(-1)^{I_C}$ is related to the convention how the C spin state in its own rest frame is transformed into the helicity state defined in the A rest frame[180]. For example, if the rotation part of the transformation is $R(\phi_1, \theta_1, 0)R_y(\pi)$, the factor is $(-1)^{J_C-\lambda_C}$, and if the rotation is $R(\phi_1, \theta_1, 0)R_x(\pi)$, the factor is $(-1)^{J_C}$. Here, $R(\phi_1, \theta_1, 0)$ denotes the rotation in the three-dimensional space, and $R_{x/y}(\pi)$ the rotation around the x/y axis by π. In general, the $(-1)^{J_C-\lambda_C}$ term in the first convention cannot be simply absorbed in the redefinition of the helicity coupling, otherwise the helicity relation in Eq. 3.18 will not hold anymore ①. The $(-1)^{J_C}$ term in the second convention is unrelated to the helicity of C and thus can be safely absorbed in the helicity coupling without violating the helicity relation in Eq. 3.18. The second convention is taken in this analysis and the particle-two factor is implicitly absorbed in the redefinition of the helicity coupling in the following text. The polar angle, θ_B is defined as the angle between the B momentum and $z_0^{\{A\}}$ direction, and the azimuthal angle ϕ_B is the angle between the $A \to BC$ decay plane and the $x_0^{\{A\}} - z_0^{\{A\}}$ plane, as shown in Fig. 3.31. The two angles are calculated as

$$\begin{aligned} \theta_B &= \cos^{-1}\left(\hat{z}_0^{\{A\}} \cdot \hat{p}_B^{\{A\}}\right), \\ \phi_B &= \tan^{-1}\left(\frac{\hat{y}_0^{\{A\}} \cdot \hat{p}_B^{\{A\}}}{\hat{x}_0^{\{A\}} \cdot \hat{p}_B^{\{A\}}}\right), \end{aligned} \tag{3.17}$$

where symbols with hats are unit vectors representing the directions of the corresponding axes or momenta. The polar angle θ_B is also referred to as the helicity angle of the $A \to BC$ decay.

---

① For the specific case of the $B^0 \to D^+D^-K^+\pi^-$ decay, there is no problem to absorb $(-1)^{J_C-\lambda_C}$ into the helicity coupling thanks to the presence of the spinless initial- and final-state particles, and the parity violation of the B^0 decay.

If $A \to BC$ is a strong or electromagnetic decay, the parity conservation requires that

$$\mathcal{H}^{A\to BC}_{-\lambda_B,-\lambda_C} = P_A P_B P_C (-1)^{J_B+J_C-J_A} \mathcal{H}^{A\to BC}_{\lambda_B,\lambda_C}, \tag{3.18}$$

where $P_{A,B,C}$ is the intrinsic parity of the particle. The helicity couplings are fit parameters in the amplitude analysis, and the above relation constrains the couplings between the positive and negative helicities. An alternative way to define fit parameters is to employ the so-called LS couplings, B_{LS}, which are connected with the helicity couplings by

$$\begin{aligned}\mathcal{H}^{A\to BC}_{\lambda_B,\lambda_c} = \sum_L \sum_S \sqrt{\frac{2L+1}{2J_A+1}} \times B_{L,S} \\ \times \left(\begin{array}{cc|c} J_B & J_C & S \\ \lambda_B & -\lambda_C & \lambda_B-\lambda_C \end{array} \right) \times \left(\begin{array}{cc|c} L & S & J_A \\ 0 & \lambda_B-\lambda_C & \lambda_B-\lambda_C \end{array} \right),\end{aligned} \tag{3.19}$$

where L is the orbital angular momentum between B and C, and S is the spin sum. The formula in parentheses is the Clebsch-Gordan coefficient. There are two advantages of the utilization of the LS couplings. The first one is that the parity conservation is implicitly imposed by only keeping the LS couplings with the orbital angular momenta allowed by the conservation rules, and the second one is that for the process with low energy release, the higher orbital angular momenta are suppressed, so it is sufficient to keep only the lowest L, which reduces the number of fit parameters.

The matrix element of the sub-sequential decay of B or C can be constructed in the analogous way. As the B helicity state in the A rest frame is obtained by boosting and rotating the B spin state defined in its own rest frame, the coordinate system of the B rest frame is correspondingly obtained by rotating A rest frame by $\mathcal{R}(\theta_B, \phi_B, 0)$, that is

$$\begin{aligned} \hat{z}_0^{\{B\}} &= \hat{p}_B^{\{A\}} = -\hat{p}_C^{\{A\}} = -\hat{p}_C^{\{B\}}, \\ \hat{x}_0^{\{B\}} &= -\hat{a}^{\{A\}}_{z_0\perp B} \quad \text{with } \vec{a}^{\{A\}}_{z_0\perp B} \equiv \hat{z}_0^{\{A\}} - \left(\hat{z}_0^{\{A\}} \cdot \hat{z}_0^{\{B\}}\right) \hat{z}_0^{\{B\}}, \\ \hat{y}_0^{\{B\}} &= \hat{z}_0^{\{B\}} \times \hat{x}_0^{\{B\}}. \end{aligned} \tag{3.20}$$

If C also decays, its rest frame is the start point to build up the secondary decays. The coordinate system is defined in the similar way as that for the B decay. The $\hat{z}_0^{\{C\}}$ axis is just $\hat{p}_C^{\{A\}}$ or the opposite of $\hat{z}_0^{\{B\}}$, but the definition of the other two axes depends on the particle-two convention. For example, for the $R(\phi_1, \theta_1, 0)R_y(\pi)$ rotation,

$$\hat{x}_0^{\{C\}} = -\hat{x}_0^{\{B\}}, \quad \hat{y}_0^{\{C\}} = \hat{y}_0^{\{B\}}. \tag{3.21}$$

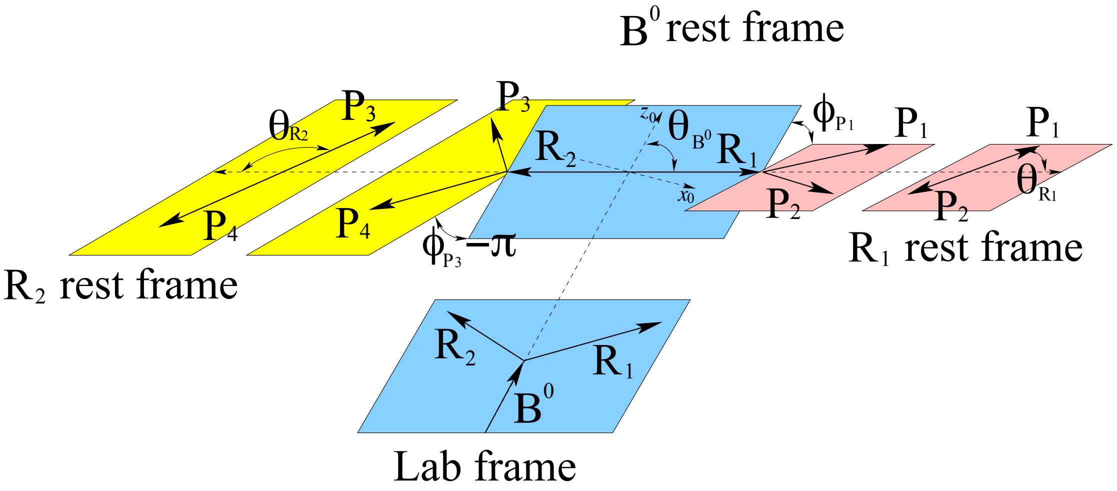

Figure 3.32 Definition of the decay angles in the $B^0 \to R_{1j}R_{2n}, R_{1j} \to P_1P_2, R_{2n} \to P_3P_4$ chain.

and for $R(\phi_1, \theta_1, 0)R_x(\pi)$ is

$$\hat{x}_0^{\{C\}} = \hat{x}_0^{\{B\}}, \quad \hat{y}_0^{\{C\}} = -\hat{y}_0^{\{B\}}, \tag{3.22}$$

The latter is taken in this analysis.

3.6.2 Matrix element for the $B^0 \to R_{1j}R_{2n}, R_{1j} \to P_1P_2, R_{2n} \to P_3P_4$ chain

Following the matrix element of the general $A \to BC$ process, each two-body decay in the $B^0 \to R_{1j}R_{2n}, R_{1j} \to P_1P_2, R_{2n} \to P_3P_4$ chain is built up step by step. The decay chain is displayed in Fig. 3.32, with the angles described in the following text.

The amplitude construction starts from the B^0 rest frame, defined as

$$\begin{aligned}
&\hat{z}_0^{\{B^0\}} = \hat{p}_{B^0}^{\{\text{Lab}\}}, \\
&\hat{x}_0^{\{B^0\}} = -\hat{a}^{\{\text{Lab}\}}_{B^0 \perp \hat{z}_0^{\{\text{Lab}\}}} \quad \text{with} \quad \vec{a}^{\{\text{Lab}\}}_{B^0 \perp \hat{z}_0^{\{\text{Lab}\}}} = \hat{z}_0^{\{\text{Lab}\}} - (\hat{z}_0^{\{\text{Lab}\}} \cdot \hat{z}_0^{\{B^0\}})\hat{z}_0^{\{B^0\}}, \\
&\hat{y}_0^{\{B^0\}} = \hat{z}_0^{\{B^0\}} \times \hat{x}_0^{\{B^0\}}.
\end{aligned} \tag{3.23}$$

The lab frame here is the same as that for the LHCb detector. The matrix element for the $B^0 \to R_{1j}R_{2n}$ decay is then constructed as

$$\mathcal{H}^{B^0 \to R_{1j}R_{2n}}_{\lambda_{R_{1j}}, \lambda_{R_{2n}}} D^{J_{B^0}}_{\lambda_{B^0}, \lambda_{R_{1j}} - \lambda_{R_{2n}}}(\phi^{R_1}_{B^0}, \theta^{R_1}_{B^0}, 0)^* = \mathcal{H}^{B^0 \to R_{1j}R_{2n}}_{\lambda_{R_{1j}}}, \tag{3.24}$$

which reduces to a constant term due to $J_{B^0} = 0$. $\lambda_{R_{1j}} - \lambda_{R_{2n}}$ must take zero, so the helicity coupling only contains $\lambda_{R_{1j}}$. The polar and azimuthal angles, $\theta^{R_1}_{B^0}$ and $\phi^{R_1}_{B^0}$①, of

---

① Symbols with superscript or subscript R_1, R_2 and D_1 containing no indices i, n are used to denote variables calculated for the chain. Their values are determined from the dataset and are the same for all resonances. The symbols R_1j, R_2n and D_1j present different resonances.

the R_1 momentum in the B^0 rest frame are calculated as

$$\begin{aligned} \theta_{B^0}^{R_1} &= \cos^{-1}\left(\hat{z}_0^{\{B^0\}} \cdot \hat{p}_{R_1}^{\{B^0\}}\right), \\ \phi_{B^0}^{R_1} &= \tan^{-1}\left(\frac{\hat{y}_0^{\{B^0\}} \cdot \hat{p}_{R_1}^{\{B^0\}}}{\hat{x}_0^{\{B^0\}} \cdot \hat{p}_{R_1}^{\{B^0\}}}\right). \end{aligned} \tag{3.25}$$

These angles do not appear in the amplitude.

The $R_{1j} \to P_1P_2$ decay is described in the R_1 rest frame, defined as

$$\begin{aligned} \hat{z}_0^{\{R_1\}} &= \hat{p}_{R_1}^{\{B^0\}}, \\ \hat{x}_0^{\{R_1\}} &= -\hat{a}^{\{B^0\}}_{R_1 \perp \hat{z}_0^{\{B^0\}}} \quad \text{with} \quad \vec{a}^{\{B^0\}}_{R_1 \perp \hat{z}_0^{\{B^0\}}} = \hat{z}_0^{\{B^0\}} - (\hat{z}_0^{\{B^0\}} \cdot \hat{z}_0^{\{R_1\}})\hat{z}_0^{\{R_1\}}, \\ \hat{y}_0^{\{R_1\}} &= \hat{z}_0^{\{R_1\}} \times \hat{x}_0^{\{R_1\}}. \end{aligned} \tag{3.26}$$

Then the matrix element is constructed as

$$\mathcal{H}_{\lambda_{R_{1j}}}^{R_{1j} \to P_1P_2} \; D_{\lambda_{R_{1j}},0}^{J_{R_{1j}}}(\phi_{R_1}^{P_1}, \theta_{R_1}^{P_1}, 0)^* \; \mathcal{A}_{1j}(m_{P_1P_2}), \tag{3.27}$$

where $\lambda_{P_1} = \lambda_{P_2} = 0$ is imposed because P_1 and P_2 are spin-zero particles. $\mathcal{A}_{1j}(m_{P_1P_2})$ is used to model the mass lineshape of R_{1j}, which together with the mass lineshapes appearing in the following text, are described in Sec. 3.6.5.2. The polar and azimuthal angles, $\theta_{R_1}^{P_1}$ and $\phi_{R_1}^{P_1}$, of the P_1 momentum in the R_1 rest frame are

$$\begin{aligned} \theta_{R_1}^{P_1} &= \cos^{-1}\left(\hat{z}_0^{\{R_1\}} \cdot \hat{p}_{P_1}^{\{R_1\}}\right), \\ \phi_{R_1}^{P_1} &= \tan^{-1}\left(\frac{\hat{y}_0^{\{R_1\}} \cdot \hat{p}_{P_1}^{\{R_1\}}}{\hat{x}_0^{\{R_1\}} \cdot \hat{p}_{P_1}^{\{R_1\}}}\right). \end{aligned} \tag{3.28}$$

The coordinate system of the R_2 rest frame is defined by reversing the y and z axes of Eq. 3.26. The process $R_{2n} \to P_3P_4$ is described by a term similar to the R_{1j} decay

$$\mathcal{H}_{\lambda_{R_{2n}}}^{R_{2n} \to P_3P_4} \; D_{\lambda_{R_{2n}},0}^{J_{R_{2n}}}(\phi_{R_2}^{P_3}, \theta_{R_2}^{P_3}, 0)^* \; \mathcal{A}_{2n}(m_{P_3P_4}), \tag{3.29}$$

where $\lambda_{P_3} = \lambda_{P_4} = 0$ is imposed because P_3 and P_4 are spin-zero particles. $\phi_{R_2}^{P_3}$ and $\theta_{R_2}^{P_3}$ are the azimuthal and polar angles of P_3 in the R_2 rest frame,

$$\begin{aligned} \theta_{R_2}^{P_3} &= \cos^{-1}\left(\hat{z}_0^{\{R_2\}} \cdot \hat{p}_{P_3}^{\{R_2\}}\right) = \cos^{-1}\left(-\hat{z}_0^{\{R_1\}} \cdot \hat{p}_{P_3}^{\{R_2\}}\right), \\ \phi_{R_2}^{P_3} &= \tan^{-1}\left(\frac{\hat{y}_0^{\{R_2\}} \cdot \hat{p}_{P_3}^{\{R_2\}}}{\hat{x}_0^{\{R_2\}} \cdot \hat{p}_{P_3}^{\{R_2\}}}\right) = \tan^{-1}\left(\frac{-\hat{y}_0^{\{R_1\}} \cdot \hat{p}_{P_3}^{\{R_2\}}}{\hat{x}_0^{\{R_1\}} \cdot \hat{p}_{P_3}^{\{R_2\}}}\right), \end{aligned} \tag{3.30}$$

Combining the matrix elements in Eqs. 3.24, 3.27 and 3.29, the amplitude for the cascade $B^0 \to R_{1j}R_{2n}, R_{1j} \to P_1P_2, R_{2n} \to P_3P_4$ process is

$$\begin{aligned}\mathcal{M}^{R_1,R_2} =& \sum_{jn}\sum_{\lambda_{R_{1j}},\lambda_{R_{2n}}} \delta_{\lambda_{R_{1j}},\lambda_{R_{2n}}} \mathcal{H}_{\lambda_{R_{1j}}}^{B^0\to R_{1j}R_{2n}} \mathcal{H}_{\lambda_{R_{1j}}}^{R_{1j}\to P_1P_2}\, D_{\lambda_{R_{1j}},0}^{J_{R_{1j}}}(\phi_{R_1}^{P_1},\theta_{R_1}^{P_1},0)^*\, \mathcal{A}_{1j}(m_{P_1P_2}) \\ & \times \mathcal{H}_{\lambda_{R_{2n}}}^{R_{2n}\to P_3P_4}\, D_{\lambda_{R_{2n}},0}^{J_{R_{2n}}}(\phi_{R_2}^{P_3},\theta_{R_2}^{P_3},0)^*\, \mathcal{A}_{2n}(m_{P_3P_4}) \\ =& \sum_{jn}\sum_{\lambda_{R_{1j}}} \mathcal{H}_{\lambda_{R_{1j}}}^{R_{1j},R_{2n}} e^{i\lambda_{R_{1j}}(\phi_{R_1}^{P_1}+\phi_{R_2}^{P_3})} d_{\lambda_{R_{1j}},0}^{J_{R_{1j}}}(\theta_{R_1}^{P_1}) d_{\lambda_{R_{1j}},0}^{J_{R_{2n}}}(\theta_{R_2}^{P_3}) \mathcal{A}_{1j}(m_{P_1P_2})\mathcal{A}_{2n}(m_{P_3P_4})\end{aligned} \tag{3.31}$$

where the summations are over all helicities and resonances. The $d_{\lambda_1,\lambda_2}^J(\theta)$ is the Wigner-d function and $\mathcal{H}_{\lambda_{R_{1j}}}^{R_{1j},R_{2n}}$ is defined as

$$\mathcal{H}_{\lambda_{R_{1j}}}^{R_{1j},R_{2n}} \equiv \mathcal{H}_{\lambda_{R_{1j}}}^{B^0\to R_{1j}R_{2n}} \mathcal{H}_{\lambda_{R_{1j}}}^{R_{1j}\to P_1P_2} \mathcal{H}_{\lambda_{R_{1j}}}^{R_{2n}\to P_3P_4}. \tag{3.32}$$

The helicity couplings are further related to the LS couplings defined in Eq.3.19 with LS defined in the $B^0 \to R_{1j}R_{2n}$ process. As P parity is not conserved in the $B^0 \to R_{1j}R_{2n}$ decay, there is no constraint on the orbital angular momentum L.

The $B^0 \to D^+D^-K^+\pi^-$ decay is a weak process, so the matrix element of the charged-conjugated $\overline{B}^0 \to D^-D^+K^-\pi^+$ decay is connected to that of the $B^0 \to D^+D^-K^+\pi^-$ process via the CP joint transformation assuming the approximate CP symmetry. The charge conjugation transforms all particles to their anti-particles, and thus the angles in the decay amplitude for the $\overline{B}^0$ decay are defined in terms of the kinematic variables of the corresponding anti-particles. The P operation inverses the momentum of all particles to the opposite directions without changing the spin polarization. Under this transformation, the polar angles remain unchanged, while the azimuthal angles are changed to the opposite. The helicity is also inversed. The CP-conjugated decay amplitude is

$$\begin{aligned}\overline{\mathcal{M}}^{\bar{R}_1,\bar{R}_2} =& \sum_{jn}\sum_{-\lambda_{\bar{R}_{1j}}} \overline{\mathcal{H}}_{-\lambda_{\bar{R}_{1j}}}^{\bar{R}_{1j},\bar{R}_{2n}} e^{i\lambda_{\bar{R}_{1j}}(\phi_{\bar{R}_1}^{\bar{P}_1}+\phi_{\bar{R}_2}^{\bar{P}_3})} d_{-\lambda_{\bar{R}_{1j}},0}^{J_{\bar{R}_{1j}}}(\theta_{\bar{R}_1}^{\bar{P}_1}) d_{-\lambda_{\bar{R}_{1j}},0}^{J_{\bar{R}_{2n}}}(\theta_{\bar{R}_2}^{\bar{P}_3}) \\ & \mathcal{A}_{1j}(m_{\bar{P}_1\bar{P}_2})\mathcal{A}_{2n}(m_{\bar{P}_3\bar{P}_4}).\end{aligned} \tag{3.33}$$

The approximate CP symmetry leads to $\overline{\mathcal{H}}_{-\lambda_{\bar{R}_{1j}}}^{\bar{R}_{1j},\bar{R}_{2n}} \approx \mathcal{H}_{\lambda_{R_{1j}}}^{R_{1j},R_{2n}}$. With redefining the summing index $\lambda'_{\bar{R}_{1j}} \equiv -\lambda_{\bar{R}_{1j}}$ and the azimuthal angle $\phi'_{\bar{X}} \equiv -\phi_{\bar{X}}$, the formula of $\overline{\mathcal{M}}^{\bar{R}_{1j},\bar{R}_{2n}}$ remains the same as that of $\mathcal{M}^{R_{1j},R_{2n}}$ with just the involved angles calculated using the momenta of the charge-conjugated particles. So in practice, with all the azimuthal angles reversed, the same decay amplitude as that for the B^0 process is

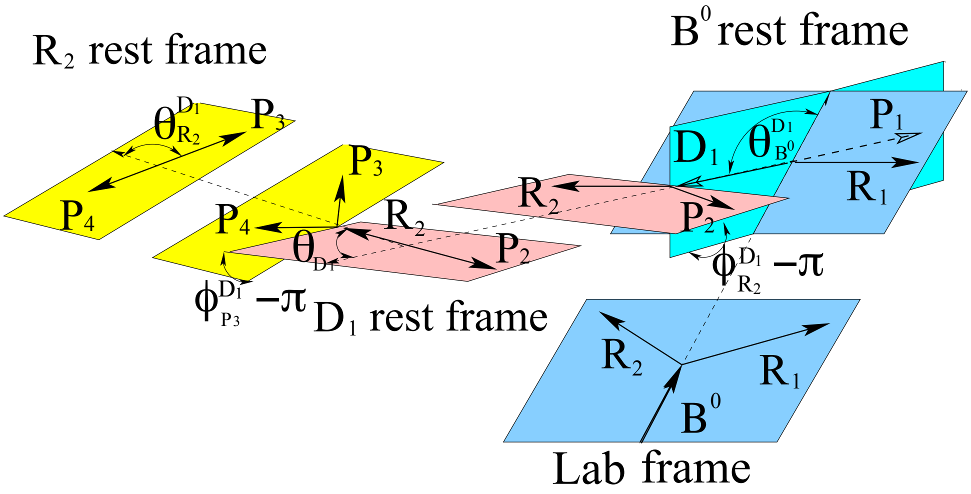

Figure 3.33 Definition of the decay angles in the $B^0 \to P_1D_{1j}, D_{1j} \to P_2R_{2n}, R_{2n} \to P_3P_4$ chain.

applicable to the $\overline{B}^0$ decay. This convention is implied throughout the analysis without distinguishing the B^0 and $\overline{B}^0$ decays.

3.6.3 Matrix element for the $B^0 \to P_1D_{1j}, D_{1j} \to P_2R_{2n}, R_{2n} \to P_3P_4$ chain

The $B^0 \to P_1D_{1j}, D_{1j} \to P_2R_{2n}, R_{2n} \to P_3P_4$ chain is shown in Fig. 3.33, with the angles defined in the amplitude construction described in this subsection.

The matrix element for the $B^0 \to P_1D_{1j}$ decay is a constant term due to $J_{B^0} = 0$,

$$\mathcal{H}^{B^0\to D_{1j}P_1}_{\lambda_{D_{1j}}}\, D^{J_{B^0}}_{\lambda_{B^0},\lambda_{R_1}}(\phi^{D_1}_{B^0}, \theta^{D_1}_{B^0}, 0)^* = \mathcal{H}^{B^0\to D_{1j}P_1}, \tag{3.34}$$

where $\lambda_{D_{1j}} = 0$, and thus there is only one complex coupling for each D_{1j}. The $\phi^{D_1}_{B^0}$ and $\theta^{D_1}_{B^0}$ are the azimuthal and polar angles of D_{1j} in the B^0 rest frame defined in Eq. 3.23,

$$\begin{aligned} \theta^{D_1}_{B^0} &= \cos^{-1}\left(\hat{z}^{\{B^0\}}_0 \cdot \hat{p}^{\{B^0\}}_{D_1}\right), \\ \phi^{D_1}_{B^0} &= \tan^{-1}\left(\frac{\hat{y}^{\{B^0\}}_0 \cdot \hat{p}^{\{B^0\}}_{D_1}}{\hat{x}^{\{B^0\}}_0 \cdot \hat{p}^{\{B^0\}}_{D_1}}\right). \end{aligned} \tag{3.35}$$

These angles do not appear in the amplitude.

The $D_{1j} \to R_{2n}P_2$ process is described in the D_1 rest frame, defined as

$$\begin{aligned}
&\hat{z}_0^{\{D_1\}} = \hat{p}_{D_1}^{\{B^0\}},\\
&\hat{x}_0^{\{D_1\}} = -\hat{a}^{\{B^0\}}_{D_1\perp\hat{z}_0^{\{B^0\}}} \quad \text{with} \quad \vec{a}^{\{B^0\}}_{D_1\perp\hat{z}_0^{\{B^0\}}} = \hat{z}_0^{\{B^0\}} - (\hat{z}_0^{\{B^0\}}\cdot\hat{z}_0^{\{D_1\}})\hat{z}_0^{\{D_1\}},\\
&\hat{y}_0^{\{D_1\}} = \hat{z}_0^{\{D_1\}}\times\hat{x}_0^{\{D_1\}}.
\end{aligned} \tag{3.36}$$

Then the matrix element is expressed as

$$\mathcal{H}^{D_{1j}\to R_{2n}P_2}_{\lambda^{D_1}_{R_{2n}}}\, D^{J_{D_{1j}}}_{0,\lambda^{D_1}_{R_{2n}}}(\phi^{R_2}_{D_1},\theta^{R_2}_{D_1},0)^*\,\mathcal{A}_j(m_{R_2P_2}), \tag{3.37}$$

with the polar and azimuthal angles, $\theta^{R_2}_{D_1}$ and $\phi^{R_2}_{D_1}$ of R_2 in the D_1 rest frame, determined as

$$\begin{aligned}
\theta^{R_2}_{D_1} &= \cos^{-1}\left(\hat{z}_0^{\{D_1\}}\cdot\hat{p}_{R_2}^{\{D_1\}}\right),\\
\phi^{R_2}_{D_1} &= \tan^{-1}\left(\frac{\hat{y}_0^{\{D_1\}}\cdot\hat{p}_{R_2}^{\{D_1\}}}{\hat{x}_0^{\{D_1\}}\cdot\hat{p}_{R_2}^{\{D_1\}}}\right).
\end{aligned} \tag{3.38}$$

The R_2 rest frame is defined as

$$\begin{aligned}
&\hat{z}_0^{\{R_2\}} = \hat{p}_{R_2}^{\{D_1\}},\\
&\hat{x}_0^{\{R_2\}} = -\hat{a}^{\{D_1\}}_{R_2\perp\hat{z}_0^{\{D_1\}}} \quad \text{with} \quad \vec{a}^{\{D_1\}}_{R_2\perp\hat{z}_0^{\{D_1\}}} = \hat{z}_0^{\{D_1\}} - (\hat{z}_0^{\{D_1\}}\cdot\hat{z}_0^{\{R_2\}})\hat{z}_0^{\{R_2\}},\\
&\hat{y}_0^{\{R_2\}} = \hat{z}_0^{\{R_2\}}\times\hat{x}_0^{\{R_2\}}.
\end{aligned} \tag{3.39}$$

The matrix element for the $R_{2n} \to P_3P_4$ process is

$$\mathcal{H}^{R_{2n}\to P_3P_4}\, D^{J_{R_{2n}}}_{\lambda^{D_1}_{R_{2n}},0}(\phi^{P_3}_{R_2},\theta^{P_3}_{R_2},0)^*\,\mathcal{A}_n(m_{P_3P_4}), \tag{3.40}$$

where $\phi^{P_3}_{R_2}$ and $\theta^{P_3}_{R_2}$ are the azimuthal and polar angles of P_3 in the R_2 rest frame. Here R_2 is from D_1, and thus the angles are different from those defined in the $B^0 \to R_{1j}R_{2n}$ decay chain.

$$\begin{aligned}
\theta^{P_3}_{R_2} &= \cos^{-1}\left(\hat{z}_0^{\{R_2\}}\cdot\hat{p}_{P_3}^{\{R_2\}}\right),\\
\phi^{P_3}_{R_2} &= \tan^{-1}\left(\frac{\hat{y}_0^{\{R_2\}}\cdot\hat{p}_{P_3}^{\{R_2\}}}{\hat{x}_0^{\{R_2\}}\cdot\hat{p}_{P_3}^{\{R_2\}}}\right).
\end{aligned} \tag{3.41}$$

With all the cascade two-body decay amplitude available in Eqs. 3.34, 3.37 and 3.40, The matrix element for the $B^0 \to P_1D_{1j}, D_{1j} \to P_2R_{2n}, R_{2n} \to P_3P_4$ chain is finally obtained as

$$\begin{aligned}\mathcal{M}^{D_1,R_2} =& \sum_{jn}\sum_{\lambda_{R_2 n}} \mathcal{H}^{B^0\to D_{1j}P_1}\mathcal{H}^{D_{1j}\to R_{2n}P_2}_{\lambda^{D_1}_{R_{2n}}}\, D^{J_{D_{1j}}}_{0,\lambda^{D_1}_{R_{2n}}}(\phi^{R_2}_{D_1},\theta^{R_2}_{D_1},0)^*\,\mathcal{A}_j(m_{R_2P_2}) \\ &\times\mathcal{H}^{R_{2n}\to P_3P_4}\, D^{J_{R_{2n}}}_{\lambda^{D_1}_{R_{2n}},0}(\phi^{P_3}_{R_2},\theta^{P_3}_{R_2},0)^*\,\mathcal{A}_n(m_{P_3P_4}) \\ =&\sum_{jn}\sum_{\lambda_{R_2 n}}\mathcal{H}^{D_{1j},P_1}_{\lambda_{R_{2n}}}e^{i\lambda_{R_2 n}\phi^{P_3}_{R_2}}d^{J_{D_{1j}}}_{0,\lambda_{R_{2n}}}(\theta^{R_2}_{D_1})d^{J_{R_{2n}}}_{\lambda_{R_{2n}},0}(\theta^{P_3}_{R_2})\mathcal{A}_j(m_{R_2P_2})\mathcal{A}_n(m_{P_3P_4}),\end{aligned} \tag{3.42}$$

where

$$\mathcal{H}^{D_{1j},P_1}_{\lambda_{R_{2n}}} \equiv \mathcal{H}^{B^0\to D_{1j}P_1}\mathcal{H}^{D_{1j}\to R_{2n}P_2}_{\lambda^{D_1}_{R_{2n}}}\mathcal{H}^{R_{2n}\to P_3P_4}, \tag{3.43}$$

which is further related to the LS couplings defined in Eq.3.19 with LS determined in the $D_{1j} \to P_2R_{2n}$ process. The LS couplings are taken as fit parameters in the amplitude analysis. As the $D_{1j} \to P_2R_{2n}$ process is the strong decay, only LS combinations conserving the P parity are taken.

3.6.4 Combining amplitudes of different decay chains

When constructing the helicity amplitude in the two above subsections, the initial and final states are all defined in their own rest frames with the spin direction parallel to their momentum in the rest frames of the originating particles. The definition of the initial B^0 state is consistent for all decay chains, but the final states are not. To combine the matrix elements for all the possible decay chains, the spins of the final states in different decay chains need to be aligned into the same direction, which are performed by rotations represented as the Wigner-D functions. The alignment is considered in the $\Lambda_b^0 \to J/\psi pK^-$ analysis[181], where the final-state muons and proton are spin-half particles. Fortunately, in the $B^0 \to D^+D^-K^+\pi^-$ decay, all the final-state particles are spinless, and the corresponding rotation is unity and there is no need to introduce alignment terms to the amplitude. and the total amplitude is directly the sum of the matrix elements of all contributing decay chains,

$$\mathcal{M}^{D_1,R_2} = \sum_{\{P_1,P_2,P_3,P_4\}}\mathcal{M}^{R_1,R_2} + \sum_{\{P_1,P_2,P_3,P_4\}}\mathcal{M}^{D_1,R_2}, \tag{3.44}$$

where $\{P_1, P_2, P_3, P_4\}$ can be any possible permutations of $\{D^+, D^-, K^+, \pi^-\}$ with the corresponding chain containing concerned intermediate resonances. For example, the decay chain to describe possible $c\bar{c}$ states associated with K^{*0} resonances is

$$B^0 \to \psi_{sj}K_n^{*0}, \psi_{sj} \to D^+D^-, K_n^{*0} \to \pi^-K^+,$$

and the decay chain to model the new D_s^+ state peaking at 2.6 GeV in the $D^+K^+\pi^-$ mass distribution is

$$B^0 \to D^- D_{sj}^+, D_{sj}^+ \to D^+ K_n^{*0}, K_n^{*0} \to \pi^- K^+.$$

3.6.5 Mass lineshapes

Mass lineshapes describe the mass-dependent parts of the decay amplitude, and they are utilized to characterize the peaking structures in the mass distributions. Unlike the angular dependent part that can be accurately described by the Wigner-D functions, the mass lineshapes do not have exact descriptions. Their formulas are usually based on some effective models. This subsection introduces the basic elements to build up the mass lineshapes.

3.6.5.1 Blatt–Weisskopf barrier factor

The first part of the mass lineshapes are the so-called Blatt–Weisskopf factor, which accounts for the difficulty of the decay products penetrating the potential barrier of the originating particle.

In the nonrelativistic limit, decaying particles are described as quasi-steady systems governed by a potential $U(r)$ in the quantum mechanics, simply approximated as

$$U(r) = \begin{cases} -U_0 & \text{for } r \leqslant d, \\ 0 & \text{for } r > d, \end{cases} \tag{3.45}$$

where d is the effective radius of the particle and U_0 is a constant potential. By solving the Schrödinger equation, the probability of the decay products penetrating the potential barrier is obtained, and it is reflected as a correction factor on the two-body decay amplitude, the so-called momentum barrier factor $p^L F_L(pd)$[182]. Here, L is the orbital angular momentum between B and C, p is the momentum of B or C in the A rest frame, and $F_L(pd)$ is the Blatt–Weisskopf barrier factor[182]. The exact formulas of $F_L(pd)$ for several low orbital angular momenta are listed below.

$$\begin{aligned}
F_0(pd) &= 1,\\
F_1(pd) &= \sqrt{\tfrac{1}{1+(pd)^2}},\\
F_2(pd) &= \sqrt{\tfrac{1}{9+3(pd)^2+(pd)^4}},\\
F_3(pd) &= \sqrt{\tfrac{1}{225+45(pd)^2+6(pd)^4+(pd)^6}},\\
F_4(pd) &= \sqrt{\tfrac{1}{11025+1575(pd)^2+135(pd)^4+10(pd)^6+(pd)^8}},\\
F_5(pd) &= \sqrt{\tfrac{1}{893025+99225(pd)^2+6300(pd)^4+315(pd)^6+15(pd)^8+(pd)^{10}}}.
\end{aligned} \tag{3.46}$$

The effective radius of a decaying particle is usually set by hand. Its value ranges $1\,\mathrm{GeV}^{-1}$ to $5\,\mathrm{GeV}^{-1}$ [163], corresponding to several femtometers. The momentum p for the two-body decay, can be expressed as a function of masses of initial- and final-state particles,

$$q_c(m_A, m_B, m_C) = \frac{\sqrt{\left[m_A^2 - (m_B + m_C)^2\right]\left[m_A^2 - (m_B - m_C)^2\right]}}{2m_A}. \tag{3.47}$$

The momentum barrier factor is introduced for each of the cascade two-body process of the $B^0 \to D^+D^-K^+\pi^-$ decay, to govern the correct threshold behavior and to reflect the difficulty of the decay proceeding via high orbital angular momenta.

3.6.5.2 Breit-Wigner function

The mass lineshape of a resonance is usually modeled by the relativistic Breit-Wigner (RBW) function[163],

$$\begin{aligned}
\mathcal{A}(m) &= \mathrm{BW}(m|m_0, \Gamma_0)\, p_{AB}^{L^{AB}}\, F_{L^{AB}}(p_{AB}d),\\
\mathrm{BW}(m|m_0, \Gamma_0) &= \frac{1}{m_0^2 - m^2 - im_0\Gamma(m)},
\end{aligned} \tag{3.48}$$

where m is the mass of the system of decay products $R \to AB$, L^{AB} is the lowest allowed orbital angular momentum between A and B, and p_{AB} is the center-of-mass momentum. $\Gamma(m)$ is the mass-dependent width, which is discussed in detail in the next paragraph. The BW mass and width, $(m_0, \Gamma_0 = \Gamma(m_0))$, are usually the parameters to characterize a resonance, and they are usually taken as the parameters that need to be determined from the amplitude analysis. For a resonance with a narrow width $\Gamma_0/m_0 \ll 1$ and far away from the mass threshold of the decay products, m_0 is approximately the peak position of the resonance in the mass spectrum, and $2\Gamma_0$ the full width at half maximum (FWHM). However, it does not hold for resonances that are too wide or too close to the production threshold. In general, the BW parameters do not have strict physical meaning. The physical quantity is the pole position of the resonance, that is, the value when the denominator of Eq. 3.48 goes to zero, $\sqrt{s_R} = m_R - i\Gamma_R/2$ with m_R (Γ_R) to be the pole mass (width), where graphically m_R is approximately the peak position in the mass spectrum and Γ_R is approximately the FWHM. To obtain the pole mass and width, one generally needs to solve a complex equation. But in a special case that $\Gamma(m)$ is just a constant Γ_0 and far smaller than m_0, the BW mass and width are approximately the pole mass and width, shown as follows.

$$m_R - i\frac{\Gamma_R}{2} = \sqrt{m_0^2 - im_0\Gamma_0} = m_0\sqrt{1 - i\frac{\Gamma_0}{m_0}} \approx m_0(1 - \frac{i}{2}\frac{\Gamma_0}{m_0}) = m_0 - i\frac{\Gamma_0}{2}. \tag{3.49}$$

In this analysis, the new D_s^+ state is close to the $D^+K^+\pi^-$ mass threshold, and thus the pole parameters are reported.

The mass-dependent width in the BW function can be generally expressed as the sum of the partial widths of all open channels,

$$\Gamma(m) = \sum_c \Gamma^c(m) \equiv \sum_c g_c^2 \rho_c'(m), \tag{3.50}$$

where in the last term g_c is the coupling factor of the decay channel c, and $\rho_c'(m)$ is proportional to the amplitude squared of the channel c, $|\mathcal{M}^c|^2$ over the N-body phase space, with N to be the number of the decay products, that is,

$$\rho_c'(m) \propto \int \mathrm{d}\Phi_N^c \, |\mathcal{M}^c|^2. \tag{3.51}$$

For a 2-body process, $M \to AB$, ρ_c' can be explicitly written as

$$\rho'_{M\to AB}(m) = \frac{q_c(m, m_A, m_B)}{m} q_c(m, m_A, m_B)^{2L_M^{AB}} F^2_{L_M^{AB}}\left(q_c(m, m_A, m_B)\, d\right), \tag{3.52}$$

where the proportional factor is absorbed in the coupling $g_{M\to AB}$. L_M^{AB} takes the lowest permitted orbital angular momentum between A and B because the higher ones are suppressed by the momentum barrier. For a 3-body process, $M \to AR$, $R \to BC$ with R being the intermediate state, ρ_c' can be expressed as

$$\begin{aligned}\rho'_{M\to ABC}(m) = \int_{m_B+m_C}^{m-m_A} \mathrm{d}m'_{BC} \cdot m'_{BC} \cdot \frac{q_c(m, m_A, m'_{BC})}{m} \frac{q_c(m'_{BC}, m_B, m_C)}{m'_{BC}} |\mathcal{A}(m'_{BC})|^2 \cdot \\ q_c(m, m_A, m'_{BC})^{2L_M^{AR}} F^2_{L_M^{AR}}(q_c(m, m_A, m'_{BC})\, d),\end{aligned} \tag{3.53}$$

where the proportional factor is absorbed in the coupling $g_{M\to ABC}$. $\mathcal{A}(m'_{BC})$ is the lineshape of the BC system, R.

The coupling g_c can be chosen as the parameter to characterize a resonance, but usually the BW width $\Gamma_0^c = \Gamma^c(m_0)$ is used, and in Eq. 3.50, g_c can be replaced by Γ_0^c,

$$\Gamma(m) = \sum_c \Gamma^c(m_0)\frac{\rho_c'(m)}{\rho_c'(m_0)}, \tag{3.54}$$

For example, the most commonly used two-body mass-dependent width is

$$\Gamma^c(m) = \Gamma^c\frac{m_0}{m}\left(\frac{q_c(m, m_A, m_B)}{q_c(m_0, m_A, m_B)}\right)^{2L_M^{AB}+1}\frac{F^2_{L_M^{AB}}\left(q_c(m, m_A, m_B)\,d\right)}{F^2_{L_M^{AB}}\left(q_c(m_0, m_A, m_B)\,d\right)}. \tag{3.55}$$

The explicit width formulas for the resonances in this analysis are discussed in Sec. 3.7.

3.6.5.3 LASS model for the $K^+\pi^-$ mass lineshape

The LASS model[183] is usually employed to describe S-wave $K^+\pi^-$ mass lineshape from the threshold to about 1.5 GeV. The amplitude includes a non-resonant term and a $K_0^*(1430)^0$ resonant contribution, that is,

$$\begin{aligned}\mathcal{A}_{\text{LASS}}(m_{K^+\pi^-}) =& \frac{m_{K^+\pi^-}}{q_{K^+\pi^-}\cot\delta_{m_{K^+\pi^-}} - iq_{K^+\pi}} + \frac{e^{2i\delta_{K^+\pi^-}}\,m_0\Gamma_0\frac{m_0}{q_0}}{\left(m_0^2 - m_{K^+\pi^-}^2\right) - im_0\Gamma_0\frac{q}{m_{K^+\pi^-}}\frac{m_0}{q_0}},\\ \cot\delta_{m_{K^+\pi^-}} =& \frac{1}{aq_{K^+\pi^-}} + \frac{bq_{K^+\pi^-}}{2},\end{aligned} \tag{3.56}$$

where $a = 1.95 \pm 0.09\,\text{GeV}^{-1}$ and $b = 1.76 \pm 0.36\,\text{GeV}^{-1}$ are the scattering length and effective range parameter to describe the non-resonant contribution, respectively. Their values are extracted from the LASS elastic scattering data[183]. The quantity $m_{K^+\pi^-}$ is the mass of $K^+\pi^-$ system and $p_{K^+\pi^-}$ is the $K^+\pi^-$ center-of-mass momentum. m_0 and Γ_0 are the BW mass and width of the $K_0^*(1430)^0$ state, and q_0 is the center-of-mass momentum at the BW mass. The LASS model is used to model the S-wave $K^+\pi^-$ contribution in the $B^0 \to D^+D^-K^+\pi^-$ decay for some cases.

3.6.6 Fit fractions and interference fractions

Fit fractions (FF) and interference fractions (IF) are useful quantities to quantifying the contributions of the involved components. The total amplitude is the sum of all the contributing components, *i.e.*, $\mathcal{M}(\vec{x} \mid \vec{\omega}) = \sum_i \mathcal{M}^i(\vec{x} \mid \vec{\omega})$, and then the fit fraction of component i is defined as

$$\mathcal{FF}^i = \frac{\int |\mathcal{M}^i(\vec{x} \mid \vec{\omega})|^2\Phi(\vec{x})d\vec{x}}{\int |\mathcal{M}(\vec{x} \mid \vec{\omega})|^2\Phi(\vec{x})d\vec{x}}, \tag{3.57}$$

and the interference fraction between components i and j is

$$\mathcal{IF}^{ij} = \frac{2\int \mathcal{R}e\left[\mathcal{M}^i(\vec{x} \mid \vec{\omega}) \cdot \mathcal{M}^{*j}(\vec{x} \mid \vec{\omega})\right] \Phi(\vec{x})d\vec{x}}{\int |\mathcal{M}(\vec{x} \mid \vec{\omega})|^2\Phi(\vec{x})d\vec{x}}. \tag{3.58}$$

The multi-dimensional integration is hard to be evaluated analytically, so the MC integration technique is employed. $B^0 \to D^+D^-K^+\pi^-$ MC events are uniformly generated in the phase space, and thus they follow the distribution of $\Phi(\vec{x})$. For a given function $f(\vec{x})$, the integration is approximated by

$$\mathcal{I}(f) = \int f(\vec{x})\Phi(\vec{x})d\vec{x} \approx \frac{1}{N}\sum_{i}^{N} f(\vec{x}_i), \tag{3.59}$$

where the summation is over all produced MC events.

3.7 Explicit amplitude model in the low $K^+\pi^-$ mass region

The resonant contributions in the low $K^+\pi^-$ mass region is discussed in Sec. 3.4.3.1. There is a large contribution from the new excited D_s^+ meson at ~ 2.6 GeV in the $D^+K^+\pi^-$ mass spectrum. The new state is hereafter denoted as D_{sJ}^+. There are also two other small resonant structures, the $J^P = 1^+$ $D_{s1}(2536)^+$ and the $J^P = 2^+$ $D_2^*(2460)^0$ states. The $D_{s1}(2536)^+$ meson exists in the $D^+K^+\pi^-$ system. Its peak is close to that of the D_{sJ}^+ resonance and the contributions of the two states could overlap with each other. So it is necessary to include the $D_{s1}(2536)^+$ contribution in the decay amplitude. The small $D_2^*(2460)^0$ peak is at the higher border of the $D^+\pi^-$ mass spectrum, and its contribution in the $D^+K^+\pi^-$ mass spectrum is also at the higher border, which is far away from the D_{sJ}^+ mass region. So in the default amplitude model, the possible $D_2^*(2460)^0$ contribution is not modeled. The contributions from potential $c\bar{c}$ states are also not described in the default model. The influence on the D_{sJ}^+ properties due to neglecting the potential contributions are evaluated as systematic uncertainties in Sec. 3.10.

Following the above discussion, only two resonant contributions need to be included in the decay amplitude, the $D_{s1}(2536)^+$ state with $J^P = 1^+$, and the D_{sJ}^+ state with J^P to be determined. To describe the direct four-body $B^0 \to D^+D^-K^+\pi^-$ decay without any intermediate resonances, a non-resonant (NR) component is also needed, whose lineshape in the $D^+K^+\pi^-$ mass spectrum is chosen as unity. The decay chain involving the two D_s^+ states and the NR component is

$$B^0 \to D^-D_{sj}^+, D_{sj}^+ \to D^+K_n^{*0}, K_n^{*0} \to \pi^-K^+,$$

which is referred to as the D_s^+ chain. In the low $K^+\pi^-$ mass region, the $K^+\pi^-$ system is expected to be in S-wave, and thus its spin-parity is 0^+. The $K^+\pi^-$ system is modeled by the broad $K_0^*(700)^0$ state[163]. The exact formula of the decay amplitude is obtained by directly specializing Eq. 3.42 with $D^-D^+K^+\pi^-$ corresponding to $P_1P_2P_4P_3$,

$$\begin{aligned}\mathcal{M} = \sum_k \mathcal{H}^{D_{sk}} d_{0,0}^{J_{D_{sk}}}(\theta_{D_s}) p^{L_{B^0}} F_{L_{B^0}}(pd) q^{L_{D_{sk}}} F_{L_{D_{sk}}}(qd) \\ \mathrm{BW}(m_{K^+\pi^-})\,\mathrm{BW}_{D_{sk}}(m_{D^+K^+\pi^-}),\end{aligned} \tag{3.60}$$

where the summation is over the three D_s^+ components. Here $\mathcal{H}^{D_{sk}}$ is the complex helicity coupling, and $d_{0,0}^{J_{D_{sk}}}(\theta_{D_s})$ is the Wigner small-d matrix with θ_{D_s} being the polar angle of the D_s^+ state in the B^0 rest frame, as defined in Eq. 3.41. The center-of-mass momenta p and q are defined as those between the decay products of the B^0 and D_{sk} mesons, respectively, and L_{B^0} ($L_{D_{sk}}$) are the orbital angular momentum between them. The Blatt–Weisskopf barrier factors $F_{L_{B^0}}(pd)$ and $F_{L_{D_{sk}}}(qd)$ are defined in Eq. 3.46. In this analysis, the effective radius d is set to $3\,\mathrm{GeV}^{-1} \sim 0.6\,\mathrm{fm}$. Alternative values are tested in Sec. 3.10 to evaluate the systematic effect on the D_{sJ}^+ properties. The mass lineshapes of the D_{sJ}^+, $D_{s1}(2536)^+$, and $K_0^*(700)^0$ states are described by the BW function, as defined in Eq. 3.48, while the NR component has a constant lineshape.

Different expressions of the mass-dependent width $\Gamma(m)$ in the BW function are used for the D_{sJ}^+, $D_{s1}(2536)^+$ and $K_0^*(700)^0$ states, based on the physical considerations of the open decay channels and the decay products.

The dominant decay channel of the $D_{s1}(2536)^+$ state is $D_{s1}(2536)^+ \to D^*K$[163] ①. The width fraction of the $D_{s1}(2536)^+ \to DK\pi$ process is only about 3%[163], due to the smaller phase space and larger orbital angular momentum compared with that of the $D_{s1}(2536)^+ \to D^*K$ decay. The $D_{s1}(2536)^+ \to D_s^+\pi(\pi)$ decay is largely suppressed by the OZI rule[94-96] and thus its width is negligible. Therefore, it is sufficient to only consider the $D_{s1}(2536)^+ \to D^*K$ process in the width description, whose explicit formula is expressed following Eq. 3.55,

$$\Gamma^{D_{s1}\to D^*K}(m_{m_{D^+K^+\pi^-}}) = \Gamma_0^{D_{s1}\to D^*K} \frac{q^{D^*K}}{q_{0D_{s1}}^{D^*K}} \frac{m_{0D_{s1}}}{m_{m_{D^+K^+\pi^-}}}. \tag{3.61}$$

where D_{s1} denotes the $D_{s1}(2536)^+$ state and $\Gamma_0^{D_{s1}\to D^*K}$ is the $D_{s1}(2536)^+$ BW width. The quantity q^{D^*K} is the center-of-mass momentum in the $D_{s1} \to D^*K$ process and $q_{0D_{s1}}^{D^*K}$

---

① For the decay without charge notations, the isospin symmetric processes are implied. Decay widths of the isospin symmetric processes are assumed the same denotes the momentum at the BW mass, $m_{0D_{s1}}$. Regarding to the fact that the $D_{s1}(2536)^+$ width is extremely narrow (0.92 ± 0.05 MeV)[163] and the fraction of the $D_{s1}(2536)^+$ state is small compared with those for the new D_s^+ state and the NR component, it is reasonable to just set the $D_{s1}(2536)^+$ width to a constant in the default model. The mass-dependent width in Eq. 3.61 is used to evaluate the systematic effect of the $D_{s1}(2536)^+$ width parameterization in Sec. 3.10.

The width formula of the D_{sJ}^+ state is dependent on its spin-parity. If its spin is not zero, the dominant decay channel of the D_{sJ}^+ state is $D_{sJ} \to D^*K$ for the same reason as that of the $D_{s1}(2536)^+$ state. If the D_{sJ}^+ state is spinless, there is no prior knowledge to judge which of the two channels, $D_{sJ} \to D^*K$ and $D_{sJ} \to DK\pi$, is dominant. The $D_{sJ} \to D^*K$ process has a larger phase space but proceeds via a larger orbital angular momentum, while the $D_{sJ} \to DK\pi$ decay proceeds via S-wave but has a smaller phase space. Anyway, in both cases the width of the D_{sJ}^+ state can be generally expressed as

$$\Gamma^{D_{sJ}}(m_{D^+K^+\pi^-}) = \Gamma^{D_{sJ}\to D^*K}(m_{D^+K^+\pi^-}) + \Gamma^{D_{sJ}\to DK\pi}(m_{D^+K^+\pi^-}), \tag{3.62}$$

where $\Gamma^{D_{sJ}\to D^*K}(m_{D^+K^+\pi^-})$ is the two-body decay width defined in Eq. 3.55, and $\Gamma^{D_{sJ}\to DK\pi}(m_{D^+K^+\pi^-})$ in principle should be the three-body width given by the integration in Eq. 3.53. However, in practice it is hard to give an adequate three-body width formula due the very limited knowledge of the resonant structures in the $D_{sJ} \to DK\pi$ process. Especially when $m_{D^+K^+\pi^-}$goes to the higher mass region, many possible D^{*0} and K^{*0} resonances could contribute. Several formulas of the partial width $\Gamma^{D_{sJ}\to DK\pi}(m_{D^+K^+\pi^-})$ are investigated in this analysis, including

a. Constant width;

b. Three-body width with the LASS $K\pi$ amplitude described in Sec. 3.6.5.3 in the integration;

c. Three-body width with a unity $K\pi$ amplitude in the integration;

d. Three-body width with the $K_0^*(700)^0$ BW amplitude in the integration.

Details can be found in Sec. 3.9 and Appendix A.3. The amplitude fits with any one of these width models can well describe the data. Finally, the constant width is taken in the default fit, and the three 3-body width formulas are used to evaluate the systematic uncertainty due to the choice of the D_{sJ}^+ width model on the D_{sJ}^+ properties. As there is no prior knowledge of the D_{sJ}^+ widths for the $D_{sJ}^+ \to D^*K$ and $D_{sJ}^+ \to DK\pi$ decays, the BW widths of the two channels, $\Gamma_0^{D_{sJ}\to D^*K}$ and $\Gamma_0^{D_{sJ}\to DK\pi}$, need to be determined in the amplitude fit. Another convenient way to define fit parameters is to take the total BW width, $\Gamma_0^{D_{sJ}}$, and the width fraction of the $D_{sJ} \to DK\pi$ channel, r, which are related to the partial widths by

$$\begin{aligned}\Gamma_0^{D_{sJ}\to DK\pi} &= r \cdot \Gamma_0^{D_{sJ}},\\ \Gamma_0^{D_{sJ}\to D^*K} &= (1-r)\cdot\Gamma_0^{D_{sJ}}.\end{aligned} \tag{3.63}$$

This convention is taken in this analysis.

For the $K_0^*(700)^0$ state, the only decay channel is the S-wave process $K_0^*(700)^0 \to K\pi$, so its width is similar to Eq. 3.61, with the involved quantities calculated in the $K\pi$ system.

$$\Gamma^{K^*\to K\pi}(m_{K\pi}) = \Gamma_0^{K^*\to K\pi}\frac{q^{K\pi}}{q_0^{K\pi}}\frac{m_0^{K^*}}{m_{K\pi}}. \tag{3.64}$$

The alternative LASS model will be tested to model the $K^+\pi^-$ mass lineshape instead of the $K_0^*(700)^0$ BW amplitude and a systematic uncertainty on the D_{sJ}^+ properties is assigned in Sec. 3.10.3.

3.8 PDF construction and fit strategy

The signal model ① to describe the $B^0 \to D^+D^-K^+\pi^-$ decay is the modulus square of the amplitude in Eq. 3.60 multiplied by a phase-space factor $\Phi(\vec{x})$ and an efficiency function $\epsilon(\vec{x})$,

$$P_{\rm sig}(\vec{x} \mid \vec{\omega}) = \frac{1}{I(\vec{\omega})}\left|\mathcal{M}(\vec{x} \mid \vec{\omega})\right|^2 \cdot \Phi(\vec{x})\epsilon(\vec{x}), \tag{3.65}$$

where $\vec{x}$ is the set of the amplitude variables, $\{m_{D^+K^+\pi^-}, m_{K^+\pi^-}, \theta_{D_s}\}$, and $\vec{\omega}$ are fit parameters, including the LS couplings representing the sizes of the amplitudes of each components and the parameters characterizing the mass lineshapes. $I(\vec{\omega})$ is the normalization factor, which is generally hard to calculate using the analytical or numerical method due to the presence of too many variables and the complicated phase-space border. The normalization factor is instead evaluated using the MC integration,

$$\begin{aligned} I(\vec{\omega}) \;&\equiv\; \int \left|M(\vec{x} \mid \vec{\omega})\right|^2 \Phi(\vec{x})\epsilon(\vec{x})\, d\vec{x} \\ &\approx\; \frac{1}{\sum\limits_j^{N_{\rm MC}} w_j^{\rm MC}} \sum_j^{N_{\rm MC}} w_j^{\rm MC}\left|\mathcal{M}(\vec{x}_j \mid \vec{\omega})\right|^2. \end{aligned} \tag{3.66}$$

---

① The widths of resonances studied in this analysis are usually ~ 100 MeV, so the detector resolution (~ 1 MeV) is neglected for most cases.

where the summation is over all MC candidates generated uniformly in the phase space and passing all the selection criteria. In this case, the generated MC events follow a distribution whose PDF is $\Phi(\vec{x})\epsilon(\vec{x})$ and the summation in Eq. 3.66 gives an unbiased estimation of the integration without the need to explicitly define the phase-space factor $\Phi(\vec{x})$ and parameterize the efficiency function $\epsilon(\vec{x})$. w_j^{MC} is the correction weight assigned to each MC candidate to improve the data/MC agreement on the detector modeling and the B^0 kinematics in the simulation. MC correction is discussed in Sec. 3.5.

The *sFit* technique[184] is employed to perform the amplitude fit, where the combinatorial background is statistically subtracted using the *sPlot* method[174], as described in Sec. 3.4.2. The estimator to be minimized is the unbinned weighted log-likelihood

$$\begin{aligned}
-\ln\mathcal{L}(\vec{\omega}) &= -\, s_W \sum_i W_i \ln P_{\mathrm{sig}}(\vec{x}_i \mid \vec{\omega}) \\
&= -\, s_W \sum_i W_i \ln|\mathcal{M}(\vec{x}_i \mid \vec{\omega})|^2 + s_W \ln I(\vec{\omega}) \sum_i W_i \\
&\quad -\, s_W \sum_i W_i \ln[\Phi(\vec{x}_i)\epsilon(\vec{x}_i)]. \qquad (3.67)
\end{aligned}$$

where the summation is over all the candidates in $B^0 \to D^+D^-K^+\pi^-$ data, with W_i to be the signal weight assigned to extract the signal component. The empirical constant factor $s_W \equiv \sum_i W_i / \sum_i W_i^2$ is introduced to account for the effect of the background subtraction on the statistical uncertainties of fit parameters. The last term in Eq. 3.67 does not depend on the fit parameters $\vec{\omega}$ and thus is dropped in the fit.

3.9 Amplitude fit results

As described in Sec. 3.7, three components in the $D^+K^+\pi^-$ system are considered in the amplitude fit: the D_{sJ}^+ state at 2.6 GeV, the $J^P = 1^+$ $D_{s1}(2536)^+$ and $J^P = 0^-$ NR components. The $K^+\pi^-$ system is modeled by the $K_0^*(700)^0$ state. The BW parameters of the known resonances are fixed to the world-average values[163], which for the $D_{s1}(2536)^+$ state are

$$m_0 = 2535.11 \pm 0.06\,\mathrm{MeV} \quad \text{and} \quad \Gamma_0 = 0.92 \pm 0.05\,\mathrm{MeV},$$

and for the $K_0^*(700)^0$ state are

$$m_0 = 824 \pm 30\,\mathrm{MeV} \quad \text{and} \quad \Gamma_0 = 478 \pm 50\,\mathrm{MeV}.$$

Table 3.8 Determined values of r and $\sqrt{-2\Delta\ln\mathcal{L}}$ for different J^P models in the amplitude fit. For $\sqrt{-2\Delta\ln\mathcal{L}}$, the value from the best one, $J^P = 0^-$, is taken as the reference. Null denotes the model without the new D_s^+ state included in the fit. NDOF denotes the number of the free fit parameters.

J^P	r	$\sqrt{-2\Delta\ln\mathcal{L}}$	NDOF
0^-	1.00 ± 0.98	0	7
1^+	0.77 ± 0.75	15	7
2^-	0.00 ± 0.93	17	7
Null	-	23	2

The BW mass and width of the new D_{sJ}^+ state, as well as the width fraction defined in Eq. 3.63, are free parameters that will be determined from the amplitude fit. Other fit parameters include the LS couplings for the D_{sJ}^+ and $D_{s1}(2536)^+$ states. The coupling for the NR component is fixed to unity as the reference. Three spin-parity models are tested for the D_{sJ}^+ state: 0^-, 1^+ and 2^-, and a fit without the D_{sJ}^+ state is also tested to evaluate the significance of the existence of the D_{sJ}^+ state.

3.9.1 Spin-parity, mass and width of the D_{sJ}^+ state

In the amplitude fit, the statistical uncertainty of the width fraction r is found extremely large for all the J^P assignments of the D_{sJ}^+ state, as listed in Table 3.8. To further investigate the $-2\ln\mathcal{L}$ dependence on the width fraction r, the $-2\ln\mathcal{L}$ value is scanned in the r range of $[0, 1]$, as shown in Fig. 3.34. It is seen that the variation of $-2\ln\mathcal{L}$ is no more than 1 for different values of r, corresponding to a discrimination power with significance of less than one standard deviation (σ), which indicates that the width fraction r cannot be determined from the current data. For any r assignments, the $J^P = 0^-$ model leads to best fit, so the spin-parity of the D_{sJ}^+ state is determined to be 0^-. There is a graphical illustration for the reason why the $J^P = 0^-$ model leads to the best fit. In the amplitude, the $\cos\theta_{D_s}$ behavior of the D_{sJ}^+ state is governed by the Wigner small-d matrix $d^J_{0,0}(\theta_{D_s})$, which is proportional to the J-th order Legendre polynomial and is squared in the signal model. Thus, the $\cos\theta_{D_s}$ distribution is described by a constant function for $J^P = 0^-$, a second-order polynomial for $J^P = 1^+$ and a forth-order polynomial for $J^P = 2^-$. The $J^P = 0^-$ model is clearly seen to be most consistent with data, as shown in Fig. 3.35

The significance to reject the disfavored spin-parity models of the D_{sJ}^+ state, and the model without the D_{sJ}^+ state, is evaluated based on the property of the delta log-likelihood

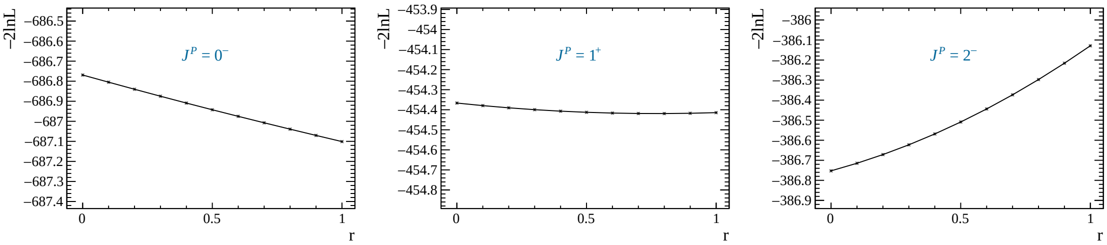

Figure 3.34 $-2\ln\mathcal{L}$ in the r range $[0,1]$ for different spin-parity hypotheses. The variation of $-2\ln\mathcal{L}$ is no more than one for all the J^P hypotheses, indicating that r can not be determined from the current data sample.

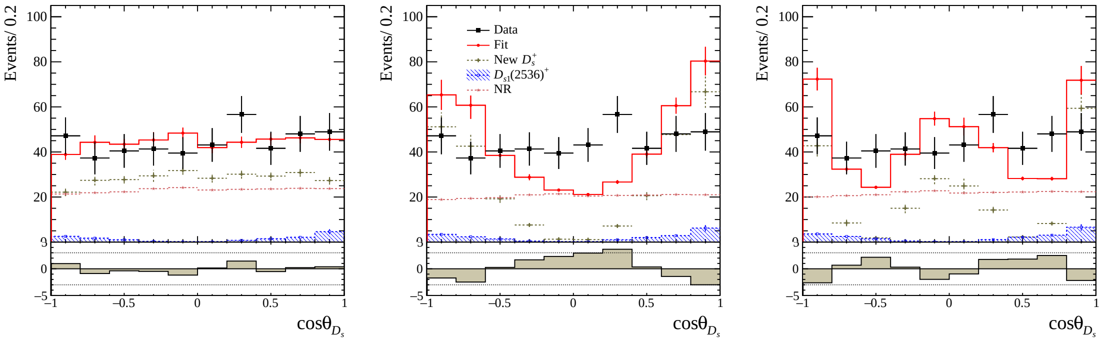

Figure 3.35 Comparison of $\cos\theta_{D_s^+}$ distributions with the spin-parity of the D_{sJ}^+ state assumed to be 0^-(left), 1^+(middle), and 2^-(right). The $J^P = 0^-$ model is more consistent with data. Constant width is taken for $\Gamma(D_{sJ}^+ \to DK\pi)$ with r free in the amplitude fits.

between two fit models, $-2\Delta\ln\mathcal{L}$, which empirically follows the χ^2 distribution with the number of degrees of freedom to be unity for the two models having as many free parameters, and two times of the difference of the free parameters for the models that have different number of free parameters[181,185]. Finally, with the values of $\sqrt{-2\Delta\ln\mathcal{L}}$ listed in Table 3.8 as the inputs, the $J^P = 1^+$ and $J^P = 2^-$ models of the D_{sJ}^+ state are rejected over 15σ, and the significance of the existence of the D_{sJ}^+ state is evaluated to be 22σ.

As the width fraction r cannot be determined in the amplitude fit, the BW parameters of the D_{sJ}^+ state are scanned in the r range $[0,1]$ to investigate the effect of the choice of r on the BW parameters, as shown in Fig. 3.36. Variations of a level of ~ 25 MeV are found in the central values of m_0 and Γ_0 when r varies, indicating the BW mass and width are not suitable parameters to characterizing the resonance. However, it is noticed that the BW mass lineshapes for different values of r are almost the same, as shown in Fig. 3.37, where the discrepancies in the phase of the BW amplitude is expected to be largely compensated by a constant shift of the phase of the helicity coupling. Almost the same peak position and FWHM of the BW mass lineshapes indicate that different values of r result in an

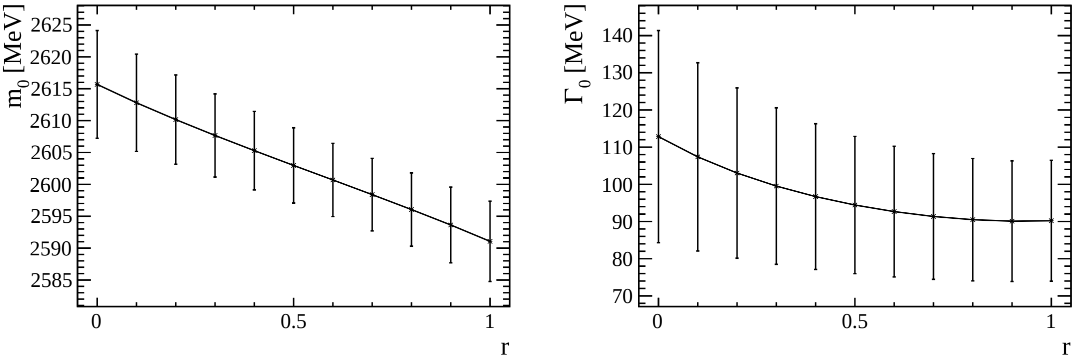

Figure 3.36 Determined BW mass m_0 and width Γ_0 of the new D_s^+ state in the r range [0, 1] in the amplitude fit for the $J^P = 0^-$ model. The statistical uncertainties from the fit are also shown. Large variation is seen for different r values.

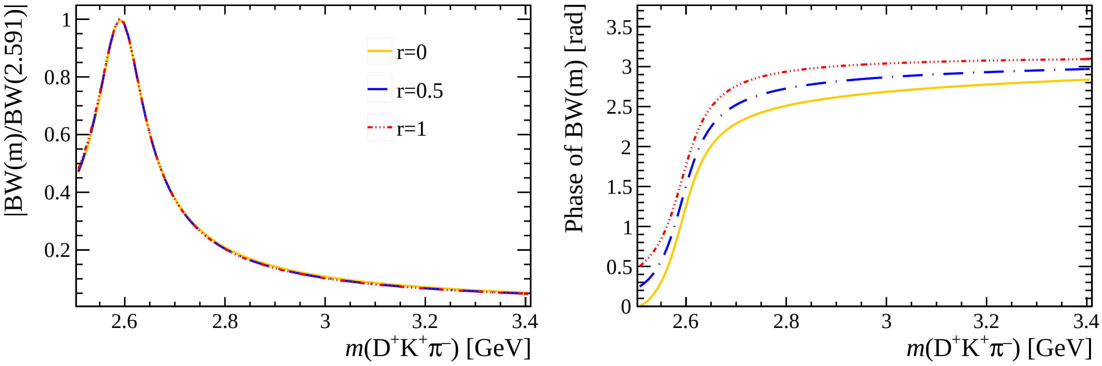

Figure 3.37 Modulus (left) and phase (right) of the BW shape of the new D_s^+ state for three different r assignments with the parameters set to the determined values in the amplitude fits. The modulus of the amplitudes almost coincide for different r assignments, but there is discrepancy on the phase, which is expected to be compensated by a constant phase in the helicity coupling.

identical pole position, regarding to the fact that the peak position is approximately the pole mass m_R and FWHM approximately twice the pole width Γ_R. To verify that, The pole mass and width as functions of r are shown in Fig. 3.38, where their values are derived based on the BW parameters in Fig. 3.36. It is seen that the pole mass and width are quite stable when r varies. As the pole parameters instead of the BW mass and width are the physical quantities to characterize a resonance and are independent of parameterizations of the lineshape, only the pole mass and width are reported in this analysis. The width fraction cannot be determined from the current data, so its value is instead fixed to 0.5 in the default result. The corresponding BW parameters determined from the amplitude fit and the derived parameters are listed in Table. 3.9. Different values of r are tested in Sec. 3.10.1 to evaluate the systematic effect on the measured quantities. Since the pole mass is about 2590 MeV and the spin-parity is 0^-, the D_{sJ}^+ state is hereafter denoted as $D_{s0}(2590)^+$.

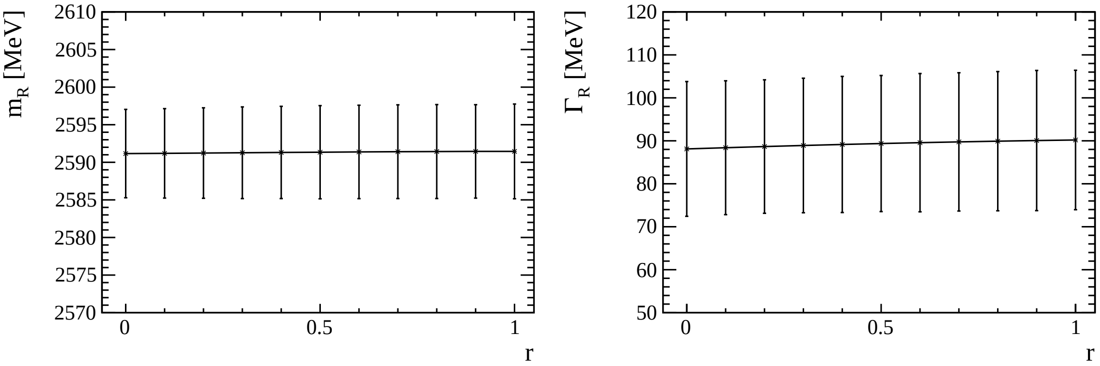

Figure 3.38 Pole mass m_R (left) and the pole width Γ_R (right) of the D_{sJ}^+ state in the r range [0, 1] for the $J^P = 0^-$ model with the BW parameters in Fig. 3.36 as the inputs. The pole parameters are stable when r varies.

Table 3.9 Measured properties of the new D_s^+ state in the default amplitude fit result with the width fraction $r = 0.5$. The uncertainties are statistic only.

Quantity	Value
J^P	0^-
m_0	2602.97 ± 5.90 MeV
Γ_0	94.44 ± 18.45 MeV
m_R	2591.34 ± 6.18 MeV
Γ_R	89.37 ± 15.84 MeV

Fit projections of several amplitude variables for the $J^P = 0^-$ model are shown in Fig. 3.39 ①. Besides the amplitude variables used in the fit, some other variables are also presented. It is seen that the fit well describes the data for all variables. The flat distribution of the polar angle $\cos\theta_{K^*}$ in data for the $K^{*0} \to K^+\pi^-$ decay supports the S-wave assumption of the $K^+\pi^-$ system. There is no evident sign of $c\bar{c}$ resonant contribution as shown in the D^+D^- mass spectrum, but several $c\bar{c}$ states are still tested in Sec. 3.10.5 to investigate the systematic influence on the measured quantities. There is a small excess at about 2.5 GeV in the $D^+\pi^-$ mass projection, and regarding to that a systematic uncertainty on the measured quantities are introduced by excluding the excess, which is discussed in Sec. 3.10.6. There is no evident resonant contribution seen in the $D^+D^-\pi^-$, D^-K^+ or $D^-K^+\pi^-$ mass distributions.

---

① Fit results for the spin-parity models with other spin-parity assignments and without the $D_{s0}(2590)^+$ contribution are shown in Appendix A.1.

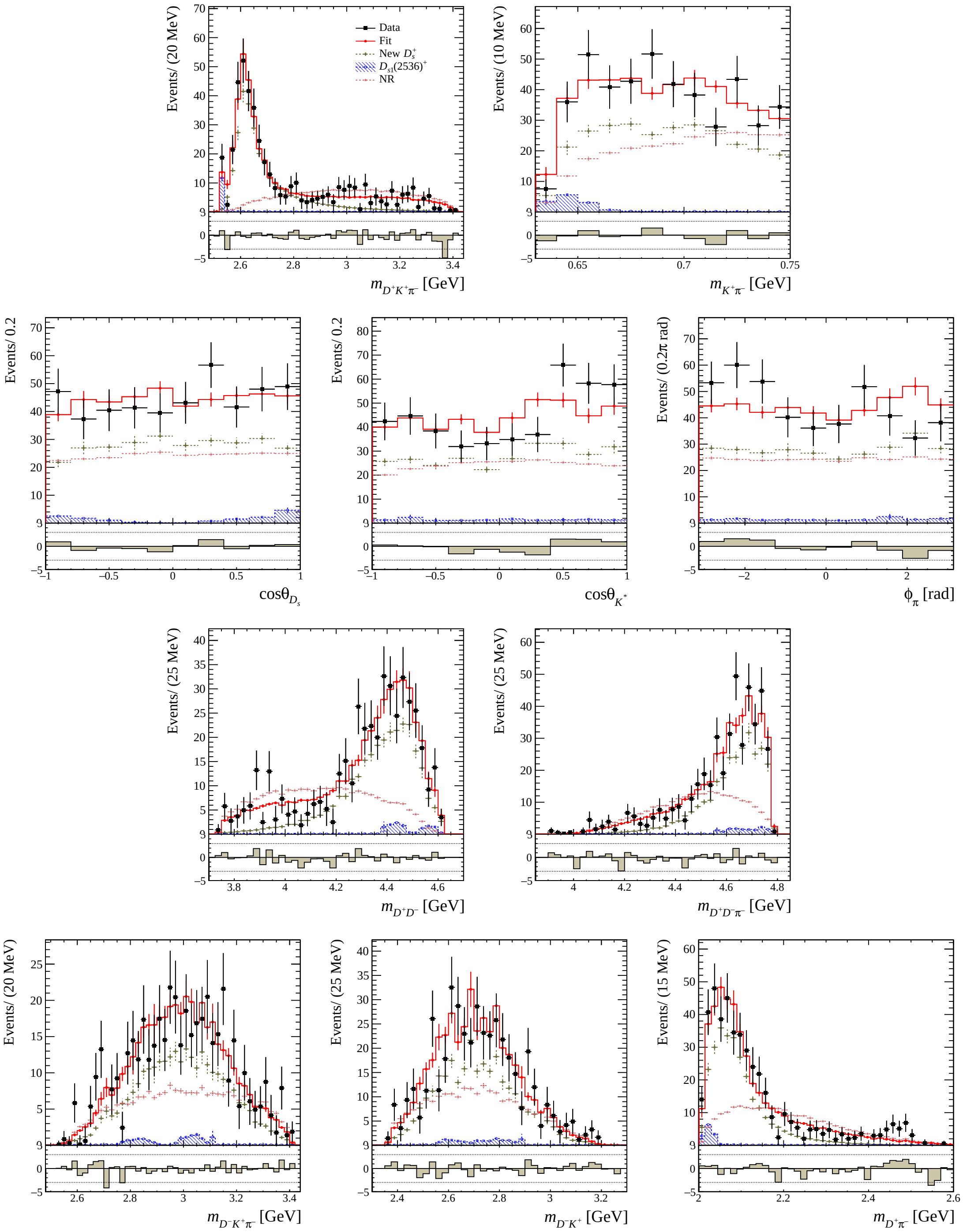

Figure 3.39 Fit projections for the $J^P = 0^-$ model. A constant width is taken for $D_{s0}(2590)^+ \to DK\pi$ channel with $r = 0.5$.

Table 3.10 Fit fractions and interference fractions obtained from the default amplitude fit model with $r = 0.5$. The uncertainties are statistical only. $D_{s0}(2590)^+$-NR denotes the interference fraction between the $D_{s0}(2590)^+$ and NR components. $D_{s1}(2536)^+/D_{s0}(2590)^+$ denotes the fit fraction ratio between the $D_{s1}(2536)^+$ and $D_{s0}(2590)^+$ states.

State	fraction($\times 10^{-2}$)
$D_{s0}(2590)^+$	63.4 ± 8.9
$D_{s1}(2536)^+$	3.9 ± 1.4
NR	50.7 ± 10.9
$D_{s0}(2590)^+$-NR	-18.0 ± 17.6
$D_{s1}(2536)^+/D_{s0}(2590)^+$	6.1 ± 2.4

3.9.2 Fit fractions and interference fractions

Fit fractions of the three D_s^+ components are their interference fractions are determined following the definitions in Sec. 3.6.6 with the fit parameters determined by the amplitude fit. The MC sample used for the phase-space integration is produced using `TGenPhaseSpace` implanted in Root, with the $m(K^+\pi^-) < 0.75\,\text{GeV}$ requirement imposed. The fractions are listed in Table 3.10. There is no $D_{s1}(2536)^+$–$D_{s0}(2590)^+$ or $D_{s1}(2536)^+$–NR interference because they have different spin-parity. The negative interference between the $D_{s0}(2590)^+$ and NR components accounts for the larger contribution of the NR component than the total in some regions of the phase space, as shown in Fig. 3.39. The statistical uncertainties are propagated from the fit parameters to the fractions using the toy MC method. The fit parameters are assumed to follow a multi-dimensional Gaussian distribution with their means and covariance matrix set to those determined in the amplitude fit. Five thousands of toy sets of fit parameters are generated and for each set the fractions are calculated. Finally there are five thousands of sets of fractions are obtained, and the standard deviations are taken as the uncertainties of the fractions of the contributing components.

3.10 Systematic uncertainties

The quantities that are reported in this analysis are the pole parameters of the $D_{s0}(2590)^+$ state, and the fit and interference fractions of the contributing components in the amplitude fit. The systematic effects on the measured quantities are evaluated for the sources listed in Table 3.11. The BW parameters obtained from the alternative amplitude fits are not shown in this section, and they are instead attached in Appendix A.2.

Table 3.11 Systematic sources.

Systematic sources
$D_{s0}(2590)^+$ width model
$D_{s1}(2536)^+$ mass shape
$K^+\pi^-$ mass shape
Blatt–Weisskopf d parameter
Including $c\bar{c}$ resonances
$D^+\pi^-$ resonance veto
MC correction
Momentum calibration

3.10.1 $D_{s0}(2590)^+$ width model

As described in Sec. 3.7, the partial width of $D_{s0}(2590)^+ \to DK\pi$ three-body decay is set to constant and its width fraction r is set to 0.5 in the default amplitude fit. Alternative configurations are tested to evaluate the systematic effect of the $D_{s0}(2590)^+$ width model.

Firstly, the three-body widths with different $K\pi$ amplitudes mentioned in Sec. 3.7 instead of the constant width are tested for the $D_{s0}(2590)^+ \to DK\pi$ partial width in the amplitude fits. The detailed investigation of the three-body width is described in Appendix A.3. Secondly, two alternative values of r are tested: $r = 0$ and 1. Here, the original constant $D_{s0}(2590)^+ \to DK\pi$ width is used. The largest differences on the measured quantities in the above alternative amplitude models from the default fit results are taken as the uncertainties, which are listed in Table 3.12. Large systematic uncertainties are seen in the fractions of the contributing components. This is understood as due to the faster decrease of the BW mass lineshapes with the increase of the $D^+K^+\pi^-$ mass for the models using the three-body widths. The detailed discussion is presented in Appendix A.3.

3.10.2 $D_{s1}(2536)^+$ mass shape

As mentioned in Sec. 3.7, a constant width is taken in the BW amplitude of the $D_{s1}(2536)^+$ state and the BW parameters are fixed to the known values[163]. Alternative choices are tested to investigate the systematic effect on the measured quantities. A test fit is performed with the $D_{s1}(2536)^+$ BW mass and width free. The resulting BW parameters of the $D_{s1}(2536)^+$ state are $m_0 = 2535.91 \pm 0.35\,\text{MeV}$, $\Gamma_0 = 0.95 \pm 0.40\,\text{MeV}$, which are consistent with the known values. The two-body width in Eq. 3.61 instead of constant

Table 3.12 Systematic uncertainties due to the $D_{s0}(2590)^+$ width model.

Quantity	LASS	Unity	$K_0^*(700)^0$ BW	$r=0$	$r=1$
m_R (MeV)	-1.28	1.26	**-6.11**	-0.18	0.11
Γ_R (MeV)	**7.97**	7.60	3.01	-1.26	0.83
$D_{s0}(2590)^+$ fraction (%)	**-4.66**	-3.45	2.64	0.11	1.13
$D_{s1}(2536)^+$ fraction (%)	0.01	**0.01**	0.01	0.00	0.00
NR fraction (%)	**-14.99**	-13.95	-1.06	3.37	-2.49
$D_{s0}(2590)^+$-NR interference (%)	**19.64**	17.39	-1.59	-3.49	1.36
$D_{s1}(2536)^+/D_{s0}(2590)^+$ ratio ($\times 10^{-2}$)	**0.50**	0.37	-0.24	-0.01	-0.11
$-2\Delta\ln\mathcal{L}$	-1.19	-1.06	-0.82	0.17	-0.16

Table 3.13 Systematic uncertainties due to $D_{s1}(2536)^+$ mass shape.

Quantity	Mass&width	Width model	Resolution
m_R (MeV)	0.24	0.24	**-0.32**
Γ_R (MeV)	**-4.30**	**-4.30**	-0.42
$D_{s0}(2590)^+$ fraction (%)	**-2.27**	0.01	-0.17
$D_{s1}(2536)^+$ fraction (%)	**0.55**	0.00	0.23
NR fraction (%)	**-3.48**	0.01	-0.59
$D_{s0}(2590)^+$-NR interference (%)	**5.25**	-0.02	0.55
$D_{s1}(2536)^+/D_{s0}(2590)^+$ ratio ($\times 10^{-2}$)	**1.12**	0.00	0.37
$-2\Delta\ln\mathcal{L}$	-8.24	0.06	-6.21

is also tested with fixed BW parameters for the $D_{s1}(2536)^+$ state. As the $D_{s1}(2536)^+$ width is very narrow, the detector resolution could have a non-negligible effect, which is taken into account in the amplitude fit. The mass resolution is found to be 1.1 MeV by investigating the distribution of the difference of the reconstructed and true $D^+K^+\pi^-$ masses in the $B^0 \to D_{s1}(2536)^+D^-$ MC sample, which is then convolved with the $D_{s1}(2536)^+$ amplitude in the amplitude fit. The differences of the measured quantities from the three above sources are listed in Table 3.13, and the largest differences from the default fit result are taken as the systematic uncertainties.

3.10.3 $K^+\pi^-$ mass shape

The $K^+\pi^-$ mass lineshape is modeled by the $K_0^*(700)^0$ BW amplitude with the BW parameters fixed to the known values[163] in the default result, as described in Sec. 3.7.

Table 3.14 Systematic uncertainties due to $K^+\pi^-$ mass shape.

Quantity	Mass&width	LASS model
m_R (MeV)	0.23	**-2.69**
Γ_R (MeV)	0.87	**-2.64**
$D_{s0}(2590)^+$ fraction (%)	-0.21	**2.99**
$D_{s1}(2536)^+$ fraction (%)	0.02	**0.20**
NR fraction (%)	0.06	**1.24**
$D_{s0}(2590)^+$-NR interference (%)	0.13	**-4.44**
$D_{s1}(2536)^+/D_{s0}(2590)^+$ ratio ($\times 10^{-2}$)	**0.05**	0.02
$-2\Delta\ln\mathcal{L}$	-0.20	6.31

The systematic effect on the choice of the $K^+\pi^-$ mass lineshape is evaluated as follows. At first, a test amplitude fit with the $K_0^*(700)^0$ BW parameters free is performed. The $K_0^*(700)^0$ BW mass and width are determined as $m_0 = 764 \pm 145\,\text{MeV}$, $\Gamma_0 = 314 \pm 305\,\text{MeV}$, which are consistent with the known values[163]. Secondly, the LASS model described in Sec. 3.6.5.3 is used to model the $K^+\pi^-$ mass lineshape in the amplitude fit. The determined quantities in the above two fits are compared with those in the default result and the differences are shown in Table 3.14, where the largest ones are taken as the systematic uncertainties.

3.10.4 Blatt–Weisskopf d parameter

The Blatt–Weisskopf d parameter in the default fit is fixed to $3.0\,\text{GeV}^{-1}$. Alternative values of $d = 1.5\,\text{GeV}^{-1}$ and $d = 4.5\,\text{GeV}^{-1}$ are tested in the amplitude fit, and the differences of the fit results from the default values are listed in Table 3.15, where the largest differences from the default values are taken as the systematic uncertainties.

3.10.5 Inclusion of $c\bar{c}$ resonances

There is no evident signature of any $c\bar{c}$ contribution as shown in Fig. 3.39. However, the statistical fluctuation in the low D^+D^- mass region is large and there could be the potential $c\bar{c}$ structures. Therefore, test fits with $c\bar{c}$ contributions are performed to investigate the systematic influence on the measured quantities. The $c\bar{c}$ state is modeled in the $B^0 \to \psi_{sj}K_n^{*0}, \psi_{sj} \to D^+D^-, K_n^{*0} \to \pi^-K^+$ chain, with the amplitude constructed following the description in Sec. 3.6.2.

Two candidate $c\bar{c}$ resonances are investigated: $\psi(3770)$ and $\chi_{c2}(2P)$. The systematic

Table 3.15 Systematic uncertainties due to the choice of the Blatt–Weisskopf d parameter.

Quantity	$d = 1.5\,\mathrm{GeV}^{-1}$	$d = 4.5\,\mathrm{GeV}^{-1}$
m_R (MeV)	**0.69**	-0.14
Γ_R (MeV)	**3.38**	-0.70
$D_{s0}(2590)^+$ fraction (%)	**2.81**	-0.89
$D_{s1}(2536)^+$ fraction (%)	**0.34**	-0.16
NR fraction (%)	-0.11	**-1.27**
$D_{s0}(2590)^+$-NR interference (%)	**-3.04**	2.32
$D_{s1}(2536)^+/D_{s0}(2590)^+$ ratio ($\times 10^{-2}$)	**0.25**	-0.17
$-2\Delta \ln \mathcal{L}$	-0.46	-0.21

Table 3.16 Fit and interference fractions of $c\bar{c}$ resonances.

Quantity	$\psi(3770)$	$\chi_{c2}(2P)$
$c\bar{c}$ fraction (%)	0.97	0.34
$D_{s0}(2590)^+$-$c\bar{c}$ interference (%)	0.04	-0.18
$D_{s1}(2536)^+$-$c\bar{c}$ interference (%)	0.15	0.03
NR-$c\bar{c}$ interference (%)	0.00	0.01

effect is evaluated by adding one of them each time in the amplitude. The fit fractions and the interference fractions of the two $c\bar{c}$ states are listed in Table 3.16. Their fractions are very small compared with those for the $D_{s0}(2590)^+$ state. The measured quantities from the fits with the two $c\bar{c}$ states involved are compared with the default values, and the differences are shown in Table 3.17, where the largest differences are taken as the systematic uncertainties.

3.10.6 $D^+\pi^-$ resonances veto

The small excess at about 2.45 GeV in the $D^+\pi^-$ mass spectrum is not described in the default fit. As the excess is near the higher border of the $D^+\pi^-$ mass, it does not overlap with the $D_{s0}(2590)^+$ contribution, and thus can be excluded by requiring $m(D^+\pi^-) < 2.4\,\mathrm{GeV}$. This requirement results in the loss of about 10% B^0 signal candidates in the $B^0 \to D^+D^-K^+\pi^-$ data sample and 8% in the MC sample. The signal extraction is then carried out on the reduced data sample by the B^0 mass fit and the *sPlot* method, and the amplitude fit is performed. The resulting systematic uncertainties on the measured quantities are listed in Table 3.18.

Table 3.17 Systematic uncertainties due to the inclusion of $c\bar{c}$ resonances.

Quantity	$\psi(3770)$	$\chi_{c2}(2P)$
m_R (MeV)	**1.05**	-0.14
Γ_R (MeV)	**5.41**	-1.37
$D_{s0}(2590)^+$ fraction (%)	**2.67**	-0.62
$D_{s1}(2536)^+$ fraction (%)	**-0.11**	-0.01
NR fraction (%)	**6.30**	-2.37
$D_{s0}(2590)^+$-NR interference (%)	**-10.02**	2.80
$D_{s1}(2536)^+/D_{s0}(2590)^+$ ratio ($\times 10^{-2}$)	**-0.42**	0.05
$-2\Delta\ln\mathcal{L}$	-9.21	-3.74

Table 3.18 Systematic uncertainties due to $D^+\pi^-$ resonances veto.

Quantity	$D^+\pi^-$ resonances veto
m_R (MeV)	-2.40
Γ_R (MeV)	-2.05
$D_{s0}(2590)^+$ fraction (%)	4.57
$D_{s1}(2536)^+$ fraction (%)	0.31
NR fraction (%)	-9.43
$D_{s0}(2590)^+$-NR interference (%)	4.55
$D_{s1}(2536)^+/D_{s0}(2590)^+$ ratio ($\times 10^{-2}$)	0.17
$-2\Delta\ln\mathcal{L}$	-

Table 3.19 Systematic uncertainties due to weights binning schemes. The total uncertainty is taken as the square root of the quadratic sum of the three contributions.

Quantity	L0Hadron_TOS		B^0 kinematic		nTracks		Total
	5 bins	15 bins	3 bins	10 bins	6 bins	18 bins	
m_R (MeV)	**-0.21**	-0.20	**0.09**	0.07	-0.05	**-0.06**	0.24
Γ_R (MeV)	0.16	**1.00**	0.01	**0.04**	**-0.40**	-0.03	1.08
$D_{s0}(2590)^+$ fraction (%)	**0.13**	0.03	**0.06**	-0.04	**-0.23**	-0.21	0.27
$D_{s1}(2536)^+$ fraction (%)	**0.05**	-0.02	-0.01	**0.01**	**0.13**	0.03	0.14
NR fraction (%)	-0.25	**0.50**	**0.05**	-0.03	**-0.44**	-0.13	0.67
$D_{s0}(2590)^+$-NR interference (%)	0.06	**-0.52**	**-0.10**	0.06	**0.54**	0.31	0.76
$D_{s1}(2536)^+/D_{s0}(2590)^+$ ratio ($\times 10^{-2}$)	**0.07**	-0.03	-0.02	**0.02**	**0.22**	0.07	0.23
$-2\Delta \ln \mathcal{L}$	-1.53	2.65	-0.44	0.09	-0.99	0.94	-

3.10.7 MC correction

The $B^0 \to D^+D^-K^+\pi^-$ and $B^0 \to D_{s1}(2536)^+D^-$ MC samples used to calculate the normalization integration in the amplitude fit is corrected using the weights obtained from the data/MC comparisons of the related distributions in the control channel $B^0 \to D_s^+D^-$. The details of the MC correction is discussed in Sec. 3.5. Systematic uncertainties related to the correction are from two sources: the binning schemes of the histograms to parameterize the weights, and the limited statistics of the $B^0 \to D_s^+D^-$ data and MC samples.

Binning schemes of the weight histograms

There are three correction weights, and the effects of choices of the binning schemes of the corresponding weights histograms are evaluated separately. The alternative binning schemes used in the systematic study are shown in Appendix A.4. New weights are obtained from the related histograms under the alternative binning schemes and are applied to the $B^0 \to D^+D^-K^+\pi^-$ and $B^0 \to D_{s1}(2536)^+D^-$ MC samples that are used to calculate the normalization integral in the amplitude fit. The resulted differences of the measured quantities from the default values are listed in Table 3.19. The systematic uncertainties due to the choice of bins for each weight histogram are taken as the larger values in the two binning schemes, and the total uncertainties to account for the three kinds of weight histograms are the square root of the quadratic sum of the individual uncertainties for each weight.

Table 3.20 Systematic uncertainties due to limited statistics in control channel.

Quantity	MC statistics
m_R (MeV)	0.20
Γ_R (MeV)	0.56
$D_{s0}(2590)^+$ fraction (%)	0.14
$D_{s1}(2536)^+$ fraction (%)	0.02
NR fraction (%)	0.30
$D_{s0}(2590)^+$-NR interference (%)	0.41
$D_{s1}(2536)^+/D_{s0}(2590)^+$ ratio ($\times 10^{-2}$)	0.03
$-2\Delta \ln \mathcal{L}$	-

Limited statistics of the $B^0 \to D_s^+ D^-$ data and MC samples

Due to the limited statistics of the $B^0 \to D_s^+ D^-$ data and MC samples, the correction weights have associated uncertainties, which are calculated under the assumptions that the L0Hadron_TOS efficiency is binomially fluctuated and the numbers of data and MC candidates follow the Possion distribution. Uncertainties of the weights are propagated to the measured quantities using the toy MC method. 100 toy MC samples for the $B^0 \to D^+ D^- K^+ \pi^-$ and $B^0 \to D_{s1}(2536)^+ D^-$ decays are produced with the weights randomly fluctuated according to a Gaussian distribution with the mean and width set to be central value and the uncertainty of the weight. Amplitude fits are then performed using the generated toy MC samples as the inputs, and the standard deviations of the distributions of the measured quantities for the 100 fits are taken as the systematic uncertainties, listed in Table 3.20.

3.10.8 Momentum calibration

The measured track momenta are calibrated to correct for potential biases due to the non-perfect alignment of the tracking system, the imprecise material map, and the uncertainty on magnetic field. The calibration information is based on the large samples of the detached J/ψ candidates in the $J/\psi \to \mu^+\mu^-$ and $B^+ \to J/\psi K^+$ decays[165]. The momentum correction factor η is determined by scaling the track momenta by $1 - \eta$ so that the measured J/ψ and B^+ masses are consistent with their world averages[163]. The uncertainty of η is $\pm 3 \times 10^{-4}$, which could have effect on the measured quantities. The influence is studied by shifting the momentum scale factor η by 1σ, $\delta\eta = \pm 3 \times 10^{-4}$ for the

Table 3.21 Systematic uncertainties due to momentum calibration.

Quantity	$\delta\eta = -3 \times 10^{-4}$	$\delta\eta = 3 \times 10^{-4}$
m_R (MeV)	**-0.48**	-0.12
Γ_R (MeV)	**-0.39**	0.32
$D_{s0}(2590)^+$ fraction (%)	**-1.25**	-0.03
$D_{s1}(2536)^+$ fraction (%)	0.04	**0.04**
NR fraction (%)	-1.27	**-1.42**
$D_{s0}(2590)^+$-NR interference (%)	**2.48**	1.41
$D_{s1}(2536)^+/D_{s0}(2590)^+$ ratio ($\times 10^{-2}$)	**0.18**	0.07
$-2\Delta \ln \mathcal{L}$	6.34	1.43

$B^0 \to D^+D^-K^+\pi^-$ data. Then the full offline procedures including the selection, signal extraction and amplitude fit are re-performed. The differences of the measured quantities from the default values are listed in Table 3.21, and the largest differences are taken as the systematic uncertainties.

3.10.9 Total systematic uncertainties

The systematic uncertainties for all the sources are listed in Table 3.22. They are added in quadrature to obtain the total uncertainties. The dominant uncertainty is from the choice of the $D_{s0}(2590)^+$ width model.

3.11 Conclusions and implications

The $B^0 \to D^+D^-K^+\pi^-$ four-body decay is studied for the first time using the proton-proton collision data collected by the LHCb experiment during the 2016-2018 period. There is no signature of the $X_{0,1}(2900)$ states in the D^-K^+ system that were found in the $B^+ \to D^+D^-K^+$ decay[13-14]. The $\psi(3770)$ and $\chi_{c0,2}(3930)$ contributions could exist but are not evident. Two new peaking structures are observed in the $D^+K^+\pi^-$ system, corresponding to candidates of undiscovered D_s^+ states. An amplitude analysis is performed on the $B^0 \to D^+D^-K^+\pi^-$ candidates in the low $K^+\pi^-$ mass region with $m(K^+\pi^-) < 0.75$ GeV to study the properties of the low-lying D_s^+ state. The significance of this state is found extremely large. The pole mass and width, and the spin parity of it are measured to be

$$m_R = 2591 \pm 6 \pm 7\,\text{MeV}, \quad \Gamma_R = 89 \pm 16 \pm 12\,\text{MeV}, \quad J^P = 0^-,$$

Table 3.22 Systematic uncertainties on the measured quantities in the amplitude fit. The uncertainties of individual sources are added in quadrature to obtain the total uncertainties. The $D_{s0}(2590)^+$ and $D_{s1}(2536)^+$ states are denoted as D_{s0}^+ and D_{s1}^+, respectively.

Source	m_R	Γ_R	Fit fraction ($\times 10^{-2}$)				
	[MeV]	[MeV]	D_{s0}^+	D_{s1}^+	NR	D_{s0}^+–NR	D_{s1}^+/D_{s0}^+
$D_{s0}(2590)^+$ width model	**6.1**	**8.0**	**4.7**	0.0	**15.0**	**19.6**	**0.5**
$D_{s1}(2536)^+$ mass shape	0.3	4.3	2.3	**0.6**	3.5	5.3	1.1
$K^+\pi^-$ mass shape	2.7	2.6	3.0	0.2	1.2	4.4	0.1
Blatt–Weisskopf factor	0.7	3.4	2.8	0.3	1.3	3.0	0.2
Including $c\bar{c}$ resonances	1.1	5.4	2.7	0.1	6.3	10.0	0.4
$D^+\pi^-$ resonance veto	2.4	2.1	4.6	0.3	9.4	4.6	0.2
MC correction	0.2	1.1	0.3	0.1	0.7	0.8	0.2
Momentum calibration	0.5	0.4	1.3	0.0	1.4	2.5	0.2
Total	7.2	11.7	8.6	0.8	19.3	23.9	1.4

Table 3.23 Fit fractions for the three D_s^+ components in the low $K^+\pi^-$ mass region ($m_{K^+\pi^-} < 0.75\,\text{GeV}$). D_{s0}^+-NR denotes the interference fraction between the $D_{s0}(2590)^+$ and NR components. D_{s1}^+/D_{s0}^+ denotes the ratio of the $D_{s1}(2536)^+$ and $D_{s0}(2590)^+$ fit fractions.

	Fit fraction ($\times 10^{-2}$)
$D_{s0}(2590)^+$	63 ± 9 (stat) $\pm$ 9 (syst)
$D_{s1}(2536)^+$	3.9 ± 1.4 (stat) $\pm$ 0.8 (syst)
NR	51 ± 11 (stat) $\pm$ 19 (syst)
D_{s0}^+–NR	-18 ± 18 (stat) $\pm$ 24 (syst)
D_{s1}^+/D_{s0}^+	6.1 ± 2.4 (stat) $\pm$ 1.4 (syst)

where the uncertainties are statistical and systematic, respectively. Fit fractions and interference fractions in the amplitude analysis are also measured, which are listed in Table 3.23. The new D_s^+ resonance, denoted as $D_{s0}(2590)^+$, is a strong candidate to be the missing $D_s(2^1S_0)^+$ state, the radial excitation of the pseudoscalar ground-state D_s^+ meson, as shown in Fig. 3.40.

The $D_{s0}(2590)^+$ mass is significantly lower than the predicted mass of the $D_s(2^1S_0)^+$ state in the GI and GI-screen models, as listed in Table 1.3 in Chapter 1. The discrepancy is larger than that for most of other states, raising the interest of many theorists to interpret the $D_{s0}(2590)^+$ inner structure. One of the possible explanations is the coupled-channel effect. Several theoretical works found that if considering the coupling of the bare $c\bar{s}$ state

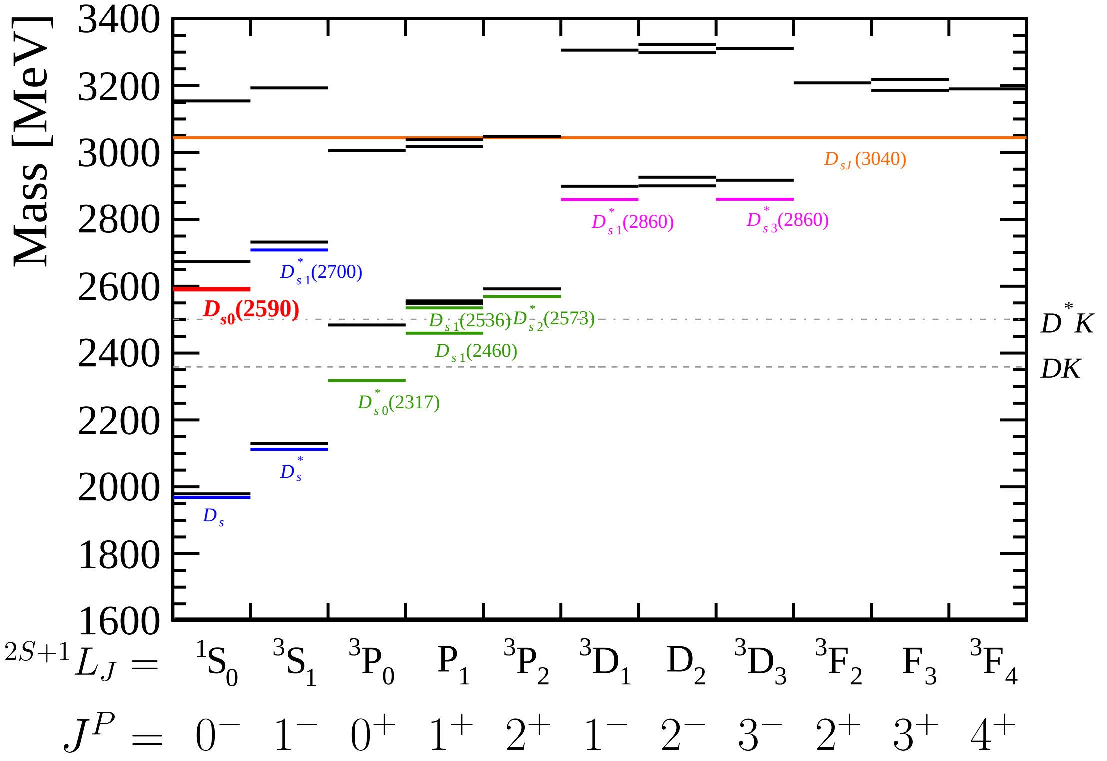

Figure 3.40 The D_s^+ spectrum with the $D_{s0}(2590)^+$ state included. The black lines are the predicted states of the GI model[5]. The colored lines denote the observed states with masses taken from Ref.[1], placed in the column with the most promising $^{2S+1}L_J$ assignments, except the $D_{sJ}(3040)$ state, whose J^P is not determined. The symbol L_L (P_1, D_2, F_3, $\cdots$) denotes the two states L_L and L'_L, super positions of ^1L_L and ^3L_L. The long dashed lines denote the thresholds of the DK and D^*K system.

and the channels with thresholds close to the $D_{s0}(2590)^+$ mass, *e.g.* D^*K, the predicted $D_s(2^1S_0)^+$ mass well agrees with the measured mass of the $D_{s0}(2590)^+$ state[186-189]. However, all theoretical works only address the two-body decay of the $D_{s0}(2590)^+$ state, but the three-body decay $D_{s0}(2590)^+ \to DK\pi$, the channel where the $D_{s0}(2590)^+$ state is observed, is not touched. Future theoretical calculations could also consider the $D_{s0}(2590)^+ \to DK\pi$ channel. there is no rule that forbids the $D_{s0}(2590)^+ \to D^*K$ decay, which can be searched for in the future. If the $D_{s0}(2590)^+ \to D^*K$ decay is observed in exclusive B-meson decays, an amplitude analysis can be performed to extract the contributing fraction of the $D_{s0}(2590)^+$ state. With the fit fraction in the $B^0 \to D^+D^-K^+\pi^-$ decay and the branching fractions of the two B-meson decays as the inputs, the width fraction $\Gamma(D_{s0}(2590)^+ \to DK\pi)/\Gamma(D_{s0}(2590)^+ \to D^*K)$ will be an important property to test the theoretical calculations. The $B^0 \to D^+D^-K^+\pi^-$ branching fraction measurement can be planned in the future.

The study of the other new D_s^+ candidate with a mass about 2.93 GeV is being carried out using an amplitude analysis of the $B^0 \to D^+D^-K^+\pi^-$ decay in the full phase space region. There could be more contributing decay chains compared with that in this analysis in the low $K^+\pi^-$ mass region, and thus the general description of the decay amplitudes described in Sec. 3.6 is useful to construct the complicated amplitude. The analysis is challenging because there are various possible combinations of the four final-state particles, and the intermediate states could exist in different decay chains, and there could also be the case that a resonance decays into several final states, *e.g.* $D_s^+ \to D^+K^{*0}$ and $D_s^+ \to D^{*0}K^+$. Due to the complexity of the B^0-decay amplitude involving four final-state particles and the larger data sample than that of the study in the low $K^+\pi^-$ mass region, the amplitude fit in the full phase space is quite time consuming on CPU. This is particularly unacceptable when many fits are required to establish the amplitude model and to evaluate systematic uncertainties. Therefore, a GPU-based amplitude fitting algorithm is developed to accelerate the computation. With the utilisation of a `GeForce RTX 3090` GPU card, the fitter for the full amplitude analysis of the $B^0 \to D^+D^-K^+\pi^-$ decay is over 50 times faster than that using 50 CPU cores.

This analysis stands as an example for the searches of D_s^+ resonances in the three-body system of the four-body exclusive b-hadron decays. Some other decays containing the $D^+K^+\pi^-$ final state can be studied in the future, *e.g.* $B^+ \to D^+\overline{D}^0K^+\pi^-$, $B_s^0 \to D^-K^-\pi^+\pi^+$, $B^0 \to D^-K^-K^+\pi^+$, where the structures observed in the $B^0 \to D^+D^-K^+\pi^-$ decay can be investigated, standing as the cross check of the discoveries in this analysis. New D_s^+ resonances could also be studied in these decays if the data statistics is allowed. Observation of the $D_{s0}(2590)^+$ state in the three-body $D^+K^+\pi^-$ also inspired the searches for excited heavy hadrons in the three-body final state. For example, the LHCb collaboration recently observed two Ξ_b^0 states in the three-body $\Lambda_b^0K^-\pi^+$ system[190]. With larger statistics of data that will be collected by the LHCb detector, more new heavy hadrons can be explored in three-body systems and multi-body decays of b-hadrons.

CHAPTER 4 STUDY OF THE $B^+ \to D_s^+ D_s^- K^+$ DECAY

The study of the $B^+ \to D_s^+ D_s^- K^+$ decay is inspired by the analysis of the $B^+ \to D^+ D^- K^+$ process[13-14]. The tree-level Feynman diagrams for the $B^+ \to D_s^+ D_s^- K^+$ decay are shown in Fig. 4.1, where charmonium mesons (both conventional and exotic) could be produced in the internal W-emission process and decay into the $D_s^+ D_s^-$ final state. Several observed states could be investigated in the $D_s^+ D_s^-$ system, including the conventional $c\bar{c}$ candidates discovered in the $D\overline{D}$ final state, *e.g.* $\chi_{c0,2}(3930)$, and the exotic states having the open-charm decay mode (*e.g.* $\psi(4660)$) or having the possible $c\bar{c}s\bar{s}$ tetraquark interpretation (*e.g.* $X(3915)$). New states could also be searched for in the $D_s^+ D_s^-$ final state.

Among the discovered $c\bar{c}$ mesons, two $J^{PC} = 0^{++}$ states near the $D_s^+ D_s^-$ mass threshold, $\chi_{c0}(3930)$ and $X(3915)$, draw particular attention. The $\chi_{c0}(3930)$ state is observed in the $D^+ D^-$ final state[13-14], and it does not well fit into the $c\bar{c}$ spectrum as discussed in Sec. 1.4.1. The $X(3915)$ state is an exotic candidate because its main decay mode is $X(3915) \to J/\psi\omega$[1]. The two states are found having comparable masses and widths, indicating the identical nature of them. The assumed identical state is hereafter denoted as X. Its near-threshold feature indicates the possibility of interpreting the state as a compact $c\bar{c}s\bar{s}$ tetraquark[15] or a $D_s^+ D_s^-$ molecule[16], and thus the $X \to D_s^+ D_s^-$ decay mode is possible. If the X state is really observed in the $D_s^+ D_s^-$ final state, its width ratio of the $D^+ D^-$ and $D_s^+ D_s^-$ decay channels will be an important property to help interpret

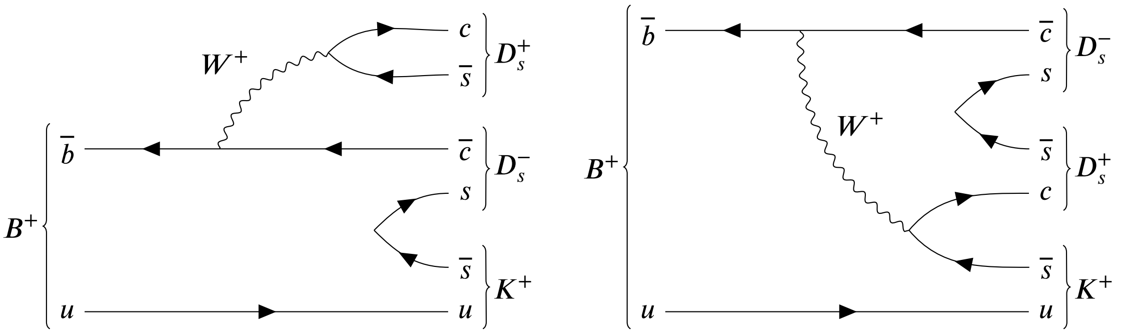

Figure 4.1 Feynman diagrams of the external (left) and internal (right) W-emissions contributing to the $B^+ \to D_s^+ D_s^- K^+$ decay.

its nature. The width ratio is expressed as

$$\frac{\Gamma\left(X \to D^+ D^-\right)}{\Gamma\left(X \to D_s^+ D_s^-\right)} = \frac{\mathcal{B}\left(B^+ \to D^+ D^- K^+\right) \mathcal{FF}^X_{B^+ \to D^+ D^- K^+}}{\mathcal{B}\left(B^+ \to D_s^+ D_s^- K^+\right) \mathcal{FF}^X_{B^+ \to D_s^+ D_s^- K^+}}, \tag{4.1}$$

where $\mathcal{B}$ is the branching fraction of the B^+ decay and $\mathcal{FF}^X$ is the fit fraction of the X state in the decay.

This chapter presents the study of the intermediate resonances in the $B^+ \to D_s^+ D_s^- K^+$ decay using the pp collision data collected by the LHCb experiment. Dataset, offline selection, background discussion and signal extraction are described in Secs. 4.1 to 4.4. The $B^+ \to D_s^+ D_s^- K^+$ branching fraction measurement is presented in Sec. 4.5, providing the essential input to calculate the decay properties of the potential resonances in the $B^+ \to D_s^+ D_s^- K^+$ decay. A near-threshold peaking structure is observed in the $D_s^+ D_s^-$ system, and an amplitude analysis is performed to measure its properties, which is presented in Sec. 4.6. The results of this analysis are summarized in Sec. 4.7, where a discussion on the new structure is also given.

4.1 Dataset

4.1.1 Data samples

This analysis makes use of the full Run 1 and Run 2 datasets collected by the LHCb detector, corresponding to an integrated luminosity of $9\,\text{fb}^{-1}$. The $B^+ \to D_s^+ D_s^- K^+$ and $B^+ \to D^+ D^- K^+$ candidates are reconstructed from the Stripping line `B2DDKBeauty2CharmLine`, where D^+ and D_s^+ candidates are formed in the $K^- \pi^+ \pi^+$ and $K^- K^+ \pi^+$ final states, respectively. In analogous to the $B^0 \to D^+ D^- K^+ \pi^-$ decay, the HLT2 pre-filter is imposed. Good-quality final-state tracks are taken to form the composite particles, and they are required to be inconsistent with originating to all PVs and have PID information consistent with their mass hypotheses. Vertices of the composite particles are required to be well reconstructed and significantly displaced from the corresponding originating points. The B^+ candidate should be consistent with originating from the associated PV. All the particles are required to have p and p_{T} larger than those for the typical soft QCD processes. The mass window on the B^+ and $D^\pm_{(s)}$ candidates are imposed to exclude the large amount of background at the sidebands. The detailed requirements are listed in Table 4.1, where the variables are all explained in the $B^0 \to D^+ D^- K^+ \pi^-$ analysis in Sec. 3.1. The $B^+ \to D_s^+ D_s^- K^+$ and $B^+ \to D^+ D^- K^+$ processes are referred to as signal and control channels, respectively.

In the reconstruction, the momentum scale calibration is performed on data to correct for possible biases due to the non-perfect alignment of the tracking system, imprecise material description, and the uncertainty on magnetic field. The calibration information is obtained from the large data samples of the detached J/ψ candidates in $B^0 \to J/\psi \mu^+ \mu^-$ and $B^0 \to J/\psi K^+$ decays[165]. Decay Tree Fitter (DTF)[166] is utilized to improve the resolutions of the B^+ reconstructed mass and the Dalitz-plot variables describing the $B^+ \to D_s^+ D_s^- K^+$ decay. In the DTF, the B^+ momentum is aligned with the vector connecting the B^+ vertex and the the associated PV. Mass constraints are also imposed. For the purpose of B^+ signal extraction, the $D^\pm$ and $D_s^\pm$ masses are fixed to their known values[1], while for the investigation of the distributions of the Dalitz-plot variables, a further constraint of the B^+ mass to its known value[1] is required.

4.1.2 MC samples

MC samples for the $B^+ \to D_s^+ D_s^- K^+$ and $B^+ \to D^+ D^- K^+$ decays are produced using the software described in Sec. 2.2.4 and filtered by `B2DDKBeauty2CharmLine`, and they are used to model the detector effect and to determine efficiencies due to the LHCb geometric acceptance, reconstruction and selection. The $B^+ \to D_s^+ D_s^- K^+$ MC events are produced uniformly in the phase space with the `PHSP` generator[167], where the $D_s^+ \to K^- K^+ \pi^+$ decay is modeled by the `D_DALITZ` generator[167] with the intermediate resonant contributions extracted from the data collected by the BaBar experiment[102]. Four kinds of $B^+ \to D^+ D^- K^+$ MC samples are utilized in this analysis. Besides the one produced using the `PHSP` generator, the other three are generated uniformly in the space of the square Dalitz variables, defined as

$$\begin{aligned} m'\left(P_1 P_2\right) &\equiv \frac{1}{\pi} \arccos\left(2\frac{m\left(P_1 P_2\right) - m\left(P_1 P_2\right)^{\min}}{m\left(P_1 P_2\right)^{\max} - m\left(P_1 P_2\right)^{\min}} - 1\right), \\ \theta'\left(P_1 P_2\right) &\equiv \frac{1}{\pi}\theta\left(P_1 P_2\right), \end{aligned} \tag{4.2}$$

where $P_1 P_2$ corresponding to $D^+ D^-$, $D^- K^+$ or $D^+ K^+$, and the rest final-state particle is denoted as P_3. The angle $\theta\left(P_1 P_2\right)$ is between the P_1 and P_3 momenta in the $P_1 P_2$ rest frame, $m(P_1 P_2)$ is the mass of the $P_1 P_2$ system and $m(P_1 P_2)^{\min,\max}$ correspond to the physical limit of $m(P_1 P_2)$, which are $m(P_1) + m(P_2)$ and $m(M) - m(P_3)$, respectively. The variables, $m'\left(P_1 P_2\right)$ and $\theta'\left(P_1, P_2\right)$, both vary from 0 to 1. The generators for the three kinds of MC samples are `sqDalitz12`, `sqDalitz23` and `sqDalitz13`[167] with

Table 4.1 Requirements in `B2DDKBeauty2CharmLine`. The notations are explained in Sec. 3.1.

Particle	Variable	Criterion	
		Run1	Run2
	HLT2	Hlt2Topo.*Decision || Hlt2.*IncPhi.*Decision	
All $K^\pm$ and $\pi^\pm$	χ^2_{trk}/ndof	< 3	< 4
	P(ghost)	< 0.4	
	p_{T}	$> 500\,\text{MeV}$	
	p	$> 5000\,\text{MeV}$	
	χ^2_{IP}	> 4	
	$\Delta \log \mathcal{L}_{\text{comb}}(K - \pi)$	> -10	
	$\Delta \log \mathcal{L}_{\text{comb}}(K - \pi)$	< 20	
$D^\pm_{(s)}$	MM	$> 1769.62\,\text{MeV}/c^2$ & $< 2068.49\,\text{MeV}$	
	SUM p_{T}	$> 1800\,\text{MeV}$	
	χ^2_{vtx}/ndof	< 10	
	DOCA(any 2 tracks)	$< 0.5\,\text{mm}$	
	χ^2_{FD}	> 36	
	BPV $\cos(\theta_p)$	> 0	
	At least one track with	$p_{\text{T}} > 500\,\text{MeV}$, $p > 5000\,\text{MeV}$	
B^+	χ^2_{vtx}/ndof	< 10	
	τ	> 0.2 ps	
	χ^2_{IP}	< 25	
	BPV $\cos(\theta_p)$	> 0.999	
	At least one track with	$p_{\text{T}} > 1.7\,\text{GeV}, p > 10\,\text{GeV}, \chi^2_{\text{minIP}} > 16, \text{minIP} > 0.1\,\text{mm}$	
	At least two tracks with	$p_{\text{T}} > 500\,\text{MeV}$, $p > 5000\,\text{MeV}$	
	SUM p_{T}	$> 5\,\text{GeV}$	
	MM	$> 4.75\,\text{GeV}$ & $< 6\,\text{GeV}$	
	B2CBBDT response	> 0.5	

the indices the same as those for $P_1P_2P_3$. The $D^+ \to K^-\pi^+\pi^+$ decay is modeled by the `D_DALITZ` generator[167] where the intermediate resonant contributions are extracted from the data collected by the CLEO experiment[168]. The sizes of the available MC samples for the $B^+ \to D_s^+ D_s^- K^+$ and $B^+ \to D^+ D^- K^+$ channels are listed in Tables 4.2 and 4.3. In the branching fraction measurement, the number of MC events for different years are expected to be roughly proportional to the signal yields in the data of the corresponding years, so only 33% of the produced $B^+ \to D_s^+ D_s^- K^+$ MC11 samples, and 33/65/40/40/40% of the produced $B^+ \to D^+ D^- K^+$ MC11/12/15/16/17 samples are used.

Before further processing, the truth matching is applied to the MC samples to select the candidates that correspond to real $B^+ \to D_s^+ D_s^- K^+$ or $B^+ \to D^+ D^- K^+$ decays. The matching is not 100% efficient but the inefficiencies in the signal and control channels are expected to be largely cancelled in the branching fraction ratio due to presence of the similar final states in the two decays. The potential residual effect is evaluated as a systematic uncertainty introduced in Sec. 4.5.3. The same DTFs with two constraints as those used in data are also applied to MC events.

As the simulation does not well describe the PID responses, the original PID variables in the MC samples are transformed using the `PIDCorr` tool in the `PIDCalib` package[169] according to the distributions of the PID variables in the calibration data in different regions of the p and p_{T} of the corresponding tracks and the multiplicity variable, nTracks. In the transformation, the new PID variable for a track is obtained by equaling the cumulative probability at the raw value of PID variable in the distribution of the MC sample to the probability at the corrected value in the distribution of the calibration sample, as illustrated in Fig. 4.2. In this way, not only the PID distributions in MC samples are corrected to match those in the real data, but also the correlations of the PID variables with other properties of the event, *e.g.* other PID variables for the same track, are preserved, due to the strong correlation between the raw and corrected PID variables.

The performance of the transformation is checked in two aspects: the distributions of the input variables for `PIDCorr` and the output PID responses in the MC samples. To verify the MC modeling of the track p and p_{T}, as well as nTracks, their distributions in MC simulation and data are compared in Figs. 4.3 and 4.5. Good agreements are found for the kinematic variables, but the nTracks in MC simulation is lower than that in data. In the default result, the original nTracks variable is taken as the input for `PIDCorr`. In the systematic study, the nTracks variable is scaled by a factor of 1.14 to match the

Table 4.2 MC events for the $B^+ \to D_s^+ D_s^- K^+$ and $B^+ \to D^+ D^- K^+$ decays. Cells with “-” are empty. “Pre-filtered” refers to the MC events before the Stripping filtering, and “Filtered” refers to the available MC events after filtering. MD and MU denote MagDown and MagUp, respectively.

Year	Magnet	Model	$B^+ \to D^+ D^- K^+$ events		$B^+ \to D_s^+ D_s^- K^+$ events	
			Pre-filtered	Filtered	Pre-filtered	Filtered
11	MD	PHSP	796000	9661	7955525	98663
		Sq.(1,2)	400000	4881	-	-
		Sq.(2,3)	398706	4576	-	-
		Sq.(1,3)	394000	4799	-	-
	MU	PHSP	391669	4623	8367745	100361
		Sq.(1,2)	396000	4386	-	-
		Sq.(2,3)	794000	9753	-	-
		Sq.(1,3)	398000	4796	-	-
12	MD	PHSP	370000	4398	3972090	52559
		Sq.(1,2)	352000	4086	-	-
		Sq.(2,3)	363999	4309	-	-
		Sq.(1,3)	364000	4494	-	-
	MU	PHSP	354000	4137	3988499	50988
		Sq.(1,2)	348000	4022	-	-
		Sq.(2,3)	362000	4034	-	-
		Sq.(1,3)	360000	4262	-	-
15	MD	PHSP	377999	4343	1787482	31419
		Sq.(1,2)	377999	4141	-	-
		Sq.(2,3)	391999	4561	-	-
		Sq.(1,3)	384000	4206	-	-
	MU	PHSP	376647	4127	1775870	30748
		Sq.(1,2)	392000	4413	-	-
		Sq.(2,3)	380270	4333	-	-
		Sq.(1,3)	387998	4145	-	-

Table 4.3 MC events for the $B^+ \to D_s^+ D_s^- K^+$ and $B^+ \to D^+ D^- K^+$ decays (continued). Cells with "-" are empty. "Pre-filtered" refers to the MC events before the Stripping filtering, and "Filtered" refers to the available MC events after filtering. MD and MU denote MagDown and MagUp, respectively.

Year	Magnet	Model	$B^+ \to D^+ D^- K^+$ events		$B^+ \to D_s^+ D_s^- K^+$ events	
			Pre-filtered	Filtered	Pre-filtered	Filtered
16	MD	PHSP	779998	10895	5374770	82902
		Sq.(1,2)	781999	11056	-	-
		Sq.(2,3)	765998	10712	-	-
		Sq.(1,3)	768000	10661	-	-
	MU	PHSP	761998	10723	5307226	82473
		Sq.(1,2)	761999	9887	-	-
		Sq.(2,3)	771996	10339	-	-
		Sq.(1,3)	390997	5186	-	-
17	MD	PHSP	781793	11877	4926163	81600
		Sq.(1,2)	750999	10941	-	-
		Sq.(2,3)	785000	11784	-	-
		Sq.(1,3)	798999	11823	-	-
	MU	PHSP	786999	11426	4788248	80326
		Sq.(1,2)	789000	11628	-	-
		Sq.(2,3)	778034	10990	-	-
		Sq.(1,3)	781000	11468	-	-
18	MD	PHSP	389000	5237	7395856	107727
		Sq.(1,2)	398999	5138	-	-
		Sq.(2,3)	379000	4942	-	-
		Sq.(1,3)	384999	5051	-	-
	MU	PHSP	398999	4842	7484330	108006
		Sq.(1,2)	388999	5477	-	-
		Sq.(2,3)	396998	5241	-	-
		Sq.(1,3)	398999	5024	-	-

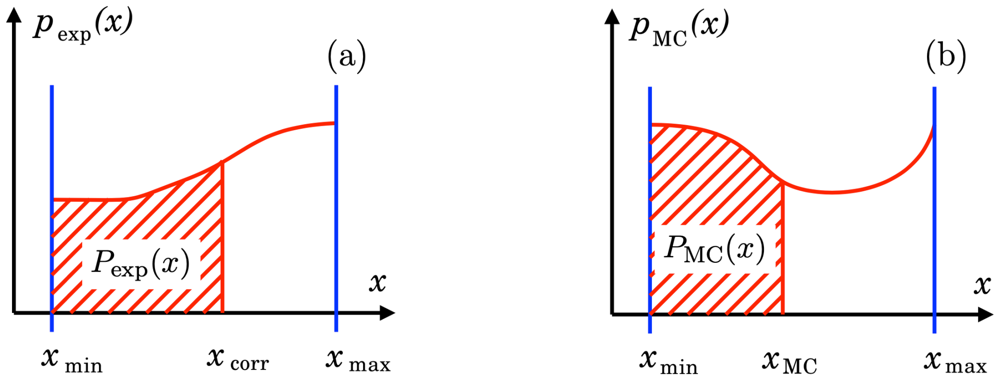

Figure 4.2 Illustrative plots showing cumulative distribution functions of a PID variable x in MC simulation (left) and the calibration data (right). The transformation of the variable $x_{\text{MC}} \to x_{\text{corr}}$ is performed by requiring $P_{\text{exp}}(x_{\text{corr}}) = P_{\text{MC}}(x_{\text{MC}})$.

distribution in data, and the scaled nTracks are taken as the input variable to `PIDCorr`. Good agreements between the transformed PID variables in MC simulation and those in data are seen in Figs. 4.4 and 4.6.

4.2 Offline selection

Several offline selection procedures are imposed to further suppress the backgrounds, including a simple cut-based selection and the offline trigger requirement, followed by a multivariate analysis that efficiently suppresses the combinatorial background and a procedure to remove multiple candidates.

4.2.1 Cut-based selection

The cut-based selection criteria are listed in Table 4.4. The PID requirements on the final-state particles significantly reduce the combinatorial background resulting from the random combinations of the final-state particles, as well as the potential physical backgrounds due to misidentification of tracks and partial reconstructions. The tighter mass windows for the $D_{(s)}^{\pm}$ candidates than those in the Stripping line exclude the huge background at the $D_{(s)}^{\pm}$ mass sidebands. To reject the background from the repeated use of the track segments in the event, the opening angle between any two final-state tracks should be $> 0.5\,\text{mrad}$. The non-double-charm (NDC) background from real B^+ decays but contains only one or zero real $D_{(s)}^{\pm}$ meson is largely suppressed by requiring a χ^2 distance of the z components of the B^+ decay vertex and the associated PV, defined as

$$dz/\sigma_{dz} = (V_z(D_{(s)}) - V_z(B))/\sqrt{\sigma_{V_z}^2(D_{(s)}) + \sigma_{V_z}^2(B)}, \tag{4.3}$$

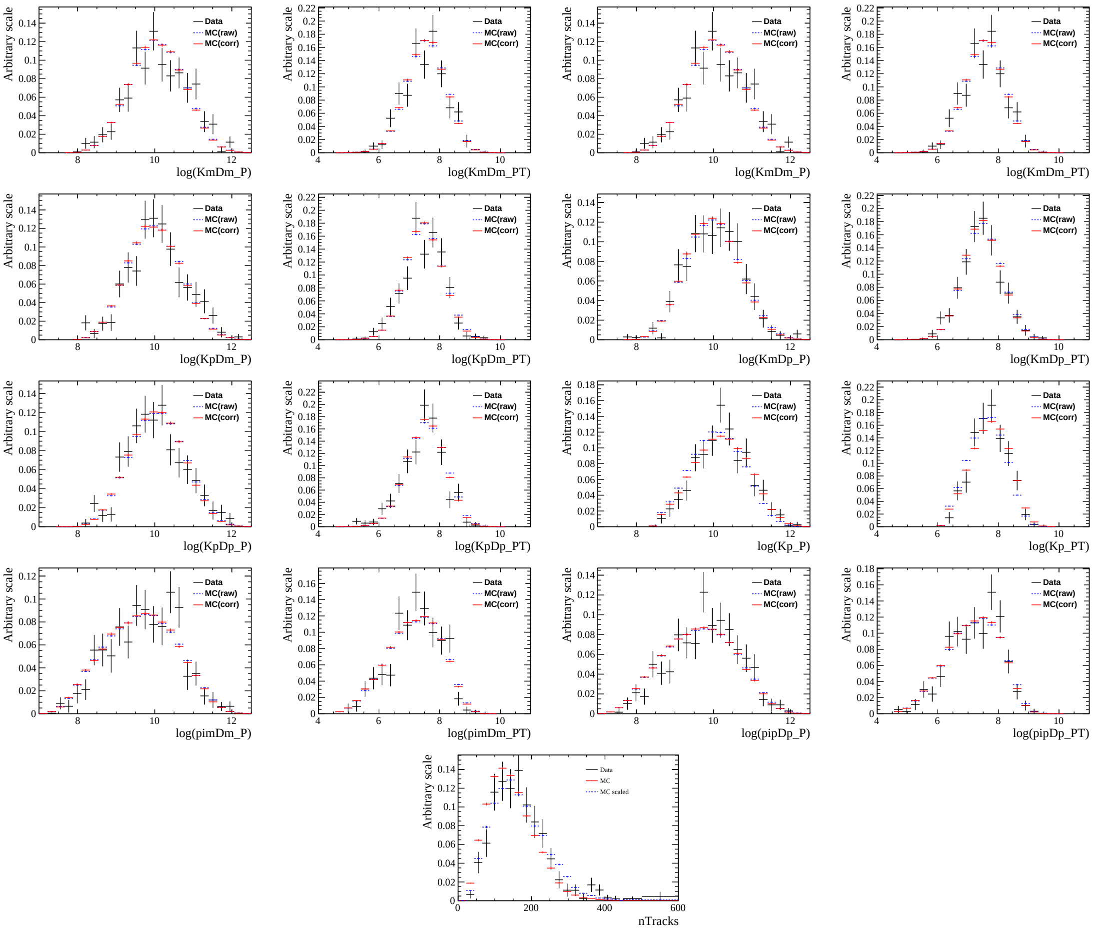

Figure 4.3 Track p and p_T comparisons in MC simulation and data for the $B^+ \to D_s^+ D_s^- K^+$ decay after all the selections. The nTracks distribution is also shown, where the scaled distribution is taken as an alternative input for `PIDCorr` to study the systematic effect. The Dalitz-weighted MC distributions are shown in red, while the unweighted distributions are shown in blue. The background in data is subtracted using the *sPlot* method[174].

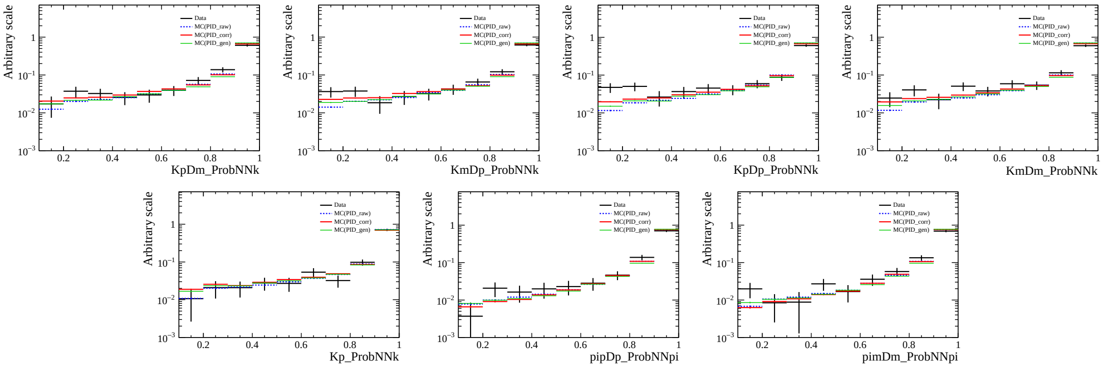

Figure 4.4 PID comparisons in MC simulation and data for the $B^+ \to D_s^+ D_s^- K^+$ decay after all the selections. PID_raw is the original value in MC simulation, PID_corr is the value transformed using `PIDCorr`, and PID_gen is the value resampled using `PIDGen`, and is used in the study of the systematic uncertainty. The Dalitz-plot distribution in MC simulation is weighted to match that in data. The background in data is subtracted using the *sPlot* method[174].

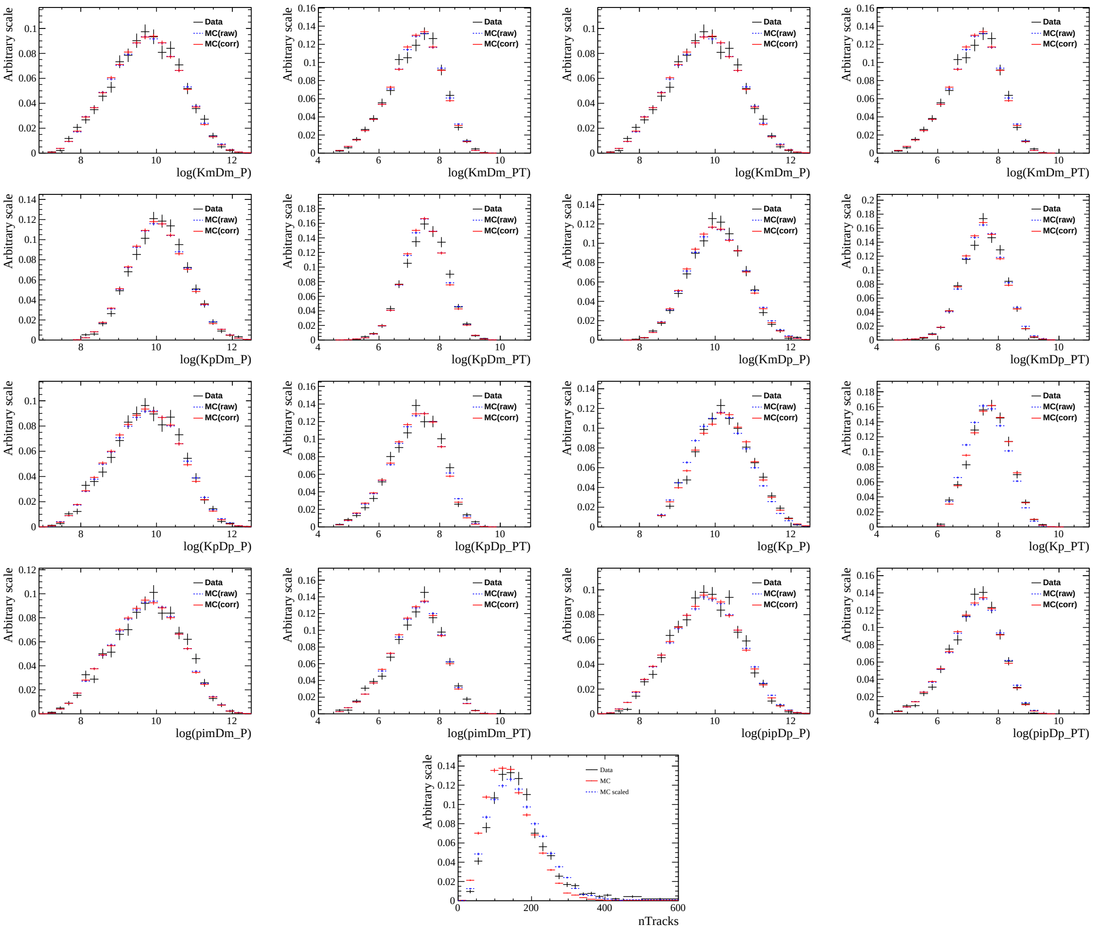

Figure 4.5 Track p and p_{T} comparisons in MC simulation and data for the $B^+ \to D^+ D^- K^+$ decay after all the selections. The nTracks distribution is also shown, where the scaled distribution is taken as an alternative input for `PIDCorr` to study the systematic effect. The Dalitz-weighted MC distributions are shown in red, while the unweighted distributions are shown in blue. The background in data is subtracted using the *sPlot* method[174].

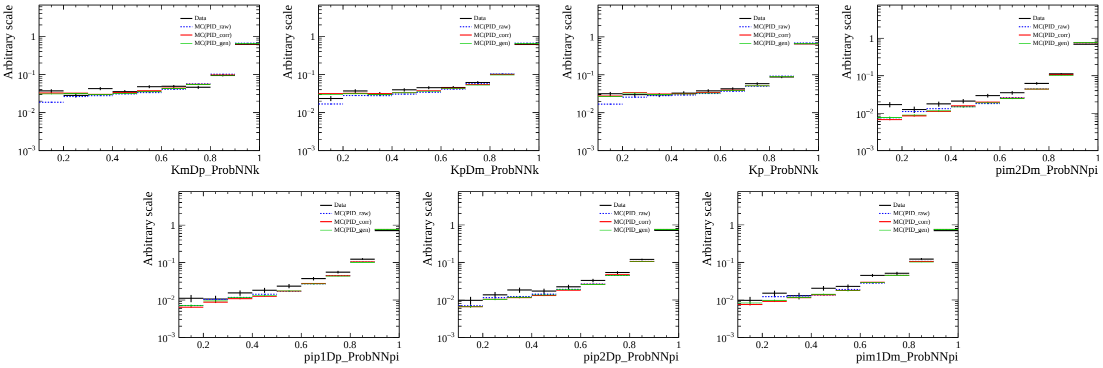

Figure 4.6 PID comparisons in MC simulation and data for the $B^+ \to D^+ D^- K^+$ decay after all the selections. PID_raw is the original value in MC, PID_corr is the value transformed using `PIDCorr`, and PID_gen is the value resampled using `PIDGen`, and is used in the study of the systematic uncertainty. The Dalitz-plot distribution in MC simulation is weighted to match that in data. The background in data is subtracted using the *sPlot* method[174].

Table 4.4 Cut-based offline requirements for the $B^+ \to D_s^+ D_s^- K^+$ and $B^+ \to D^+ D^- K^+$ channels.

$B^+ \to D_s^+ D_s^- K^+$	$B^+ \to D^+ D^- K^+$
ProbNNpi > 0.1 for all pions	
ProbNNk > 0.1 for all kaons	
$D_{(s)}^{\pm}$ MM window: ±25 MeV	
Open angle > 5 mrad for any two tracks	
$D_{(s)}^{\pm}$ $dz/\sigma_{dz} > 2$	
B^+ mass window: ±80 MeV	B^+ mass window: +80(−60) MeV

Table 4.5 Offline trigger requirements for the $B^+ \to D_s^+ D_s^- K^+$ and $B^+ \to D^+ D^- K^+$ channels.

	Run1	Run2
L0	Bu_L0HadronDecision_TOS || Bu_L0Global_TIS	
HLT1	Bu_TrackAllL0Decision_TOS	Bu_Hlt1TrackMVADecision_TOS || Bu_Hlt1TwoTrackMVADecision_TOS
HLT2	Bu_Hlt2Topo2BodyBBDTDecision_TOS || Bu_Hlt2Topo3BodyBBDTDecision_TOS || Bu_Hlt2Topo4BodyBBDTDecision_TOS	Bu_Hlt2Topo2BodyDecision_TOS || Bu_Hlt2Topo3BodyDecision_TOS || Bu_Hlt2Topo4BodyDecision_TOS

where $V_z(B)$ and $V_z(D_{(s)})$ are the z coordinates of positions of the PV and decay vertex, and $\sigma_{V_z}(X)$ the corresponding reconstruction uncertainties. In the discussions in Secs. 4.3.1.2 and 4.3.1.2, it is found that $dz/\sigma_{dz} > 2$ is an adequate requirement for both the $B^+ \to D_s^+ D_s^- K^+$ and $B^+ \to D^+ D^- K^+$ channels. It not only sufficiently reduces the NDC backgrounds, but also keeps as many signal candidates as possible.

4.2.2 Offline trigger requirements

Several trigger decisions fired by the components associated with the $B^+ \to D_s^+ D_s^- K^+$ and $B^+ \to D^+ D^- K^+$ candidates are required, listed in Table 4.5. The Run 2 triggers are explained in the $B^0 \to D^+ D^- K^+ \pi^-$ analysis in Sec. 3.2.3. In the Run 1 requirements, the L0 and HLT2 triggers are similar to those in Run 2. For the HLT1 trigger, `TrackAllL0Decision` for any of candidate tracks in the signal decay is required. The decision acquires the events passing any of the L0 trigger and is dedicated to select hadron decays that are significantly from a PV.

Table 4.6 Input variables used in the multivariate analysis.

Particle	Input variable
B^+ candidate	arccos(B^+ direction angle (DIRA))
	Decay vertex χ^2
	Impact parameter (IP) χ^2 w.r.t. PV
	B^+ flight distance χ^2 w.r.t. PV
	Transverse momentum (p_T)
$D^{\pm}_{(s)}$ candidates	log($D^{\pm}_{(s)}$ IP χ^2 w.r.t. PV)
	log(min IP χ^2 of $D^{\pm}_{(s)}$ decay products w.r.t. PV)
	$K^{\pm}$ (from $D_s^{\pm}$) ProbNNk
Bachelor K^+	log($K^{\pm}$ IP χ^2 w.r.t. PV)
	$K^{\pm}$ ProbNNK

4.2.3 Multivariate analysis

The multivariate analysis (MVA)[191-192] is employed to further suppress the background in the $B^+ \to D_s^+ D_s^- K^+$ and $B^+ \to D^+ D^- K^+$ data passing the cut-based and offline trigger selections. The input signal events are from the corresponding MC samples after the offline and trigger selections in Tables 4.4 and 4.5 , and the input background events are from the upper sideband of the B^+ MM distribution with $>$ 5360 MeV of the corresponding data with offline and trigger selections applied. The candidates in the lower sideband are not taken as they contain potential contributions from the partially reconstructed background, as discussed in Sec. 4.3. The number of the input signal and background events are 129963 and 19116 for the $B^+ \to D_s^+ D_s^- K^+$ channel, and 49890 and 28557 for the $B^+ \to D^+ D^- K^+$ channel, respectively. The signal and background samples are randomly split into two categories, one for training and the other for testing.

The full list of variables used in the MVA is given in Table 4.6, including the PID variables of the final-state kaons, some topological variables of the B^+ decay and the kinematic variable, p_{T} of the B^+ candidate. Distributions of these variables in the input samples are shown in Figs. 4.7 and 4.8 for the $B^+ \to D_s^+ D_s^- K^+$ and $B^+ \to D^+ D^- K^+$ channels, respectively, all exhibiting strong power to discriminate signal and background. The variables are also compared between MC simulation and data in the B^+ peak region in Figs. 4.9 and 4.10, and the good agreements indicate that the input variables are well simulated in the MC samples.

The Gradient Boosted Decision Tree (BDTG) classifier[191-192] is employed in

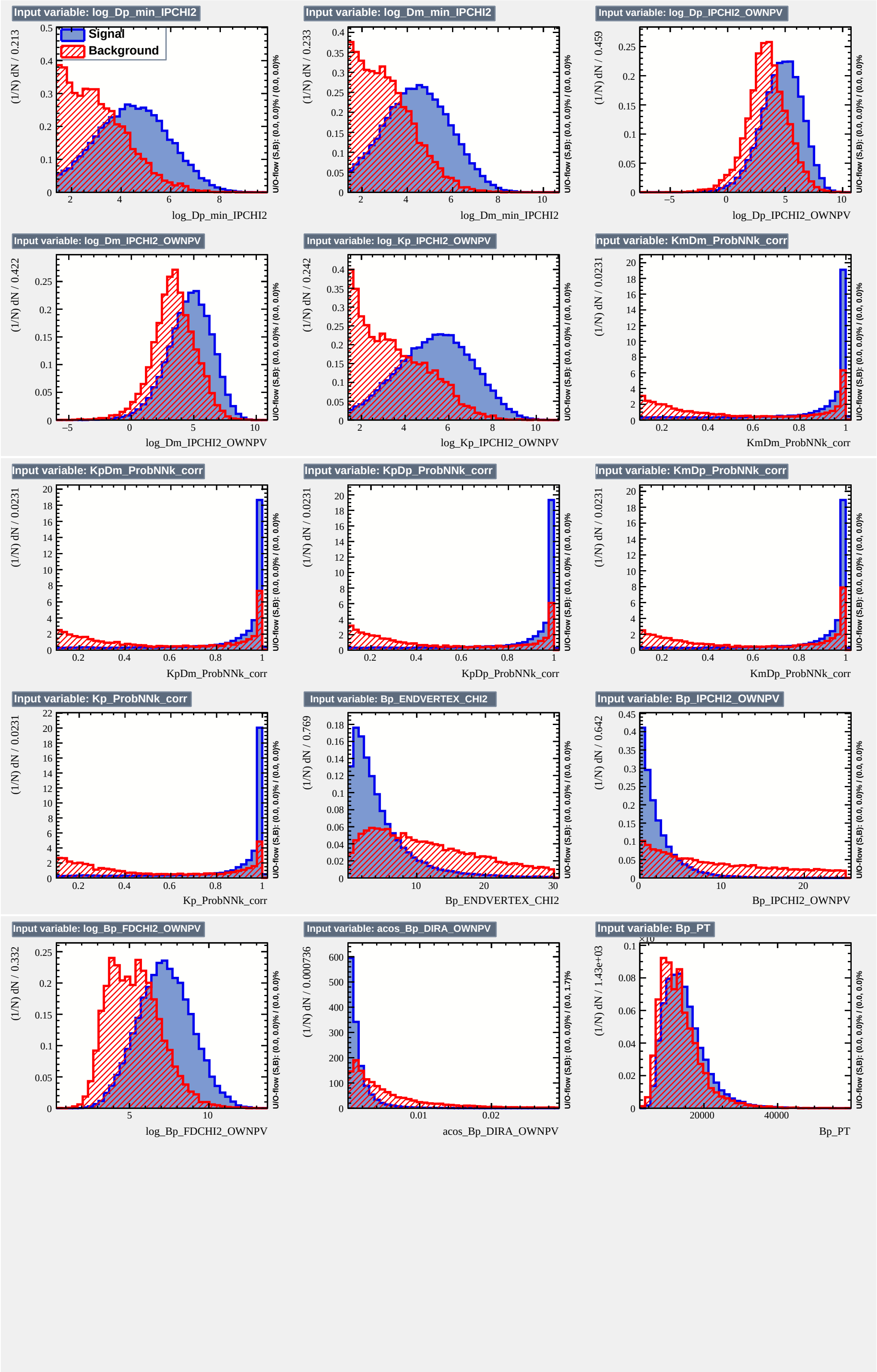

Figure 4.7 Discriminating variables used in the MVA training for the $B^+ \to D_s^+ D_s^- K^+$ channel.

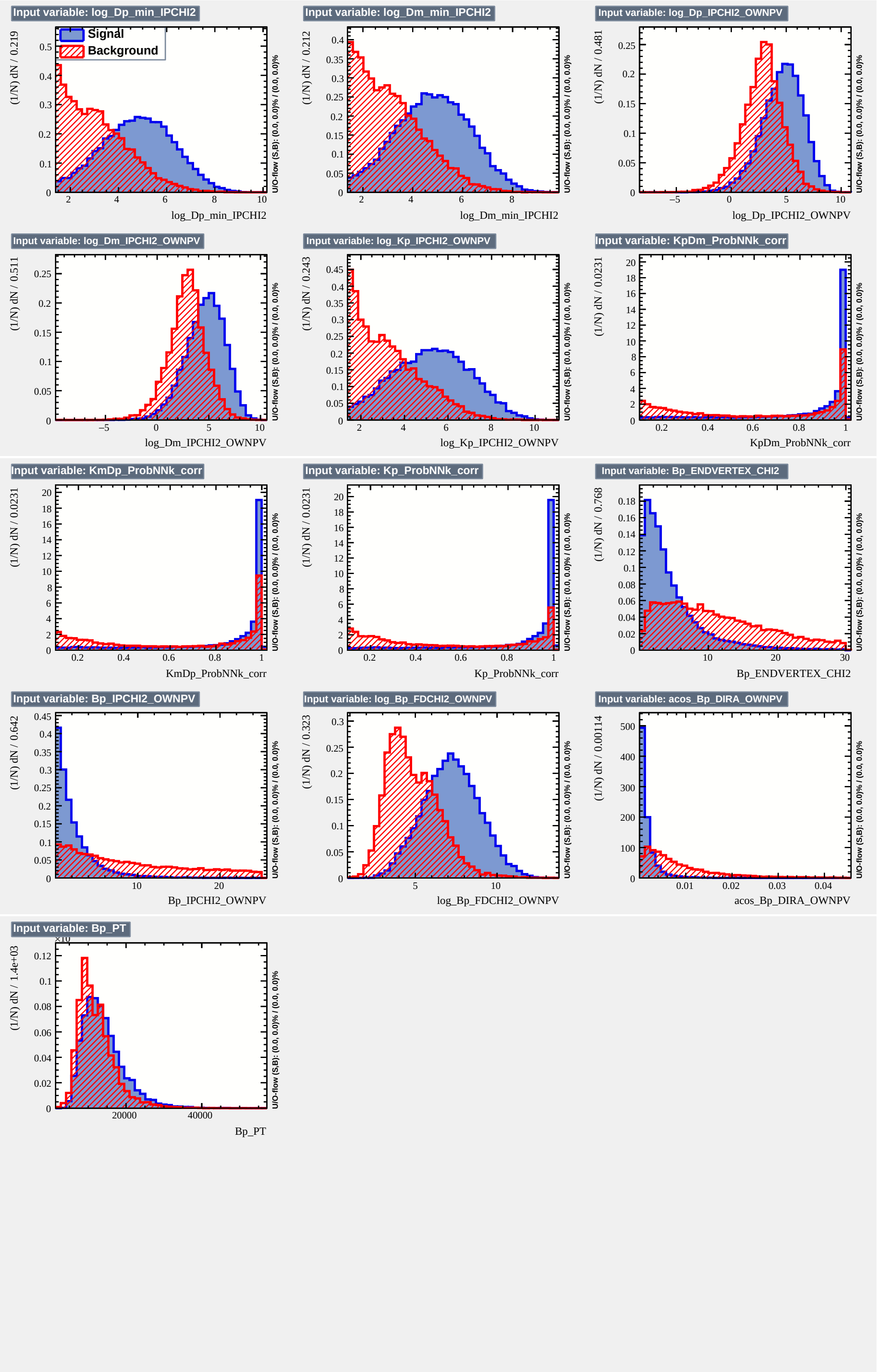

Figure 4.8 Discriminating variables used in the MVA training for the $B^+ \to D^+ D^- K^+$ channel.

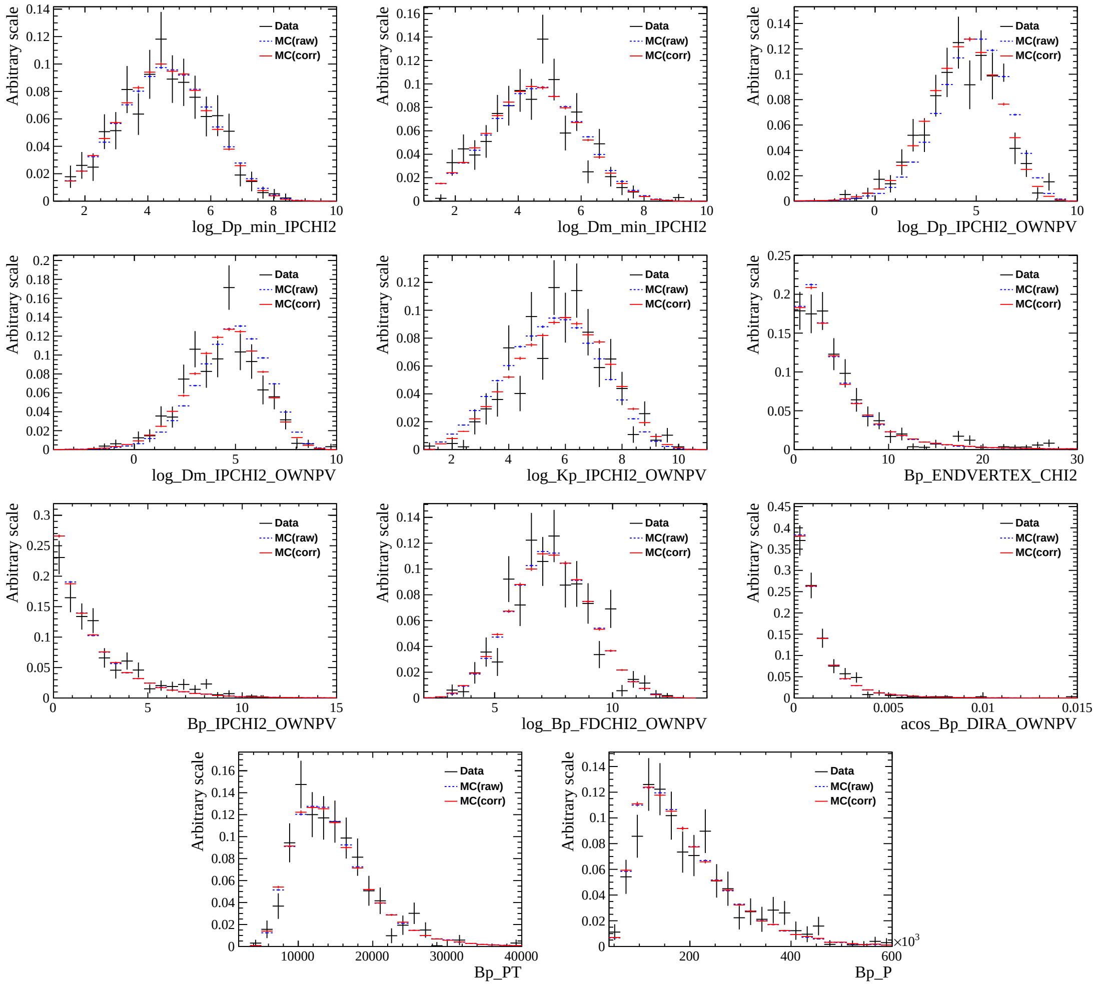

Figure 4.9 Comparisons of MVA input variables in MC simulation and data for $B^+ \to D_s^+ D_s^- K^+$ decays after all the selections. In the MC distributions, The blue line is the original one without Dalitz weights applied, and the red line is weighted to match the Dalitz-plot distribution of data. The background in data is subtracted using the *sPlot* method. All offline selections except the BDTG cut are applied.

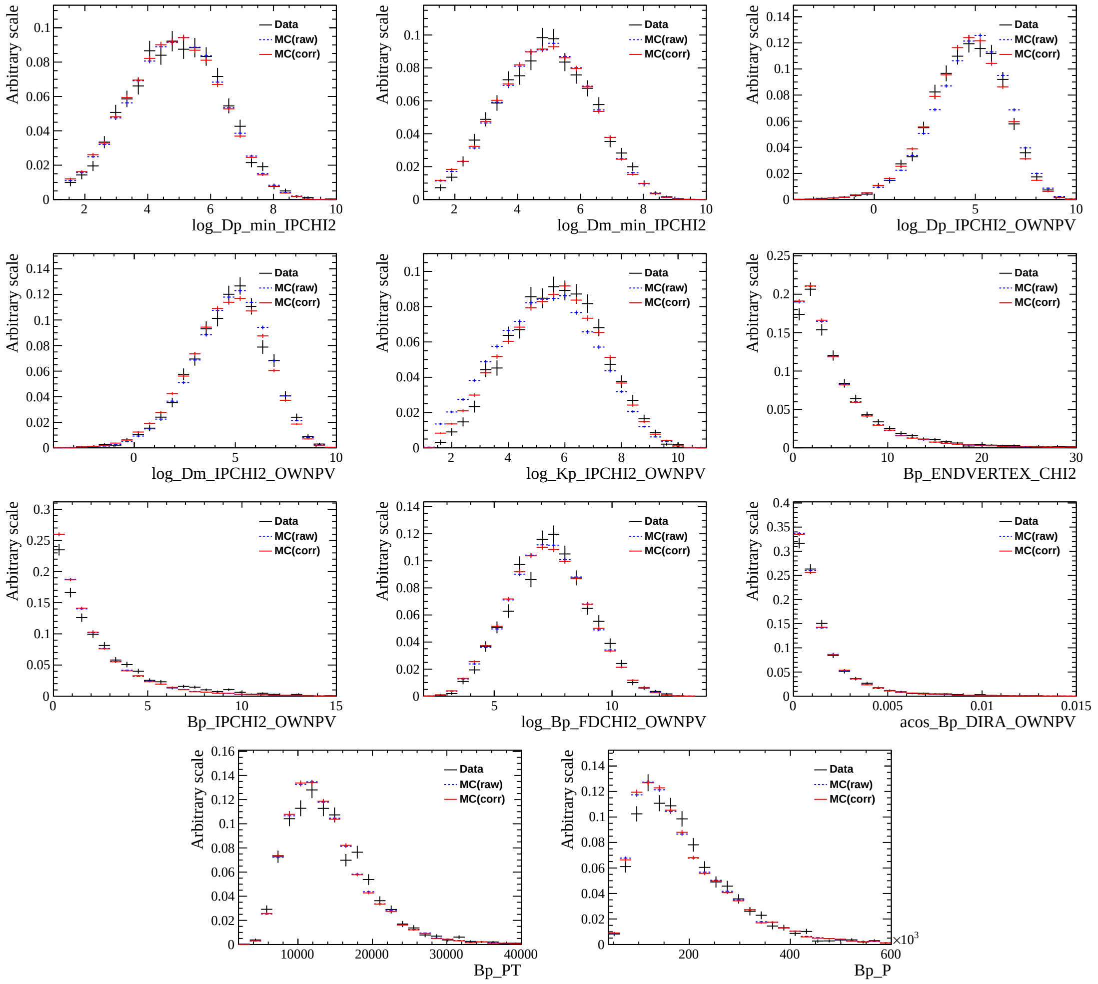

Figure 4.10 Comparisons of MVA input variables in MC and data samples for $B^+ \to D^+ D^- K^+$ decays after all the selections. In the MC distributions, The blue line is the original one without Dalitz weights applied, and the red line is weighted to match the Dalitz-plot distribution of data. The background in data is subtracted using the *sPlot* method. All offline selections except the BDTG cut are applied.

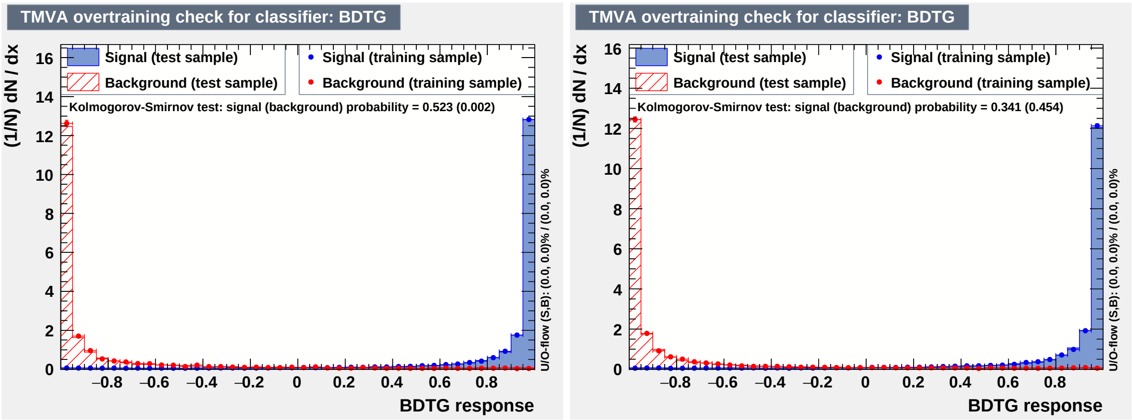

Figure 4.11 BDTG response comparisons between the training and testing samples for the $B^+ \to D_s^+ D_s^- K^+$ (left) and $B^+ \to D^+ D^- K^+$ (right) channels. No effect of overtraining is found.

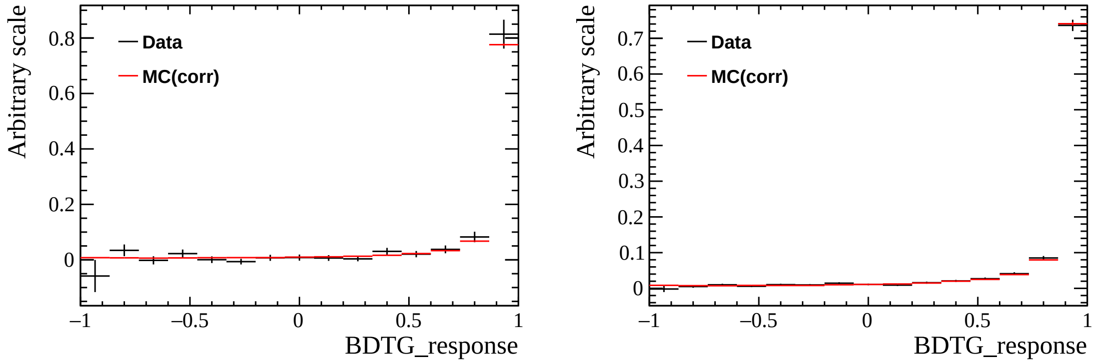

Figure 4.12 BDTG response comparisons between MC simulation and data after all the selections except the BDTG cut for the $B^+ \to D_s^+ D_s^- K^+$ (left) and $B^+ \to D^+ D^- K^+$ (right) channels. The Dalitz-plot distribution in MC simulation is weighted to match that in data, and the background in data is subtracted using the *sPlot* method[174].

the MVA, whose responses for the $B^+ \to D_s^+ D_s^- K^+$ and $B^+ \to D^+ D^- K^+$ channels are compared between the training and testing samples in Figs. 4.11. The good agreements indicate that no overtraining effect is found and the trained classifiers work well. Responses of Dalitz-weighted MC and background-subtracted data samples are shown in Fig. 4.12. The good agreement indicates the MC simulation well describes the BDTG responses of the real B^+ signals in data.

The BDTG working point is optimized by maximizing the signal significance, $S(t)/\sqrt{S(t)+B(t)}$, as a function of the BDTG cut t, for the data candidates in the $\pm 20\,\text{MeV}$ mass window around the B^+ mass[1], where $S(t)$ ($B(t)$) is the number of the signal (background) candidates in the mass window, estimated as the signal (background) yield S_0 (B_0) before the BDTG selection, multiplying the signal (background) efficiency $\epsilon_S(t)$ ($\epsilon_B(t)$). Signal and background yields before the BDTG selection, S_0 and B_0, are estimated by simple unbinned maximum-likelihood fits on the B^+ reconstructed mass. The signal PDF is chosen as a Gaussian function, and the background PDF is exponential,

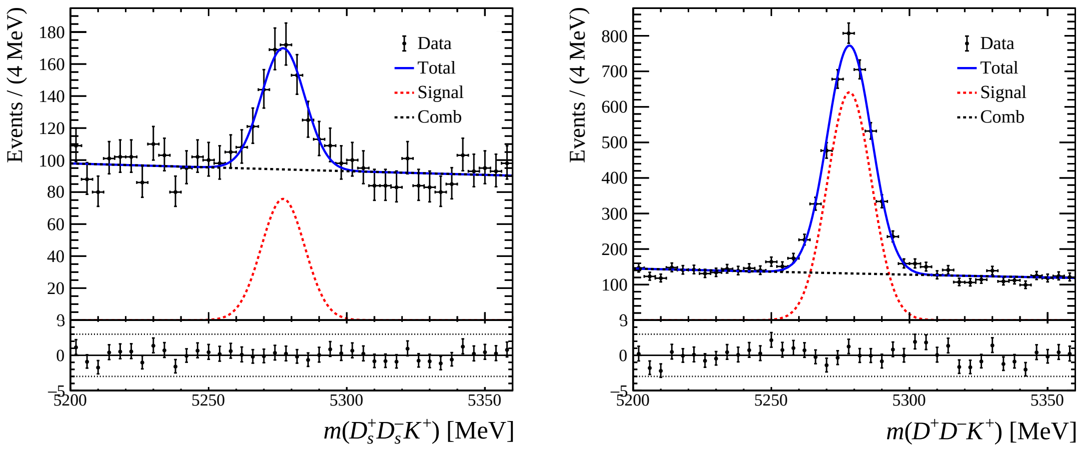

Figure 4.13 Simple fits to obtain the signal and background yields before the BDTG cut for the $B^+ \to D_s^+ D_s^- K^+$ (left) and $B^+ \to D^+ D^- K^+$ (right) channels.

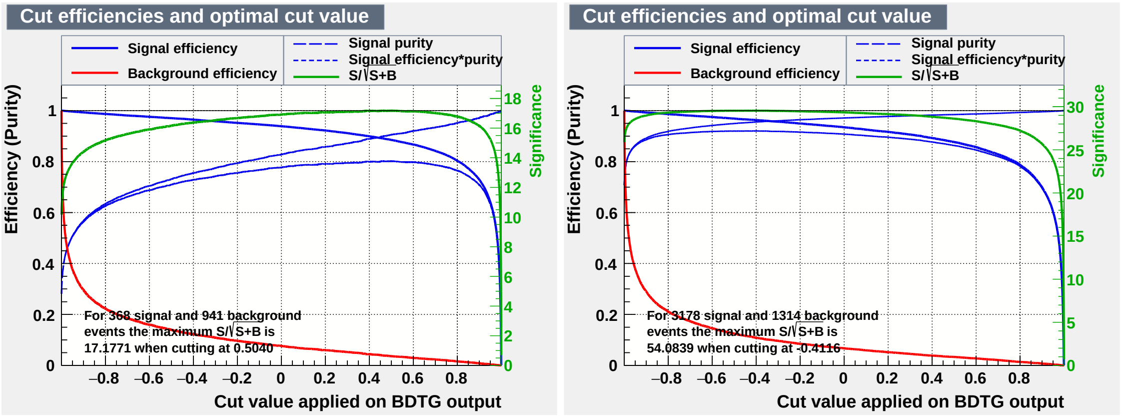

Figure 4.14 Signal significance as a function of the BDTG cut for the $B^+ \to D_s^+ D_s^- K^+$ (left) and $B^+ \to D^+ D^- K^+$ (right) channels. The efficiencies are taken from the testing samples.

where all parameters are left free. A larger mass range, 5280 ± 80 MeV, is chosen in the fits, to include more candidates from the sideband and thus to achieve a better description of backgrounds. The fit results for the $B^+ \to D_s^+ D_s^- K^+$ and $B^+ \to D^+ D^- K^+$ channels are shown in Fig. 4.13. The signal (background) yield in the ±20 MeV mass window is evaluated as the signal (background) probability ratio of the ±20 MeV and ±80 mass windows times the numbers of the signal (background) candidates obtained from the fits. The numbers are $S_0 = 368 \pm 44$ ($B_0 = 941 \pm 18$) for the $B^+ \to D_s^+ D_s^- K^+$ channel and $S_0 = 3178 \pm 73$ ($B_0 = 1314 \pm 22$) for the $B^+ \to D^+ D^- K^+$ channel. Signal and background efficiencies, $\epsilon_S(t)$ and $\epsilon_B(t)$, are estimated directly from the testing samples as the ratio of the numbers of the signal (background) candidates with and without the BDTG cut t applied. The significance functions are shown in Fig. 4.14, where the optimal working point is determined to be > 0.50 for the $B^+ \to D_s^+ D_s^- K^+$ channel, and > -0.41 for the $B^+ \to D^+ D^- K^+$ channel.

4.2.4 Multiple candidate removal

After the MVA selection, multiple candidates are found in some proton-proton collision events. The sources are listed in Table 4.7, and they are mainly classified into two categories. The first case is that the candidates in a single event have the identical set of track keys ①, but two or more keys are assigned to different final-state tracks. This case is referred to as the internal exchange. For example, in an event containing two candidates, the keys sets of the two candidates could be $\{12, 0, 16, 4, 13, 11, 2\}$ and $\{12, 0, 16, 2, 11, 13, 4\}$. It is seen that the two sets have the same elements but two pairs of keys are swapped, $2 \leftrightarrow 4$ and $11 \leftrightarrow 13$. The other case is the external exchange where one or more track keys in a multiple candidate are different from other candidates in the same event. For example, in an event containing two candidates, the keys sets are $\{24, 21, 2, 16, 36, 14, 7\}$ and $\{24, 21, 2, 16, 36, 13, 7\}$, where the key 14 in the first set and 13 in the second set are different, and they are from the rest of the events. The candidates in the internal-exchange category is further classified into three types: D^--K^+, D^+-K^+ and D^+-D^- swaps with X-Y indicating one or more track keys of X and Y are swapped. From Table 4.7, it is seen that the multiple candidate fractions for internal exchanges are quite different for the $B^+ \to D_s^+ D_s^- K^+$ and $B^+ \to D^+ D^- K^+$ channels. This is understood as that there are more exchange possibilities for the three K^+ and two K^- final-state tracks of the $B^+ \to D_s^+ D_s^- K^+$ decay compared with those of the only two K^+ tracks in the $B^+ \to D^+ D^- K^+$ decay. The total multiple candidate fraction is found to be 3.0% and 1.1% for the $B^+ \to D_s^+ D_s^- K^+$ and $B^+ \to D^+ D^- K^+$ candidates, respectively, both in a ± 80 MeV window around the known B^+ mass[1]. In the default result, only the candidate with the smallest DTF-χ^2 under the $D^\pm$ ($D_s^\pm$) mass and PV constraints is kept in each event. The random-removing strategy is tested in Sec. 4.5.3 to evaluate the systematic effect in the branching fraction measurement.

The efficiency of the multiple candidate removal is expected to extremely high but the potential difference in the signal and control channel could introduce bias on the branching fraction ratio, which is considered in the systematic study presented in Sec. 4.5.3.11. To verify the MC modeling of the multiple candidates, they are investigated in MC samples without truth matching applied. The fractions are found to be consistent with those in data within the uncertainties, as shown in Table 4.7, proving that it is reliable to use MC samples to evaluate the systematic effect of the efficiency due to multiple candidate removal.

---

① Track key is a unique quantity for a track in a proton-proton collision event, and can be used to justify whether a same track is repeatedly used to construct the decay in two multiple candidates.

Table 4.7 Multiple candidate fractions. Truth matching is applied to the MC events.

Source	$B^+ \to D_s^+ D_s^- K^+$		$B^+ \to D^+ D^- K^+$	
	Data	MC	Data	MC
Internal exchange	$(2.05 \pm 0.56)\%$	$(2.56 \pm 0.04)\%$	$(0.42 \pm 0.10)\%$	$(0.72 \pm 0.04)\%$
· D^--K^+ swap	$(0.47 \pm 0.27)\%$	$(0.95 \pm 0.03)\%$	$(0.35 \pm 0.09)\%$	$(0.70 \pm 0.04)\%$
· D^+-K^+ swap	$(0.32 \pm 0.22)\%$	$(0.78 \pm 0.02)\%$	$(0.07 \pm 0.04)\%$	$(0.01 \pm 0.00)\%$
· D^+-D^- swap	$(0.95 \pm 0.38)\%$	$(0.43 \pm 0.02)\%$	$(0.00 \pm 0.00)\%$	$(0.00 \pm 0.00)\%$
External exchange	$(0.95 \pm 0.38)\%$	$(0.64 \pm 0.02)\%$	$(0.65 \pm 0.12)\%$	$(0.58 \pm 0.03)\%$
Total	$(3.00 \pm 0.68)\%$	$(3.19 \pm 0.05)\%$	$(1.07 \pm 0.16)\%$	$(1.30 \pm 0.05)\%$

4.3 Backgrounds

There could be residual backgrounds after all the selections, including the potential partially reconstructed and misidentified backgrounds, as well as the NDC background.

4.3.1 Backgrounds in the $B^+ \to D_s^+ D_s^- K^+$ data

4.3.1.1 Partially reconstructed and misidentified backgrounds

The reconstructed B^+ mass distribution in the $B^+ \to D_s^+ D_s^- K^+$ data after all the selections is shown in Fig. 4.15. The wide bumps below 5200 MeV are from the partially reconstructed backgrounds, $B \to D_s^+ D_s^- K^*$ with a missing pion and $B^+ \to D_s^{(*)+} D_s^{(*)-} K^+$ with a missing photon or neutral pion. To investigate the influence of such backgrounds, simulated samples are produced using the `RapidSim` package[193] with a simple detector effect taken into account. The corresponding reconstructed B^+ mass distributions are shown in Fig. 4.16. It is seen that a ±80 MeV mass window around the known B^+ mass[1] can sufficiently exclude these backgrounds. There is a small tail of $B^+ \to D_s^{(*)+} D_s^{(*)-} K^+$ background entering the mass window, but is negligible compared with the level of combinatorial background. The background contribution from the misidentification of a K or π is Cabibbo suppressed. Such background is further reduced by the PID requirements. Such background is also expected to be excluded outside the B^+ mass window due to the mass difference between K and π. Therefore, only the combinatorial background needs to be handled in the chosen B^+ mass window.

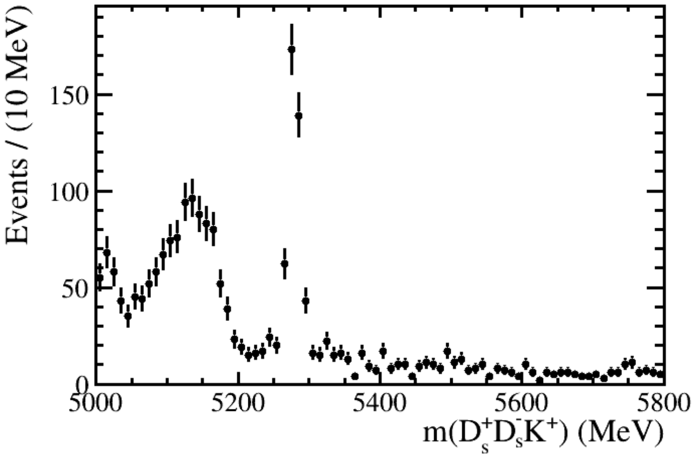

Figure 4.15 Mass distribution of the $D_s^+ D_s^- K^+$ system in data after all the selections.

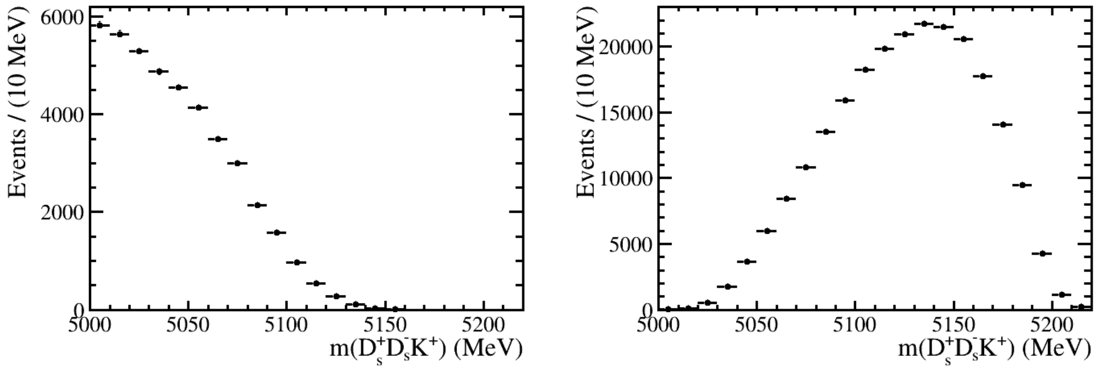

Figure 4.16 Mass distributions of the $D_s^+ D_s^- K^+$ system in simulated samples for partially reconstructed $B^+ \to D_s^+ D_s^- K^{*+}$ (left) and $B^+ \to D_s^{*+} D_s^- K^+$ (right) decays. The simulated samples are generated using `RapidSim`[193].

4.3.1.2 Non-double-charm background

The NDC background in the $B^+ \to D_s^+ D_s^- K^+$ data contains two categories of candidates: the single charm decay with only one real D_s meson reconstructed, *e.g.* $B^+ \to K^- K^+ \pi^+ D_s^- K^+$, and the charmless decay with no real D_s meson reconstructed, $B^+ \to K^- K^+ \pi^+ K^+ K^- \pi^- K^+$. The NDC background can be suppressed by requiring a proper distance of the B^+ and D_s vertices. In this analysis, $dz/d\sigma_{dz}$ defined in Eq. 4.3 is used. The thresholds are set to > 2 for both D_s^+ and D_s^- candidates as listed in Table 4.4. To verify this requirement, the B^+ MM distribution is investigated for the candidates in the D_s^+ or D_s^- MM sideband under different dz/σ_{dz} cuts. Other selection criteria except the D_s^+ and D_s^- signal mass windows are the same as the nominal procedure discussed in Sec. 4.2. Multiple candidates are not removed, either. A proper criterion of $dz/d\sigma_{dz}$ should sufficiently suppress the reconstructed B^+ MM peak due to the NDC background, while keeping as many real $B^+ \to D_s^+ D_s^- K^+$ signal candidates as possible. From the B^+

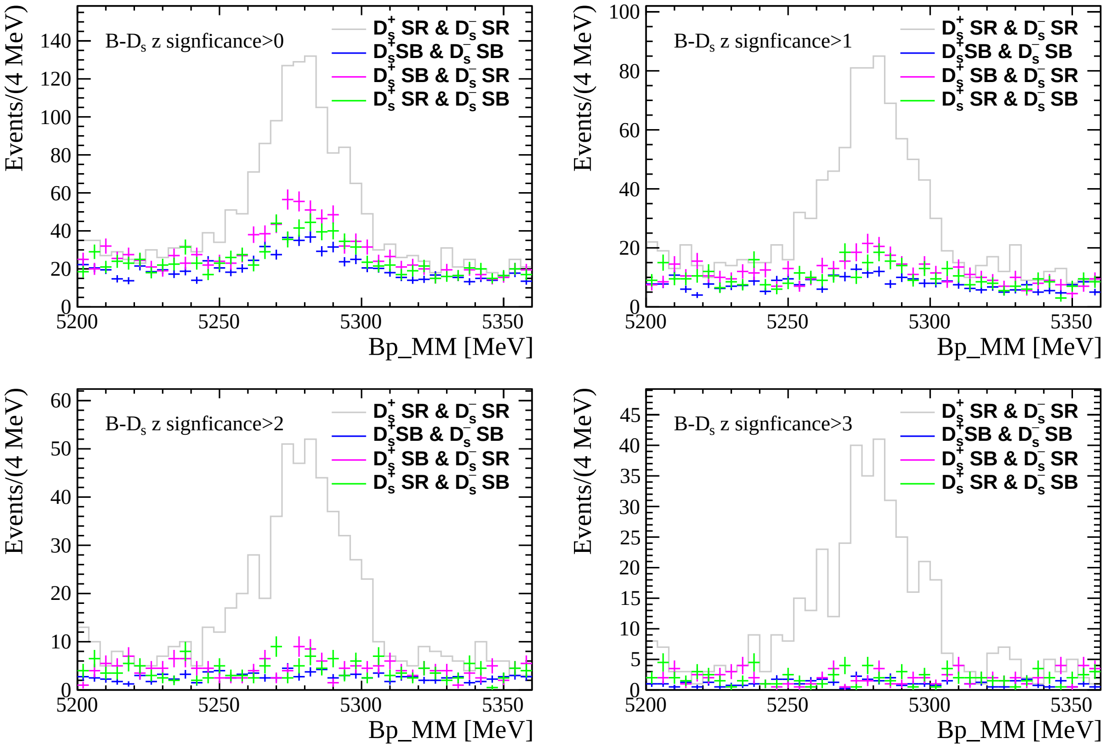

Figure 4.17 B^+ MM distributions under different $dz/d\sigma_{dz}$ cuts in the $B^+ \to D_s^+ D_s^- K^+$ data. The $D_s^\pm$ signal region (SR) is ±25 MeV around the $D_s^\pm$ known mass[1], whilst the $D_s^\pm$ sideband (SB) is 30−80 MeV away. The distributions in each region is scaled by the areas ratio of the corresponding region and the D_s^+ &D_s^- signal region with both D_s^+ and D_s^- in the ±25 MeV range around the $D_s^\pm$ known mass.

MM distributions in Fig. 4.17, it is seen $dz/\sigma_{dz} > 2$ is an adequate criterion.

The yield of the residual NDC background is estimated using the candidates shown in Fig. 4.18, including two regions: a. one D_s is in the D_s signal region, ±25 MeV around the $D_s^\pm$ known mass[1], and the other in the sideband, 30 − 80 MeV away from the $D_s^\pm$ known mass[1]; b. Both D_s^+ and D_s^- are in the sidebands. The corresponding $D_s^\pm$ mass distributions are shown in Fig. 4.18. In each region, the B^+ signal yield is evaluated using a simple fit. The signal is modeled by a Gaussian function with its mean set to the B^+ known mass[1] and width set to the typical mass resolution of 13 MeV obtained from MC simulation. The background is described by an exponential function with the parameter λ free. A fit to the data in the D_s^+ &D_s^- signal region filled by red in Fig. 4.18, is performed to obtain the real $B^+ \to D_s^+ D_s^- K^+$ signal yield, serving as the comparison. The fit results are shown in Fig. 4.19, and the resulting yields are listed in Table 4.8. Both the green and blue regions contain single charm and charmless backgrounds. The addition of the two yields scaled to the value in the D_s^+ &D_s^- signal region gives the estimation of the single charm background yield but counts the charmless background twice, one of which

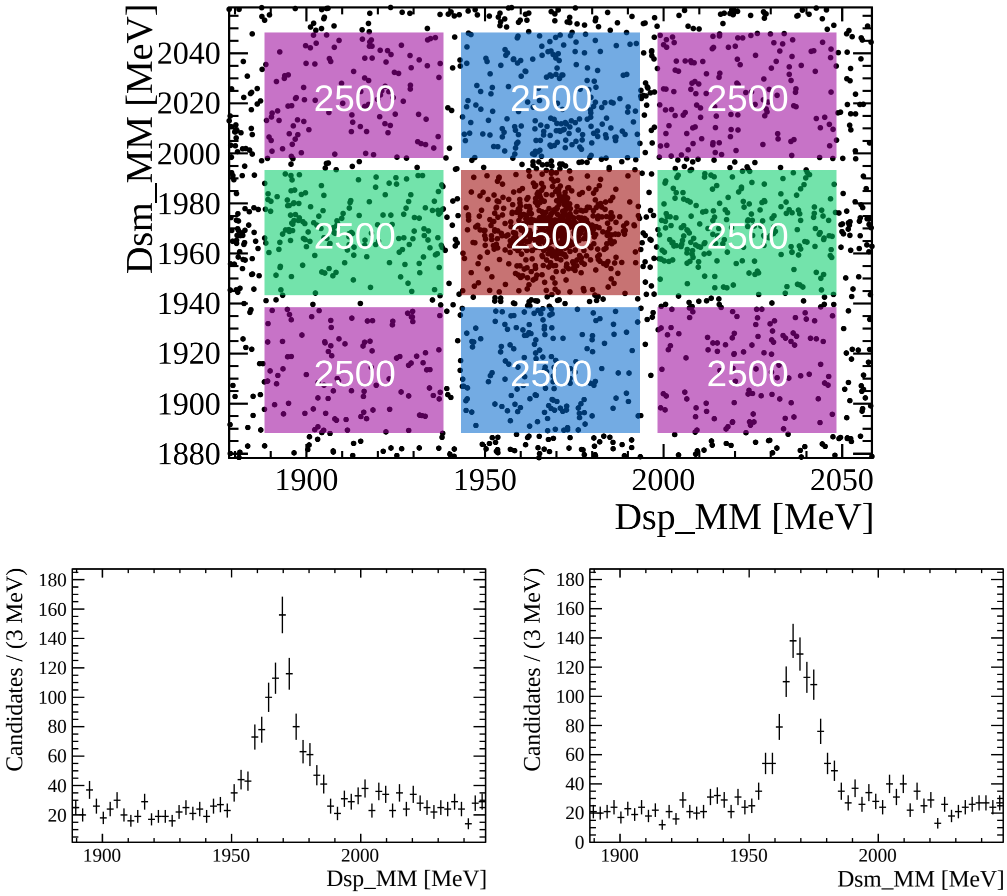

Figure 4.18 $D_s^\pm$ mass regions (top) and distributions (bottom) in the NDC background estimation for the $B^+ \to D_s^+ D_s^- K^+$ channel. The $D_s^\pm$ signal region is ±25 MeV around the $D_s^\pm$ known mass[1], whilst the $D_s^\pm$ mass sideband is 30 − 80 MeV away.

needs to be subtracted, with the charmless background yield estimated in the D_s^+ &D_s^- sidebands filled by pink in Fig. 4.18. Therefore, the NDC background yield in the D_s^+ &D_s^- signal region is estimated as

$$
\begin{aligned}
n_{\text{NDC}} &= n_{\text{sig}}^{\text{green}} \cdot \frac{S_{\text{red}}}{S_{\text{green}}} + n_{\text{sig}}^{\text{blue}} \cdot \frac{S_{\text{red}}}{S_{\text{blue}}} - n_{\text{sig}}^{\text{pink}} \cdot \frac{S_{\text{red}}}{S_{\text{pink}}} \\
&= n_{\text{sig}}^{\text{a}} \cdot \frac{S_{\text{sig}}}{S_{\text{a}}/2} - n_{\text{sig}}^{\text{b}} \cdot \frac{S_{\text{sig}}}{S_{\text{b}}},
\end{aligned}
\tag{4.4}
$$

where $n_{\text{sig}}^{\text{x}}$ is the B^+ signal yield for region x, and S_{x} is its area, corresponding to all the rectangles filled by the corresponding color(s): $S_{\text{a}} = 2S_{\text{green}} = 2S_{\text{blue}}$, $S_b = S_{\text{pink}}$ and $S_{\text{sig}} = S_{\text{red}}$. The NDC background ratio in the D_s^+ &D_s^- region, $f_{\text{NDC}} = n_{\text{NDC}}/n_{\text{sig}}$, is also listed in Table 4.8. The NDC background ratio will be used in the branching fraction calculation to subtract the NDC contribution in Sec. 4.5.2.

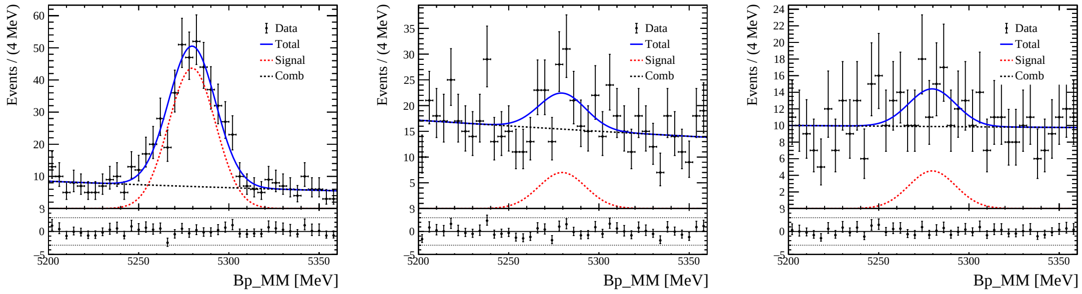

Figure 4.19 B^+ MM fit results for the $B^+ \to D_s^+ D_s^- K^+$ channel. Left: D_s^+ &D_s^- signal region. Middle: D_s^+ or D_s^- signal region. Right: D_s^+ &D_s^- sideband.

Table 4.8 Results of the B^+ mass fit for the $B^+ \to D_s^+ D_s^- K^+$ NDC background estimation. Regions a and b are described in the text. n_{sig} and n_{bkg} are the fitted signal and background yields for each region, and λ is the parameter of the exponential function. The quantity n_{NDC} is the estimated NDC background yield in the D_s^+ &D_s^- signal region. The NDC background ratio is obtained as $f_{\text{NDC}} = n_{\text{NDC}}/n_{\text{sig}}$.

Region	n_{sig}	n_{bkg}	λ (MeV^{-1})
a	57.0 ± 17.7	618.0 ± 29.4	$(-1.3 \pm 0.9) \times 10^{-3}$
b	36.9 ± 14.5	395.1 ± 23.7	$(-0.2 \pm 1.1) \times 10^{-3}$
Signal	355.7 ± 22.7	276.2 ± 20.9	$(-2.7 \pm 1.3) \times 10^{-3}$
n_{NDC}	19.3 ± 9.5		
f_{NDC} (%)	5.4 ± 2.7		

4.3.2 Backgrounds in the $B^+ \to D^+ D^- K^+$ data

4.3.2.1 Partially reconstructed and misidentified backgrounds

Partially reconstructed background in $B^+ \to D^+ D^- K^+$ data has been thoroughly investigated in Refs.[13-14]. It is found that all the partially reconstructed backgrounds can be sufficiently excluded by requiring $m(D^+ D^- K^+) > 5220$ MeV. Therefore, the mass window for the $B^+ \to D^+ D^- K^+$ channel is chosen to be $-60(+80)$ MeV around the known B^+ mass[1]. Similar to the $B^+ \to D_s^+ D_s^- K^+$ channel, the misidentified background in the $B^+ \to D^+ D^- K^+$ channel is also expected to be negligible.

4.3.2.2 Non-double-charm background

Analogous to the $B^+ \to D_s^+ D_s^- K^+$ channel, The $dz/d\sigma_{dz} > 2$ requirement can also sufficiently suppress the NDC background in the $B^+ \to D^+ D^- K^+$ data, as shown in Fig. 4.20. The amount of the residual NDC background is estimated using the same method as that for the $B^+ \to D_s^+ D_s^- K^+$ channel. The corresponding regions and $D^\pm$ mass

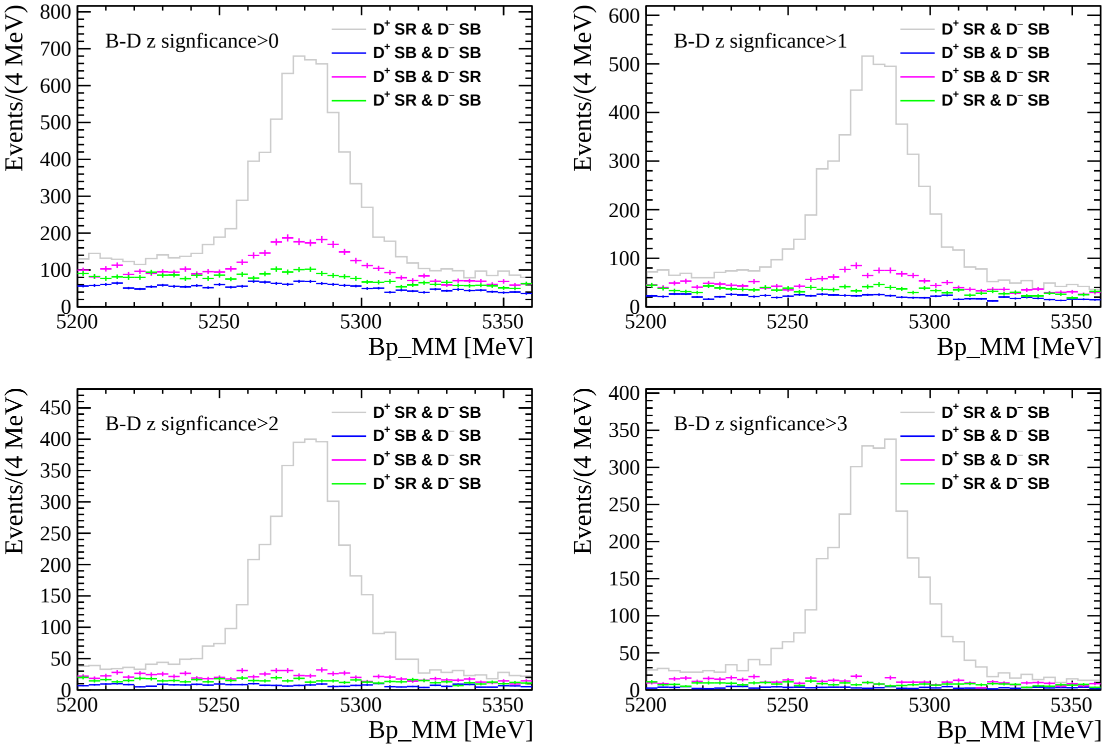

Figure 4.20 B^+ MM distributions under different $dz/d\sigma_{dz}$ cuts in the $B^+ \to D^+ D^- K^+$ data. The $D^\pm$ signal region (SR) is ±25 MeV around the $D^\pm$ known mass[1], whilst the D^+ sideband (SB) is 30−80 MeV away. The distributions in each region is scaled by the areas ratio of the corresponding region and the D^+ &D^- signal region with both D^+ and D^- in the ±25 MeV range around the $D^\pm$ known mass.

distributions are shown in Fig. 4.21. The B^+ mass fit results are shown in Fig. 4.22, and the determined yields are listed in Table 4.9. The NDC background will be taken into account in branching fraction calculation in Sec. 4.5.2.

4.4 Signal extraction

The B^+ mass fits are performed on the $B^+ \to D_s^+ D_s^- K^+$ and $B^+ \to D^+ D^- K^+$ data to estimate signal yields. The determined PDFs are used to determine the signal weights in the *sPlot* method[174] to subtract the combinatorial background in the Dalitz-plot distributions. In the fits, the Run1&2 data are combined together as a single input for the two channels.

The fit strategy is the same as that in the $B^0 \to D^+ D^- K^+ \pi^-$ analysis described in Sec. 3.4. The unbinned extended maximum likelihood method is employed in the fit. The signal model is the sum of two CB functions with tails on the opposite sides, and the background model is an exponential function. Before fitting to data, the tail parameters of the signal model are fixed to the values obtained from the fit to the MC sample. Alternative

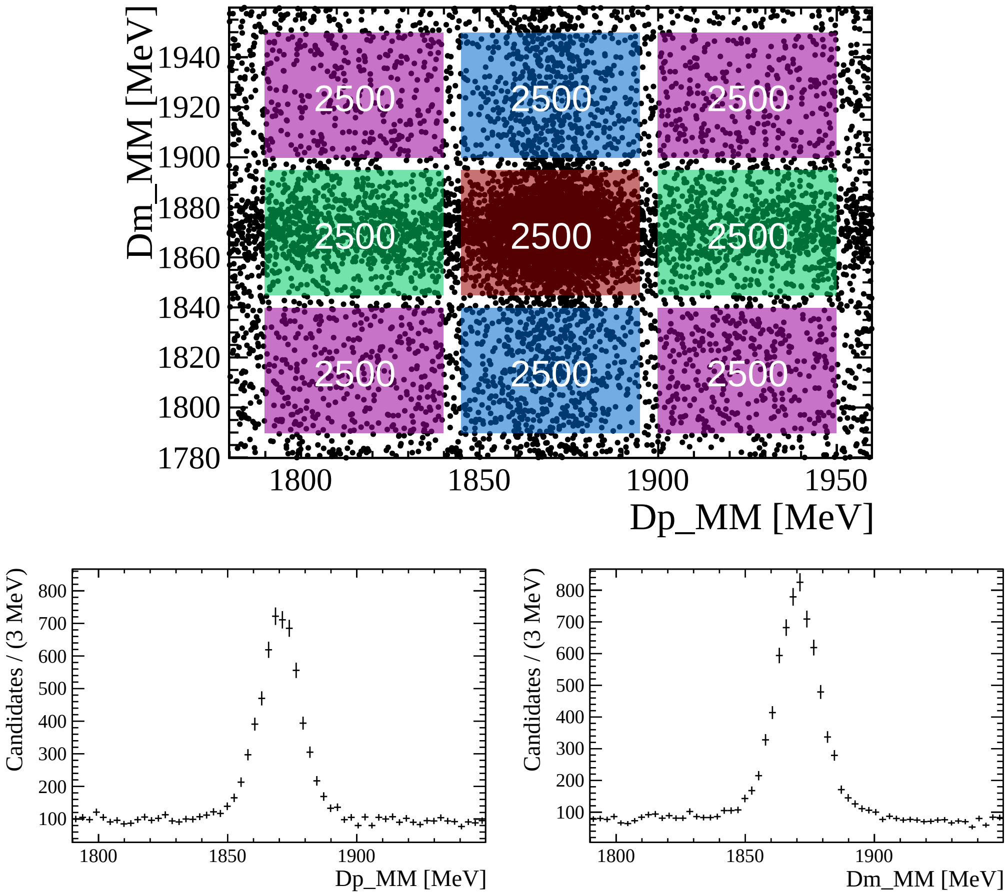

Figure 4.21 $D^\pm$ mass regions (top) and distributions (bottom) in the NDC background estimation for the $B^+ \to D^+ D^- K^+$ channel. The $D^\pm$ signal region is ±25 MeV around the $D^\pm$ known mass[1], whilst the $D^\pm$ mass sideband is 30 − 80 MeV away.

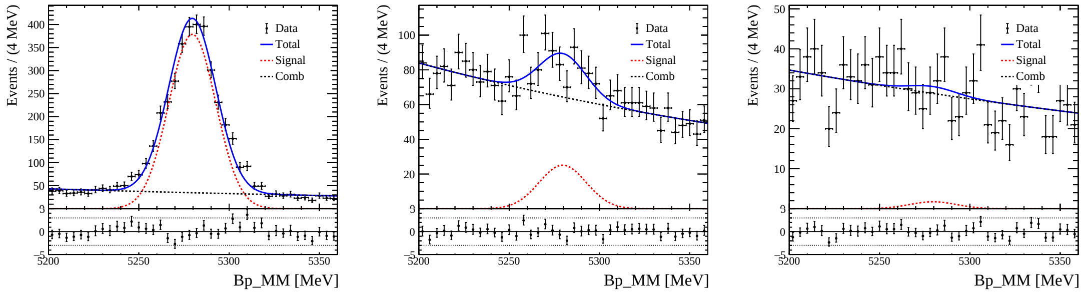

Figure 4.22 B^+ MM fit results for the $B^+ \to D^+ D^- K^+$ channel. Left: D^+ & D^- signal region. Middle: D^+ or D^- signal region. Right: D^+ & D^- sideband.

Table 4.9 Results of the B^+ mass fits for the $B^+ \to D^+ D^- K^+$ NDC background estimation. Regions a and b are described in the text. n_{sig} and n_{bkg} are the fitted signal and background yields for each region, and λ is the parameter of the exponential function. n_{NDC} is the estimated NDC background yield in the D^+ &D^- signal region. The NDC background ratio, $f_{\text{NDC}} = n_{\text{NDC}}/n_{\text{sig}}$, is shown in the last row.

Case	n_{sig}	n_{bkg}	λ (MeV^{-1})
Region a	204.2 ± 36.4	2601.8 ± 61.0	$(-3.3 \pm 0.4) \times 10^{-3}$
Region b	14.2 ± 22.2	1159.0 ± 39.9	$(-2.3 \pm 0.6) \times 10^{-3}$
Signal	3084.7 ± 63.7	1399.6 ± 48.8	$(-2.7 \pm 0.6) \times 10^{-3}$
n_{NDC}	98.6 ± 19.0		
f_{NDC} (%)	3.2 ± 0.6		

models are tested to evaluate the systematic effect of the choices of the fit models on the branching fraction ratio in Secs. 4.5.3.

4.4.1 B^+ mass fit for the $B^+ \to D_s^+ D_s^- K^+$ decay

The fit is applied to the $B^+ \to D_s^+ D_s^- K^+$ candidates after all the selections. The fit range is ±80 MeV around the known B^+ mass. The signal yield is 360 ± 22 in the data, where the uncertainty is statistical only. The purity in the ±20 MeV window around the B^+ mass peak is found to be 84.4%. The determined parameters are listed in Table 4.10, and the B^+ mass spectrum is shown in Fig. 4.23. The $D_s^+ D_s^-$, $D_s^- K^+$ and $D_s^+ K^+$ mass projections are shown in Fig. 4.24, where a significant peak is seen near the $D_s^+ D_s^-$ mass threshold. The Dalitz-plot distributions are shown in Fig. 4.25. It is seen that the near-threshold peak appears as a band in the $m(D_s^+ D_s^-)^2$ axis, indicting resonant nature of it. To verify that the peaking structure in the $D_s^+ D_s^-$ mass is not due to combinatorial background, the mass projections and Dalitz-plot distributions for the candidates in the B^+ upper sideband are shown in Fig. 4.26, where no near-threshold peak is seen. An amplitude analysis is performed to measure the properties of the near-threshold structure, which is presented in Sec. 4.6.

4.4.2 B^+ mass fit for the $B^+ \to D^+ D^- K^+$ decay

The fit range for the $B^+ \to D^+ D^- K^+$ channel is chosen to be +80/−60 MeV around the known B^+ mass[1] to exclude the peaking backgrounds as discussed in Sec. 4.3.2. About 3215 ± 65 signal candidates are obtained in the data. The purity in the ±20 MeV window around the B^+ mass peak is found to be 91%. The determined parameters are

Table 4.10 Fit parameters in the $B^+ \to D_s^+ D_s^- K^+$ channel.

Parameter	MC simulation	Data
a	0.5 (fixed)	0.5 (fixed)
N_{sig}	114879.50 ± 338.94	360.38 ± 21.81
N_{bkg}	-	254.61 ± 19.23
m_0(MeV)	5278.99 ± 0.02	5278.43 ± 0.48
σ_1(MeV)	5.00 ± 0.04	7.94 ± 1.87
σ_2(MeV)	7.67 ± 0.05	7.11 ± 1.69
α_1	1.92 ± 0.05	1.92 (fixed)
α_2	-2.51 ± 0.04	-2.51 (fixed)
n	2.01 ± 0.11	2.01 (fixed)
λ(MeV^{-1})	-	$(-0.77 \pm 13.83) \times 10^{-4}$

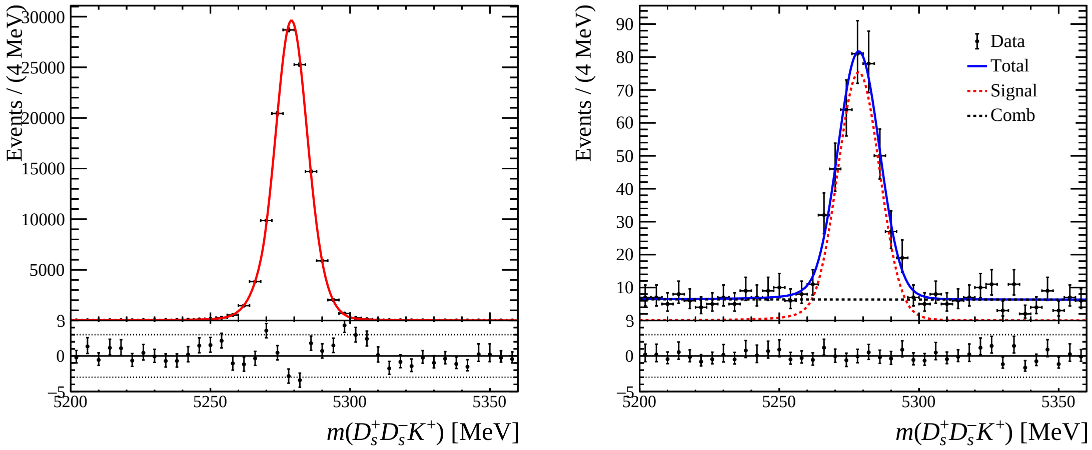

Figure 4.23 B^+ mass fit results for the selected $B^+ \to D_s^+ D_s^- K^+$ candidates for MC simulation (left) and data (right).

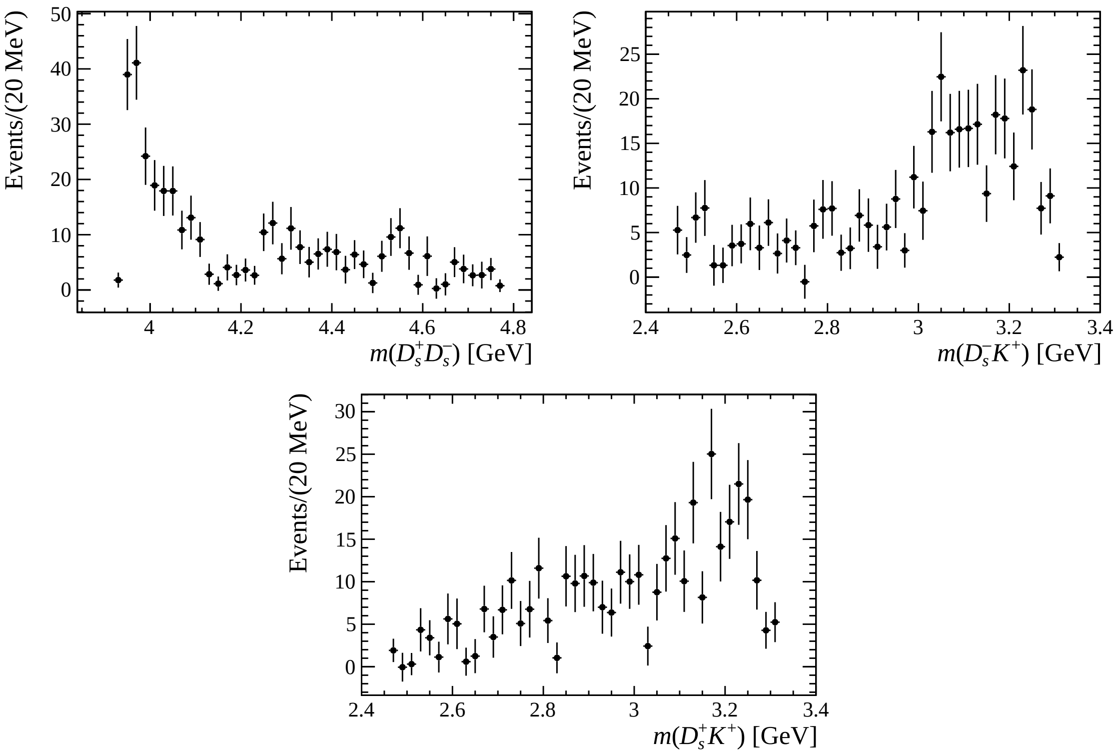

Figure 4.24 Mass projections in the $B^+ \to D_s^+ D_s^- K^+$ data. The background is statistically subtracted using the *sPlot* method[174].

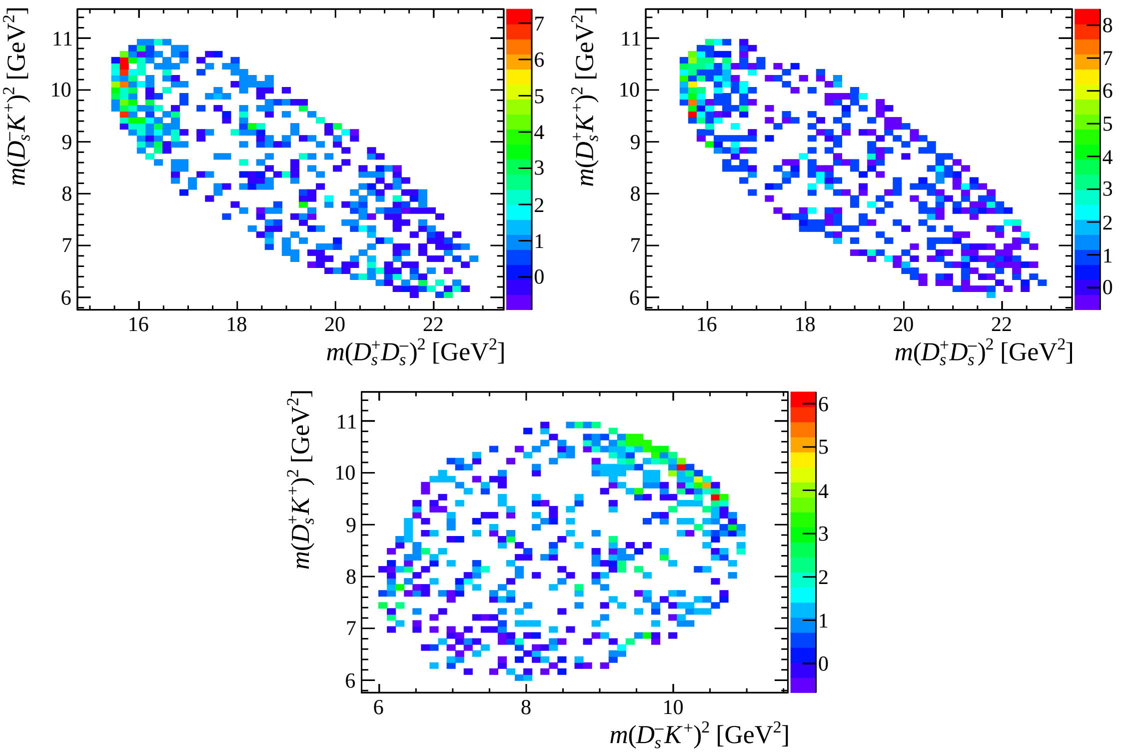

Figure 4.25 Dalitz-plot distributions in the $B^+ \to D_s^+ D_s^- K^+$ data. The background is statistically subtracted using the *sPlot* method[174].

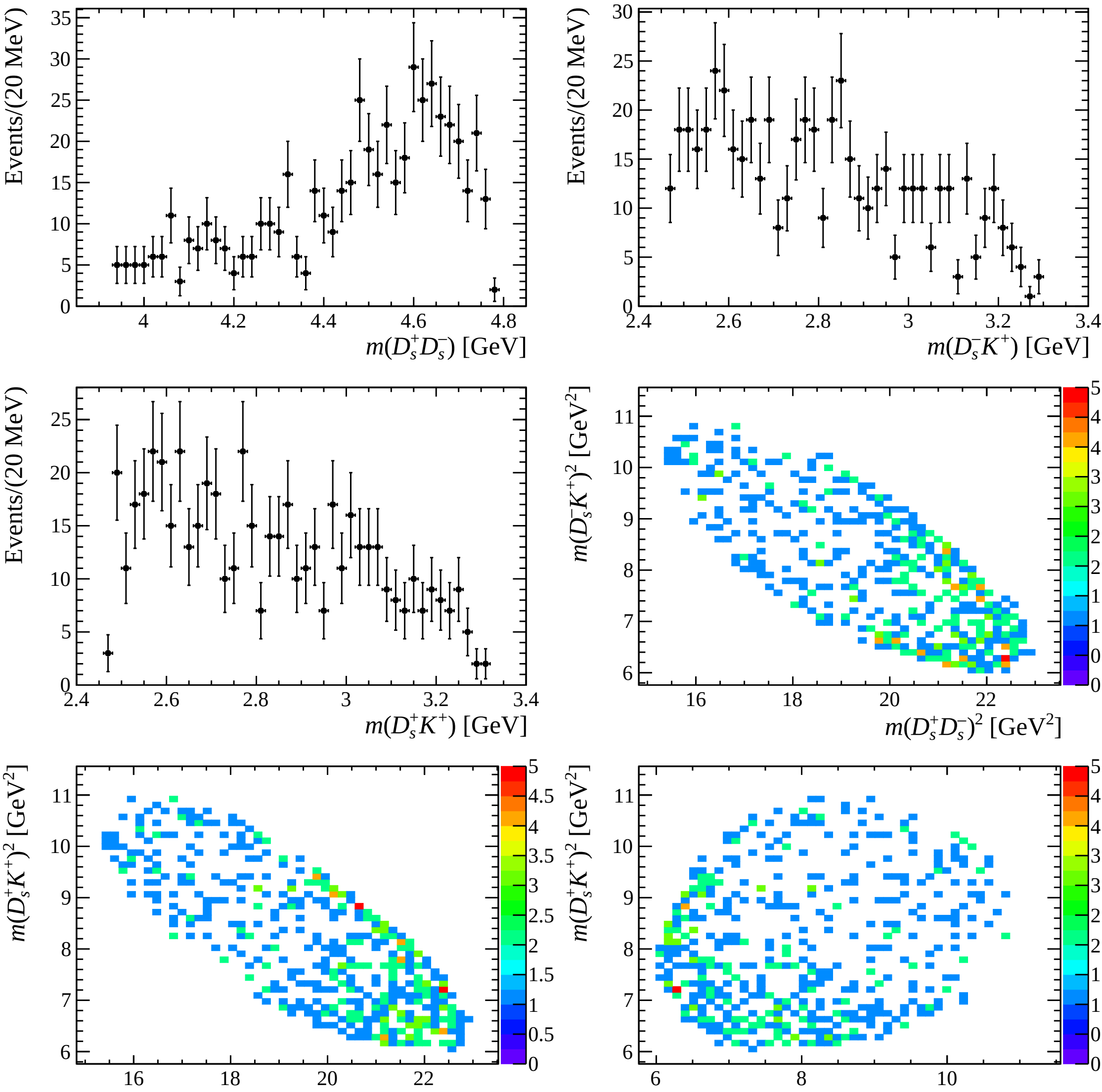

Figure 4.26 Mass projections and Dalitz-plot distributions for the $B^+ \to D_s^+ D_s^- K^+$ data in the B^+ upper mass sideband by requiring $m(D_s^+ D_s^- K^+) > 5300$ MeV.

Table 4.11 Fit parameters in the $B^+ \to D^+ D^- K^+$ channel.

Parameter	MC simulation	Data
a	0.5 (fixed)	0.5 (fixed)
N_{sig}	47933.14 ± 218.93	3215.43 ± 64.80
N_{bkg}	-	1046.63 ± 45.06
m_0(MeV)	5279.42 ± 0.04	5278.53 ± 0.16
σ_1(MeV)	5.71 ± 0.06	6.14 ± 0.27
σ_2(MeV)	9.10 ± 0.08	10.23 ± 0.42
α_1	2.16 ± 0.09	2.16 (fixed)
α_2	-2.74 ± 0.08	-2.74 (fixed)
n	1.49 ± 0.19	1.49 (fixed)
λ(MeV^{-1})	-	$(-37.91 \pm 8.07) \times 10^{-4}$

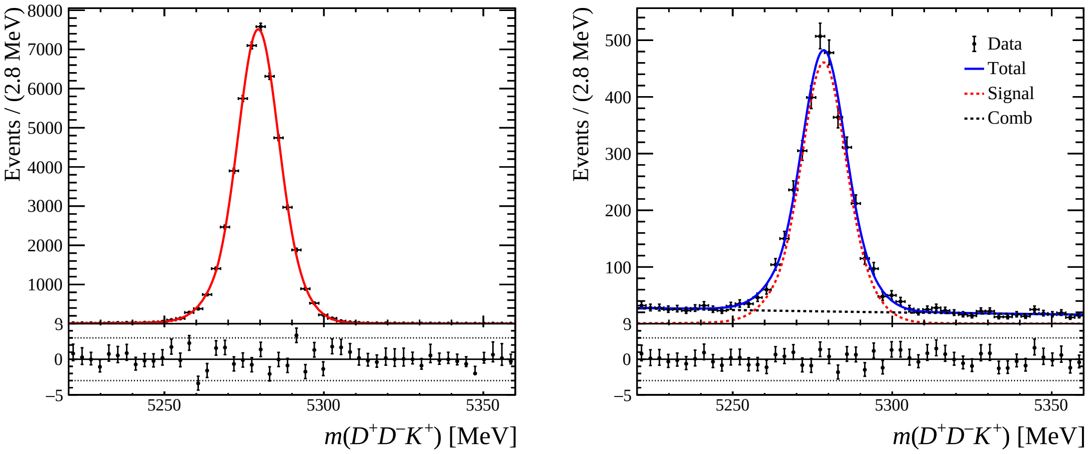

Figure 4.27 The B^+ mass fit results for the selected $B^+ \to D^+ D^- K^+$ candidates for MC simulation (left) and data (right).

listed in Table 4.11, and the B^+ mass spectrum is shown in Fig. 4.27. The $D^+ D^-$, $D^- K^+$ and $D^+ K^+$ mass projections are shown in Fig. 4.28. Several peaking structures are seen in the $D^+ D^-$ and $D^- K^+$ mass distributions, and they correspond to bands in the Dalitz-plot distributions shown in Fig. 4.29, indicating their resonant nature. These structures are studied in the previous LHCb analyses[13-14], which are briefly reviewed in Secs. 1.3.3 and 1.4 of Chapter 1.

4.4.3 Check on possible fit bias

The potential bias on the signal yields could leads to the bias on the branching fraction ratio, so it is checked using the toy MC method. 10K sets of toy B^+ mass values are

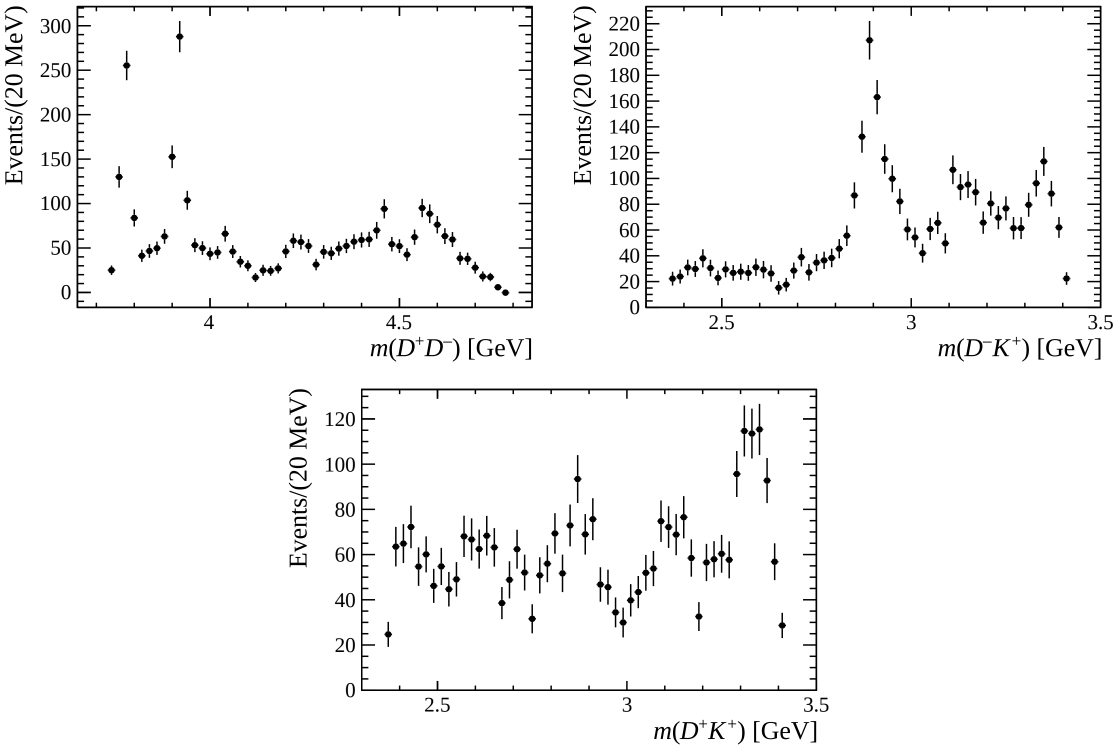

Figure 4.28 Mass projections in the $B^+ \to D^+ D^- K^+$ data. The background is statistically subtracted using the *sPlot* method[174].

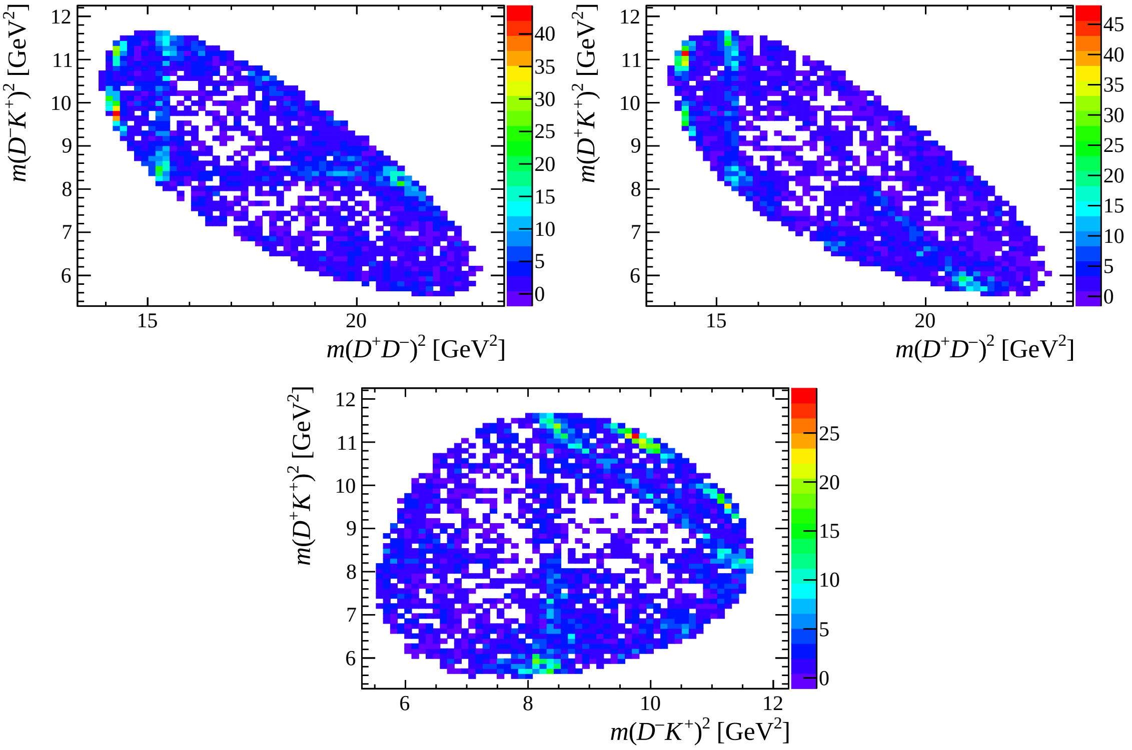

Figure 4.29 Dalitz-plot distributions in the $B^+ \to D^+ D^- K^+$ data. The background is statistically subtracted using the *sPlot* method[174].

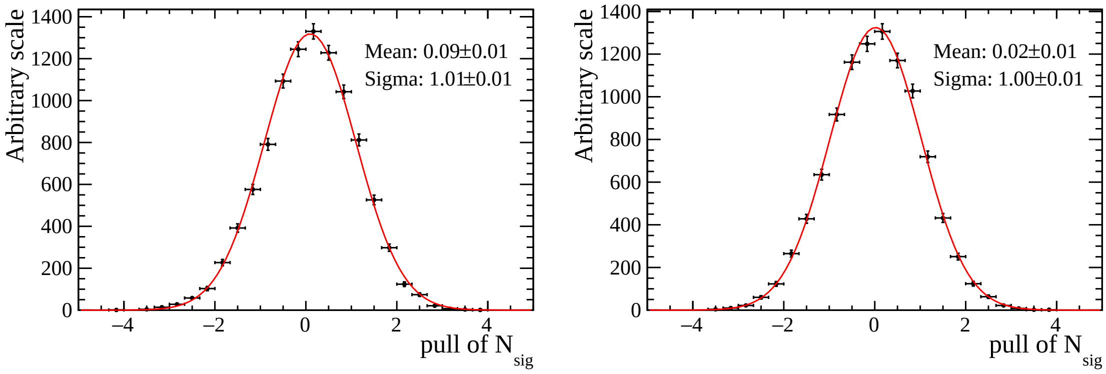

Figure 4.30 Pull distributions of the 10K toy fits for the $B^+ \to D_s^+ D_s^- K^+$ (left) and $B^+ \to D^+ D^- K^+$ (right) channels. No obvious bias is seen for the $B^+ \to D^+ D^- K^+$ channel, but there is a 9% bias observed in the $B^+ \to D_s^+ D_s^- K^+$ channel.

generated randomly according to the determined signal and background PDFs as shown in Figs. 4.23 and 4.27 for the $B^+ \to D_s^+ D_s^- K^+$ and $B^+ \to D^+ D^- K^+$ channels, respectively. The number of signal and background candidates in each set is fluctuated according to a Poisson distribution with the mean set to the corresponding yields listed in Tables 4.10 and 4.11. Then the same fit procedure as described in Secs. 4.4.1 and 4.4.2, is applied to these generated samples. The pull of the signal yield for the i-index toy fit is then calculated as $\frac{N^i_{sig} - N_{sig}}{\sigma_{N^i_{sig}}}$, where N^i_{sig} and $\sigma_{N^i_{sig}}$ are the signal yield and the statistical uncertainty determined in each toy fit, and N_{sig} is the input yield to generate the toys. The pull distributions are shown in Fig. 4.30 for the $B^+ \to D_s^+ D_s^- K^+$ and $B^+ \to D^+ D^- K^+$ channels. No obvious bias is seen for the $B^+ \to D^+ D^- K^+$ channel, but there is a 9% bias observed in the $B^+ \to D_s^+ D_s^- K^+$ channel, for which a correction factor is introduced in the branching fraction calculation in Sec. 4.5.2.

4.4.4 Independence check of the B^+ mass and the Dalitz-plot variables

The *sPlot* method[174] is employed to subtract the combinatorial background in the branching fraction measurement as illustrated in Eq. 4.8. To verify that the subtraction does not bring any bias, the independence of the B^+ mass (the discriminating variable) and the Dalitz-plot variables (the control variables) needs to be checked, which is performed by comparing the background-subtracted distributions of the Dalitz-plot variables with the signal weights determined from B^+ mass fits in a set of regions of the Dalitz-plot variables and from a single B^+ mass fit.

For the $B^+ \to D_s^+ D_s^- K^+$ channel, the binning edges of the Dalitz-plot variables to

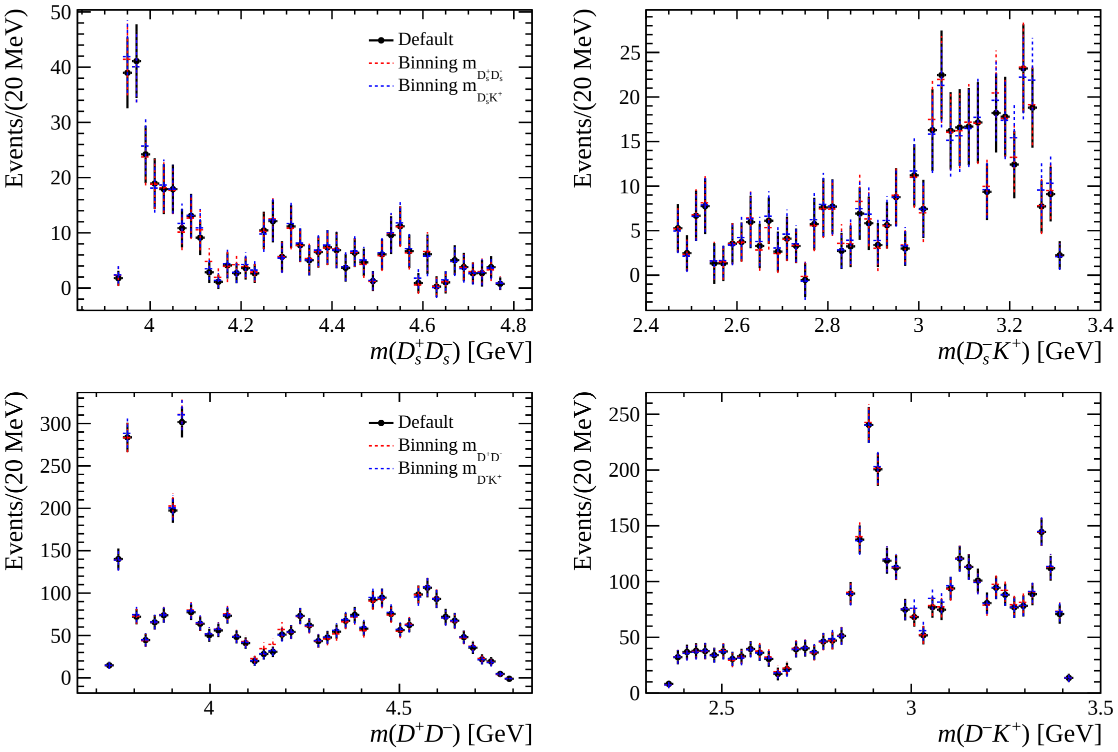

Figure 4.31 Background-subtracted mass projections in the $B^+ \to D_s^+ D_s^- K^+$ (top) and $B^+ \to D^+ D^- K^+$ (bottom) data, where the signal weights are obtained using three different strategies as described in text.

split the data sample are

$$(3.90, 3.95, 4.00, 4.05, 4.10, 4.20, 4.40, 4.65, 4.65, 4.90)\ \text{GeV}$$

in the $D_s^+ D_s^-$ mass, and

$$(2.40, 2.60, 2.70, 2.90, 3.00, 3.05, 3.10, 3.20, 3.25, 3.35)\ \text{GeV}$$

in the $D_s^- K^+$ mass. The background-subtracted distributions of the $D_s^+ D_s^-$ and $D_s^- K^+$ masses with signal weights determined using the default single B^+ mass fit to the whole data sample, and B^+ mass fits in different regions of the $D_s^+ D_s^-$ and $D_s^- K^+$ masses are compared in Fig. 4.31. Good agreement is seen between the distributions with signal weights determined from the three strategies, indicating no evident dependence between the B^+ mass and the Dalitz-plot variables.

Analogously, the binning schemes for the $B^+ \to D^+ D^- K^+$ channel are

$$(3.7, 3.85, 4.0, 4.1, 4.2, 4.3, 4.4, 4.5, 4.6, 4.7, 4.9)\ \text{GeV}$$

for the $D^+ D^-$ mass, and

$$(2.3, 2.5, 2.6, 2.7, 2.8, 2.9, 3.0, 3.1, 3.2, 3.3, 3.5)\ \text{GeV}$$

in the $D^- K^+$ mass. The background-subtracted distributions of the $D^+ D^-$ and $D^- K^+$ masses are shown in Fig. 4.31. The consistency of the distributions for three weighting strategies validate the independence of the B^+ mass and the Dalitz-plot variables.

4.5 Branching fraction measurement

The branching fraction of the $B^+ \to D_s^+ D_s^- K^+$ decay is an essential parameter to evaluate the partial width fractions of the resonances in the $D_s^+ D_s^-$ system and thus is important information to help interpret these states. In this section, the relative branching fraction of the $B^+ \to D_s^+ D_s^- K^+$ decay with respect to that of the $B^+ \to D^+ D^- K^+$ process is measured according to

$$\mathcal{R} \equiv \frac{\mathcal{B}(B^+ \to D_s^+ D_s^- K^+)}{\mathcal{B}(B^+ \to D^+ D^- K^+)} = \frac{N_{\text{sig}}^{\text{corr}}}{N_{\text{con}}^{\text{corr}}} \left[\frac{\mathcal{B}(D^+ \to K^- \pi^+ \pi^+)}{\mathcal{B}(D_s^+ \to K^- K^+ \pi^+)}\right]^2 . \tag{4.5}$$

The known branching fractions are taken as the world-average values[1], which are

$$\begin{aligned} \mathcal{B}(B^+ \to D^+ D^- K^+) &= (2.2 \pm 0.7) \times 10^{-4} , \\ \mathcal{B}(D^+ \to K^- \pi^+ \pi^+) &= (9.38 \pm 0.16)\% , \\ \mathcal{B}(D_s^+ \to K^- K^+ \pi^+) &= (5.39 \pm 0.15)\% , \end{aligned} \tag{4.6}$$

The quantities $N_{\text{sig}}^{\text{corr}}$ and $N_{\text{con}}^{\text{corr}}$ are efficiency-corrected yields for the $B^+ \to D_s^+ D_s^- K^+$ and $B^+ \to D^+ D^- K^+$ decays, respectively, which are defined as

$$N_{\text{sig}}^{\text{corr}} = \sum_i \frac{w_{\text{sig},\,i}}{\epsilon_{\text{sig},\,i}(m^2(D_s^+ D_s^-), m^2(D_s^- K^+))} , \tag{4.7}$$

$$N_{\text{con}}^{\text{corr}} = \sum_i \frac{w_{\text{con},\,i}}{\epsilon_{\text{con},\,i}(m^2(D^+ D^-), m^2(D^- K^+))} , \tag{4.8}$$

where the index i runs over all the candidates of the selected data in the corresponding channel. The weights $w_{\text{sig},\,i}$ and $w_{\text{con},\,i}$ are assigned to each candidate to statistically subtract the background contributions in the two channels using the *sPlot* method[174]. The single-event efficiencies $\epsilon_{\text{sig},\,i}$ and $\epsilon_{\text{con},\,i}$ are parameterized as functions of the Dalitz-plot variables of the two decays, and are determined using MC samples. The statistical uncertainties on the efficiency-corrected yields are calculated as

$$\sigma(N_{\text{sig}}^{\text{corr}}) = \sqrt{\sum_i \left(\frac{w_{\text{sig},\,i}}{\epsilon_{\text{sig},\,i}(m^2(D_s^+ D_s^-), m^2(D_s^- K^+))}\right)^2} . \tag{4.9}$$

$$\sigma(N_{\text{con}}^{\text{corr}}) = \sqrt{\sum_i \left(\frac{w_{\text{con},\,i}}{\epsilon_{\text{con},\,i}(m^2(D^+ D^-), m^2(D^- K^+))}\right)^2} . \tag{4.10}$$

Table 4.12 Luminosities for each year. The numbers are taken from Ref.[194].

Year	11	12	15	16	17	18
Lumi (fb^{-1})	1.0	2.0	0.3	1.6	1.7	2.1

4.5.1 Efficiency determination

Efficiency is calculated using MC samples in different regions of the Dalitz plots. The efficiency for each year is at first determined. Then, the efficiencies for the Run 1 and Run 2 periods, which are the inputs for the branching fraction calculation, are obtained as the weighted-average of the efficiencies for the corresponding years in the two periods. The weights are chosen as the luminosities of these years, listed in Table 4.12.

Basically, only the total efficiency is required as the input for the branching fraction calculation. Nevertheless, to have a better understanding of the MC performance, efficiencies at several intermediate stages are also calculated, including

- ϵ_{geom}: geometric efficiency due to the LHCb acceptance.
- ϵ_{strip}: Stripping and reconstruction efficiency, defined as the probability of an event being correctly reconstructed and passing the Stripping criteria in Table 4.1, given that it is in the LHCb acceptance. ϵ_{strip} includes part of the trigger efficiency due to the imposed trigger requirement.
- ϵ_{off}: offline efficiency for an event passing the offline selection in Table 4.4 and the B^+ mass windows required in the B^+ mass fits in Sec. 4.4, given that it survives the Stripping selection.
- ϵ_{trig}: offline trigger efficiency for the requirements listed in Table 3.1, given that it is selected by the offline requirement.
- ϵ_{BDT}: BDTG classifier efficiency given that the events pass the offline trigger decisions.

4.5.1.1 Geometric efficiency

The geometric efficiency is determined using generator-level MC samples produced by Gauss with the same configurations described in Sec. 4.1. The determined efficiencies for the $B^+ \to D_s^+ D_s^- K^+$ and $B^+ \to D^+ D^- K^+$ decays in the Run 1 and Run 2 periods are shown in Fig. 4.32. It is seen that the geometric efficiency for the $B^+ \to D_s^+ D_s^- K^+$ decay is slightly larger than that of the $B^+ \to D^+ D^- K^+$ process. This is understood as that the slightly larger probability of the final-state particles in the $B^+ \to D^+ D^- K^+$ decay to

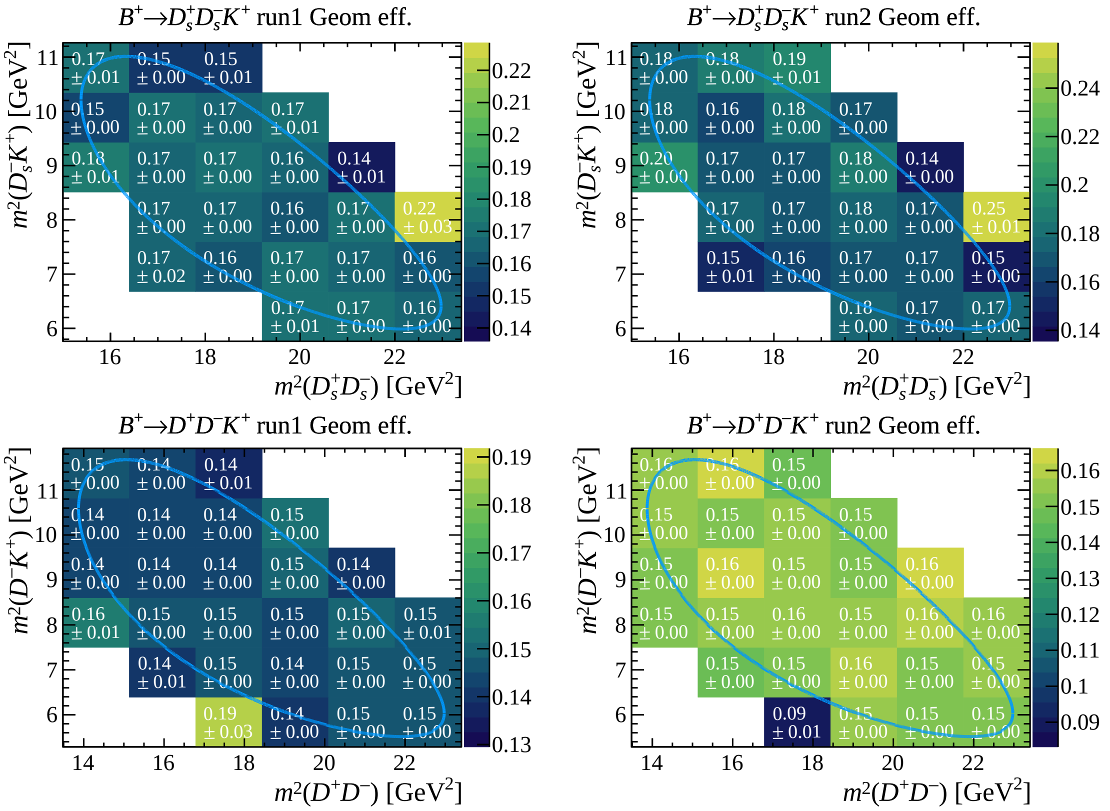

Figure 4.32 Geometric efficiencies for the $B^+ \to D_s^+ D_s^- K^+$ (top) and $B^+ \to D^+ D^- K^+$ (bottom) channels for Run1 (left) and Run2 (right).

fall outside the LHCb acceptance because they tends to have higher-p_{T} that results from the slightly larger phase space of the $B^+ \to D^+ D^- K^+$ and $D^+ \to K^- \pi^+ \pi^+$ decays. The geometric efficiency is slightly larger in Run 2 than that in Run 1, because the larger collision energy in Run 2 boosts the final-state particles in a more forward region.

4.5.1.2 Stripping and reconstruction efficiency

The $B^+ \to D_s^+ D_s^- K^+$ and $B^+ \to D^+ D^- K^+$ MC samples are filtered by the Stripping line, and the corresponding generator-level MC samples without the Stripping requirement are not available. Therefore, the generator-level MC samples used in the the geometric efficiency calculation are used to obtain the denominator of the Stripping and reconstruction efficiency. The number of the generated events are scaled to match that of the generated events in the MC samples listed in Tables 4.2 and 4.3. The Stripping and reconstruction efficiency is obtained as the ratio of the MC events in the fully simulated samples described in Sec. 4.1 without any offline selection applied, and the re-scaled generator-level MC sample. The efficiency maps are shown in Fig. 4.33.

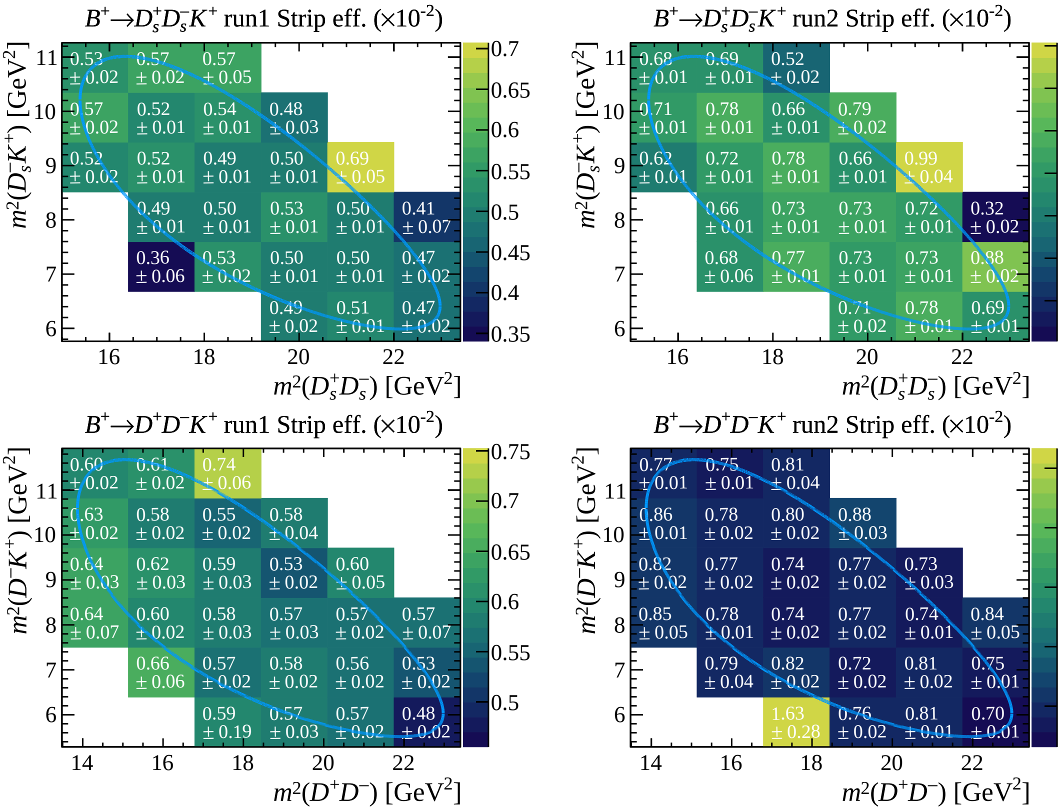

Figure 4.33 Stripping efficiencies for the $B^+ \to D_s^+ D_s^- K^+$ (top) and $B^+ \to D^+ D^- K^+$ (bottom) channels for Run1 (left) and Run2 (right).

4.5.1.3 Offline selection, offline trigger and BDTG efficiencies

The offline, offline trigger and BDTG efficiencies are determined using the MC samples after the Stripping selection. All of them are all given as the ratio of the numbers of the events with and without the concerned selection criteria, as defined in Sec. 4.5.1. The efficiencies at the three stages are shown in Figs. 4.34, 4.35 and 4.36, respectively.

It is known that the simulation does not correctly model the L0_Hadron_TOS trigger response, so the L0_Hadron_TOS efficiency obtained from MC simulation is biased. Fortunately, the bias is expected to be largely cancelled in the branching fraction ratio of the $B^+ \to D_s^+ D_s^- K^+$ and $B^+ \to D^+ D^- K^+$ decays as they have similar decay topology and final-state tracks. As mentioned above, in the default result, the offline trigger efficiency is directly determined using MC samples. An alternative data-driven method is tested in Sec. 4.5.3.1 to correct the L0_Hadron_TOS efficiency, and a systematic uncertainty is assigned.

It is seen that the BDTG efficiency for the $B^+ \to D^+ D^- K^+$ decay is extremely high. This is due to the quite low background level in the $B^+ \to D^+ D^- K^+$ data before the MVA selection and thus the quite loose BDTG working point.

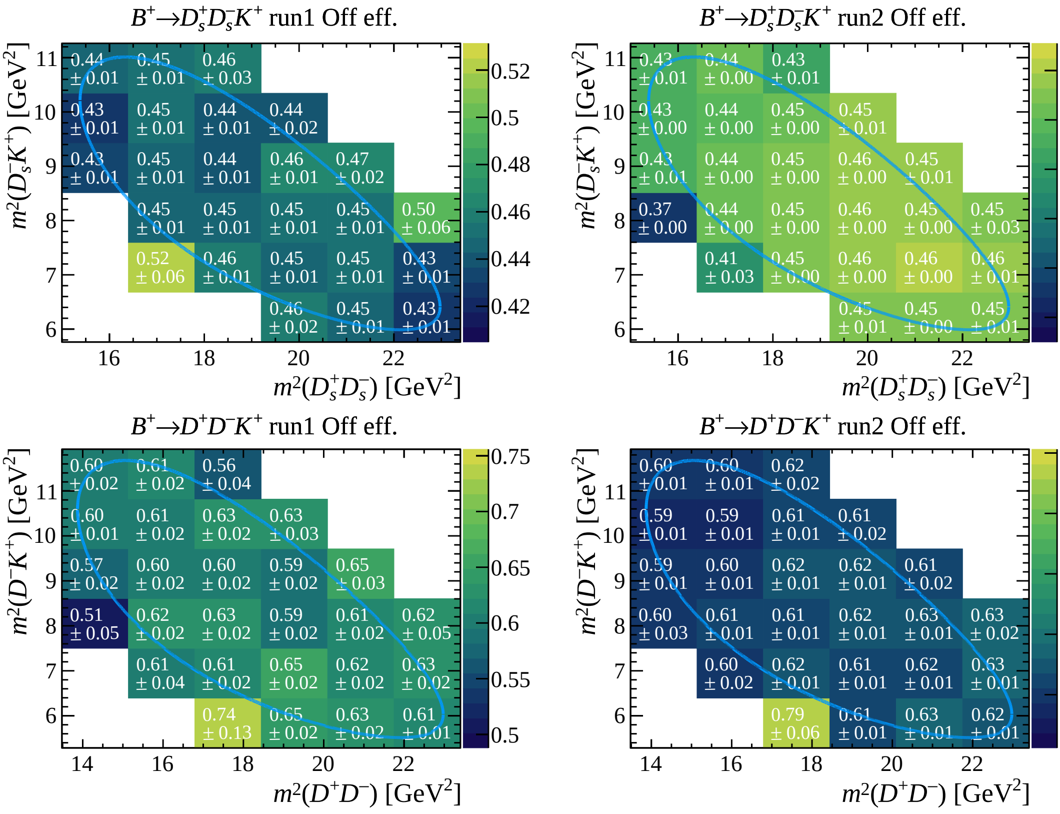

Figure 4.34 Offline selection efficiencies for the $B^+ \to D_s^+ D_s^- K^+$ (top) and $B^+ \to D^+ D^- K^+$ (bottom) channels for Run1 (left) and Run2 (right).

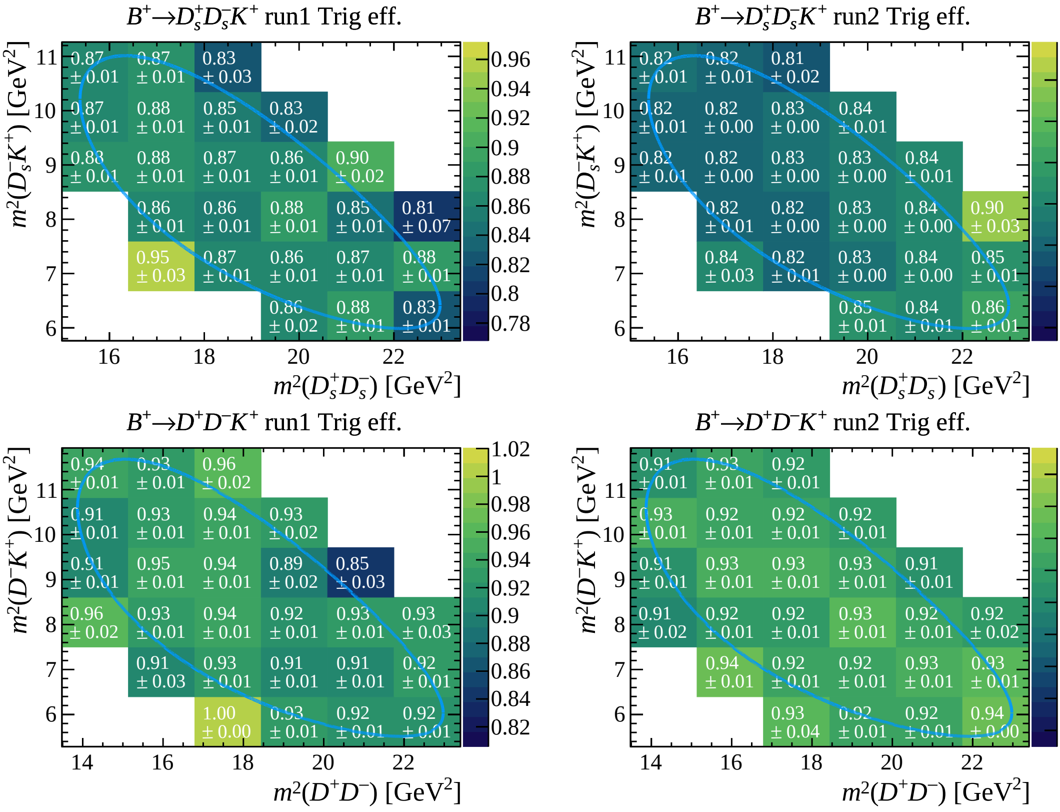

Figure 4.35 Offline trigger efficiencies for the $B^+ \to D_s^+ D_s^- K^+$ (top) and $B^+ \to D^+ D^- K^+$ (bottom) channels for Run1 (left) and Run2 (right).

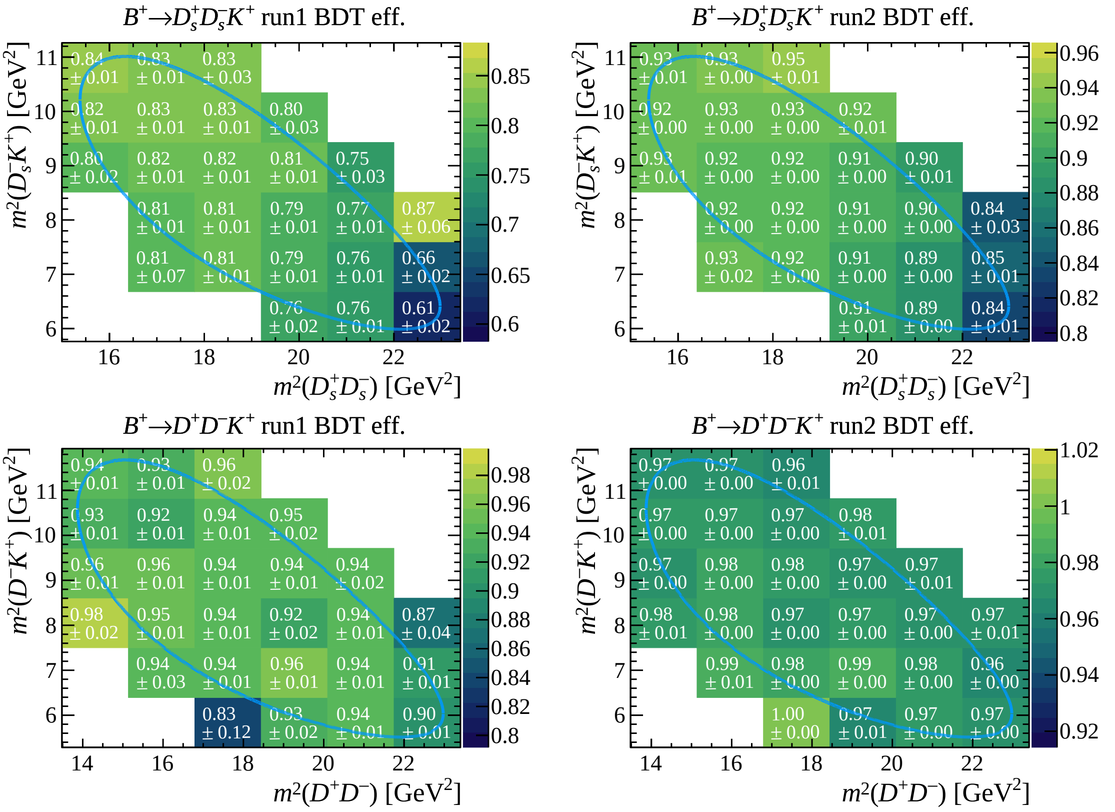

Figure 4.36 BDTG efficiencies for the $B^+ \to D_s^+ D_s^- K^+$ (top) and $B^+ \to D^+ D^- K^+$ (bottom) channels for Run1 (left) and Run2 (right).

4.5.1.4 Total efficiency

To calculate the total efficiency, the generator-level MC samples described in Sec. 4.5.1.1 without the LHCb acceptance are utilized to obtain the denominator, where the events in the LHCb acceptance are scaled to match the amount of generated events for the reconstructed MC samples. The reconstructed MC samples after all the selections are used to obtain the numerator. To obtain a smooth efficiency function in the phase space, the unbinned kernel density estimation (KDE) implanted in `Meerkat`[195] is employed to estimate the Dalitz-plot distributions in MC samples. The `Meerkat` package provides several novel techniques using the convolution of the approximate PDF and the KDE function to deal with the boundary problem in the traditional KDE method. In this analysis, the `BinnedKernelDensity` method is utilized, where the convolution is evaluated using MC integration and the function obtained from the convolution is approximated by the linear interpolation of binned nodes. Details can be found in Ref.[195]. The width of the kernel is chosen to be 2 GeV^2 and the MC events for the convolution is 5e4. These hyper parameters are varied to introduce a systematic uncertainty in Sec. 4.5.3.

To conveniently visualize and use the KDE functions that model the Dalitz-plot distributions in the denominator and numerator, the functions are projected into two-dimensional histograms with very fine binning (1000 bins for each axis). As the bin width is extremely narrow, the projected histograms are expected to not bring any loss of precision. The two histograms are scaled to match the events of the corresponding samples for the numerator and denominator, respectively, and their ratio is taken as the efficiency, as shown in the right column of Fig. 4.37. Total efficiencies obtained using the binned method, *i.e.* histograms, are shown in the left column, which are compared with the average KDE efficiencies in the corresponding bins, shown in text in the right column. Good agreements between the efficiencies from the histograms and the KDE method are seen.

4.5.2 Branching fraction ratio determination

The branching fraction ratio is determined following Eq. 4.5. The efficiency-corrected yields for the $B^+ \to D_s^+ D_s^- K^+$ and $B^+ \to D^+ D^- K^+$ channels are calculated using the signal weights obtained from the *sPlot* method[174] with the PDFs determined in the B^+ mass fits described in Secs. 4.4, and the phase-space-dependent efficiencies determined using the KDE method shown in Fig. 4.37,

$$\begin{aligned} N_{\mathrm{sig}}^{\mathrm{corr}} &= 950406.31 \pm 56534.18\,(\mathrm{stat}), \\ N_{\mathrm{con}}^{\mathrm{corr}} &= 5329569.64 \pm 103700.12\,(\mathrm{stat}). \end{aligned} \tag{4.11}$$

Before calculating the branching fraction ratio, two corrections are introduced. The first correction is to subtract the NDC background as described in Sec. 4.3, and the corresponding correction factor is $(1 - f_{\mathrm{NDC}}^{\mathrm{sig}})/(1 - f_{\mathrm{NDC}}^{\mathrm{con}})$ with the NDC background ratios taken from Tables 4.8 and 4.9. The second is to correct the fit bias described in Sec. 4.4.3, and the correction factor is $1 - \frac{\sigma_{\mathrm{sig}}}{N_{\mathrm{sig}}} \cdot b$ with σ_{sig} to be the statistical uncertainty of $B^+ \to D_s^+ D_s^- K^+$ signal yield N_{sig} and b the bias in the pull distributions of N_{sig} shown in Fig. 4.30. Finally, the branching fraction ratio is determined to be

$$\mathcal{R} = 0.525 \pm 0.033\,(\mathrm{stat}). \tag{4.12}$$

4.5.3 Systematic uncertainties on the branching fraction ratio

Thanks to the similar decay topology and the analogous final-state particles in the signal $B^+ \to D_s^+ D_s^- K^+$ and control $B^+ \to D^+ D^- K^+$ channels, many systematic uncertainties are expected to be largely cancelled, *e.g.* the imperfect simulation of the B^+

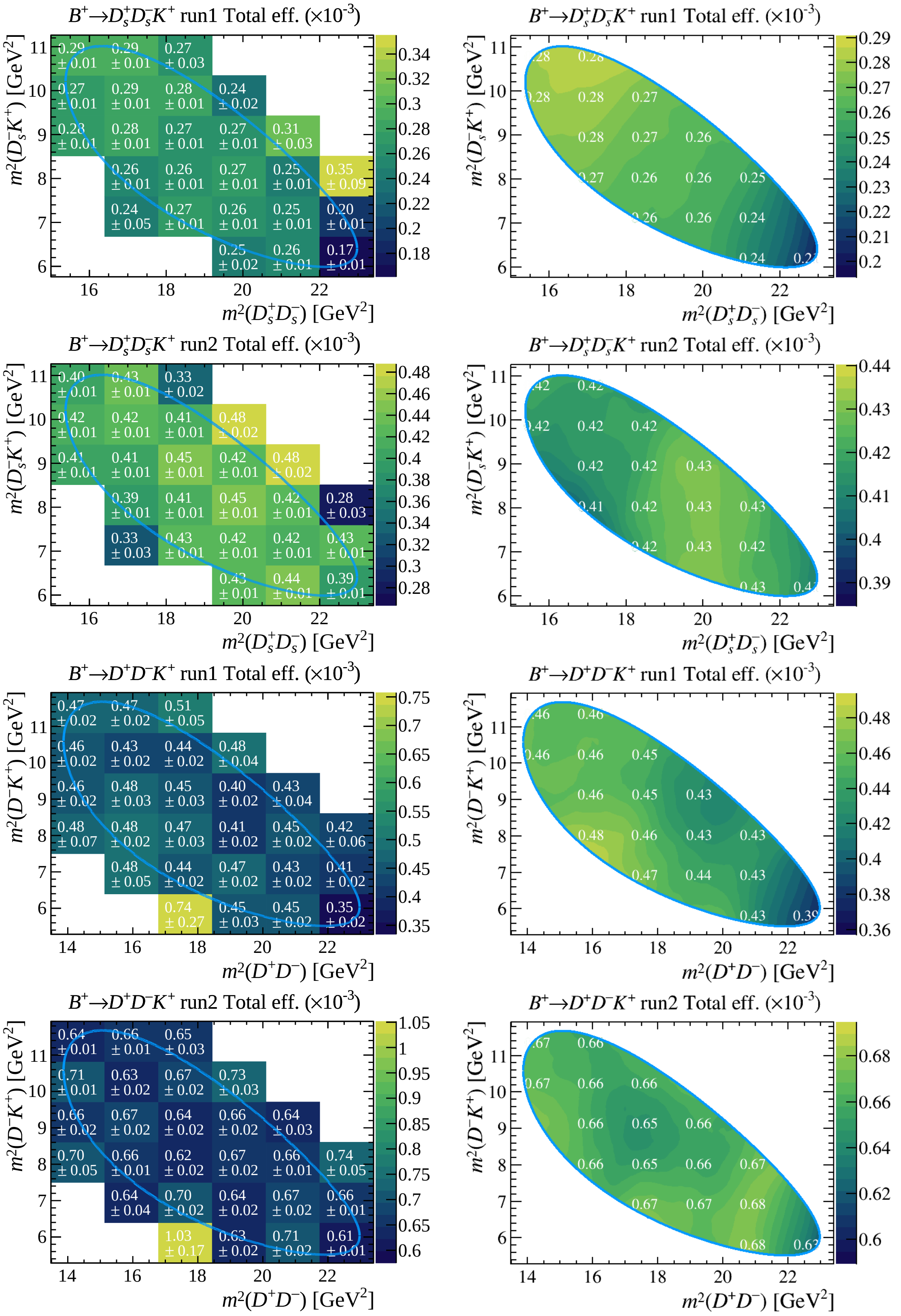

Figure 4.37 Total efficiencies for the $B^+ \to D_s^+ D_s^- K^+$ (top two rows) and $B^+ \to D^+ D^- K^+$ (bottom two rows) channels. Efficiencies from KDE method (histograms) are shown on the right (left) column. The KDE efficiencies in text are the average values in the corresponding bins of the histograms in the left column.

Table 4.13 Systematic sources in branching fraction measurement. The statistical uncertainty is also shown in the brackets.

Systematic source	Relative uncertainty (%)
L0_Hadron efficiency correction	2.3
Choice of the signal model choice	0.3
Choice of the background model choice	0.1
Uncertainty on the B^+ mass fit bias	0.1
Limited MC statistics	0.5
Variation of the KDE parameters	0.4
Uncertainty on the NDC background fraction	2.9
PID modeling	2.8
Choice of the BDTG working point	1.6
Tracking efficiency	1.0
Multiple candidate removal	0.7
MC truth matching efficiency	0.6
Total syst. (stat.)	5.1 (6.3)

kinematics and the large uncertainties on the tracking efficiencies, L0_trigger efficiencies, *etc.* In this section, several systematic sources contributing to the branching fraction ratio are considered, which are listed in Table 4.13. The evaluated uncertainties are also presented in the table. The uncertainties from all the sources are added in quadrature, and then the square root of the sum is taken as the total systematic uncertainty. Details of the uncertainty evaluations for all the sources are described in the following subsections.

4.5.3.1 L0Hadron_TOS efficiency correction

The LHCb simulation does not reproduce correctly the L0Hadron trigger response, so in principle the L0Hadron_TOS efficiency determined from MC simulation is unreliable and thus it should instead be calculated using data. The effect of the imperfect efficiency modeling in MC simulation is expected to be similar in the $B^+ \to D_s^+ D_s^- K^+$ signal and $B^+ \to D^+ D^- K^+$ control channels and thus is largely cancelled in the branching fraction ratio, so in the default result the L0Hadron_TOS efficiency in MC is still taken. An additional correction on the L0Hadron_TOS efficiency is tested in this subsection to evaluate the residual effect of the L0Hadron_TOS mismodeling. The correction is performed as described below.

The absolute L0Hadron_TOS efficiency for kaons or pions determined using the TISTOS method from the high-statistic and high-purity calibration data sample of D^0 in D^* decays. The efficiency is parameterized as a function of the real transverse energy E_{T} of the final-state particles when arriving the HCAL surface, and the inner or outer region of the HCAL. For the efficiencies in the Run2 period, the effect of the overlap between tracks, the detector occupancy and calibration effect are also taken into account. To utilize the efficiency determined from the calibration data, single-event efficiency weights ε_i with $i \in \{1, 2, \cdots, 7\}$ are introduced for all the tracks in each event of the $B^+ \to D_s^+ D_s^- K^+$ and $B^+ \to D^+ D^- K^+$ MC samples according to the corresponding efficiency functions, and the total weight for an event is $1 - (1 - \varepsilon_1)(1 - \varepsilon_2) \cdots (1 - \varepsilon_7)$, which replaces the effect of the L0Hadron_TOS cut. The efficiency is then obtained as the ratio of the weight sum and the number of all MC events. Unfortunately, the L0Hadron_TOS trigger in the $B^+ \to D_s^+ D_s^- K^+$ and $B^+ \to D^+ D^- K^+$ MC samples has already been partially included in the Stripping line due to the requirement of the specific HLT2 lines, and thus cannot be isolated, so it is impracticable to replace the L0Hadron_TOS requirement with the efficiency weight and the above efficiency determination method cannot be directly used. It is known that the absolute TOS efficiency can be obtained using the TISTOS method, so the correction on the L0Hadron_TOS efficiency in MC simulation is possible by comparing the L0Hadron_TOS TOS efficiencies determined using the TOS cut and the efficiency weight in the MC samples with L0Hadron_TIS triggered, as shown in Fig. 4.38 in different regions of the Dalitz plots and separately for Run1 and Run2 for the $B^+ \to D_s^+ D_s^- K^+$ and $B^+ \to D^+ D^- K^+$ decays. The correction factors are then applied as weights to MC samples. Efficiencies are obtained with the weights considered. The difference between the resulting branching fraction ratio and the default result is taken as the systematic uncertainty, which is 2.3% of the default branching fraction ratio.

4.5.3.2 Choice of the signal model

To evaluate the systematic effect of the choice of the signal model, the Hypatia function[196], which is usually utilized to model peaks with asymmetric tails, is taken alternatively to describe the signal distributions in the B^+ mass fits to the $B^+ \to D_s^+ D_s^- K^+$ and $B^+ \to D^+ D^- K^+$ candidates, instead of the sum of two CB functions. The fit strategy is the same as that for the default result. The $B^+ \to D_s^+ D_s^- K^+$ and $B^+ \to D^+ D^- K^+$ signal yields are determined to be 361.8 ± 21.9 and 3214.7 ± 63.4, respectively, where the uncertainties are statistical only. The signal weights are extracted from the alternative

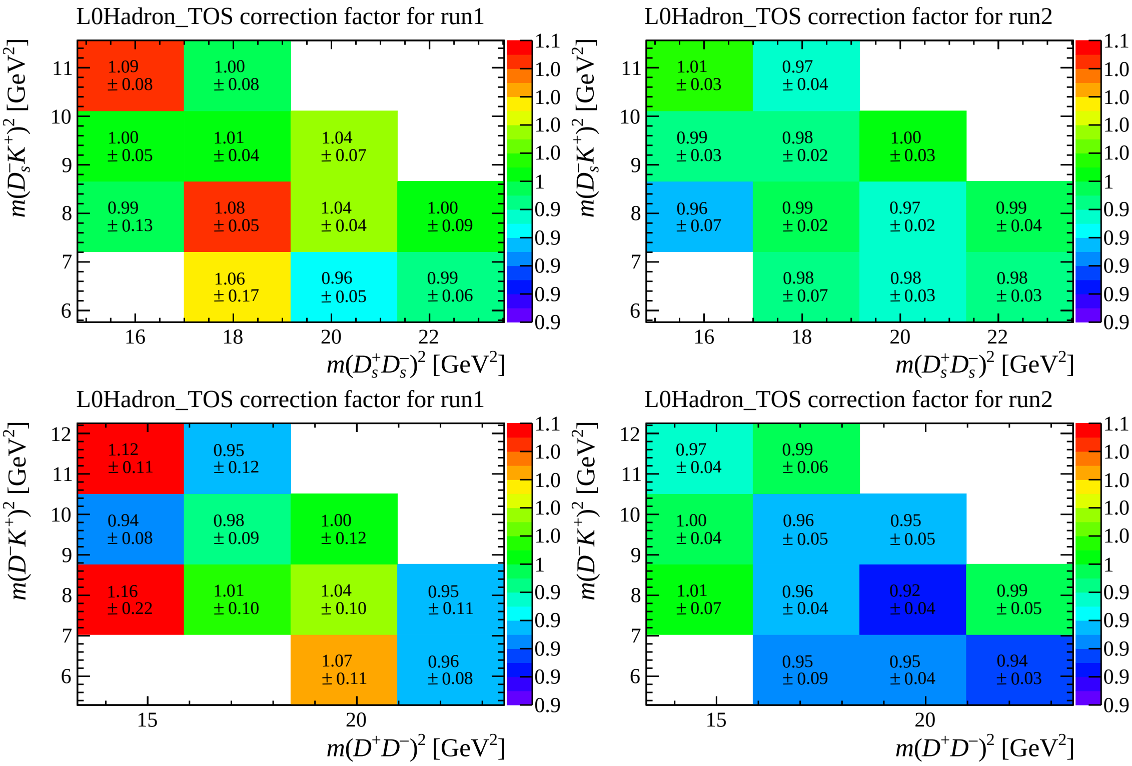

Figure 4.38 L0Hadron_TOS correction factors in Dalitz plots for the $B^+ \to D_s^+ D_s^- K^+$ (top) and $B^+ \to D^+ D^- K^+$ (bottom) decays.

fits, and are further used to determine the branching fraction ratio, the difference of which from the default result is taken as the systematic uncertainty. The relative value is 0.3%.

4.5.3.3 Choice of the background model

In the default result, an exponential function is employed to model the background shape in the B^+ mass fits. Alternatively, a second-order Chebyshev polynomial is taken to evaluate the effect of the choice of the background model. The determined signal yields are 356.4 ± 23.4 and 3183.5 ± 72.0 for the $B^+ \to D_s^+ D_s^- K^+$ and $B^+ \to D^+ D^- K^+$ channels, respectively. The branching fraction ratio is then calculated using the signal weights obtained from the alternative fits, and its difference from the default result is taken as the systematic uncertainty. The relative value is 0.1%.

4.5.3.4 Uncertainty on the B^+ mass fit bias

In the default B^+ mass fit to the $B^+ \to D_s^+ D_s^- K^+$ data, a small bias of 0.09 ± 0.01 times of the statistical uncertainty is found, as shown in Fig. 4.30. The bias is corrected in the default branching fraction ratio as described in Sec. 4.5.2. The uncertainty on the bias is treated as a systematic source, whose effect is propagated to the branching fraction ratio and the relative systematic uncertainty is 0.1%.

4.5.3.5 Limited MC statistics

The limited sizes of the MC samples to determine efficiencies in Sec. 4.5.1.4 bring a systematic uncertainty on the branching fraction ratio, whose effect is propagated using the bootstrap method[197]. For both the $B^+ \to D_s^+ D_s^- K^+$ and $B^+ \to D^+ D^- K^+$ channels, one thousand sets of toy events, each containing two samples used to determine the denominator and numerator in the efficiency calculation, are produced from the generator-level and full-reconstructed MC samples, respectively. Events in a toy sample are randomly extracted from the corresponding MC sample with replacement and the number of the events of the generated and original MC samples are equal. Then one thousand efficiency maps are obtained using the sets of the toy samples with the KDE method described in Sec. 4.5.1.4, each resulting in a branching fraction ratio. The systematic uncertainty is taken as the standard deviation of the one thousand branching fraction ratios, and is evaluated separately for the $B^+ \to D_s^+ D_s^- K^+$ and $B^+ \to D^+ D^- K^+$ MC samples. The total uncertainty is the square root of the quadratic sum of the uncertainties resulted from the limited sizes the MC samples of the two channels. The uncertainty is 0.5%.

4.5.3.6 Variation of the KDE parameters

As described in Sec. 4.5.1.4, the kernel width is 2 GeV^2 and the MC events used in the convolution is $5e4$ in the KDE method to obtain the default result. These hyper parameters are chosen by hand. Alternative values of them are tested to evaluate the systematic effect on the branching fraction ratio, including two different choices of the kernel widths, 1 GeV^2 and 3 GeV^2, and 5e5 events for the convolution. Efficiency maps are obtained using the alternative KDE configurations, and they are further used to determine the branching fraction ratio. The resulting differences are 0.4%, -0.06% and 0%, respectively. The three uncertainties are added in quadrature to obtain a total systematic uncertainty: 0.4%.

4.5.3.7 Uncertainty on the NDC background fraction

The contributions of the residual NDC backgrounds in the $B^+ \to D_s^+ D_s^- K^+$ and $B^+ \to D^+ D^- K^+$ data are subtracted in the default result as described in Sec. 4.5.2. The uncertainties on the NDC background fractions are propagated to the branching fraction ratio as a systematic uncertainty, taken as 2.9%.

4.5.3.8 PID modeling

In the default result, the `PIDcorr`[169] tool is employed to transform the PID variables in the $B^+ \to D_s^+ D_s^- K^+$ and $B^+ \to D^+ D^- K^+$ MC samples according to the corresponding distributions in the calibration sample, whose limited size is a source of the systematic uncertainty. The PID distributions in the calibration sample are estimated using the KDE method, and thus the choice of the hyper parameters could also bring systematic effect. Furthermore, the PID resampling procedure acquires the nTracks information as the input. It is known that the nTracks information is not well described in MC samples, and an uncertainty to account for the imperfect simulation is necessary. Besides the three systematic sources discussed above, the transformation method itself is also a systematic source. The systematic effect of the four above sources are evaluated as follows.

- Limited statistics of calibration sample: The PID variables in MC simulation are transformed using an alternative bootstrapped calibration sample, and the efficiencies are determined based on the newly transformed PID variables. The resulting relative difference in the branching fraction ratio is 0.24%.
- Variation of the KDE parameters: The PID variables in MC simulation are transformed according to the estimated distributions using an alternative configuration of the KDE parameters, and the efficiencies are determined based on the newly transformed PID variables. The resulting relative difference in the branching fraction ratio is 0.026%.
- nTrack scaling: The PID variables in MC simulation are transformed with the scaled nTracks variable as the input, as described in Sec. 4.1.2, and the efficiencies are calculated using MC samples containing the newly transformed PID variables. The resulting relative systematic uncertainty on the branching fraction ratio is -0.3%.
- PID correction method: The `PIDGen` tool is employed to resample the PID variables in MC simulation, and the efficiencies are determined based on the resampled PID variables. The resulting systematic uncertainty on the relative branching fraction ratio is -2.8%. The difference is mainly due to the imperfect PID corrections for the two different final-state particles in the $B^+ \to D_s^+ D_s^- K^+$ and $B^+ \to D^+ D^- K^+$ decays. The effect on the same species of the final-state particles is cancelled.

The uncertainties from the above four sources are added in quadrature to obtain the total systematic uncertainty due to the PID modeling. The uncertainty is 2.8%.

Table 4.14 Relative uncertainties of the branching fraction ratio $\mathcal{R}$ at different BDT working points, where the RMS of all the values is taken as the systematic uncertainty. The abbreviations “sig” and “con” denote the signal and control channels, respectively.

% sig con	0.1	0.3	0.7
-0.8	-0.4	1.0	-2.6
-0.2	0.6	2.0	-1.6
0.0	0.9	2.2	-1.4

4.5.3.9 Choice of BDTG working point

The BDTG efficiencies obtained from MC simulation could be biased due to the potentially imperfect modeling of the input variables. The systematic effect is investigated by comparing the branching fraction ratios at different BDTG working points. The differences from the default result are listed in Table 4.14, and the root mean square (RMS) of all the differences is taken as the systematic uncertainty, which is 1.6%.

4.5.3.10 Tracking efficiency

The systematic uncertainty on the tracking efficiency mainly arises from the imperfect simulation of the LHCb material budget and the interactions of pions and kaons with the material. The systematic uncertainties on the same tracks in the $B^+ \to D_s^+ D_s^- K^+$ and $B^+ \to D^+ D^- K^+$ decays are expected to be cancelled in the branching fraction ratio. Two tracks in the two decays are different, and an uncertainty accounting for the imperfect modeling of them in MC simulation is necessary. The Refs.[198-199] found the relative uncertainty on the tracking efficiency due to the difference of a K track and a π track is typically 0.5%. This analysis directly takes this value. As there are two different tracks in the signal and control channels, and the uncertainty is fully correlated for the two K-π differences, the relative uncertainty on the branching fraction ratio is evaluated to be 1%.

4.5.3.11 Multiple candidate removal

The efficiency of multiple candidate removal is expected to be 100% and thus is not explicitly discussed in the default result, but actually the efficiency needs to be checked. Besides, multiple candidates are removed based on the values of the DTF χ^2, and this strategy could also have systematic effect on the branching fraction ratio. The systematic uncertainties due to the two sources are evaluated as below.

Multiple candidate fractions of several sources are evaluated in Sec. 4.2.4, and it is found that MC simulation can well model the multiple candidate contributions in data. Therefore, it is reliable to use MC simulation to estimate the efficiency of the multiple candidate removal. The efficiency is obtained as the ratio of the numbers of the truth-matched events after and before the multiple candidate removal. The efficiency is found extremely high, just as expected, which are 99.6% and 99.8% for the $B^+ \to D_s^+ D_s^- K^+$ and $B^+ \to D^+ D^- K^+$ decays, respectively. The correction on the branching fraction ratio is then obtained as the ratio of the efficiencies, and thus the resulting systematic uncertainty is taken as 99.8%/99.6% $-$ 1 = 0.2%.

For the strategy of the multiple candidate selection, the random removal instead of the lowest DTF-χ^2 method is tested. The branching fraction ratio is re-calculated using the signal weights extracted from the B^+ mass fits to the $B^+ \to D_s^+ D_s^- K^+$ and $B^+ \to D^+ D^- K^+$ data after the random multiple candidate removal. The difference from the default value is taken as the systematic uncertainty, which is -0.63%.

The total systematic uncertainty in the multiple candidate removal sector is the square root of the quadratic sum of the two above uncertainties. It is 0.7%.

4.5.3.12 MC truth matching efficiency

The signal candidates in MC samples are selected by the truth matching. The matching algorithm is not 100% efficient and thus results in the underestimate of the efficiencies determined from MC simulation. The efficiency of MC truth matching is not considered in the default result because it is expected to be largely cancelled in the branching fraction ratio due to the same decay topology of the $B^+ \to D_s^+ D_s^- K^+$ signal and $B^+ \to D^+ D^- K^+$ control channels and almost the same final-state particles. A further check on the branching fraction ratio with the truth matching efficiency taken into account is performed and a systematic uncertainty is introduced.

At first, the truth matching efficiency is obtained as the ratio of the number of signal candidates with and without the truth matching requirement with the yields determined from the same B^+ mass fits as that to data. Some of the multiple candidates in the MC samples also contribute to the B^+ mass peak especially those belonging to the Internal Exchange category as shown in Table 4.7, and thus leads to the overestimate of the signal yield. Therefore, the events containing multiple candidates are removed in the fits. The truth matching efficiency is finally estimated to be 88.1% and 88.6%

for the $B^+ \to D_s^+ D_s^- K^+$ and $B^+ \to D^+ D^- K^+$ channels, respectively. The corresponding correction on the branching fraction ratio is 88.1%/88.6% $\approx$ 0.94%, and thus the systematic uncertainty is taken as $1 - 0.94\% = 0.6\%$.

4.5.4 Results of the branching fraction measurement

With the systematic uncertainty taken into account, the branching fraction ratio is finally determined as

$$\mathcal{R} = \frac{\mathcal{B}(B^+ \to D_s^+ D_s^- K^+)}{\mathcal{B}(B^+ \to D^+ D^- K^+)} = 0.525 \pm 0.033 \pm 0.027 \pm 0.034, \tag{4.13}$$

and the absolute branching fraction of the $B^+ \to D_s^+ D_s^- K^+$ decay is then obtained as

$$\mathcal{B}(B^+ \to D_s^+ D_s^- K^+) = (1.15 \pm 0.07 \pm 0.06 \pm 0.38) \times 10^{-4}, \tag{4.14}$$

where the first uncertainty is statistical, the second systematic, and the third is due to the uncertainties on the known branching fractions of $D^+ \to K^- \pi^+ \pi^+$, $D_s^+ \to K^- K^+ \pi^+$ and $B^+ \to D^+ D^- K^+$ processes[1]. The branching fraction of the $B^+ \to D_s^+ D_s^- K^+$ decay is an essential input to help interpret the near-threshold peaking structure in the $D_s^+ D_s^-$ mass spectrum shown in Fig. 4.24, as discussed in Sec. 4.7.

4.6 Amplitude analysis

An amplitude analysis is employed to measure the properties of the near-threshold structure in the $D_s^+ D_s^-$ mass spectrum shown in Fig. 4.24, with a partial contribution from the author of this thesis. For the complete description of the study of the $B^+ \to D_s^+ D_s^- K^+$ decay, the amplitude analysis is briefly summarized in this section.

4.6.1 Amplitude construction and fit strategy

The matrix element for the $B^+ \to D_s^+ D_s^- K^+$ decay is constructed using the helicity formalism[179], in analogous to the amplitude analysis of the $B^0 \to D^+ D^- K^+ \pi^-$ process presented in Chapter 3. The decay amplitude for a certain decay chain, generally denoted as $B^+ \to R_n P_3$, $R_n \to P_1 P_2$, is

$$\mathcal{M}(m_{P_1P_2}, \theta_R \mid \vec{\omega}) = \sum_n \mathcal{H}^{R_n}\, d_{0,0}^{J_{R_n}}(\theta_R)\, p^{L_B}\, F_{L_B}(pd)\, q^{L_{R_n}}\, F_{L_{R_n}}(qd)\, \mathrm{BW}(m_{P_1P_2}), \tag{4.15}$$

where $P_1 P_2 P_3$ can be any permutation of the final-state particles $D_s^+ D_s^- K^+$, and R_n is a resonance in the $P_1 P_2$ system with n to distinguish different resonances. The decay amplitude only depends on two variables, $m(P_1 P_2)$ and the helicity angle θ_R. The latter is defined as the angle between the directions of the P_1 and P_3 momenta in the R rest frame. The angular-dependent part of the R_n amplitude is described by the Wigner-d function, $d^{J_{R_n}}_{0,0}(\theta_X)$, where the superscript corresponds to the spin of X_n and the two subscripts are set to zero because both the initial- and final-state particles are spinless. The momentum barrier factors ① for the $B^+ \to R_i P_3$ and $R_i \to P_1 P_2$ decays are denoted as $p^{L_B} F_{L_B}(pd)$ and $q^{L_{R_n}} F_{L_{R_n}}(qd)$, respectively, where the quantity p (q) is the momentum of the decay products of the B (R_n) state in its rest frame, and L_B (L_{R_n}) is the orbital angular momentum between the decay products of the B (R_n) state. The conservation of the orbital angular momentum restricts $L_B = L_{R_n}$. The effective radius d in the Blatt–Weisskopf barrier factor $F_L(z)$ is set to $3\,\mathrm{GeV}^{-1} \sim 0.6\,\mathrm{fm}$. The mass lineshape of a resonance R_n is usually modeled by the BW function, as detailed in Sec. 3.6.5.2. The default width model for the resonances are taken as the two-body mass-dependent formula in Eq. 3.55 The unknown parameters that need to be determined are denoted as the vector $\vec{\omega}$, including the complex helicity H^{R_n} that describes the magnitude and the phase of the R_n amplitude, and the BW parameters of the resonances.

The *sFit* method[184] is utilized to determine the unknown parameters $\vec{\omega}$. The PDF and log-likelihood constructions are the same as those in Sec. 3.8. The background in $B^+ \to D_s^+ D_s^- K^+$ data is statistically subtracted using the *sPlot* method[174], with the B^+ mass fit described in Sec. 4.4.1 as the input to extract the signal weights. The normalization factor of the PDF is evaluated by the MC integration using the $B^+ \to D_s^+ D_s^- K^+$ MC candidates shown in Fig. 4.23. The MC candidates are generated uniformly in the phase space and pass all the selection criteria.

4.6.2 Amplitude fit results

The default model includes several natural-parity resonances ($J^{PC} = 0^{++}, 1^{--}, 2^{++}$, *etc.*) in the $D_s^+ D_s^-$ system: the $J^{PC} = 1^{--}$ $\psi(4260)$ state, the $J^{PC} = 1^{--}$ $\psi(4660)$ state, a new state near the $D_s^+ D_s^-$ mass threshold with J^{PC} to be determined, and a new state accounts for the dip at about 4.14 GeV with the same J^{PC} as that of the near-threshold state. A non-resonant (NR) term is also included in the amplitude model with its matrix element set to unity. Three spin-parity models of the near-threshold state are tested in the amplitude fit, $J^{PC} = 0^{++}$, 1^{--} and 2^{++}. It is found that the $J^{PC} = 0^{++}$ model leads to the best fit, and the other two spin-parity hypotheses are rejected by significance over than

---

① A detailed introduction to the momentum barrier factor is given in Sec. 3.6.5.1.

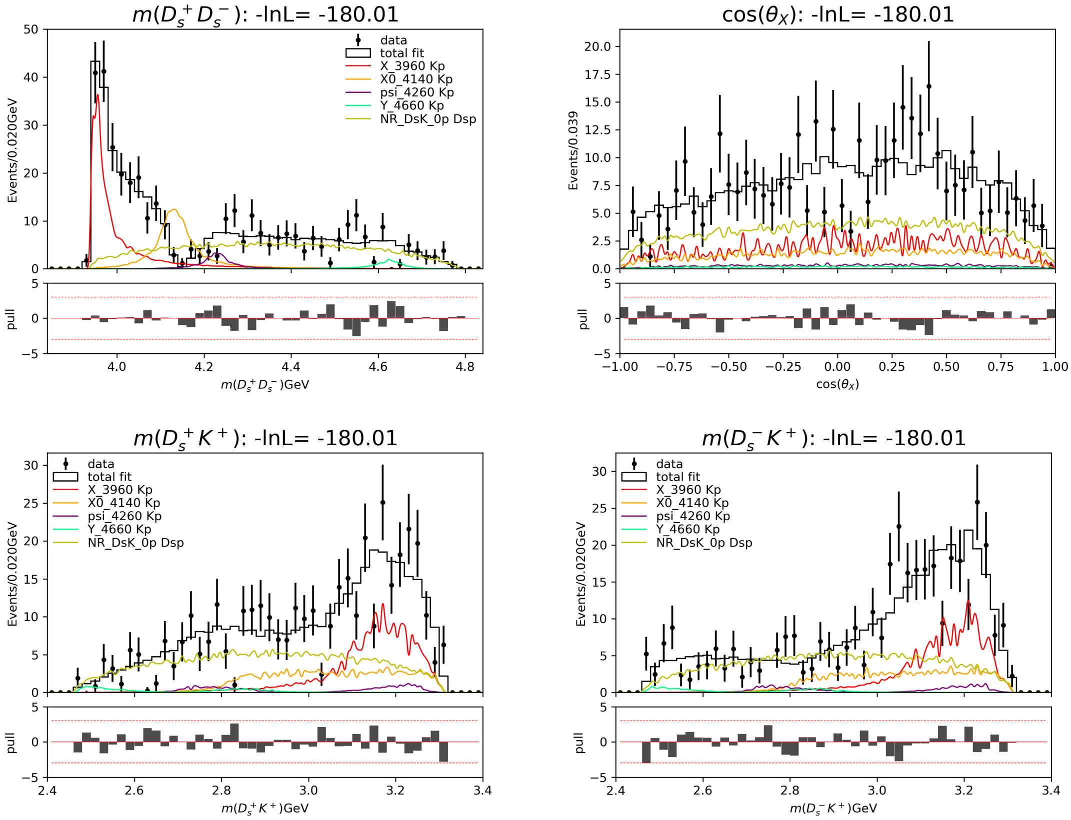

Figure 4.39 Distributions of the $D_s^+ D_s^-$, $D_s^- K^+$ and $D_s^+ K^+$ masses and the cosine of the helicity angle θ_X in the $B^+ \to D_s^+ D_s^- K^+$ data with the background statistically subtracted using the *sPlot* method[174]. The amplitude fit results are overlaid.

9σ ①. The significance of the existence of the near-threshold state is found over 10σ. Fit results are overlaid with the mass distributions of the $D_s^+ D_s^-$, $D_s^- K^+$ and $D_s^+ K^+$ systems, and the cosine of the helicity angle θ_X in Fig. 4.39. The fit well describes the data.

The BW mass and width of the near-threshold state are measured to be

$$m_0 = 3955 \pm 6 \pm 11\,\text{MeV}, \quad \Gamma_0 = 48 \pm 17 \pm 10\,\text{MeV}, \tag{4.16}$$

where the uncertainties are statistical and systematic, respectively. The new state is denoted as $X(3960)$. The dip at 4.14 GeV in the $D_s^+ D_s^-$ mass spectrum is well modeled by the interference between the $X(3960)$ and $X(4140)$ states. The latter is also a new resonant candidate. However, an alternative K-matrix model considering the coupled-channel effect of the $D_s^+ D_s^-$ and $J/\psi\phi$ processes for the $J^{PC} = 0^{++}$ $X(3960)$ state and the NR component can also well describe the dip at 4.14 GeV without introducing the $X(4140)$ state. Therefore, the $X(4140)$ state is not reported in this analysis. The full list of the properties determined in the amplitude fit is shown in Table 4.15, where the systematic

---

① The significance evaluation method is the same as that in Sec. 3.9.1.

Table 4.15 Measured properties in the default amplitude fit result. The first uncertainties are statistical, and the second systematic. The fixed parameters are taken from Ref.[1].

Component	J^{PC}	m_0 (MeV)	Γ_0 (MeV)	Fit fraction (%)	$\mathcal{S}$ (σ)
$X(3960)$	0^{++}	$3955 \pm 6 \pm 11$	$48 \pm 17 \pm 10$	$24.2 \pm 7.6 \pm 7.8$	12.6
$X(4140)$	0^{++}	$4133 \pm 7 \pm 11$	$69 \pm 17 \pm 7$	$17.7 \pm 4.9 \pm 7.5$	3.7
$\psi(4260)$	1^{--}	4230 (fixed)	55 (fixed)	$3.7 \pm 0.4 \pm 3.0$	3.1
$\psi(4660)$	1^{--}	4633 (fixed)	64 (fixed)	$2.2 \pm 0.2 \pm 0.4$	2.9
NR $D_s^+ D_s^-$	0^{++}	-	-	$46.6 \pm 13.3 \pm 10.7$	3.1

uncertainties result from several sources. The primary one is the mass lineshape of the $X(3960)$ state, where a constant width instead of the mass-dependent width is used. Other sources include the variation of the fixed parameters in the amplitude fit, the potential additional resonant contributions, the imperfect modelling of the L0Hadron_TOS trigger and the imperfect correction on the PID responses in MC simulation. The fit fraction of the $X(3960)$ state is an important input to help interpret its inner structure, as discussed in the next section.

4.7 Conclusions and discussion

In conclusion, the $B^+ \to D_s^+ D_s^- K^+$ decay is observed for the first time using the pp collision data collected by the LHCb experiment during the Run1 and Run2 periods, corresponding to an integrated luminosity of 9 fb^{-1}. This analysis measures the branching fraction of the $B^+ \to D_s^+ D_s^- K^+$ decay with respect to that of the $B^+ \to D^+ D^- K^+$ process,

$$\frac{\mathcal{B}(B^+ \to D_s^+ D_s^- K^+)}{\mathcal{B}(B^+ \to D^+ D^- K^+)} = 0.525 \pm 0.033 \pm 0.027 \pm 0.034, \tag{4.17}$$

and the absolute branching fraction is

$$\mathcal{B}(B^+ \to D_s^+ D_s^- K^+) = (1.15 \pm 0.07 \pm 0.06 \pm 0.38) \times 10^{-4}, \tag{4.18}$$

where the first and second uncertainties are statistical and systematic, respectively, and the last uncertainty is due to the uncertainties on the known branching fractions of $D^+ \to K^- \pi^+ \pi^+$, $D_s^+ \to K^- K^+ \pi^+$ and $B^+ \to D^+ D^- K^+$ decays[1].

A near-threshold structure is observed in the $D_s^+ D_s^-$ mass spectrum in the $B^+ \to D_s^+ D_s^- K^+$ decay. The significance of this structure is found over 10 standard deviations. An amplitude analysis is performed to measure the properties of this state, with a partial contribution from the author of this thesis. The BW mass and width, as well as the spin-parity of the near-threshold state, are determined to be $m_0 = 3955 \pm 6 \pm 11$ MeV, $\Gamma_0 = 48 \pm 17 \pm 10$ MeV and $J^{PC} = 0^{++}$. The fit fraction of the state is $\mathcal{FF}^X_{B^+ \to D_s^+ D_s^- K^+} = (24.2 \pm 7.6\,(\text{stat}) \pm 7.8\,(\text{syst}))\%$. Here, the first uncertainties are statistical and the second systematic. This state is denoted as $X(3960)$, whose properties are comparable to those of the $X(3915)$ and $\chi_{c0}(3930)$ mesons as discussed in Sec. 1.4. If assuming they are the same state, X, the width fractions of different decay modes will be important quantities to help understand the inner structure of the X state. Currently, the width fraction ratio can be obtained for the $X \to D^+D^-$ and $X \to D_s^+D_s^-$ processes,

$$\begin{aligned}\frac{\Gamma(X \to D^+D^-)}{\Gamma(X \to D_s^+D_s^-)} &= \frac{\mathcal{B}(B^+ \to D^+D^-K^+)\,\mathcal{FF}^X_{B^+ \to D^+D^-K^+}}{\mathcal{B}(B^+ \to D_s^+D_s^-K^+)\,\mathcal{FF}^X_{B^+ \to D_s^+D_s^-K^+}} \\ &= 0.29 \pm 0.09\,(\text{stat}) \pm 0.10\,(\text{syst}) \pm 0.08\,(\text{ext}),\end{aligned} \tag{4.19}$$

where $\mathcal{FF}^X_{B^+ \to D^+D^-K^+} = (3.70 \pm 0.92)\%$① is the fit fraction of the $\chi_{c0}(3930)$ state in the $B^+ \to D^+D^-K^+$ process[14]. The external uncertainty on the width fraction ratio is due to the uncertainties on the external properties, $\mathcal{B}(D^+ \to K^-\pi^+\pi^+)$, $\mathcal{B}(D_s^+ \to K^-K^+\pi^+)$, and $\mathcal{FF}^X_{B^+ \to D^+D^-K^+}$. The fact that $\Gamma(X \to D^+D^-) < \Gamma(X \to D_s^+D_s^-)$ suggests the exotic nature of the X state now that an ordinary charmonium state predominantly decays into the $D^{(*)}\overline{D}^{(*)}$ pair if it is kinematically allowed, because it is harder to excite an $s\bar{s}$ pair than a $d\bar{d}$ pair from vacuum. The inferred X state locates near the $D_s^+D_s^-$ mass threshold, and thus the phase-space volume of the $X \to D_s^+D_s^-$ decay is smaller than that of the $X \to D^+D^-$ process, which further implies the stronger coupling of the X state to the $D_s^+D_s^-$ final state regarding to the larger decay width and suggests the exotic nature of the X state. The width fraction ratio of $X \to D_s^+D_s^-$ (D^+D^-) and $X \to J/\psi\omega$ is inaccessible for now because the $J/\psi\omega$ process is only observed in the inclusive production[1]. The future studies of the $J/\psi\omega$ system in the exclusive B-meson decays, *e.g.* $B^+ \to J/\psi\omega K^+$, will provide more experimental information to interpret the nature of the $X(3915)/\chi_{c0}(3930)/X(3960)$ state.

This is the first time that the $D_s^+D_s^-$ system is investigated in the exclusive B-meson decay. Currently, the study is limited by the low statistics of data. In this analysis, the D_s^+ meson is only reconstructed from the $K^-K^+\pi^+$ final state in the Stripping line. In the future, it is possible to include the $D_s^+ \to \pi^-\pi^+\pi^+$ decay as well, and a 40% increase of the $B^+ \to D_s^+D_s^-K^+$ signal candidates are expected. A larger data statistics enables a more precision measurement on the branching fraction of the $B^+ \to D_s^+D_s^-K^+$ decay and the properties of the $X(3960)$ state. The underlying potential resonant structures in the

---

① The uncertainty is the square root of the sum of the statistical and systematic uncertainties.

$D_s^+ D_s^-$ system with small contributions could also be revealed with the increase of the data statistics. The $D_s^+ D_s^-$ system can also be studied in other exclusive B-meson decays, *e.g.* $B^0 \to D_s^+ D_s^- K^+ \pi^-$, $B_s^0 \to D_s^+ D_s^- K^+ K^-$, and so on. These decays can be searched for in the future using larger data samples, and they provide a chance to re-observe the states in the $B^+ \to D_s^+ D_s^- K^+$ decay, and to search for new resonances.

While the $D_s^+ D_s^-$ system can only access the natural-parity states, the $D_s^{*+} D_s^- + D_s^+ D_s^{*-}$ final states can be utilize to study both natural- and unnatural-parity states ($J^{PC} = 0^{++}$ excepted). Partially reconstructed candidates from the $B^+ \to D_s^{*+} D_s^- K^+ + D_s^+ D_s^{*-} K^+$ decays are observed in the B^+ mass distributions shown in Fig. 4.15. The full reconstruction of such decays is inefficient and the resolution is bad at the LHCb experiment, but alternative methods to solve the momentum of the missing particle using the constraints of the B^+ flight direction and the masses of the reconstructed particles could achieve a promising resolution of the Dalitz-plot variables of the $B^+ \to D_s^{*+} D_s^- K^+ + D_s^+ D_s^{*-} K^+$ decays. and thus offers an opportunity to search for both conventional and exotic charmonium states in the $D_s^{*+} D_s^- + D_s^+ D_s^{*-}$ system.

The analysis of the $B^+ \to D_s^+ D_s^- K^+$ decay exhibits as an example to study resonances in the open-charm final states other than the most usually investigated $D^{(*)}\overline{D}^{(*)}$ combination in exclusive b-hadron decays. Extensions of the $B^+ \to D_s^+ D_s^- K^+$ and $B^+ \to D^+ D^- K^+$ decays could be $B^+ \to \Lambda_c^+ \overline{\Lambda}_c^- K^+$, $\Lambda_b^0 \to \Lambda_c^+ \overline{D}^0 K^-$ and so on. These processes provide opportunities to search for potential conventional and exotic hadrons containing a $c\bar{c}$ pair and measure their properties using the amplitude-analysis technique. The larger data sample that will be collected by the LHCb experiment will enable the searches of such decays and the studies of the intermediate hadrons.

CHAPTER 5 SUMMARY AND PROSPECTS

In summary, this thesis presents studies of hadron spectroscopy in the decays $B^0 \to D^+D^-K^+\pi^-$ and $B^+ \to D_s^+D_s^-K^+$ using pp collision data collected by the LHCb experiment. Both decays belong to the $b \to c\bar{c}s$ family with the two charm quarks hadronizing into two open-charm mesons. The two analyses aim at searching for new excited mesons containing charm quarks and measuring their properties, to provide new experimental inputs to spectra of charm-strange mesons and charmonium states.

The four-body decay $B^0 \to D^+D^-K^+\pi^-$ is studied for the first time using the LHCb data collected during the 2016–2018 period. There is no evident contribution of the intermediate resonances that were observed in the $B^+ \to D^+D^-K^+$ decay[13-14], *e.g.* the $cs\bar{u}\bar{d}$ tetraquark candidates $X_{0,1}(2900)$ in the D^-K^+ system, and the $c\bar{c}$ states (*e.g.* $\psi(3770)$ and $\chi_{c0,2}(3930)$) in the D^+D^- system. However, two fascinating peaking structures are clearly seen in the $D^+K^+\pi^-$ mass spectrum at about 2.6 GeV and 2.93 GeV, corresponding to candidates of new D_s^+ resonances. This is the first time that excited D_s^+ candidates are observed in the three-body $D^+K^+\pi^-$ final state in an exclusive B-meson decay.

The new excited D_s^+ candidate with a mass of around 2.6 GeV locates near the $D^+K^+\pi^-$ mass threshold and is far away from the messy structures at the higher $D^+K^+\pi^-$ mass. The state can be isolated by restricting the $K^+\pi^-$ mass lower than 0.75 GeV, referred to as the low $K^+\pi^-$ mass region. An amplitude analysis is performed in the low $K^+\pi^-$ mass region to measure the properties of the near-threshold D_s^+ state. The significance of its existence is found over 10 standard deviations, and its spin-parity is determined to be $J^P = 0^-$. The pole mass and width of the new D_s^+ state are measured to be

$$m_R = 2591 \pm 6 \pm 7\,\text{MeV}, \quad \Gamma_R = 89 \pm 16 \pm 12\,\text{MeV}\ ,$$

where the uncertainties are statistical and systematic, respectively. The new resonance, denoted as $D_{s0}(2590)^+$, is a strong candidate to be the missing $D_s(2^1S_0)^+$ state, the radial excitation of the pseudoscalar ground-state D_s^+ meson. The predicted mass of the $D_s(2^1S_0)^+$ state in the GI model is 2646 MeV and 2673 MeV with and without the screen effect considered[5-6], both significantly larger than the measured mass of the $D_{s0}(2590)^+$ state. The large discrepancy aroused the interest of theorists to interpret the inner structure of the $D_{s0}(2590)^+$ state. The most commonly addressed description is the coupled-channel effect[186-189], which explains that the unexpected low $D_{s0}(2590)^+$ mass is due to the coupling of the bare $c\bar{s}$ state and the channels with thresholds close to the $D_{s0}(2590)^+$ mass, *e.g.* D^*K. The coupled-channel effect implies the possibility that the $D_{s0}(2590)^+$ state could decay into coupled-channel final states. Such processes can be searched for in the future.

The study of the other new excited D_s^+ candidate with a mass of around 2.93 GeV requires an amplitude analysis of the $B^0 \to D^+D^-K^+\pi^-$ decay in the full phase space region. The B^0 decay amplitude is more complicated than that in the low $K^+\pi^-$ mass region due to the presence of more resonances in different decay chains, and the data sample is about seven times larger than that in the low $K^+\pi^-$ mass region, both bringing challenges to the amplitude analysis in the full phase space region. To accelerate the fit, a novel GPU-based analysis framework is developed. The amplitude analysis in the full phase space region is underway.

The $B^+ \to D_s^+D_s^-K^+$ process provides a unique opportunity to search for conventional and exotic charmonium states in the $D_s^+D_s^-$ system of the exclusive B-meson decay. This thesis made the first observation of the $B^+ \to D_s^+D_s^-K^+$ process using the full Run 1 and Run 2 data collected by the LHCb experiment. The branching fraction of the $B^+ \to D_s^+D_s^-K^+$ decay is measured relative to that of the $B^+ \to D^+D^-K^+$ process as

$$\frac{\mathcal{B}(B^+ \to D_s^+D_s^-K^+)}{\mathcal{B}(B^+ \to D^+D^-K^+)} = 0.525 \pm 0.033 \pm 0.027 \pm 0.034,$$

where the first and second uncertainties are statistical and systematic, respectively, and the third is due to the limited knowledge of the branching fractions of $D^+ \to K^-\pi^+\pi^+$ and $D_s^+ \to K^-K^+\pi^+$[1].

A near-threshold structure is observed in the $D_s^+D_s^-$ system of the $B^+ \to D_s^+D_s^-K^+$ decay, corresponding to a conventional or exotic charmonium candidate. An amplitude analysis is performed to measure its properties. The significance of the new state is found to be larger than 10σ. Its BW mass and width, and spin-parity are measured to be

$$m_0 = 3955 \pm 6 \pm 11\,\text{MeV} \quad \Gamma_0 = 48 \pm 17 \pm 10\,\text{MeV} \quad \text{and} \quad J^{PC} = 0^{++},$$

and the fit fraction is determined to be $\mathcal{FF}^X_{B^+ \to D_s^+D_s^-K^+} = (24.2 \pm 7.6 \pm 7.8)\%$. Here, the first and second uncertainties are statistical and systematic, respectively. There could be the possibility that the $X(3960)$ state is the same particle as the $\chi_{c0}(3930)$ meson observed in the D^+D^- system of the $B^+ \to D^+D^-K^+$ decay[13-14], because they have comparable masses and widths, as well as the same spin-parity of $J^{PC} = 0^{++}$. Under this assumption, the ratio of the partial widths of the $X \to D^+D^-$ and $X \to D_s^+D_s^-$ decays (X denotes $\chi_{c0}(3930)/X(3960)$) is determined to be

$$\begin{aligned}\frac{\Gamma(X \to D^+D^-)}{\Gamma(X \to D_s^+D_s^-)} &= \frac{\mathcal{B}(B^+ \to D^+D^-K^+)\,\mathcal{FF}^X_{B^+\to D^+D^-K^+}}{\mathcal{B}(B^+ \to D_s^+D_s^-K^+)\,\mathcal{FF}^X_{B^+\to D_s^+D_s^-K^+}} \\ &= 0.29 \pm 0.09\,(\text{stat}) \pm 0.10\,(\text{syst}) \pm 0.08\,(\text{ext}),\end{aligned} \tag{5.1}$$

where $\mathcal{FF}^X_{B^+\to D^+D^-K^+}$ is the fit fraction of the $\chi_{c0}(3930)$ state in the $B^+ \to D^+D^-K^+$ decay[14]. The external uncertainty on the partial width ratio is due to the uncertainties on the external properties: $\mathcal{B}(D^+ \to K^-\pi^+\pi^+)$, $\mathcal{B}(D_s^+ \to K^-K^+\pi^+)$, and $\mathcal{FF}^X_{B^+\to D^+D^-K^+}$. The fact that the $X \to D^+D^-$ width is smaller than that of the $X \to D_s^+D_s^-$ process stands as a negative evidence of the conventional nature of the $\chi_{c0}(3930)/X(3960)$ state now that the dominant decay of a conventional charmonium state is $c\bar{c} \to D^{(*)}\overline{D}^{(*)}$ if the process is kinematically allowed.

The $B^0 \to D^+D^-K^+\pi^-$ and $B^+ \to D_s^+D_s^-K^+$ decays studied in this thesis, together with the processes in the $B \to D^{(*)}\overline{D}^{(*)}K^{(*)}$ family analyzed in previous works[9-14], have shown excellent potential to discover new charm-strange and charmonium mesons (both conventional and exotic), as well as to measure their properties. However, studies of such decays are still limited by the low data statistics due to the small branching fraction $\mathcal{B}(B \to D^{(*)}\overline{D}^{(*)}K^{(*)}) \times \mathcal{B}(D^{(*)} \to nh)^2 \sim 10^{-7}$ and the low reconstruction efficiency caused by the presence of too many final-state particles. The processes involving K^0_{S}, π^0 and γ are even rarely touched due to the much worse resolution and much lower efficiency of the LHCb detector for the neutral final-state particles compared with those for the charged hadrons. The larger data sample that is going to be collected by the LHCb experiment in the future will provide new opportunities to study the intermediate excited mesons containing the charm quark(s) in the $B \to D^{(*)}\overline{D}^{(*)}K^{(*)}$ decays. The future data collection plan of the LHCb experiment is illustrated in Fig. 5.1. By the end of Run 3 in 2024, the LHCb experiment will collect a data sample of an integrated luminosity of 23 fb^{-1}, roughly three times of that in the Run 1 and Run 2 periods. The available B-meson signal yield is expected to be six times of that in the current data thanks to the efficiency improvement that benefits from the removal of the hardware trigger. The amount of data will be further doubled by the end of Run 4 in 2029. With such a huge data sample, a more detailed investigation of the $B^0 \to D^+D^-K^+\pi^-$ and $B^+ \to D_s^+D_s^-K^+$ decays will be possible. The uncertainties on the properties of the intermediate resonances, *e.g.* $D_{s0}(2590)^+$ and $X(3960)/\chi_{c0}(3930)$, are expected to be much reduced, providing more

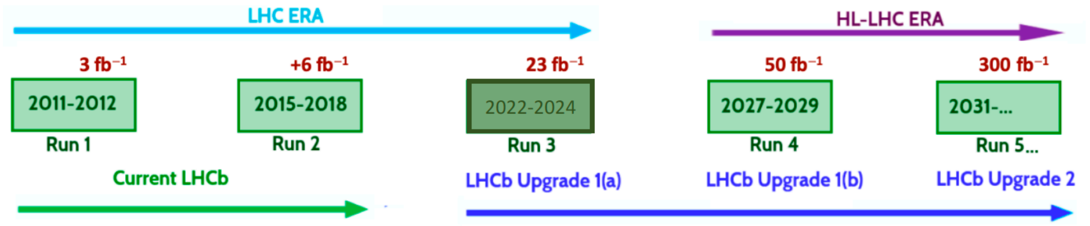

Figure 5.1 Data collection plan and the expected integrated luminosity at the LHCb experiment[200] in the periods of the operations of the LHC and High-luminosity LHC (HL-LHC).

precision tests to the theoretical calculations of the charm-strange meson and charmonium spectra. The possible underlying states that do not show up in the current data sample, *e.g.* $X_{0,1}(2900)$, could have detectable contributions in the two decays and thus could be studied. The future high data statistics also enables searches for the charm-strange mesons and charmonium states in other $B \to D^{(*)}\overline{D}^{(*)}K^{(*)}$ decays, especially the ones involving neutral final-state particles. For example, the predicted $D_{s0}(2590)^+ \to D^*K$ process could be searched for in the $B \to D^*\overline{D}^{(*)}K$ decays, and the $X(3960)/\chi_{c0}(3930)$ state could be investigated in other processes containing the $D_s^+D_s^-/D\overline{D}$ system, *e.g.* $B^0 \to D_s^+D_s^-K^+\pi^-$ and $B^+ \to D^0\overline{D}^0K^+$.

Exotic charmonium candidates usually have the decay modes involving charmonium mesons in the final state. Investigations of such processes can provide extra experimental information to help identify the nature of the inferred exotic $c\bar{c}$ states observed in the open-charm final states. For example, the $X(3915)$ state observed in the $J/\psi\omega$ system has comparable mass and width to those of the $X(3960)/\chi_{c0}(3930)$ state[1], indicating the possibility that they are the same state, also denoted as X. However, the spin-parity of the $X(3915)$ meson has not been determined yet due to the current limited data statistics. The large LHCb data sample that will be available in the near future could enable the studies of the $J/\psi\omega$ system in exclusive B-meson decays, *e.g.* $B^+ \to J/\psi\omega K^+$, and the amplitude analysis technique could be utilized to determine the spin-parity of the $X(3915)$ state, as well as the fit fraction. When the fit fraction is available, the width fraction $\Gamma(X \to J/\psi\omega)/\Gamma(X \to D_s^+D_s^-)$ will be obtained, providing additional experimental information to reveal the $X(3915)/X(3960)/\chi_{c0}(3930)$ nature.

REFERENCES

[1] Zyla P A, et al. Review of particle physics[J/OL]. Prog. Theor. Exp. Phys., 2020, 2020(8): 083C01. DOI: 10.1093/ptep/ptaa104.

[2] Choi S K, Olsen S L, Abe K, et al. Observation of a narrow charmoniumlike state in exclusive $B^{\pm} \to K^{\pm}\pi^{+}\pi^{-}J/\psi$ decays[J/OL]. Phys. Rev. Lett., 2003, 91: 262001. https://link.aps.org/doi/10.1103/PhysRevLett.91.262001.

[3] Aubert B, et al. Observation of a narrow meson decaying to $D_s^+\pi^0$ at a mass of 2.32 GeV/c^2 [J/OL]. Phys. Rev. Lett., 2003, 90: 242001. DOI: 10.1103/PhysRevLett.90.242001.

[4] Besson D, et al. Observation of a narrow resonance of mass 2.46 GeV/c^2 decaying to $D_s^{*+}\pi^0$ and confirmation of the $D_{sJ}^*(2317)$ state[J/OL]. Phys. Rev. D, 2003, 68: 032002. DOI: 10.1103/PhysRevD.68.032002.

[5] Godfrey S, Moats K. Properties of excited charm and charm-strange mesons[J/OL]. Phys. Rev. D, 2016, 93(3): 034035. DOI: 10.1103/PhysRevD.93.034035.

[6] Song Q T, Chen D Y, Liu X, et al. Charmed-strange mesons revisited: mass spectra and strong decays[J/OL]. Phys. Rev. D, 2015, 91: 054031. DOI: 10.1103/PhysRevD.91.054031.

[7] Barnes T, Godfrey S, Swanson E S. Higher charmonia[J/OL]. Phys. Rev. D, 2005, 72: 054026. DOI: 10.1103/PhysRevD.72.054026.

[8] Li B Q, Chao K T. Higher charmonia and X, Y, Z states with screened potential[J/OL]. Phys. Rev. D, 2009, 79: 094004. DOI: 10.1103/PhysRevD.79.094004.

[9] Brodzicka J, et al. Observation of a new D_{sJ} meson in $B^+ \to \bar{D}^0 D^0 K^+$ decays[J/OL]. Phys. Rev. Lett., 2008, 100: 092001. DOI: 10.1103/PhysRevLett.100.092001.

[10] Aubert B, et al. Study of resonances in exclusive B decays to $\bar{D}^{(*)}D^{(*)}K$[J/OL]. Phys. Rev. D, 2008, 77: 011102. DOI: 10.1103/PhysRevD.77.011102.

[11] Aushev T, et al. Study of the decays $B \to D_{s1}(2536)^+\bar{D}^{(*)}$[J/OL]. Phys. Rev. D, 2011, 83: 051102. DOI: 10.1103/PhysRevD.83.051102.

[12] Lees J P, et al. Dalitz plot analyses of $B^0 \to D^- D^0 K^+$ and $B^+ \to \overline{D}^0 D^0 K^+$ decays[J/OL]. Phys. Rev. D, 2015, 91(5): 052002. DOI: 10.1103/PhysRevD.91.052002.

[13] Aaij R, et al. Model-independent study of structure in $B^+ \to D^+ D^- K^+$ decays[J/OL]. Phys. Rev. Lett., 2020, 125: 242001. DOI: 10.1103/PhysRevLett.125.242001.

[14] Aaij R, et al. Amplitude analysis of the $B^+ \to D^+ D^- K^+$ decay[J/OL]. Phys. Rev., 2020, D102: 112003. DOI: 10.1103/PhysRevD.102.112003.

[15] Prelovsek S, Collins S, Mohler D, et al. Charmonium-like resonances with $J^{PC} = 0^{++}, 2^{++}$ in coupled $D\overline{D}$, $D_s D_s$ scattering on the lattice[J/OL]. JHEP, 2021, 06: 035. DOI: 10.1007/JHEP06(2021)035.

[16] Meng L, Wang B, Zhu S L. Predicting the $\bar{D}_s^{(*)}D_s^{(*)}$ bound states as the partners of $X(3872)$ [J/OL]. Sci. Bull., 2021, 66: 1413. DOI: 10.1016/j.scib.2021.03.016.

[17] Schwinger J. On quantum-electrodynamics and the magnetic moment of the electron[J/OL]. Phys. Rev., 1948, 73: 416-417. https://link.aps.org/doi/10.1103/PhysRev.73.416.

[18] Lamb W E, Retherford R C. Fine structure of the hydrogen atom by a microwave method[J/OL]. Phys. Rev., 1947, 72: 241-243. https://link.aps.org/doi/10.1103/PhysRev.72.241.

[19] Weinberg S. Essay: Half a century of the standard model[J/OL]. Phys. Rev. Lett., 2018, 121: 220001. https://link.aps.org/doi/10.1103/PhysRevLett.121.220001.

[20] Tuve M A, Heydenburg N P, Hafstad L R. The scattering of protons by protons[J/OL]. Phys. Rev., 1936, 50: 806-825. https://link.aps.org/doi/10.1103/PhysRev.50.806.

[21] Breit G, Condon E U, Present R D. Theory of scattering of protons by protons[J/OL]. Phys. Rev., 1936, 50: 825-845. https://link.aps.org/doi/10.1103/PhysRev.50.825.

[22] Breit G, Feenberg E. The possibility of the same form of specific interaction for all nuclear particles[J/OL]. Phys. Rev., 1936, 50: 850-856. https://link.aps.org/doi/10.1103/PhysRev.50.850.

[23] Gell-Mann M. Isotopic spin and new unstable particles[J/OL]. Phys. Rev., 1953, 92: 833-834. https://link.aps.org/doi/10.1103/PhysRev.92.833.

[24] Nakano T, Nishijima K. Charge independence for V-particles[J/OL]. Progress of Theoretical Physics, 1953, 10(5): 581-582. https://doi.org/10.1143/PTP.10.581.

[25] Gell-Mann M. The eightfold way: A theory of strong interaction symmetry[J/OL]. 1961. DOI: 10.2172/4008239.

[26] Ne'eman Y. Derivation of strong interactions from a gauge invariance[J/OL]. Nuclear Physics, 1961, 26(2): 222-229. https://www.sciencedirect.com/science/article/pii/0029558261901341. DOI: https://doi.org/10.1016/0029-5582(61)90134-1.

[27] Gell-Mann M. A schematic model of baryons and mesons[J/OL]. Phys. Lett., 1964, 8: 214-215. DOI: 10.1016/S0031-9163(64)92001-3.

[28] Zweig G. An SU_3 model for strong interaction symmetry and its breaking; Version 1: CERN-TH-401[R]. Geneva: CERN, 1964.

[29] Tkachov F. A contribution to the history of quarks: Boris Struminsky's 1965 JINR publication [J]. 2009.

[30] Greenberg O W. Spin and unitary-spin independence in a paraquark model of baryons and mesons[J/OL]. Phys. Rev. Lett., 1964, 13: 598-602. https://link.aps.org/doi/10.1103/PhysRevLett.13.598.

[31] Han M Y, Nambu Y. Three-triplet model with double SU(3) symmetry[J/OL]. Phys. Rev., 1965, 139: B1006-B1010. https://link.aps.org/doi/10.1103/PhysRev.139.B1006.

[32] Bloom E D, Coward D H, DeStaebler H, et al. High-energy inelastic $e - p$ scattering at 6° and 10°[J/OL]. Phys. Rev. Lett., 1969, 23: 930-934. https://link.aps.org/doi/10.1103/PhysRevLett.23.930.

[33] Breidenbach M, Friedman J I, Kendall H W, et al. Observed behavior of highly inelastic electron-proton scattering[J/OL]. Phys. Rev. Lett., 1969, 23: 935-939. https://link.aps.org/doi/10.1103/PhysRevLett.23.935.

[34] Fritzsch H, Gell-Mann M, Leutwyler H. Advantages of the color octet gluon picture[J/OL]. Physics Letters B, 1973, 47(4): 365-368. https://www.sciencedirect.com/science/article/pii/0370269373906254. DOI: https://doi.org/10.1016/0370-2693(73)90625-4.

[35] Fermi E. An attempt of a theory of beta radiation. 1.[J/OL]. Z. Phys., 1934, 88: 161-177. DOI: 10.1007/BF01351864.

[36] Lee T D, Yang C N. Question of parity conservation in weak interactions[J/OL]. Phys. Rev., 1956, 104: 254-258. https://link.aps.org/doi/10.1103/PhysRev.104.254.

[37] Wu C S, Ambler E, Hayward R W, et al. Experimental test of parity conservation in beta decay [J/OL]. Phys. Rev., 1957, 105: 1413-1415. https://link.aps.org/doi/10.1103/PhysRev.105.1413.

[38] Friedman J I, Telegdi V L. Nuclear emulsion evidence for parity nonconservation in the decay chain $\pi^+ - \mu^+ - e^+$[J/OL]. Phys. Rev., 1957, 105: 1681-1682. https://link.aps.org/doi/10.1103/PhysRev.105.1681.2.

[39] Garwin R L, Lederman L M, Weinrich M. Observations of the failure of conservation of parity and charge conjugation in meson decays: the magnetic moment of the free muon[J/OL]. Phys. Rev., 1957, 105: 1415-1417. https://link.aps.org/doi/10.1103/PhysRev.105.1415.

[40] Sudarshan E C G, Marshak R E. Chirality invariance and the universal fermi interaction[J/OL]. Phys. Rev., 1958, 109: 1860-1862. https://link.aps.org/doi/10.1103/PhysRev.109.1860.2.

[41] Feynman R P, Gell-Mann M. Theory of the fermi interaction[J/OL]. Phys. Rev., 1958, 109: 193-198. https://link.aps.org/doi/10.1103/PhysRev.109.193.

[42] Schwinger J S. A Theory of the Fundamental Interactions[J/OL]. Annals Phys., 1957, 2: 407-434. DOI: 10.1016/0003-4916(57)90015-5.

[43] Bludman S A. On the universal fermi interaction[J]. Il Nuovo Cimento (1955-1965), 1958, 9 (3): 433-445.

[44] Lopes J L. A model of the universal fermi interaction[J]. Nuclear Physics, 1958, 8: 234-236.

[45] Lee T D, Yang C N. Implications of the intermediate boson basis of the weak interactions: Existence of a quartet of intermediate bosons and their dual isotopic spin transformation properties[J/OL]. Phys. Rev., 1960, 119: 1410-1419. https://link.aps.org/doi/10.1103/PhysRev.119.1410.

[46] Glashow S L. Partial-symmetries of weak interactions[J]. Nuclear physics, 1961, 22(4): 579-588.

[47] Salam A, Ward J C. Electromagnetic and weak interactions[J/OL]. Phys. Lett., 1964, 13: 168-171. DOI: 10.1016/0031-9163(64)90711-5.

[48] Weinberg S. A model of leptons[J/OL]. Phys. Rev. Lett., 1967, 19: 1264-1266. https://link.aps.org/doi/10.1103/PhysRevLett.19.1264.

[49] Salam A, Svartholm N. Elementary particle physics: Relativistic groups and analyticity, eight nobel symposium[J]. Stockholm: Almquvist and Wiksell. p367, 1968.

[50] Nambu Y. Quasi-particles and gauge invariance in the theory of superconductivity[J/OL]. Phys. Rev., 1960, 117: 648-663. https://link.aps.org/doi/10.1103/PhysRev.117.648.

[51] Nambu Y, Jona-Lasinio G. Dynamical model of elementary particles based on an analogy with superconductivity. i[J/OL]. Phys. Rev., 1961, 122: 345-358. https://link.aps.org/doi/10.1103/PhysRev.122.345.

[52] Anderson P W. Plasmons, gauge invariance, and mass[J/OL]. Phys. Rev., 1963, 130: 439-442. https://link.aps.org/doi/10.1103/PhysRev.130.439.

[53] Englert F, Brout R. Broken symmetry and the mass of gauge vector mesons[J/OL]. Phys. Rev. Lett., 1964, 13: 321-323. https://link.aps.org/doi/10.1103/PhysRevLett.13.321.

[54] Higgs P. Broken symmetries, massless particles and gauge fields[J/OL]. Physics Letters, 1964, 12(2): 132-133. https://www.sciencedirect.com/science/article/pii/0031916364911369. DOI: https://doi.org/10.1016/0031-9163(64)91136-9.

[55] Guralnik G S, Hagen C R, Kibble T W B. Global conservation laws and massless particles [J/OL]. Phys. Rev. Lett., 1964, 13: 585-587. https://link.aps.org/doi/10.1103/PhysRevLett.13.585.

[56] Hooft G. Renormalizable lagrangians for massive yang-mills fields[J/OL]. Nuclear Physics B, 1971, 35(1): 167-188. https://www.sciencedirect.com/science/article/pii/0550321371901398. DOI: https://doi.org/10.1016/0550-3213(71)90139-8.

[57] Cabibbo N. Unitary symmetry and leptonic decays[J/OL]. Phys. Rev. Lett., 1963, 10: 531-533. DOI: 10.1103/PhysRevLett.10.531.

[58] Glashow S L, Iliopoulos J, Maiani L. Weak interactions with lepton-hadron symmetry[J/OL]. Phys. Rev. D, 1970, 2: 1285-1292. https://link.aps.org/doi/10.1103/PhysRevD.2.1285.

[59] Kobayashi M, Maskawa T. CP-violation in the renormalizable theory of weak interaction[J]. Progress of theoretical physics, 1973, 49(2): 652-657.

[60] Chatrchyan S, et al. Observation of a new boson at a mass of 125 GeV with the CMS experiment at the LHC[J/OL]. Phys. Lett. B, 2012, 716: 30-61. DOI: 10.1016/j.physletb.2012.08.021.

[61] Aad G, et al. Observation of a new particle in the search for the Standard Model Higgs boson with the ATLAS detector at the LHC[J/OL]. Phys. Lett. B, 2012, 716: 1-29. DOI: 10.1016/j.physletb.2012.08.020.

[62] Fukugita M, Yanagida T. Physics of neutrinos: and application to astrophysics[M]. Springer Science & Business Media, 2013.

[63] Wikipedia contributors. Standard model — Wikipedia, the free encyclopedia[EB/OL]. 2021. https://en.wikipedia.org/w/index.php?title=Standard_Model&oldid=1060203113.

[64] Amhis Y S, et al. Averages of b-hadron, c-hadron, and τ-lepton properties as of 2018[J/OL]. Eur. Phys. J. C, 2021, 81(3): 226. DOI: 10.1140/epjc/s10052-020-8156-7.

[65] Schwartz M D. Quantum field theory and the standard model[M]. Cambridge University Press, 2014.

[66] Deur A, Brodsky S J, de Teramond G F. The QCD running coupling[J/OL]. Nucl. Phys., 2016, 90: 1. DOI: 10.1016/j.ppnp.2016.04.003.

[67] Feynman R P. The behavior of hadron collisions at extreme energies[J]. Conf. Proc. C, 1969, 690905: 237-258.

[68] Bjorken J D, Paschos E A. Inelastic electron-proton and γ-proton scattering and the structure of the nucleon[J/OL]. Phys. Rev., 1969, 185: 1975-1982. https://link.aps.org/doi/10.1103/PhysRev.185.1975.

[69] Richard J M. An introduction to the quark model[C]//Ferrara International School Niccolò Cabeo 2012: Hadronic spectroscopy. 2012.

[70] Thomson M. Modern particle physics[M]. Cambridge University Press, 2013.

[71] Guzey V, Polyakov M V. SU(3) systematization of baryons[J]. 2005.

[72] Aaij R, et al. Observation of the doubly charmed baryon Ξ_{cc}^{++}[J/OL]. Phys. Rev. Lett., 2017, 119: 112001. DOI: 10.1103/PhysRevLett.119.112001.

[73] Aaij R, et al. Search for the doubly charmed baryon Ξ_{cc}^{+}[J/OL]. JHEP, 2013, 12: 090. DOI: 10.1007/JHEP12(2013)090.

[74] Aaij R, et al. Search for the doubly charmed baryon Ξ_{cc}^{+}[J/OL]. Sci. China Phys. Mech. Astron., 2020, 63: 221062. DOI: 10.1007/s11433-019-1471-8.

[75] Aaij R, et al. Search for the doubly heavy baryons Ω_{bc}^{0} and Ξ_{bc}^{0} decaying to $\Lambda_c^+\pi^-$ and $\Xi_c^+\pi^-$ [J/OL]. Chin. Phys., 2021, C45: 093002. DOI: 10.1088/1674-1137/ac0c70.

[76] Aaij R, et al. Search for the doubly charmed baryon Ω_{cc}^{+}[J/OL]. Sci. China Phys. Mech. Astron., 2021, 64: 101062. DOI: 10.1007/s11433-021-1742-7.

[77] Aaij R, et al. Search for the doubly charmed baryon Ξ_{cc}^{+} in the $\Xi_c^+\pi^-\pi^+$ final state[J]. 2021.

[78] Rosner J L. Possibility of baryon-antibaryon enhancements with unusual quantum numbers [J/OL]. Phys. Rev. Lett., 1968, 21: 950-952. https://link.aps.org/doi/10.1103/PhysRevLett.21.950.

[79] Rossi G C, Veneziano G. A possible description of baryon dynamics in dual and gauge theories [J/OL]. Nucl. Phys. B, 1977, 123: 507-545. DOI: 10.1016/0550-3213(77)90178-X.

[80] Karliner M, Rosner J L, Skwarnicki T. Multiquark states[J/OL]. Ann. Rev. Nucl. Part. Sci., 2018, 68: 17-44. DOI: 10.1146/annurev-nucl-101917-020902.

[81] Olsen S L, Skwarnicki T, Zieminska D. Nonstandard heavy mesons and baryons: Experimental evidence[J/OL]. Rev. Mod. Phys., 2018, 90: 015003. https://link.aps.org/doi/10.1103/RevModPhys.90.015003.

[82] Maiani L, Piccinini F, Polosa A D, et al. Diquark-antidiquarks with hidden or open charm and the nature of $X(3872)$[J/OL]. Phys. Rev. D, 2005, 71: 014028. DOI: 10.1103/PhysRevD.71.014028.

[83] Browder T E, Pakvasa S, Petrov A A. Comment on the new $D_s^{(*)+}\pi^0$ resonances[J/OL]. Phys. Lett. B, 2004, 578: 365-368. DOI: 10.1016/j.physletb.2003.10.067.

[84] Barnes T, Close F E, Lipkin H J. Implications of a DK molecule at 2.32 GeV[J/OL]. Phys. Rev. D, 2003, 68: 054006. DOI: 10.1103/PhysRevD.68.054006.

[85] van Beveren E, Rupp G. Observed $D_s(2317)$ and tentative $D(2100$–$2300)$ as the charmed cousins of the light scalar nonet[J/OL]. Phys. Rev. Lett., 2003, 91: 012003. DOI: 10.1103/PhysRevLett.91.012003.

[86] Eichten E, Gottfried K, Kinoshita T, et al. Charmonium: The model[J/OL]. Phys. Rev. D, 1978, 17: 3090-3117. https://link.aps.org/doi/10.1103/PhysRevD.17.3090.

[87] Brandelik R, Braunschweig W, Martyn H U, et al. Evidence for the F meson[J]. Physics Letters B, 1977, 70(1): 132-136.

[88] Albrecht H, Gläser R, Harder G, et al. Observation of a new charmed-strange meson[J]. Physics Letters B, 1989, 230(1-2): 162-168.

[89] Kubota Y, et al. Observation of a new charmed strange meson[J/OL]. Phys. Rev. Lett., 1994, 72: 1972-1976. DOI: 10.1103/PhysRevLett.72.1972.

[90] Aubert B, et al. Observation of a new D_s meson decaying to DK at a mass of 2.86 GeV/c^2 [J/OL]. Phys. Rev. Lett., 2006, 97: 222001. DOI: 10.1103/PhysRevLett.97.222001.

[91] Aubert B, et al. Study of D_{sJ} decays to D^*K in inclusive e^+e^- interactions[J/OL]. Phys. Rev. D, 2009, 80: 092003. DOI: 10.1103/PhysRevD.80.092003.

[92] Aaij R, et al. Observation of overlapping spin-1 and spin-3 $\overline{D}^0K^-$ resonances at mass 2.86 GeV/c^2[J/OL]. Phys. Rev. Lett., 2014, 113: 162001. DOI: 10.1103/PhysRevLett.113.162001.

[93] Aaij R, et al. Dalitz plot analysis of $B_s^0 \to \overline{D}^0K^-\pi^+$ decays[J/OL]. Phys. Rev., 2014, D90: 072003. DOI: 10.1103/PhysRevD.90.072003.

[94] Okubo S. φ-meson and unitary symmetry model[J]. Physics Letters, 1963, 5(2): 165-168.

[95] Zweig G. Cern report 8419[J]. TH412, 1964, 243.

[96] Iizuka J. A systematics and phenomenology of meson family[J]. Progress of Theoretical Physics Supplement, 1966, 37: 21-34.

[97] Aaij R, et al. Measurement of B_s^0 and D_s^- meson lifetimes[J/OL]. Phys. Rev. Lett., 2017, 119: 101801. DOI: 10.1103/PhysRevLett.119.101801.

[98] Palano A. Experimental status of excited D_s^+ mesons[J]. 2020.

[99] Aaij R, et al. Study of D_{sJ}^+ mesons decaying to $D^{*+}K_S^0$ and $D^{*0}K^+$ final states[J/OL]. JHEP, 2016, 02: 133. DOI: 10.1007/JHEP02(2016)133.

[100] Frabetti P L, et al. Analysis of the D^+, $D_s^+ \to K^+K^-\pi^+$ Dalitz plots[J/OL]. Phys. Lett. B, 1995, 351: 591-600. DOI: 10.1016/0370-2693(95)00427-M.

[101] Mitchell R E, et al. Dalitz Plot analysis of $D_s^+ \to K^+K^-\pi^+$[J/OL]. Phys. Rev. D, 2009, 79: 072008. DOI: 10.1103/PhysRevD.79.072008.

[102] del Amo Sanchez P, et al. Dalitz plot analysis of $D_s^+ \to K^+K^-\pi^+$[J/OL]. Phys. Rev. D, 2011, 83: 052001. DOI: 10.1103/PhysRevD.83.052001.

[103] Lewis R, Woloshyn R M. S and P wave heavy light mesons in lattice NRQCD[J/OL]. Phys. Rev. D, 2000, 62: 114507. DOI: 10.1103/PhysRevD.62.114507.

[104] Moir G, Peardon M, Ryan S M, et al. Excited spectroscopy of charmed mesons from lattice QCD[J/OL]. JHEP, 2013, 05: 021. DOI: 10.1007/JHEP05(2013)021.

[105] Cichy K, Kalinowski M, Wagner M. Mass spectra of mesons containing charm quarks - continuum limit results from twisted mass fermions[J]. PoS, 2015, LATTICE2015: 093.

[106] Godfrey S, Isgur N. Mesons in a relativized quark model with chromodynamics[J/OL]. Phys. Rev. D, 1985, 32: 189-231. https://link.aps.org/doi/10.1103/PhysRevD.32.189.

[107] Capstick S, Isgur N. Baryons in a relativized quark model with chromodynamics[J/OL]. AIP Conf. Proc., 1985, 132: 267-271. DOI: 10.1063/1.35361.

[108] Dai Y B, Li X Q, Zhu S L, et al. Contribution of DK continuum in the QCD sum rule for $D_{sJ}(2317)$[J/OL]. Eur. Phys. J. C, 2008, 55: 249-258. DOI: 10.1140/epjc/s10052-008-0591-9.

[109] Liu Y R, Liu X, Zhu S L. Light pseudoscalar meson and heavy meson scattering lengths[J/OL]. Phys. Rev. D, 2009, 79: 094026. DOI: 10.1103/PhysRevD.79.094026.

[110] Micu L. Decay rates of meson resonances in a quark model[J]. Nuclear Physics B, 1969, 10(3): 521-526.

[111] Godfrey S, Moats K. Bottomonium Mesons and Strategies for their Observation[J/OL]. Phys. Rev. D, 2015, 92(5): 054034. DOI: 10.1103/PhysRevD.92.054034.

[112] Chen B, Wei K W, Liu X, et al. Low-lying charmed and charmed-strange baryon states[J/OL]. Eur. Phys. J. C, 2017, 77(3): 154. DOI: 10.1140/epjc/s10052-017-4708-x.

[113] Colangelo P, De Fazio F. Open charm meson spectroscopy: Where to place the latest piece of the puzzle[J/OL]. Phys. Rev. D, 2010, 81: 094001. DOI: 10.1103/PhysRevD.81.094001.

[114] He X G, Wang W, Zhu R. Open-charm tetraquark X_c and open-bottom tetraquark X_b[J/OL]. Eur. Phys. J. C, 2020, 80(11): 1026. DOI: 10.1140/epjc/s10052-020-08597-1.

[115] Liu M Z, Xie J J, Geng L S. $X_0(2866)$ as a $D^*\overline{K}^*$ molecular state[J/OL]. Phys. Rev. D, 2020, 102: 091502. https://link.aps.org/doi/10.1103/PhysRevD.102.091502.

[116] He J, Chen D Y. Molecular picture for $X_0(2900)$ and $X_1(2900)$[J/OL]. Chin. Phys. C, 2021, 45 (6): 063102. DOI: 10.1088/1674-1137/abeda8.

[117] Hu M W, Lao X Y, Ling P, et al. $X_0(2900)$ and its heavy quark spin partners in molecular picture [J]. Chinese Physics C, 2021, 45(2): 021003.

[118] Qi J J, Wang Z Y, Zhang Z F, et al. Studying the $\bar{D}_1K$ molecule in the Bethe–Salpeter equation approach[J/OL]. Eur. Phys. J. C, 2021, 81(7): 639. DOI: 10.1140/epjc/s10052-021-09422-z.

[119] Xue Y, Jin X, Huang H, et al. Tetraquarks with open charm flavor[J/OL]. Phys. Rev. D, 2021, 103(5): 054010. DOI: 10.1103/PhysRevD.103.054010.

[120] Chen H X, Chen W, Dong R R, et al. $X_0(2900)$ and $X_1(2900)$: Hadronic molecules or compact tetraquarks[J/OL]. Chinese Physics Letters, 2020, 37(10): 101201. https://doi.org/10.1088/0256-307x/37/10/101201.

[121] Agaev S S, Azizi K, Sundu H. New scalar resonance $X_0(2900)$ as a molecule: mass and width [J/OL]. J. Phys. G, 2021, 48(8): 085012. DOI: 10.1088/1361-6471/ac0b31.

[122] Chen H, Qi H R, Zheng H Q. $X_1(2900)$ as a $\bar{D}_1K$ molecule[J/OL]. Eur. Phys. J. C, 2021, 81 (9): 812. DOI: 10.1140/epjc/s10052-021-09603-w.

[123] Burns T J, Swanson E S. Kinematical cusp and resonance interpretations of the $X(2900)$[J/OL]. Phys. Lett. B, 2021, 813: 136057. DOI: 10.1016/j.physletb.2020.136057.

[124] Liu X H, Yan M J, Ke H W, et al. Triangle singularity as the origin of $X_0(2900)$ and $X_1(2900)$ observed in $B^+ \to D^+D^-K^+$[J/OL]. Eur. Phys. J. C, 2020, 80(12): 1178. DOI: 10.1140/epjc/s10052-020-08762-6.

[125] Aaij R, et al. Observation of new resonances decaying to $J/\psi K^+$ and $J/\psi\phi$ [J/OL]. Phys. Rev. Lett., 2021, 127: 082001. DOI: 10.1103/PhysRevLett.127.082001.

[126] Ablikim M, et al. Observation of a near-threshold structure in the K^+ recoil-mass spectra in $e^+e^- \to K^+(D_s^- D^{*0} + D_s^{*-} D^0)$[J/OL]. Phys. Rev. Lett., 2021, 126(10): 102001. DOI: 10.1103/PhysRevLett.126.102001.

[127] Cronin-Hennessy D, et al. Measurement of charm production cross sections in e^+e^- annihilation at energies between 3.97 and 4.26 GeV[J/OL]. Phys. Rev. D, 2009, 80: 072001. DOI: 10.1103/PhysRevD.80.072001.

[128] del Amo Sanchez P, et al. Exclusive production of $D_s^+ D_s^-$, $D_s^{*+} D_s^-$, and $D_s^{*+} D_s^{*-}$ via e^+e^- annihilation with initial-state-radiation[J/OL]. Phys. Rev. D, 2010, 82: 052004. DOI: 10.1103/PhysRevD.82.052004.

[129] Pakhlova G, et al. Measurement of $e^+e^- \to D_s^{(*)+} D_s^{(*)-}$ cross sections near threshold using initial-state radiation[J/OL]. Phys. Rev. D, 2011, 83: 011101. DOI: 10.1103/PhysRevD.83.011101.

[130] Tornqvist N A. Isospin breaking of the narrow charmonium state of Belle at 3872-MeV as a deuson[J/OL]. Phys. Lett. B, 2004, 590: 209-215. DOI: 10.1016/j.physletb.2004.03.077.

[131] Swanson E S. Short range structure in the $X(3872)$[J/OL]. Phys. Lett. B, 2004, 588: 189-195. DOI: 10.1016/j.physletb.2004.03.033.

[132] Gamermann D, Oset E. Isospin breaking effects in the $X(3872)$ resonance[J/OL]. Phys. Rev. D, 2009, 80: 014003. DOI: 10.1103/PhysRevD.80.014003.

[133] Dong Y b, Faessler A, Gutsche T, et al. Estimate for the $X(3872) \to \gamma J/\psi$ decay width[J/OL]. Phys. Rev. D, 2008, 77: 094013. DOI: 10.1103/PhysRevD.77.094013.

[134] Wu J, Liu Y R, Chen K, et al. $X(4140)$, $X(4270)$, $X(4500)$ and $X(4700)$ and their $cs\bar{c}\bar{s}$ tetraquark partners[J/OL]. Phys. Rev. D, 2016, 94(9): 094031. DOI: 10.1103/PhysRevD.94.094031.

[135] Alves Jr. A A, et al. The LHCb detector at the LHC[J/OL]. JINST, 2008, 3 (LHCb-DP-2008-001): S08005. DOI: 10.1088/1748-0221/3/08/S08005.

[136] LHC Machine[J/OL]. JINST, 2008, 3: S08001. DOI: 10.1088/1748-0221/3/08/S08001.

[137] Aamodt K, et al. The ALICE experiment at the CERN LHC[J/OL]. JINST, 2008, 3: S08002. DOI: 10.1088/1748-0221/3/08/S08002.

[138] Aad G, et al. The ATLAS experiment at the CERN Large Hadron Collider[J/OL]. JINST, 2008, 3: S08003. DOI: 10.1088/1748-0221/3/08/S08003.

[139] Chatrchyan S, et al. The CMS experiment at the CERN LHC[J/OL]. JINST, 2008, 3: S08004. DOI: 10.1088/1748-0221/3/08/S08004.

[140] Haffner J. The CERN accelerator complex. Complexe des accélérateurs du CERN[J/OL]. 2013. https://cds.cern.ch/record/1621894.

[141] LHCb collaboration. LHCb cumulative integrated recorded luminosity in pp, 2010-2018 [EB/OL]. 2022. https://lbgroups.cern.ch/online/OperationsPlots/index.htm.

[142] Elsässer C. $\bar{b}b$ production angle plots[EB/OL]. https://lhcb.web.cern.ch/lhcb/speakersbureau/html/bb_ProductionAngles.html.

[143] Aaij R, et al. Performance of the LHCb Vertex Locator[J/OL]. JINST, 2014, 9: P09007. DOI: 10.1088/1748-0221/9/09/P09007.

[144] Aaij R, et al. LHCb detector performance[J/OL]. Int. J. Mod. Phys., 2015, A30: 1530022. DOI: 10.1142/S0217751X15300227.

[145] Borghi S, et al. First spatial alignment of the LHCb VELO and analysis of beam absorber collision data[J/OL]. Nucl. Instrum. Meth., 2010, A618: 108-120. DOI: 10.1016/j.nima.2010.02.109.

[146] Adinolfi M, et al. Performance of the LHCb RICH detector at the LHC[J/OL]. Eur. Phys. J., 2013, C73: 2431. DOI: 10.1140/epjc/s10052-013-2431-9.

[147] Alves Jr. A A, et al. Performance of the LHCb muon system[J/OL]. JINST, 2013, 8: P02022. DOI: 10.1088/1748-0221/8/02/P02022.

[148] Archilli F, et al. Performance of the muon identification at LHCb[J/OL]. JINST, 2013, 8: P10020. DOI: 10.1088/1748-0221/8/10/P10020.

[149] LHCb collaboration. Trigger plots and diagrams for conferences[EB/OL]. . https://twiki.cern.ch/twiki/bin/view/LHCb/LHCbTriggerConferenceDiagramsPlots.

[150] Aaij R, et al. The LHCb trigger and its performance in 2011[J/OL]. JINST, 2013, 8: P04022. DOI: 10.1088/1748-0221/8/04/P04022.

[151] Abellan Beteta C, et al. Calibration and performance of the LHCb calorimeters in Run 1 and 2 at the LHC[J]. 2020.

[152] Aaij R, et al. Tesla: an application for real-time data analysis in High Energy Physics[J/OL]. Comput. Phys. Commun., 2016, 208: 35-42. DOI: 10.1016/j.cpc.2016.07.022.

[153] Aaij R, et al. Performance of the LHCb trigger and full real-time reconstruction in Run 2 of the LHC[J/OL]. JINST, 2019, 14(LHCb-DP-2019-001): P04013. DOI: 10.1088/1748-0221/14/04/P04013.

[154] Aaij R, et al. A comprehensive real-time analysis model at the LHCb experiment[J/OL]. JINST, 2019, 14: P04006. DOI: 10.1088/1748-0221/14/04/P04006.

[155] Sjöstrand T, Mrenna S, Skands P. A brief introduction to PYTHIA 8.1[J/OL]. Comput. Phys. Commun., 2008, 178: 852-867. DOI: 10.1016/j.cpc.2008.01.036.

[156] Belyaev I, et al. Handling of the generation of primary events in Gauss, the LHCb simulation framework[J/OL]. J. Phys. Conf. Ser., 2011, 331: 032047. DOI: 10.1088/1742-6596/331/3/032047.

[157] Lange D J. The EvtGen particle decay simulation package[J/OL]. Nucl. Instrum. Meth., 2001, A462: 152-155. DOI: 10.1016/S0168-9002(01)00089-4.

[158] Davidson N, Przedzinski T, Was Z. PHOTOS interface in C++: Technical and physics documentation[J/OL]. Comp. Phys. Comm., 2016, 199: 86. DOI: https://doi.org/10.1016/j.cpc.2015.09.013.

[159] Allison J, Amako K, Apostolakis J, et al. Geant4 developments and applications[J/OL]. IEEE Trans.Nucl.Sci., 2006, 53: 270. DOI: 10.1109/TNS.2006.869826.

[160] Agostinelli S, et al. Geant4: A simulation toolkit[J/OL]. Nucl. Instrum. Meth., 2003, A506: 250. DOI: 10.1016/S0168-9002(03)01368-8.

[161] Clemencic M, et al. The LHCb simulation application, Gauss: Design, evolution and experience [J/OL]. J. Phys. Conf. Ser., 2011, 331: 032023. DOI: 10.1088/1742-6596/331/3/032023.

[162] Müller D, Clemencic M, Corti G, et al. ReDecay: A novel approach to speed up the simulation at LHCb[J/OL]. Eur. Phys. J., 2018, C78: 1009. DOI: 10.1140/epjc/s10052-018-6469-6.

[163] Tanabashi M, et al. Review of particle physics[J/OL]. Phys. Rev., 2018, D98: 030001. DOI: 10.1103/PhysRevD.98.030001.

[164] Gligorov V V, Williams M. Efficient, reliable and fast high-level triggering using a bonsai boosted decision tree[J/OL]. JINST, 2013, 8: P02013. DOI: 10.1088/1748-0221/8/02/P02013.

[165] Aaij R, et al. Measurement of b-hadron masses[J/OL]. Phys. Lett., 2012, B708: 241. DOI: 10.1016/j.physletb.2012.01.058.

[166] Hulsbergen W D. Decay chain fitting with a Kalman filter[J/OL]. Nucl. Instrum. Meth., 2005, A552: 566-575. DOI: 10.1016/j.nima.2005.06.078.

[167] Ryd A, Lange D, Kuznetsova N, et al. EvtGen: A Monte Carlo Generator for B-Physics[J]. 2005.

[168] Bonvicini G, et al. Dalitz plot analysis of the D+ —> K- pi+ pi+ decay[J/OL]. Phys. Rev. D, 2008, 78: 052001. DOI: 10.1103/PhysRevD.78.052001.

[169] LHCb collaboration. Unbinned pid resampling using kernel density estimation[EB/OL]. . https://twiki.cern.ch/twiki/bin/view/LHCb/MeerkatPIDResampling.

[170] Gulin A, Kuralenok I, Pavlov D. Winning the transfer learning track of yahoo!'s learning to rank challenge with yetirank[C/OL]//Chapelle O, Chang Y, Liu T Y. Proceedings of Machine Learning Research: volume 14 Proceedings of the Learning to Rank Challenge. Haifa, Israel: PMLR, 2011: 63-76. https://proceedings.mlr.press/v14/gulin11a.html.

[171] Aaij R, et al. Measurement of b-hadron fractions in 13 TeV pp collisions[J/OL]. Phys. Rev., 2019, D100: 031102(R). DOI: 10.1103/PhysRevD.100.031102.

[172] Aaij R, et al. Measurement of f_s/f_u variation with proton-proton collision energy and B-meson kinematics[J/OL]. Phys. Rev. Lett., 2020, 124: 122002. DOI: 10.1103/PhysRevLett.124.122002.

[173] Aaij R, et al. Study of beauty hadron decays into pairs of charm hadrons[J/OL]. Phys. Rev. Lett., 2014, 112: 202001. DOI: 10.1103/PhysRevLett.112.202001.

[174] Pivk M, Le Diberder F R. sPlot: A statistical tool to unfold data distributions[J/OL]. Nucl. Instrum. Meth., 2005, A555: 356-369. DOI: 10.1016/j.nima.2005.08.106.

[175] Skwarnicki T. A study of the radiative cascade transitions between the Upsilon-prime and Upsilon resonances[D]. Institute of Nuclear Physics, Krakow, 1986.

[176] Verkerke W, Kirkby D P. The RooFit toolkit for data modeling[J]. eConf, 2003, C0303241: MOLT007.

[177] Dembinski H, Kenzie M, Langenbruch C, et al. Custom Orthogonal Weight functions (COWs) for Event Classification[J]. 2021.

[178] Balagura V, et al. Observation of $D_{s1}(2536)^+ \to D^+\pi^-K^+$ and angular decomposition of $D_{s1}(2536)^+ \to D^{*+}K^0_S$[J/OL]. Phys. Rev. D, 2008, 77: 032001. DOI: 10.1103/PhysRevD.77.032001.

[179] Richman J D. An experimenter's guide to the helicity formalism[J]. 1984.

[180] Mikhasenko M, et al. Dalitz-plot decomposition for three-body decays[J/OL]. Phys. Rev. D, 2020, 101(3): 034033. DOI: 10.1103/PhysRevD.101.034033.

[181] Aaij R, et al. Observation of $J/\psi p$ resonances consistent with pentaquark states in $\Lambda_b^0 \to J/\psi p K^-$ decays[J/OL]. Phys. Rev. Lett., 2015, 115: 072001. DOI: 10.1103/PhysRevLett.115.072001.

[182] Blatt J M, Weisskopf V F. Theoretical nuclear physics[M/OL]. New York: Springer, 1952. DOI: 10.1007/978-1-4612-9959-2.

[183] Aston D, et al. A study of $K^-\pi^+$ scattering in the reaction $K^-p \to K^-\pi^+n$ at 11-GeV/c[J/OL]. Nucl. Phys., 1988, B296: 493-526. DOI: 10.1016/0550-3213(88)90028-4.

[184] Xie Y. sFit: A method for background subtraction in maximum likelihood fit[J]. 2009.

[185] Aaij R, et al. Amplitude analysis of $B^+ \to J/\psi \phi K^+$ decays[J/OL]. Phys. Rev., 2017, D95: 012002. DOI: 10.1103/PhysRevD.95.012002.

[186] Xie J M, Liu M Z, Geng L S. $D_{s0}(2590)$ as a dominant $c\bar{s}$ state with a small D*K component [J/OL]. Phys. Rev. D, 2021, 104(9): 094051. DOI: 10.1103/PhysRevD.104.094051.

[187] Ortega P G, Segovia J, Entem D R, et al. The $D_{s0}(2590)^+$ as the dressed $c\bar{s}(2^1S_0)$ meson in a coupled-channels calculation[J]. 2021.

[188] Gao Z, Wang G Y, Lü Q F, et al. Canonical interpretation of the $D_{s0}(2590)^+$ resonance[J]. 2022.

[189] Ni R H, Li Q, Zhong X H. Mass spectra and strong decays of charmed and charmed-strange mesons[J]. 2021.

[190] Aaij R, et al. Observation of two new excited Ξ_b^0 states decaying to $\Lambda_b^0 K^-\pi^+$[J]. 2021.

[191] Voss H, Hoecker A, Stelzer J, et al. TMVA - Toolkit for Multivariate Data Analysis with ROOT [J/OL]. PoS, 2007, ACAT: 040. DOI: 10.22323/1.050.0040.

[192] Hoecker A, et al. TMVA 4 — Toolkit for Multivariate Data Analysis with ROOT. Users Guide. [J]. 2009.

[193] Cowan G A, Craik D C, Needham M D. RapidSim: an application for the fast simulation of heavy-quark hadron decays[J/OL]. Comput. Phys. Commun., 2017, 214: 239-246. DOI: 10.1016/j.cpc.2017.01.029.

[194] LHCb collaboration. Standard set of performance numbers[EB/OL]. 2022. https://lhcb.web.cern.ch/speakersbureau/html/PerformanceNumbers.html.

[195] Poluektov A. Kernel density estimation of a multidimensional efficiency profile[J/OL]. JINST, 2015, 10(02): P02011. DOI: 10.1088/1748-0221/10/02/P02011.

[196] Martínez Santos D, Dupertuis F. Mass distributions marginalized over per-event errors[J/OL]. Nucl. Instrum. Meth., 2014, A764: 150-155. DOI: 10.1016/j.nima.2014.06.081.

[197] Efron B. Bootstrap methods: Another look at the jackknife[J/OL]. Ann. Statist., 1979, 7(1): 1-26. DOI: 10.1214/aos/1176344552.

[198] Aaij R, et al. Measurement of the branching fraction and CP asymmetry in $B^+ \to J/\psi \rho^+$ decays [J/OL]. Eur. Phys. J., 2019, C79: 537. DOI: 10.1140/epjc/s10052-019-6698-3.

[199] Aaij R, et al. Measurement of the branching fraction of the $B^0 \to D_s^+\pi^-$ decay[J/OL]. Eur. Phys. J., 2021, C81: 314. DOI: 10.1140/epjc/s10052-020-08790-2.

[200] Aaij R, et al. Physics case for an LHCb Upgrade II - Opportunities in flavour physics, and beyond, in the HL-LHC era[J]. 2018.

APPENDIX A SUPPLEMENTAL MATERIAL OF THE $B^0 \to D^+D^-K^+\pi^-$ ANALYSIS

A.1 Amplitude fit projections for J^P assignments other than $J^P = 0^-$

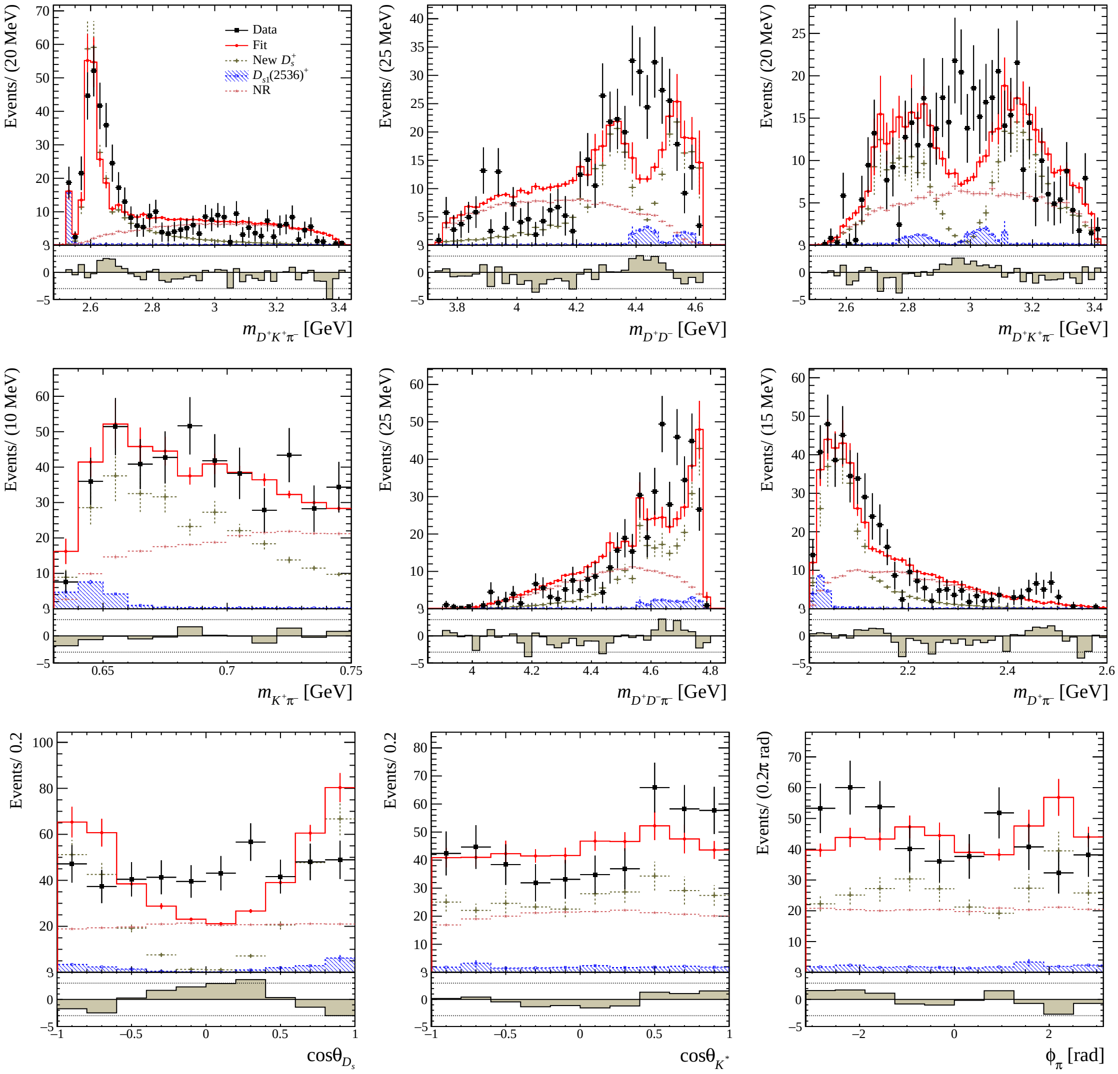

Figure A.1 Fit projections for the $J^P = 1^+$ model. A constant width is taken for the decay channel $D_{s0}(2590)^+ \to DK\pi$ with the width fraction r free in the fit.

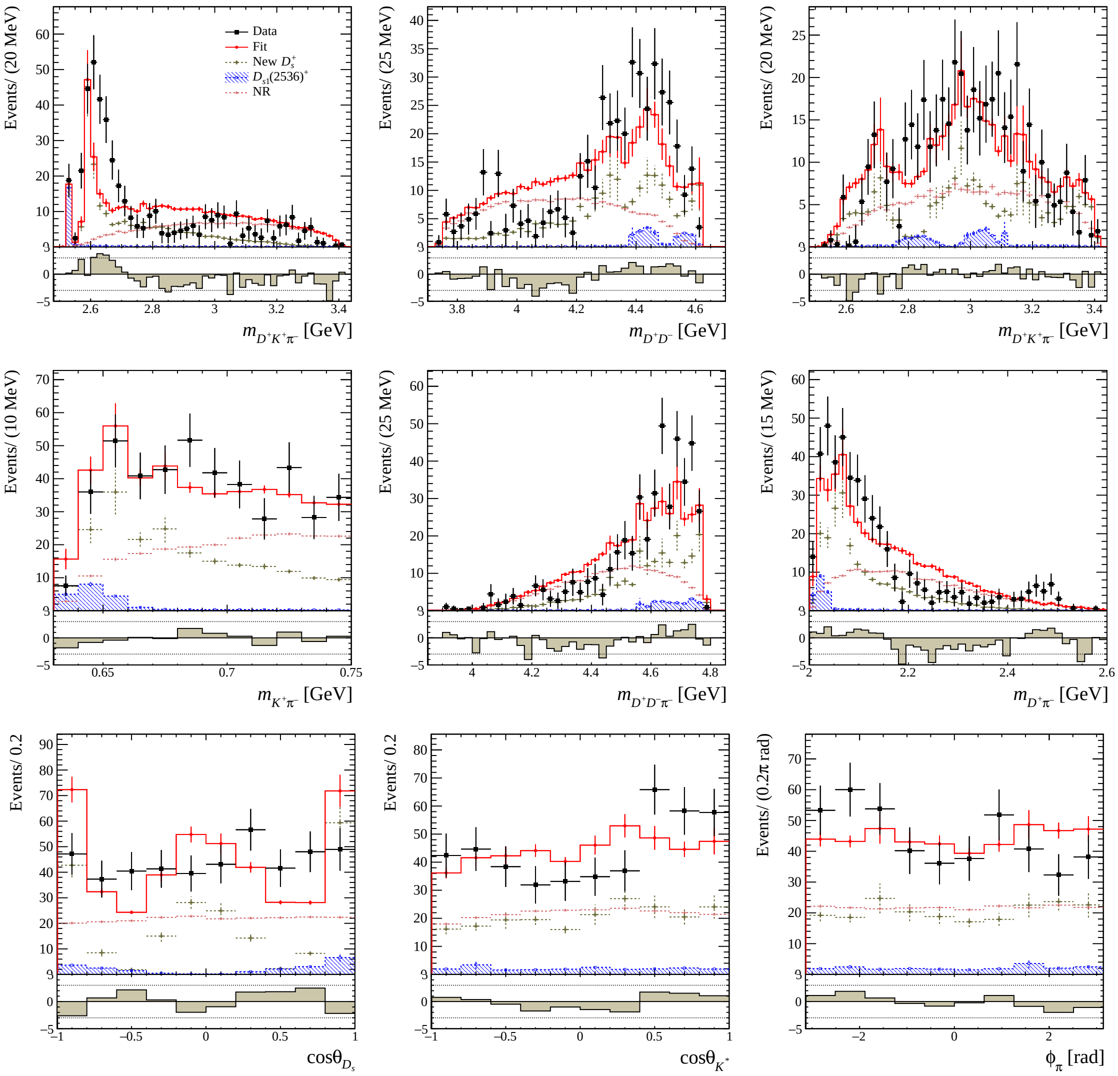

Figure A.2 Fit projections for the $J^P = 2^-$ model. A constant width is taken for the $D_{s0}(2590)^+ \to DK\pi$ channel with the width fraction r free in the fit.

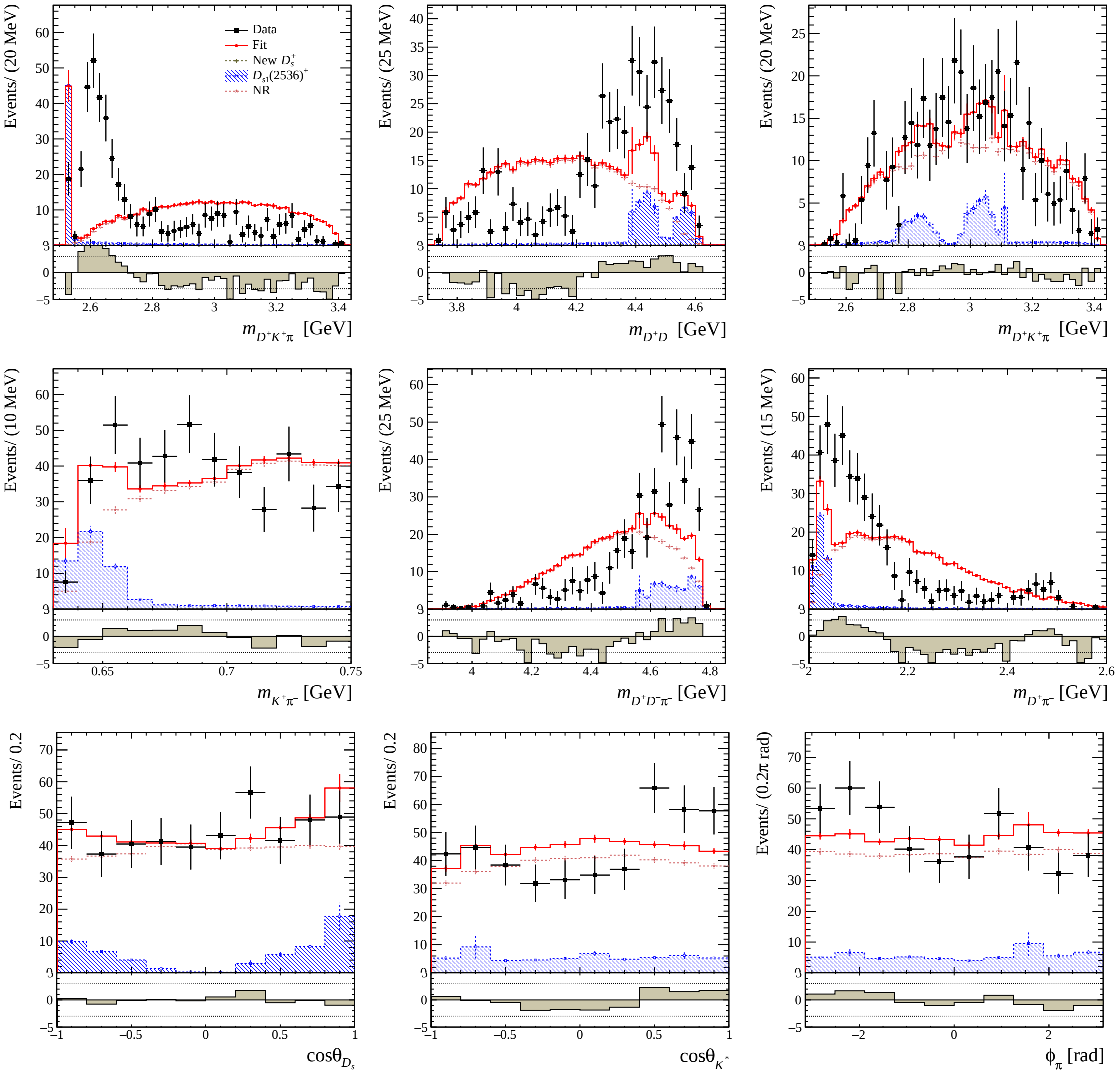

Figure A.3 Fit projections for the amplitude model without the $D_{s0}(2590)^+$ contribution.

A.2 BW and pole parameters for the amplitude fits in the systematic study

In Sec. 3.10, the systematic uncertainties of the pole mass and width are reported. The pole mass and width are not the direct outputs of the amplitude fits but are derived from the fitted BW parameters. The pole and BW parameters in the systematic studies are shown in Table A.1. It is seen that the BW mass and width vary a lot for different $D_{s0}(2590)^+$ width parameterizations, but the pole mass and width are stable.

Table A.1 The BW and pole parameters of the $D_{s0}(2590)^+$ state determined by the amplitude fits in systematic studies. The statistical uncertainties of the pole mass and width are not evaluated for the systematic sources due to the complexity of the error propagation.

Source	Sub-source	m_0 (MeV)	Γ_0 (MeV)	m_R (MeV)	Γ_R (MeV)
Nominal	-	2602.97 ± 5.90	94.44 ± 18.45	2591.34 ± 6.18	89.37 ± 15.84
D_{s0}^+ width model	LASS	2637.18 ± 16.78	201.73 ± 90.58	2590.06	97.33
	Unity	2636.46 ± 21.05	197.38 ± 77.30	2592.60	96.97
	$K_0^*(700)^0$ BW	2634.07 ± 15.15	178.80 ± 71.82	2585.23	92.38
	$r = 0$	2615.68 ± 8.45	112.83 ± 28.53	2591.16	88.11
	$r = 1$	2591.06 ± 6.30	90.21 ± 16.25	2591.45	90.19
D_{s1}^+ mass shape	D_{s1}^+ mass&width	2602.15 ± 6.94	89.49 ± 21.40	2591.58	85.07
	D_{s1}^+ width formula	2602.97 ± 5.90	94.46 ± 18.45	2591.34	89.39
	D_{s1}^+ mass resolution	2602.60 ± 5.95	94.01 ± 17.90	2591.03	88.95
$K^+\pi^-$ mass shape	$K_0^*(700)^0$ mass&width	2603.38 ± 6.11	95.40 ± 18.81	2591.57	90.24
	LASS model	2600.04 ± 5.63	91.83 ± 17.74	2588.65	86.73
d_0 variation	$d_0 = 1.5\ \mathrm{GeV}^{-1}$	2607.43 ± 6.55	105.27 ± 23.44	2592.03	92.74
	$d_0 = 4.5\ \mathrm{GeV}^{-1}$	2600.40 ± 5.70	90.49 ± 16.86	2591.20	88.67
Including $c\bar{c}$	$\psi(3770)$	2605.19 ± 6.22	100.49 ± 20.17	2592.39	94.77
	$\chi_{c2}(2P)$	2602.52 ± 5.86	92.89 ± 18.18	2591.20	88.00
MC correction	L0Hadron_TOS 5 bins	2602.83 ± 5.92	94.65 ± 18.45	2591.13	89.53
	L0Hadron_TOS 15 bins	2603.04 ± 5.98	95.62 ± 18.82	2591.14	90.37
	B^0 kinematic 3 bins	2603.05 ± 5.89	94.43 ± 18.42	2591.43	89.37
	B^0 kinematic 10 bins	2603.04 ± 5.91	94.47 ± 18.46	2591.41	89.41
	nTracks 6 bins	2602.83 ± 5.88	93.98 ± 18.35	2591.29	88.97
	nTracks 18 bins	2602.91 ± 5.92	94.42 ± 18.42	2591.28	89.34
Momentum calibration	$\delta\eta = -3 \times 10^{-4}$	2602.47 ± 5.92	94.06 ± 18.60	2590.86	88.98
	$\delta\eta = +3 \times 10^{-4}$	2602.94 ± 5.95	94.82 ± 18.60	2591.22	89.68

A.3 Tests of the $D_{s0}(2590)^+$ width parameterization

As mentioned in Sec. 3.9, the partial width $\Gamma^{D_{s0}\to DK\pi}(\mathrm{m})$ is set to constant and its width fraction r is fixed to 0.5 in the default fit result. Then three alternative three-body width formulas are investigated and different value of r are tested to evaluate the systematic effect on the measured properties in Sec. 3.10.1. This section describes the detailed information of the fits using three-body width formulas for $\Gamma^{D_{sk}\to DK\pi}$.

A.3.1 J^P confirmation using three-body width formulas for $\Gamma^{D_{sk}\to DK\pi}$

The three-body width formulas of $\Gamma^{D_{sk}\to DK\pi}$ described in Sec. 3.7 instead of the constant are tested in the amplitude fits with the width fraction r free for the three spin-parity hypotheses of the $D_{s0}(2590)^+$ state. The resulted $\sqrt{-2\Delta\ln\mathcal{L}}$ values are listed in Table A.2. The $J^P = 1^+$ and $J^P = 2^-$ are strongly rejected for all $D_{s0}(2590)^+$ width models.

Table A.2 $\sqrt{-2\Delta\ln\mathcal{L}}$ for different spin-parity hypotheses and $D_{s0}(2590)^+$ width model. r is also shown.

J^P	$\Gamma^{D_{sk}\to DK\pi}$	r	$\sqrt{-2\Delta\ln\mathcal{L}}$
0^-	Constant	1.00 ± 0.98	0
	LASS	0.64 ± 0.49	$\sqrt{-1}$
	Unity	0.64 ± 0.74	$\sqrt{-1}$
	$K_0^*(700)^0$ BW	0.60 ± 0.35	0
1^+	Constant	0.77 ± 0.75	15
	LASS	0.84 ± 0.10	14
	Unity	0.81 ± 0.11	14
	$K_0^*(700)^0$ BW	0.77 ± 0.10	14
2^-	Constant	0.00 ± 0.99	17
	LASS	0.40 ± 0.19	15
	Unity	0.45 ± 0.08	15
	$K_0^*(700)^0$ BW	0.00 ± 0.01	17

A.3.2 Amplitude fit results using three-body width formulas for $\Gamma^{D_{sk}\to DK\pi}$

The $-2\Delta\ln\mathcal{L}$ value is scanned at different values of r in the range of [0, 1] using the different width formulas of the $D_{s0}(2590)^+$ state, shown in Fig. A.4. The variation is no

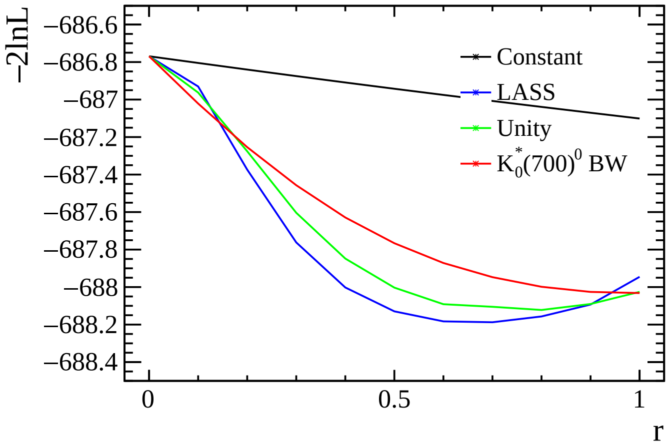

Figure A.4 $-2\ln\mathcal{L}$ in the r range [0, 1] for $J^P = 0^-$ using different $D_{s0}(2590)^+$ width models. The variation of $-2\ln\mathcal{L}$ is no more than 2 for all the cases.

more than 2, supporting that the width fraction r cannot be determined under the current data statistics and fixing it to 0.5 in the default fit is an adequate choice.

The fitted BW masses and widths, as well as the corresponding pole parameters for different values of r are shown in Figs. A.5 and A.6. Large variations are seen for the BW masses and widths for different r assignments, while the pole parameters are stable. This can be further confirmed graphically by the almost the same peak position and FWHM of $D_{s0}(2590)^+$ BW mass lineshapes in Fig. A.7.

From Fig. A.7 and A.8, it is seen that the main discrepancies of the BW line shape is the higher-mass tail. Faster decrease at the higher mass is seen with the increase of the value of r for all the width models, as shown in Fig. A.7. The suppression at the higher mass is also stronger for the LASS and Unity models than that for the $K_0^*(700)^0$ BW model. The reason for the above phenomena roots in the behavior of the $\Gamma^{D_{sk}\to DK\pi}$ with the increase of $m_{D^+K^+\pi^-}$, shown in Fig. A.9, where more rapid increase of the $D_{s1}(2536)^+$ width is seen for the LASS and Unity models, leading to the faster decrease in the BW mass lineshapes. Consequently, the $D_{s0}(2590)^+$ and NR fit fractions, and their interference fraction, vary a lot for different width models and different values of r, as shown in Fig. A.10. The large variances cause the large systematic uncertainty of these quantities, as listed in Table 3.12.

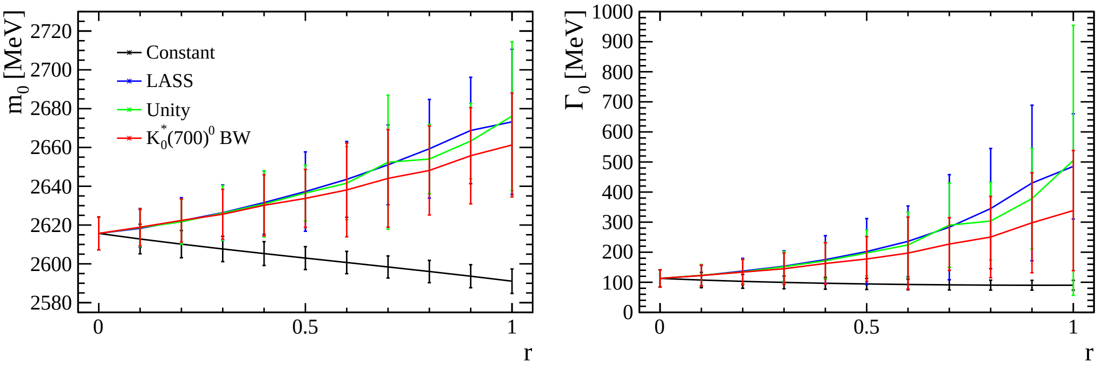

Figure A.5 BW mass m_0 and width Γ_0 of the $D_{s0}(2590)^+$ state in the r range $[0, 1]$ determined in the amplitude fit for $J^P = 0^-$. The statistical uncertainties from the fit are also shown. Large variations are seen for different r assignments.

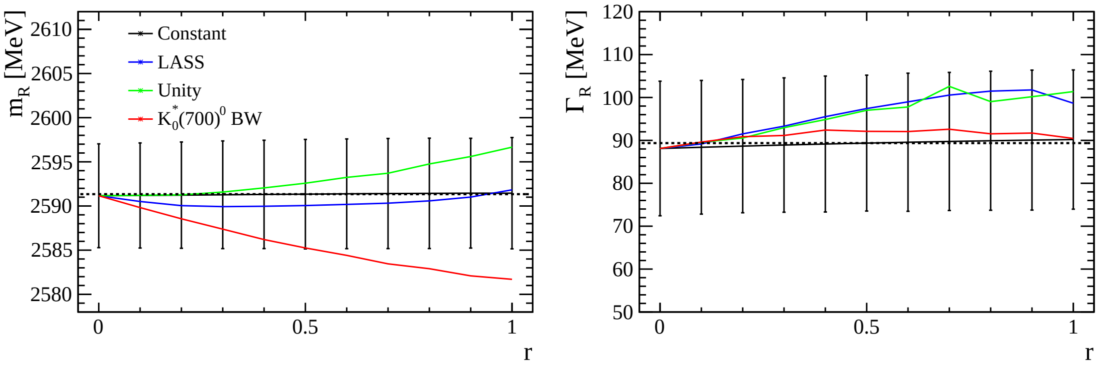

Figure A.6 Pole mass m_R and width Γ_R of the $D_{s0}(2590)^+$ state in the r range $[0, 1]$ for $J^P = 0^-$ corresponding to the BW parameters in Fig. A.5, where the statistical uncertainty of the three-body width cases are not shown due to the complexity of calculation. The variations of the pole parameters at $r = 0.5$ for different width formulas are taken systematic uncertainties of the pole parameters.

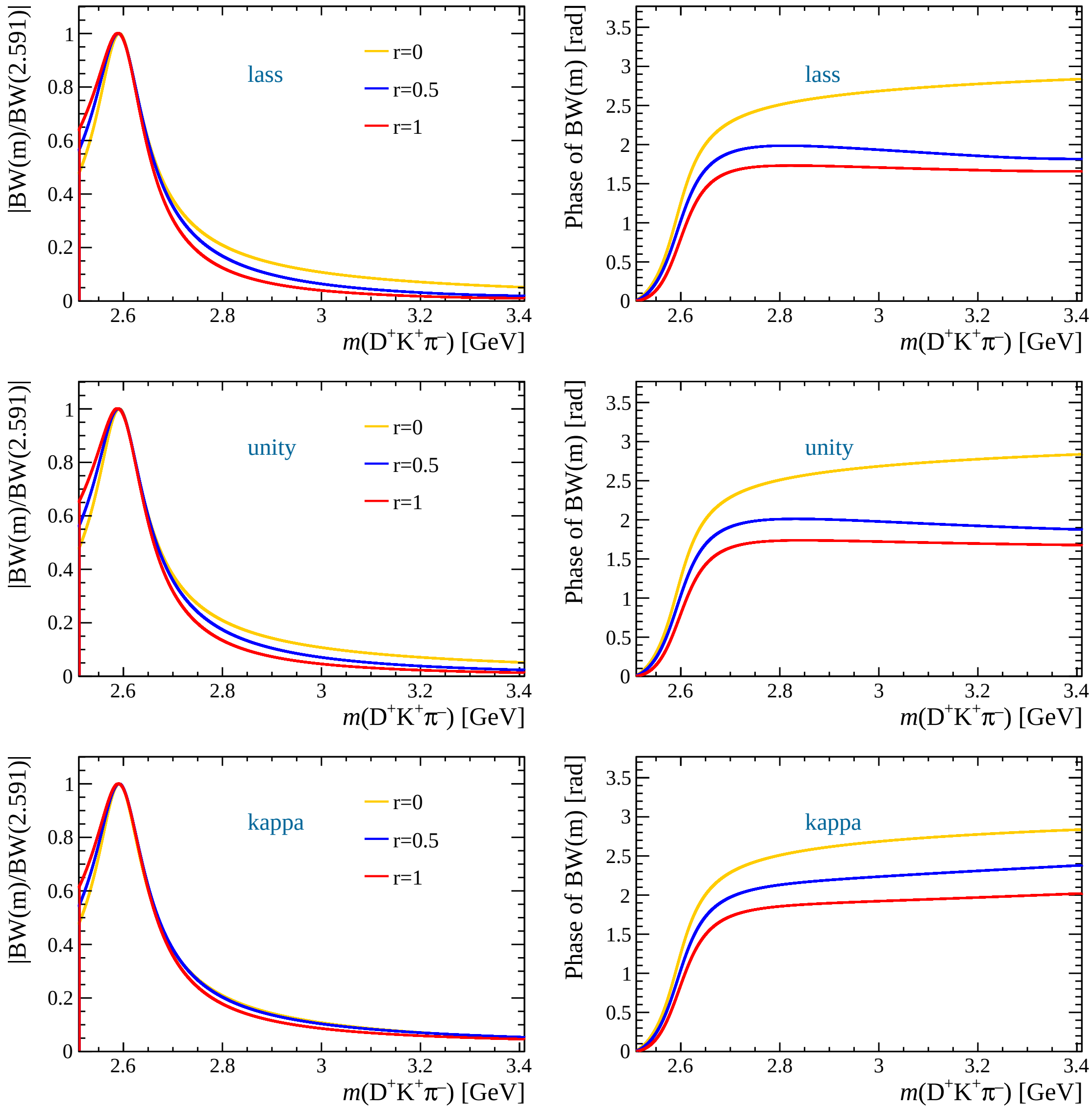

Figure A.7 BW mass lineshapes for different $\Gamma^{D_{sk} \to DK\pi}$ formulas with different r assignments. For all the width models, faster decrease at the higher mass is seen for larger r.

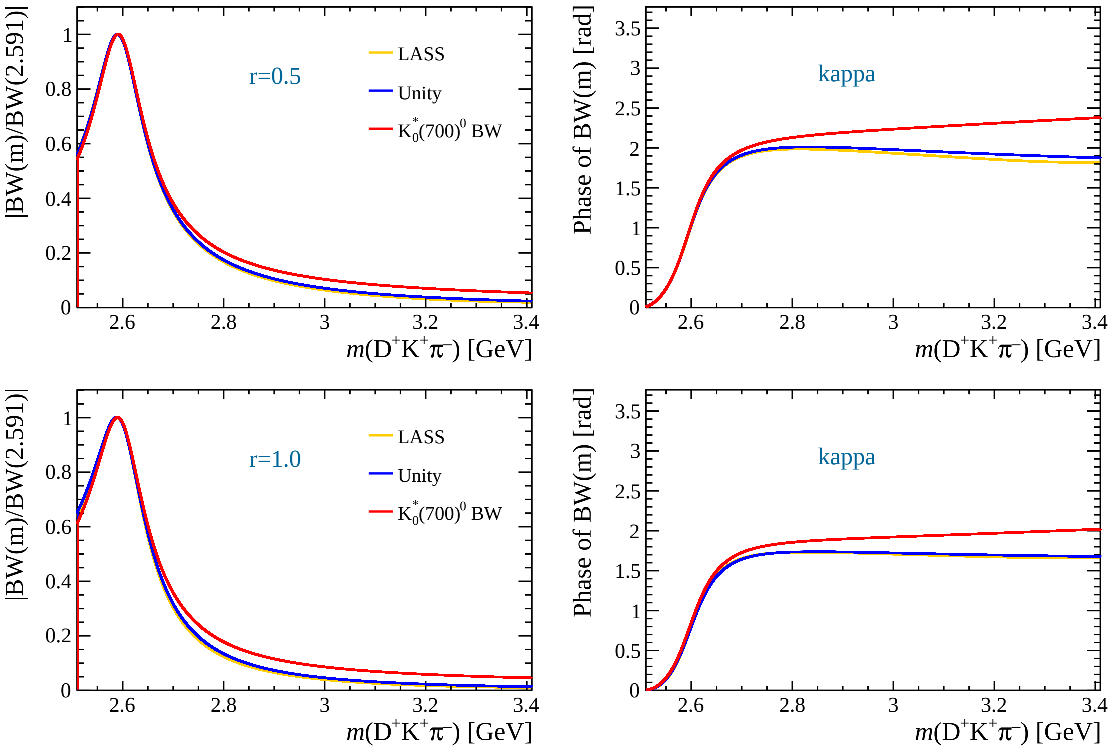

Figure A.8 BW mass lineshapes for different r assignments with different $\Gamma^{D_{sk}\to DK\pi}$ formulas. Faster decrease at the higher mass is seen for LASS and Unity model, compared to that of the $K_0^*(700)^0$ BW model.

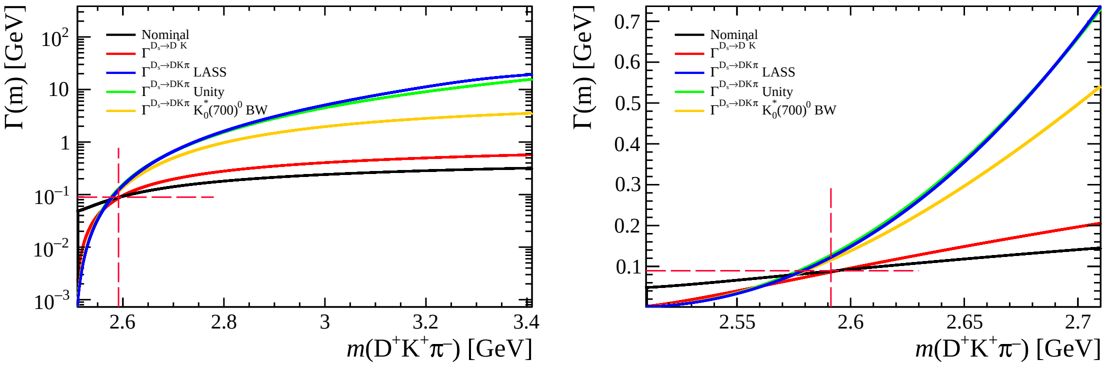

Figure A.9 $D_{s0}(2590)^+$ width function for different model. The right plot shows the zoomed-in region at the $D_{s0}(2590)^+$ peak region. The red dashed lines show the pole mass and width. Faster increase at the higher mass is seen for LASS and Unity model.

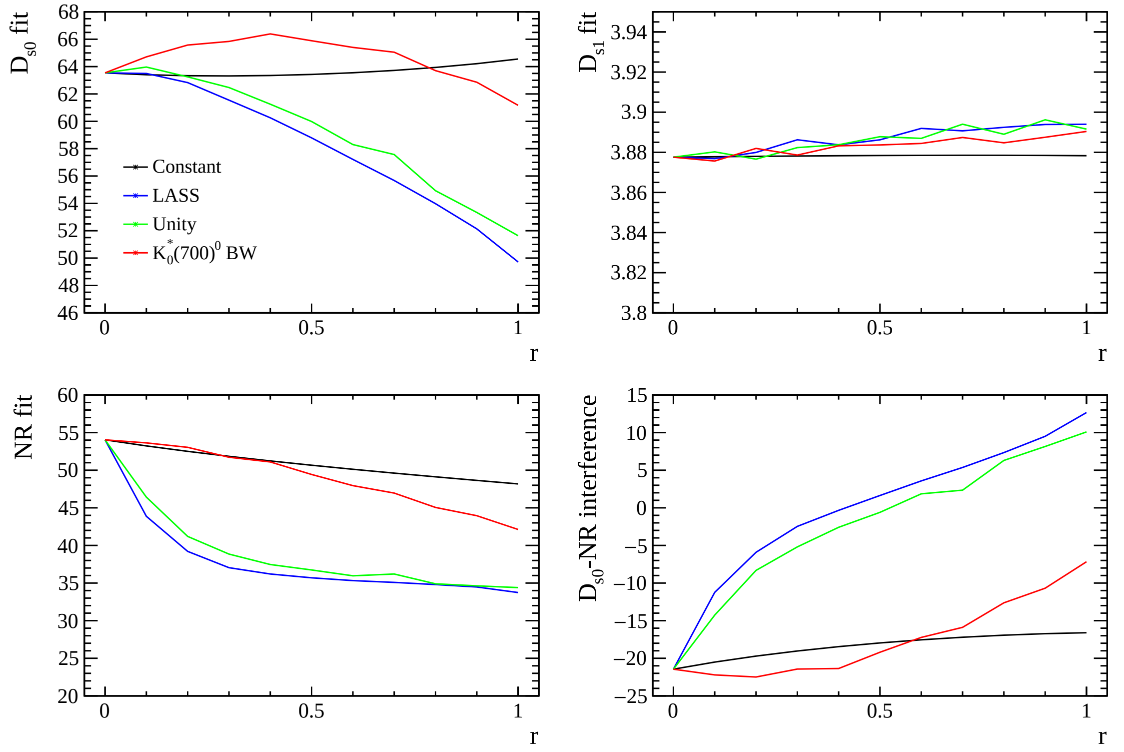

Figure A.10 $D_{s0}(2590)^+$, $D_{s1}(2536)^+$ and NR fit fraction as well as the $D_{s0}(2590)^+$-NR interference fraction for different r assignments with different $\Gamma^{D_{sk} \to DK\pi}$ models. The $D_{s1}(2536)^+$ fit fraction is stable, while others vary a lot due to the different behavior of the models at the higher $D^+K^+\pi^-$ mass.

A.4 Binning schemes for MC weight histograms

This section shows the binning schemes to obtain the three weights for the default results in Sec. 3.5 and the systematic studies in Sec. 3.10.7.

For the L0Hadron_TOS efficiency weight, the range of max_PT is $(1.8 \times 10^3,\ 15 \times 10^3)$ MeV, which is uniformly divided into 10 bins, 5 (15) bins, for nominal analysis and systematic study, respectively.

For the B^0 kinematic weight, the bin widths of B^0 momentum and B^0 transverse momentum are not uniform due to the low statistics for high momentum and transverse momentum. The binning schemes are listed in Table A.3.

For the nTracks weight, the bin width of nTracks is not uniform due to the low statistics for high nTracks. The binning schemes are listed in Table A.4.

Table A.3 Binning schemes for the B^0 p and p_{T} in kinematic correction weight extractions (Unit: GeV).

Default		Systematic studies			
5 bins		3 bins		10 bins	
B^0 p	B^0 p_T	B^0 p	B^0 p_T	B^0 p	B^0 p_T
$[0, 98.5]$	$[0, 8.2]$	$[0, 121]$	$[0, 9.8]$	$[0, 81]$	$[0, 6.8]$
$(98.5, 132]$	$(8.2, 10.6]$	$(121, 192.5]$	$(9.8, 14]$	$(81, 98.5]$	$(6.8, 8.2]$
$(132, 174]$	$(10.6, 13.1]$	$(192.5, 1600]$	$(14, 100]$	$(98.5, 115]$	$(8.2, 9.4]$
$(174, 239]$	$(13.1, 16.6]$			$(115, 132]$	$(9.4, 10.6]$
$(239, 1600]$	$(16.6, 100]$			$(132, 152]$	$(10.6, 11.7]$
				$(152, 174]$	$(11.7, 13.1]$
				$(174, 202]$	$(13.1, 14.6]$
				$(202, 239]$	$(14.6, 16.6]$
				$(239, 303]$	$(16.6, 19.9]$
				$(303, 1600]$	$(19.9, 100]$

Table A.4 Binning schemes of nTracks in nTracks weight determinations.

Default	Systematic studies		
10 bins	6 bins	18 bins	
[0, 50]	[0, 100]	[0, 25]	(25, 50]
(50, 100]	(100, 200]	(50, 75]	(75, 100]
(100, 150]	(200, 300]	(100, 125]	(125, 150]
(150, 200]	(300, 400]	(150, 175]	(175, 200]
(200, 250]	(400, 500]	(200, 225]	(225, 250]
(250, 300]	(500, 600]	(250, 275]	(275, 300]
(300, 350]		(300, 325]	(325, 350]
(350, 400]		(350, 375]	(375, 400]
(400, 500]		(400, 500]	(500, 600]
(500, 600]			

ACKNOWLEDGEMENTS

感谢我的导师张黎明副教授对本论文工作的精心指导。张老师的科研创新精神和科研能力是我以后工作学习中的榜样。感谢杨振伟教授在学习、科研及生活中的帮助。尤其在我迷茫之时，和杨老师的交谈，使我重塑良好心态。感谢高原宁教授，他豁达洒脱的人生态度对我有着巨大影响。感谢近物所老师们在本论文课题各个环节提供帮助和建议。感谢实验室一众大小朋友的帮助。感谢父母一如既往的关心和支持。

承蒙学校、院系、自然科学基金委和LHCb合作组等提供平台和资源，特此致谢。